DESIGN, MODELING AND CONTROL OF MICRO-SCALE AND MESO-SCALE TENDON-DRIVEN SURGICAL ROBOTS

A Dissertation
Presented to
The Academic Faculty

By

Yash Chetan Chitalia

In Partial Fulfillment
of the Requirements for the Degree
Doctor of Philosophy in
Robotics

Georgia Institute of Technology

August 2021

DESIGN, MODELING AND CONTROL OF MICRO-SCALE AND MESO-SCALE TENDON-DRIVEN SURGICAL ROBOTS

Thesis committee:

Dr. Jaydev P. Desai, Advisor
Wallace H. Coulter Department of Biomedical Engineering
Georgia Institute of Technology

Dr. Frank L. Hammond III
George W. Woodruff School of Mechanical Engineering
Georgia Institute of Technology

Dr. Ellen Yi Chen Mazumdar
George W. Woodruff School of Mechanical Engineering
Georgia Institute of Technology

Dr. Zachary L. Bercu, MD, RPVI
Department of Radiology and Imaging Sciences, School of Medicine
Emory University

Dr. Joshua Chern, MD, PhD
Department of Neurosurgery
Emory University

Date approved: June 30, 2021

Sacrifices must be made!

Otto Lilienthal (last words)

Dedicated to all the people this work might someday help and heal.

ACKNOWLEDGMENTS

First and foremost, I would like to thank my advisor, Dr. Jaydev P. Desai, for giving me this opportunity to contribute to the fascinating field of medical robotics. His guidance has helped me navigate through many academic hurdles. I will eternally be grateful to him for this opportunity and his support throughout this journey. I would like to specially thank Dr. Joshua J. Chern, for the many days spent brainstorming over my robots and allowing us to observe him at work. His work serves as an inspiration for much of this thesis. I would also like to thank Dr. Frank L. Hammond, Dr. Ellen Mazumdar, and Dr. Zachary L. Bercu for serving on my dissertation committee.

Research reported in this dissertation was supported in part by funding from the Children's Healthcare of Atlanta, Georgia Research Alliance, and the GT/Emory Coulter Translational Research Partnership Program. Research reported in this dissertation was also supported in part by the National Heart, Lung, And Blood Institute of the National Institutes of Health under Award Number R01HL144714 and the Eunice Kennedy Shriver National Institute Of Child Health & Human Development of the National Institutes of Health under Award Number R21HD101321. The content, opinions, findings, and conclusions or recommendations expressed in this material are solely the responsibility of the author and does not necessarily represent the official views of the National Institutes of Health.

I want to thank the staff at Georgia Tech who contributed in innumerable ways to the work I have done here. I would like to thank Mr. Richard Shafer in particular, my partner-in-crime on femtosecond laser wizardry. Also Ms. Camellia Henry, whose help through all these years kept the ride very smooth. I also would like to thank all my fellow RoboMed lab members, past and present. This work would have been incomplete without their able assistance and guidance. Specifically, I would like to thank Dr. Seokhwan Jeong, a fantastic collaborator and researcher par excellence. Last but not least, I would like to thank Drs. Niyati and Chetan Chitalia, my best friends, able doctors, and good people.

TABLE OF CONTENTS

LIST OF TABLES

LIST OF FIGURES

SUMMARY

Manual manipulation of passive surgical tools is time consuming with uncertain results in cases of navigating tortuous anatomy, avoiding critical anatomical landmarks, and reaching targets not located in the linear range of these tools. For example, in many cardiovascular procedures, manual navigation of a micro-scale passive guidewire results in increased procedure times and radiation exposure. This thesis introduces the design of two steerable guidewires: 1) A two degree-of-freedom (2-DoF) robotic guidewire with orthogonally oriented joints to access points in a three dimensional workspace, and 2) a micro-scale coaxially aligned steerable (COAST) guidewire robot that demonstrates variable and independently controlled bending length and curvature of the distal end. The 2-DoF guidewire features two micromachined joints from a tube of superelastic nitinol of outer diameter 0.78 mm. Each joint is actuated with two nitinol tendons. The joints that are used in this robot are called bidirectional asymmetric notch (BAN) joints, and the advantages of these joints are explored and analyzed. The design of the COAST robotic guidewire involves three coaxially aligned tubes with a single tendon running centrally through the length of the robot. The outer tubes are made from micromachined nitinol allowing for tendon-driven bending of the robot at variable bending curvatures, while an inner stainless steel tube controls the bending length of the robot. By varying the lengths of the tubes as well as the tendon, and by insertion and retraction of the entire assembly, various joint lengths and curvatures may be achieved. Kinematic and static models, a compact actuation system, and a controller for this robot are presented. The capability of the robot to accurately navigate through phantom anatomical bifurcations and tortuous angles is also demonstrated in three dimensional phantom vasculature. At the meso-scale, manual navigation of passive pediatric neuroendoscopes for endoscopic third ventriculostomy may not reach target locations in the patient's ventricle. This work introduces the design, analysis and control of a meso-scale two degree-of-freedom robotic bipolar electrocautery tool that increases the

workspace of the neurosurgeon. A static model is proposed for the robot joints that avoids problems arising from pure kinematic control. Using this model, a control system is developed that comprises of a disturbance observer to provide precise force control and compensate for joint hysteresis. A handheld controller is developed and demonstrated in this thesis. To allow the clinician to estimate the shape of the steerable tools within the anatomy for both micro-scale and meso-scale tools, a miniature tendon force sensor and a high deflection shape sensor are proposed and demonstrated. The force sensor features a compact design consisting of a single LED, dual-phototransistor, and a dual-screen arrangement to increase the linear range of sensor output and compensate for external disturbances, thereby allowing force measurement of up to 21 N with 99.58% accuracy. The shape sensor uses fiber Bragg grating based optical cable mounted on a micromachined tube and is capable of measuring curvatures as high as 145 m^{-1}. These sensors were incorporated and tested in the guidewire and the neuroendoscope tool robots and can provide robust feedback for closed-loop control of these devices in the future.

CHAPTER 1
INTRODUCTION AND BACKGROUND

1.1 Motivation

1.1.1 Cardiovascular Diseases

Cardiovascular diseases (CVDs) are a group of disorders of the heart and blood vessels that can lead to heart attack, heart failure, cardiomyopathy, and peripheral vascular disease, accounting for an estimated 17.8 million deaths in 2017 with projected costs reaching $1.1 trillion by 2035 [1]. CVDs are the leading global cause of death, eclipsing deaths from all types of cancers combined [2]. The prevalence of peripheral vascular disease, in particular, has increased globally by 34.4 % between 2005 and 2015 [3], resulting in approximately 60,000 deaths in the United States in 2015 [1]. PVD is caused due to lesions formed in the vascular structures at the extremities of the patients' bodies, such as calcification in the arteries at the lower legs and feet i.e., Lower Extremity Arterial Disease (LEAD). Endovascular treatment for critical limb ischemia, a form of PVD, has increased from 5.1% to 11.0% from 2003-2011 in the United States, contributing to lower hospital stays, lower mortality, and lower risk of limb amputation [1]. In the endovascular treatment of most CVDs (including PVD), clinicians typically begin the procedure by inserting a guidewire from a suitable location in the patient's vasculature to the blocked blood vessel. This guidewire is a passive wire, typically made of nitinol, with a diameter of 0.3556 mm - 0.889 mm (typically in the range of 0.3556 mm - 0.4572 mm). Once the guidewire is navigated manually to the blocked vasculature, the clinician can use the wire as a carrier for a variety of catheters that help remove the blockage. To navigate the guidewire to the target location, clinicians usually determine the optimal access strategy considering pathophysiology, potential treatment options, vascular anatomy/possible variants of each patient

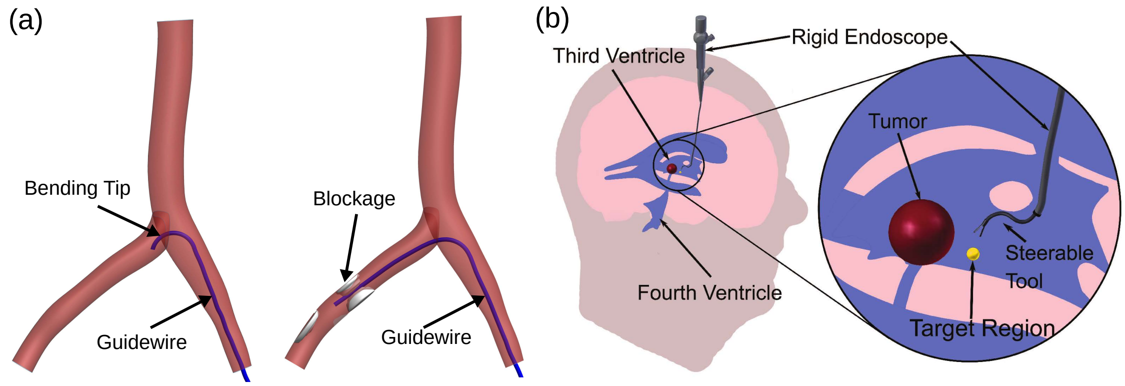

Figure 1.1: (a) Contralateral retrograde femoral approach for infrainguinal occlusions requires steerability around the aortic bifurcation, (b) Proposed steerable instruments for endoscopic third ventriculostomy (ETV) in cases of obstructive hydrocephalus [Image courtesy: Nancy Deaton for Fig. 1.1(b).]

[4]. For example, in the treatment of Peripheral Vascular Diseases (PVDs), the physician usually makes an incision into the femoral artery of the healthy leg in a procedure commonly known as the contralateral retrograde femoral approach [5] (see Fig. 1.1(a)). However, angulation, vessel tortuosity or calcification of the blood vessel precludes the use of this approach [6] and the clinician requires extra operation such as advancing a catheter over the guidewire and chaining the wire to stiffer/alternative guidewires [7, 8]. However, this requires wires of multiple stiffnesses, and could result in twisting of the wires. This approach also increases the diameter of the guidewire, making it difficult for the wire to reach smaller peripheral arteries. Otherwise, alternative paths such as approach from an upper extremity [9], popliteal artery [10], or dorsalis pedis artery are considered [11]. In any case, navigation of the guidewire remains largely manual, with proximal insertion, retraction and rotation being the only degrees-of-freedom available to the clinician to control the distal tip. In many cases, high tortuosity or the blood vessels may restrict success of the ability to reach target manually [12]. High tortuosity may also result in kinking and breakage of the guidewire [13]. Manual navigation also results in an inability to control angle of entry into a chronic total occlusion (CTO), where the diseased artery may be almost completely blocked. This results in an inability to cross the CTO, which results in

80% of failure cases with CTOs [14]. Furthermore, the clinician has little control over the stiffness of the guidewire. While soft guidewires may help in navigating tortuous vasculature without the possibility of perforation, stiffer guidewires are required to overcome calcification [15]. Stiffness of the wire tip cannot be changed in-situ and the wires must be exchanged. This exchange, coupled with the difficulties of manual navigation result in increased procedure times and exposure to radiation [16, 17]. In a survey conducted by Klein *et al.* in 2014, over 49% of the interviewed interventional cardiologists reported orthopedic injuries and approximately 7% reported reduced workload due to excessive radiation exposure [18]. All of these concerns motivate the use of robotic devices for percutaneous coronary intervention (PCI), which has demonstrated high success rates with up to 97% reduction in radiation exposure [19].

1.1.2 Pediatric Hydrocephalus

Hydrocephalus is a common pediatric disease at a rate of about 0.7 cases per thousand in most developed countries. This number is even higher in developing countries [20]. This condition occurs due to a buildup of cerebrospinal fluid (CSF) in the brain leading to the enlargement of the ventricles and intracranial pressure increase. CSF is believed to be produced in the lateral ventricles, passing successively through third ventricle, cerebral aqueduct, fourth ventricle prior to its exit into the cisternal spaces around the craniocervical junction. One of the most common causes of hydrocephalus is due to blockage of CSF circulation at the level of cerebral aqueduct, which connects the third and fourth ventricles (see Fig. 1.1(b)). Delay in the treatment of hydrocephalus can result in the loss of motor function, epilepsy, chronic headaches, sensory damage and death [21]. Most commonly, clinicians would treat hydrocephalus by diverting the CSF through implantation of a silicone tubing between the brain and the abdomen (CSF shunts). However, six decades worth of experiences with CSF shunts had shown that they are imperfect devices, with the blockage of shunts being the number one cause of mobility and mortality [22, 23]. An alternative to CSF shunt placement were brain endoscopic procedures, with the purpose of removing the blockage or bypassing the blockage within the brain, thus avoiding implantation of a CSF shunt altogether. One of the most common brain endoscopic procedures is the endoscopic third ventriculostomy (ETV). During ETV, the surgeon first makes an entry into the ventricle using an endoscope, composed of a high definition camera, a light source, and working channels. Under direct visualization, she then makes a perforation on the floor bottom wall of the third ventricle using a rigid instrument passed through one of the working channels of the endoscope. This perforation allows the CSF to bypass the blockage at the cerebral aqueduct and to egress into the prepontine cisterns located under the third ventricle. In this procedure, a rigid endoscope such as the MINOP Neuroendoscope (Aesculap Inc., PA, United States) or the OI HandyPro endoscope (Karl Storz SE & Co. KG, Tuttlingen, Germany) is used along with rigid minimally invasive surgical (MIS) instruments to operate at the target site in the brain at the floor of the third ventricle. The instruments used with these endoscopes must be cylindrical, with a diameter of about 1 mm - 2 mm [24]. For example, a cylindrical rigid instrument called the NICO Myriad resection tool (NICO Corporation, IN, United States) coupled with the rigid MINOP endoscope (with a built-in camera) has seen success in cases of loculated hydrocephalus [25]. While the ETV procedure has seen a success rate of over 80% in infants [20, 26, 27], reaching a suitable location in the third ventricle for penetration in an ETV procedure is non-trivial. Because of the rigid nature of the endoscope, a linear pathway from the scalp, through the brain parenchyma, down to the level of the third ventricular floor is required. This linear pathway must avoid traversing important blood vessels, functional areas and cranial nerves to avoid hemorrhaging [28]. Further complicating the issue is the fact that the brain anatomy is often distorted due to the disease process. Because of all these restrictions, finding an optimal linear pathway may not always be possible. Furthermore, the ETV procedure is often combined with cauterization of the choroid plexus (the major source of CSF secretion) in a procedure called CPC, showing superior results to ETV alone in infants under the age of one [29], with higher likelihood of shunt independence [30]. A rigid endoscope with rigid tools leads to reduced maneuverability and visualization of the choroid plexus, especially in the temporal horns and other areas of the ventricular cavity. In preliminary studies, comparisons between flexible and rigid endoscopes for the ETV/CPC procedure has suggested better outcomes with flexible endoscopes (although the authors concede that the difference could be a result of other contributing factors) [31]. However, flexible endoscopes suffer from lower optical quality and potential for disorientation in a non-straight configuration, which may reduce over time and with training [32].

A more ideal situation would be to design steerable, flexible instruments to circumvent obstacles to reach suitable target locations passed through a rigid endoscope [33] (see Fig. 1.1(b)). Furthermore, it is important for this flexible robotic tool to be highly maneuverable in its workspace, so that it can have a better chance of avoiding obstacles. Finally, in the operating room, it is often desirable to have two surgeons participating in these endoscopic surgeries, where one surgeon directs the endoscope, inserting and retracting the scope body, while the other surgeon operates the instrument itself, including the insertion, retraction and rotation of the tool in the working channel of the endoscope. As a result, any robotic solution to this problem must include actuation strategies that must fit into a small hand-held package. All of the above requirements are addressed in the device proposed in this thesis.

1.2 Related Works

1.2.1 Surgical Robots in Cardiovascular Surgery

The first recorded use of robotics for cardiovascular surgery was in May 1998, where the da Vinci robot (Intuitive Surgical, Mountain View, CA, United States) was used successfully in atrial septal defect repair and a septal aneurysm resection in a 52 year old patient [34]. Starting in the same month, the Intuitive Surgical system was used to perform coronary artery bypass grafting (CABG) procedures on five patients [35]. In the same year, the voicecontrolled ZEUS system (formerly Computer Motion Inc., Goleta, CA, United States) was used for endoscopic CABG on seven patients [36]. By 2001, robotic surgeries with the ZEUS and the da Vinci robots had been widely adopted, with the da Vinci system being used in 1250 endoscopic cardiovascular surgeries like CABG, mitral valve surgeries, and vascular harvesting [37]. In interventional cardiology, an extremely important motivation behind robotics was the increasing concern over long-term consequences of orthopedic load and radiation exposure during percutaneous coronary intervention (PCI) [38]. In the industry and academia, small-scale catheters have traditionally used five types of actuation strategies for steering: magnetic, thermal (SMA-based), pressure-based, and mechanical (tendon-driven or concentric) [39].

Magnetic navigation of a catheter was first explored in a complex cardiovascular case back in 1991, where a strong permanent magnet was moved across the body of a neonate suffering from a complicated congenital heart condition [40]. By 2002, Faddis *et al.* had tested a novel magnetic navigation system (MNS) called the Telstar system (Stereotaxis Inc., St. Louis, MO, United States) to navigate a magnetic ablation catheter to 51 total target sites in 6 animals (dogs and pigs) with a sub-millimeter accuracy [41]. The Telstar MNS consisted of three orthogonal superconducting electromagnets, a bi-planar fluoroscopy system and a control computer. The controlling computer generates an electric current across the three magnets controlling the orientation of the resultant composite magnetic field, which in turn controls the orientation of an ablation catheter equipped with a permanent magnetic tip. Insertion/retraction of the catheter was performed manually. The authors concluded that navigation with the MNS was precise,safe, and had comparable or better success rates in comparison to standard ablation catheters in navigation to all chambers of the heart. Between May-October 2003, a newer MNS from Stereotaxis Inc. called the Niobe was tested on 42 patients for catheter-based mapping and ablation of atrioventricular nodal re-entrant tachycardia [42]. The system consisted of two permanent magnets on either side of the hospital bed. The relative position of these permanent magnets could be remotely controlled with respect to each other thereby allowing for modulation of the direction of a stable external magnetic field of 0.08 T. This field was used in conjunction with a magnetized catheter to orient the tip of the catheter, while a motor drive unit (Cardiodrive, Stereotaxis Inc.) was responsible for the axial motion of the catheter. Since then, the Niobe system has been used for a number of catheter ablations for a variety of conditions like atrial fibrillation or atrioventricular reentry tachycardia [43, 44, 45], magnet-tipped guidewire navigation in PCI for coronary artery disease [16, 46], and capsule endoscopy for gastroenterology [47]. However, the Niobe system has several limitations such as a bulky and time-consuming setup, lack of speed in rotating the permanent magnets and the inability to modulate and reduce/eliminate the magnetic field entirely requiring OR rooms with magnetic shielding [48, 49]. More recently Stereotaxis has unveiled their newest addition to their line of MNS products known as the Genesis system, that accounts for some of these limitations with a speedier magnet rotation system. The Catheter Guidance Control and Imaging (CGCI) system from Magnetics Corp. (Inglewood, CA, United States) is another commercially available MNS that offers a solution to the low speed of the rotating permanent magnets in the Niobe system [50]. The CGCI system consists of 8 electromagnets that generate a spherical magnetic field around the patient's torso. Unlike the Niobe system, these magnets are stationary, but can generate and modify in near real-time, a dynamic magnetic field in any particular direction. The structure of the eight electromagnets has been designed to reduce parasitic external magnetic fields, thereby eliminating the need for an OR room with magnetic isolation. The ability to control the amplitude of the applied resultant magnetic field on the magnetized catheter also differentiates the CGCI system from the Niobe. In the last decade, few animal [51] and human trials [52, 53] were conducted with the CGCI system with promising results. The authors report increased speed of operation and potential increase in contact forces arising from an increased magnetic field strength of 0.16 T. However, unlike the Niobe system, the surgeon cannot be present in the vicinity of the patient due to the bulky magnets surrounding the surgical site making monitoring the patient's condition extremely challenging; a major limitation of the CGCI system.

A large body of research has explored magnetic navigation systems for a variety of minimally invasive cardiovascular applications, and so we will look into these in some depth. Traditionally, these systems can be both stationary or mobile. Among the stationary systems, the OctoMag system proposed by Kummer *et al.* of the Multi-Scale Robotics Laboratory (ETH Zurich, Switzerland) has been widely explored for untethered and tethered microbot control [54] (see Fig. 1.2(a)). The OctoMag system consists of an 8 soft-magnetic-core electromagnet setup generating a complex non-uniform magnetic field in the workspace, and was initially proposed to achieve 5-DoF control of an untethered microbot for retinal procedures. This system was then miniaturized by Kratochvil *et al.* for a spherical workspace of 10 mm, known as the MiniMag, such that the entire electromagnet setup was moved to one hemisphere (unlike the OctoMag, which completely surrounds the target area) [55]. Jeon *et al.* designed a flexible microbot tipped guidewire for the MiniMag system [56] (see Fig. 1.2(b)). The body of the microbot was designed using a neodymium magnet encased within a polydimethylsiloxane (PDMS) cylinder with a microspring connecting the robot to the guidewire tip. The authors demonstrated the ability of the microbot to be steered in a two dimensional plane with the MiniMag system and extremely low-intensity magnetic fields (approximately 5-15 mT). The biocompatibility of this robot was also demonstrated in this work. Recently, the authors used the OctoMag system to steer an improved soft microbot attached to the tip of a guidewire in three dimensions [57]. The microbot was designed with two neodymium magnets of diameter 0.4 mm placed within a PDMS beam of diameter 0.5 mm, the proximal end of which was connected to a tradition 0.014" guidewire via a microspring. The distal tip orientation was then controlled using the OctoMag to achieve bending angles of up to almost 133°, while a master-slave system was used for the insertion and retraction of the guidewire. A commercially available MNS from the Multi-Scale Robotics Lab known as the Aeon Phocus (Aeon Scientific, Aeon Sci-

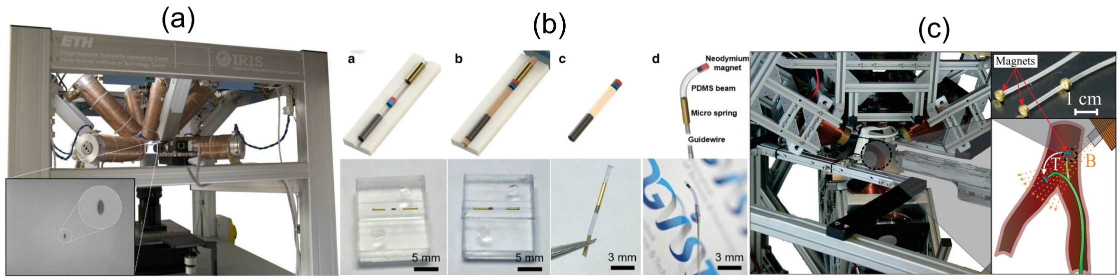

Figure 1.2: Examples of magnetic navigation systems in literature: (a) OctoMag system from ETH Zurich ©IEEE 2010 [54], (b) Guidewire robot for the MiniMag system [56], (c) BigMag system from the Surgical Robotics Laboratory at the University of Twente ©IEEE 2017 [59].

entific GmbH, Switzerland, now defunct), was also used to steer a magnetic microbot that was attached to the tip of a catheter using a tether [58]. While this approach allows for the use of commercially available catheters without the explicit design of flexible catheters, the design permits control only when the tether is in tension. Furthermore, the slow rotating magnetic field gradients allowed for very low bandwidth open-loop control of the tethered magnetic distal end of the robot. In 2015, Lalande *et al.* proposed a novel method to achieve steering of a magnetized guidewire tip by making use of a modified magnetic resonance imaging (MRI) system with an additional steering gradient coil system mounted on the MRI system. The authors propose a novel imaging and steering platform consisting of high-amplitude gradient generating coils for steering and low-amplitude coils for MR imaging along with a magnetic bead tipped guidewire [60]. However, presently, the coils used to steer the guidewire would interfere with the imaging and tracking system, and would have to be removed for imaging, making real-time tracking impossible. This resulted in a number of failures in reaching vascular target sites in the animal tests performed by the authors.

In 2017, the Surgical Robotics Laboratory (University of Twente, The Netherlands) introduced a six rotating electromagnetic coil setup known as the BigMag system that can generate a field of 40 mT in a spherical workspace of diameter 10 cm [59] (see Fig. 1.2(c)). The system consists of two mobile frames that hold three magnets each, both above and below the horizontal plane of the patient's torso. The six coils thus can apply 3D wrenches on the tip of a magnetized catheter for 3D steering of the catheter. The added advantage of the BigMag setup is that the reduced number of magnets allow for increased access to the surgical workspace. Using this system the authors have demonstrated 3D non-linear inverse-model position closed-loop control of a single passive magnet tipped continuum manipulator (catheter) under stereo-vision based shape and tracking feedback [61]. More recently a multi-magnet tipped continuum catheter of square cross-section of 1 cm x 1 cm was controlled using the BigMag system to achieve higher order shapes (S-Shaped curves, etc.) of the catheter tip [62].

Recently, Kim *et al.* proposed a way for avoiding the need to add magnets to the tip of guidewires/catheters by developing a novel soft guidewire tip with uniformly dispersed ferromagnetic microparticles within it and a hydrogel skin on the surface [63]. The authors composed the guidewire tip by mixing non-magnetized NdFeB particles with PDMS resin or dissolved TPU. The whole mixture was then magnetized by applying a strong impulse of magnetic fields. This magnetized ink was then printed or injection molded and heat treated to fuse with the guidewire body. As proof-of-concept, the authors demonstrated the navigation of the guidewire through 3D phantom vasculature using a single permanent magnet to orient the robot tip. While this work was demonstrated for a guidewire of outer diameter 0.5 mm, it demonstrated the ability to scale these types of systems further, since the ability to miniaturize this guidewire depends largely on the printer resolution.

While all of these commercial and academic achievements show promise and scalability, any MNS will not be able to completely eliminate three major limitations: 1) Usage in patients with implanted devices can potentially be impossible and dangerous, 2) Special shielding is required in the construction of the OR room where the MNS is placed due to the high permanent magnetic field (which limits its portability), 3) Requirement to use magnetic catheters, which make the surgical procedures impossible to conduct under MRI observation [64].

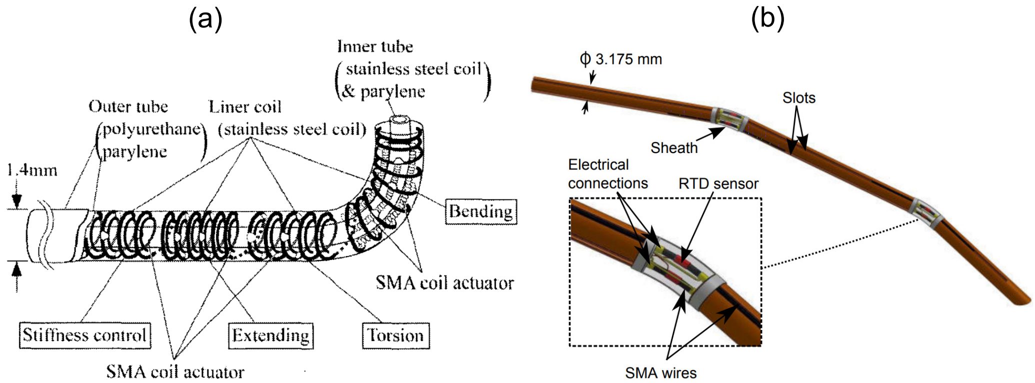

Figure 1.3: Examples of shape memory property used for active catheters in literature: (a) SMA driven nitinol catheter ©IEEE 2002 [66], (b) Multi-joint active cannula with antagonistically trained SMA wires ©IEEE 2012 [67].

In 2006, Beyar *et al.* described the first ever use of a remotely non-magnetically controlled robotic surgical system, known as the Remote Navigation System (NaviCath, Haifa, Israel) for percutaneous coronary interventions (PCIs) [65]. The RNS was introduced primarily as a way to minimize clinician exposure to radiation and secondarily as a promising way to improve stent placement precision. The RNS was designed as a bedside unit consisting of a mechanical transmission module to perform axial translation (insertion/retraction) and rotation of a guidewire. The mechanical transmission unit consisted of catheter and guidewire navigation units. The guidewire unit consisted of axial and torsional transmission mechanisms, while the catheter navigation unit consisted of two pairs of rollers for axial control and position feedback. A control unit, not present in the immediate vicinity of the patient was used to remotely control the degrees-of-freedom on the transmission module. This control unit consisted of a joystick (for continuous control) and a touchscreen interface (for making discrete steps). A non-steerable 0.014” guidewire was used by the authors for tests with 18 patients, with clinical success achieved in all cases. However, the procedures for which this system was initially used were fairly simple.

The shape memory effect displayed by a nickel titanium alloy known as ‘Nitinol’ has been used in the past to design thermally actuated miniature catheters. Two modes of operation are typically in use for nitinol: 1) Superelastic mode (where up to 8% strain in the material is recoverable), and 2) as Shape Memory Alloy (SMA) where the material transitions between Martensite and Austenite phases when thermally excited. In the shape memory mode of operation, the percentage of Nickel and Titanium, the cold working process, annealing time and temperature determine the transformation temperatures. Once annealed, the SMA demonstrates a one-way phase transformation when heated. In short, when the SMA is heated above its phase transformation temperature (determined by the annealing time and temperature), it undergoes a phase transition from Martensite phase to its Austenite phase thereby recovering its trained curvature. The curvature is trained into the material while annealing. Now, when the SMA wire is cooled back to room temperature, the phase transitions again from Austenite to twinned Martensite, without any changes in curvature.

In 2002, the authors in [66] and [68] designed a 0.5 mm diameter steerable guidewire consisting of a Nitinol SMA actuator and an outer stainless steel spring. The actuator consisted of a meandering design to improve bending and compression compliance of the actuator. This meandering shape was manufactured from a nitinol SMA sheet using photolithography and electrochemical etching (see Fig. 1.3(a)). The actuator was housed within the outer steel spring, and heated with an electric current passed through a lead wire attached to the actuator (causing the guidewire to reach angles as high as $60°$). When the heating was stopped, the outer spring allowed the actuator to return to a lower bending angle of $20°$. However, a completely straight configuration could not be achieved with this actuator, when the electric current on the actuator was turned off and the actuator was 'relaxed'. Some researchers have avoided this flaw by using a pair of antagonistically trained SMA wires to design SMA-driven robot joints [67, 69] (see Fig. 1.3(b)). Another early approach to the design of SMA-driven active catheter actuators was in 2006 by Tung *et al.*, where a laser-machined SMA nitinol tubing with an outer diameter of 1.27 mm was used (with a high transformation temperature of 112.6 °C) to design actuators [70]. However, the authors did not specify how the new actuator design could be incorporated into a catheter with the ability to reset its original shape on cooling. Ayvali *et al.* worked on the design of a multi-joint discretely actuated robotic steerable cannula with shape-memory nitinol actuators for PCI based diagnostic and therapeutic capabilities [71]. This robot had an outer diameter of 3 mm. Each SMA joint in the robot was characterized to find a temperature-bending angle relationship for temperature feedback control. Each joint was able to bend up to $\pm 19^{\circ}$ in phantom gelatin models. A novel SMA wire based soft torsional actuator was proposed by Shim *et al.* in 2015 for the design of a robotic catheter [72]. The actuator was designed by torquing a single SMA wire and housing it within a black of PDMS. When heated, the wire underwent torsion to recover its original shape thereby achieving torsional motion of the entire actuator system. The authors made use of this twisting actuator, in conjunction with a bending SMA-wire to design a two joint robotic catheter with one 80 mm torsion joint and a 50 mm bending joint and a total outer diameter of 4 mm. While the robot was capable of 1-DoF planar bending in any plane using a combination of bending and torsion, the authors did not address how the original shape of the catheter would be regained, and did not have antagonistic SMA wires built within the system. Recently, Sheng *et al.* designed a 5-DoF steerable robotic catheter for radiofrequency ablation for the treatment of atrial fibrillation [73]. Each actuator for the robot was designed to have two antagonistic SMA wires wrapped by Nichrome coils which were individually heated using Joule heating and encased within adapters of outer diameter 2.9 mm. The authors exploited the resistivity and tight wrapping of the Nichrome coils to achieve high temperatures with low electric currents. The authors demonstrated the feasibility of using this catheter by demonstrating it in a cadaver inferior vena cava. While SMA-driven actuators are scalable and MRI compatible, a major disadvantage of SMA-driven actuators is the low bandwidth of this modality of actuation. Due to the slow heating and cooling processes, without any active cooling strategies, these types of actuation strategies cannot be used for real-time control of robots. Furthermore, the angles achieved by the individual joints of the robot are also quite low. While the antagonistic pair of SMA-wires achieve total angles of up to $\pm 20°$, these are much lower than those required in active catheter applications, specifically for peripheral vascular disease procedures. Furthermore, the inability for a single SMA wire to reset its shape on cooling can add limitations to the maximum outer diameter achievable using SMA-driven actuation. Another major disadvantage of SMA-driven actuators in literature was the inability for these catheters to achieve follow-the-leader (FTL) motion, which we believe, is critical for navigating through long and tortuous vasculature.

Among the pressure-driven actuators, a multi-segment catheter proposed by Ikuta *et al.* in 2002 featured a set of micro-hydraulic actuators [74]. The authors developed a "single-input, multi-output" system to control the joints of the robot, consisting of Band Pass Valves (see Fig. 1.4(a)). These valves were designed to open only for a selected band of pressure values, and therefore allowed for individual control (but not simultaneous control) of the joints of the robot using a single inlet. Using these valves and miniature bellows designed using silicone asymmetrical structures, the authors designed a 2-DoF pressure-driven catheter with an outer diameter of 3 mm. While this mechanism was an effective pressure-driven system, it suffers from a lack of precision in controlling the bending angle and simultaneous control of multiple joints. The authors elaborated on these problems in [75], where a novel 'pressure pulse drive' system was proposed to address both of the above shortcomings. In this method, the proximal joint is controlled with pressure pulses, generated by rapidly translating a syringe in conjunction with the pure-pressure control for the distal joint (see Fig. 1.4(b).

The bellows design proposed by Ikeuchi *et al.* [76] in 2008 achieved the smallest cross-sectional area, with a width of 400 μm and a thickness of only 200 μm and is a viable design for a miniature guidewire. The authors apply a MeME-X process to manufacture the bellows, which is a combination of the MeME process used to design membrane microchannels and excimer laser ablation (see Fig. 1.4(c)). The process involves molding of a thermoplastic polymer membrane by sandwiching it between a master mold and a deformable plastic substrate, followed by excimer laser micromachining of the membrane and connection to a microtube. When the microtube is then pressurized with a saline solution, the bellows, which have an asymmetric extension property undergo deformation resulting in distal tip bending of the catheter. Using this novel mechanism, the authors were able to demonstrate basic bending capabilities in a 3D phantom vascular structure to reach an aneurysm (see Fig. 1.4(d)). However, the challenge of higher curvatures or multiple joints was not addressed in this work. Similarly, [77] discussed the construction and actuation of a one degree-of-freedom hydraulically driven catheter made from a 0.94 mm diameter nitinol tube covered with a silicone sheath. The nitinol tube was femtosecond laser micromachined into a joint known as the 'unidirectional asymmetric' type of joint (further elaborated upon in future chapters). This bending joint works using the principle of negative pressure of water (or a saline heparin solution in practice) injected within the catheter. When the water is sucked out of the catheter, it causes the sleeve to be sucked into the gaps between the notches of the unidirectional asymmetric joint, causing deflection in the joint. Releasing the negative pressure causes the sleeve's shape to be restored and the joint to become straight again. The authors demonstrated the feasibility of using this catheter in acute vascular phantom models corresponding to 45°-90° turns, however, the joint was unable to perform any follow-the-leader types of motion to enter these phantom blood vessels. Using the same principle, the authors proposed a smaller 0.47 mm prototype of the nitinol micromachined joint as a hydraulic steerable guidewire for PCI procedures. The type of fluid used for pressure-driven actuators is an important consideration from the point of view of safety. Furthermore, due to the lack of control resolution in these types of catheters, these catheters have not found a large commercial interest [39].

Among the catheter/guidewire prototypes that are tendon driven, the authors in [78, 79] designed a 0.8 mm diameter tendon-driven steerable guidewire. It consisted of a nitinol rod passed through a flexible tube extracted from an existing microcatheter whose distal end was bent by pulling a tendon connected to it. The superelasticity of the nitinol rod was used to bring the tendon back to its original configuration. The entire distal tip was

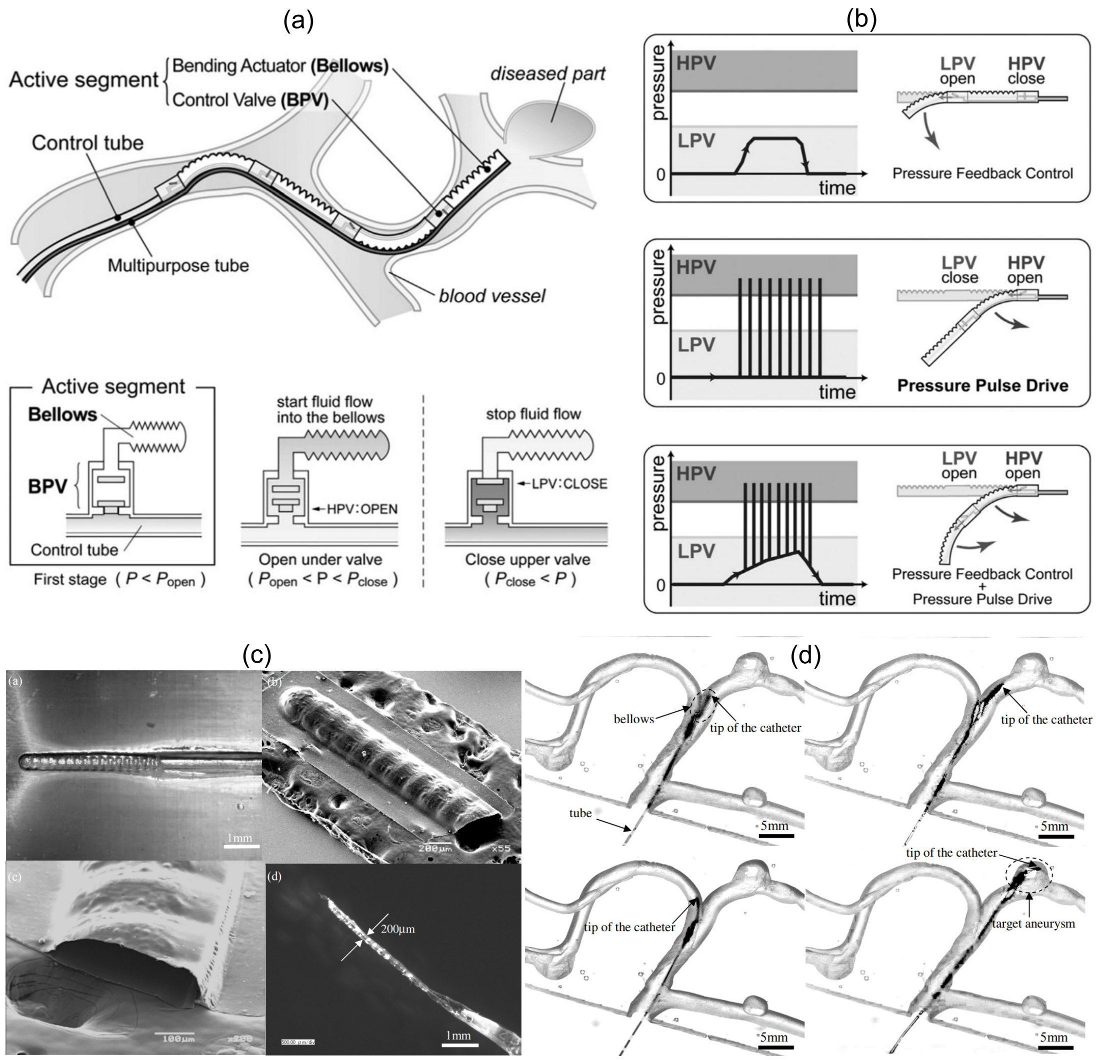

Figure 1.4: Examples of pressure-driven actuators used in active catheters: (a) Band pass valves designed to open in a pre-determined pressure ranges ©IEEE 2011 [75], (b) Pressure-pulse drive for simultaneous multi-joint control ©IEEE 2011 [75], (c)-(d) Bellows-design using the MeME-X process and the catheter designed with this process navigating through phantom vasculature ©IEEE 2008 [76].

connected to a PEEK tube housed within a polyethylene shrinking tube, and the tendon was manually controlled with a handheld controller with a friction based slider mechanism for translational motion of the tendon. The entire setup was designed to be assembled and disassembled within 30 seconds.

Early prototypes of a cable-driven catheter system (Catheter Control System, Hansen Medical, Palo Alto, CA, United States) were tested on 12 porcine hearts with 8 targets each, and the authors demonstrated a significant drop in time for navigation and precise placement of the distal tip of the catheter [80]. This study was followed up with cardiac mapping and navigation tests in dogs [81] followed by human clinical trials for atrial mapping and ablation of atrial fibrillation and flutter [82, 83], fenestrated stent grafting [84]. The system, further developed into the Sensei®Robotic Navigation System consisted of two steerable sheaths (Artisan®, Hansen Medical) along with a controller connected to the operating table, was primarily designed for operation around the heart, and had an outer diameter of 14 Fr. The Magellan®Robotic Navigation System from Hansen Medical was further developed for deploying devices around peripheral vascular structures and had outer diameters of 6 Fr, 9 Fr, or 10 Fr. These catheters had two cable-driven joints, a proximal joint capable of reaching 90° and a distal joint capable of exceeding 180°, and could have a guidewire passed through their inner lumen. The wire and catheter system could be advanced, retracted and rotated remotely. This system too, has been tested for catheterization and angioplasty in animals [85] and for fenestrated endovascular aneurysm repair, transarterial chemoembolization, uterine artery embolization among many other procedures in human subjects [86, 87, 88]. The use of tendon-driven joints makes the tool vulnerable to errors arising from tendon routing within the body of the tool. For example, in multi-joint tendon-driven robots, tensioning the tendons of distal joints could affect the more proximal joints near the base of the robot, causing inter-joint coupling. This coupling may be minimized by design, by routing the distal tendons along the central axes of the proximal joints [89]. In some cases, the tendons corresponding to a certain distal joint are routed along

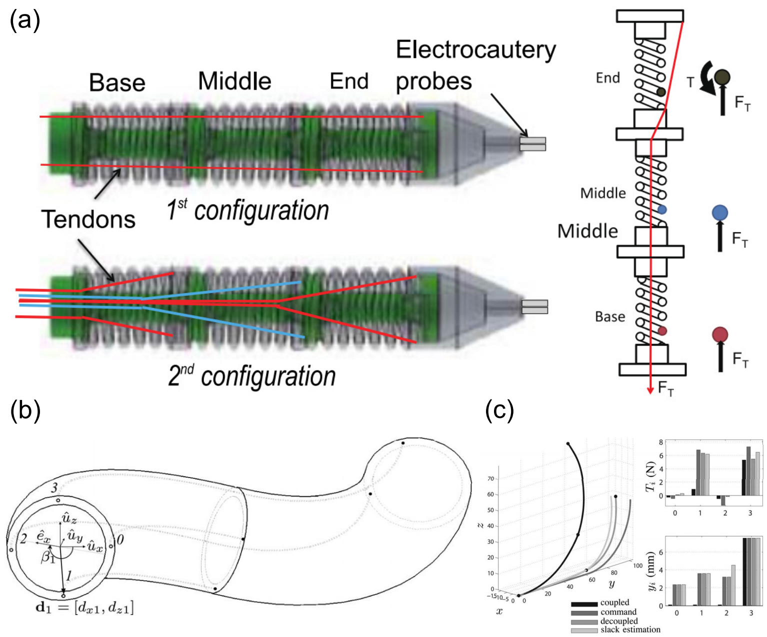

Figure 1.5: Tendon-driven multi-joint systems may require decoupling, which can be achieved by: (a) Design ©IEEE 2017 [89], (b) or by modeling ©IEEE 2009 [90].

dedicated channels created within the joint [91, 92]. A tendon decoupling model may also be included within the static model of the robot [93, 90].

Chapter 2 explores more on the design of tendon-driven miniature tools and catheters and potential joint designs for the same. Three potential joint designs are explored and analyzed further as potential candidates for the robotic guidewires introduced in Chapters 3 and 4.

1.2.2 Surgical Robots in Neurosurgery

The first use of robotics in a recorded neurosurgical procedure was in 1985 where surgeons used an industrial robotic arm for stereotactic biopsy on a 52-year old patient with a malignant brain lesion [94]. Using CT data to identify a target point, a UNIMATION PUMA 200 robot with a biopsy probe mounted on its end effector was used to probe a suspected target lesion site. The PUMA 200 robot was selected due to its high accuracy, stability, programmability and due to the 6 degrees-of-freedom allowing for dexterity similar to the human arm. The authors demonstrated that the use of the robot resulted in faster and more accurate biopsies. The same robot (a PUMA 200) was used in 1991 to extract deep-seated benign astrocytomas in six pediatric cases [95]. The Minerva project, initiated by the Group for Surgical Robotics and Instrumentation, Swiss Federal Institute of Technology of Lausanne (EPFL, Laussanne, Switzerland), was used to perform stereotactic aspiration of intracerebral lesions on two patients in September 1993 [96]. Unlike previously performed stereotactic neurosurgeries, the Minerva project aimed to replace the manual and largely blind stereotactic procedures with a robotic procedure performed within a CT scanner environment. This made it possible for surgeons to get real-time tracking of the surgical instruments, while being able to control surgical gestures like aspiration, biopsy, etc. The entire surgical procedure (including drilling, incision, manipulation of the surgical instruments) would be done by the robot. The doctor's role would therefore be elevated to higher-level decision making and focusing on patient evaluation during the procedure. Unlike previous attempts, where manufacturing tolerances would lead to loss of accuracy, the Minerva project made use of a custom designed seven degree-of-freedom robot [97]. In 1995, eight patients with suspected intracranial lesions (which were malignant brain tumors) were operated upon using this setup, resulting in a very high accuracy in comparison to a manual procedure [98]. The operating procedure duration was also drastically reduced due to it being conducted in the CT scanner environment.

The Neuromate robotic system (Renishaw PLC, Gloucestershire, United Kingdom, originally developed by Integrated Surgical Systems Inc., Davis, CA, United States) is a five degree-of-freedom robotic arm and a software visualization, planning and positioning system. This robotic system can be integrated with 3D visualization obtained from preoperative CT or MRI images, with either stereotactic frame-based or frameless localization. This system had been used for over 1600 neurosurgical procedures between 1989 and 2001 and was among the very first to be FDA approved [99]. In 2002, authors in [100] demonstrated that the application accuracy of the Neuromate system was equivalent to that of standard localizing systems of the day. After the early phantom studies, this system has demonstrated a very high application accuracy during *in vitro* and *in vivo* studies for frame-based procedures [101] or during frameless operation [102].

To offset the high costs associated with the development of neuronavigation systems like the Neuromate system (with development costs as high as \$30 million), the RObotic NeuroNAvigation (RONNA) system was proposed by the authors in [103] for biopsy, DBS, tumor resection, among other procedures. The original version of the system consisted of a 6-DoF KUKA KR6 arm acting as a Master robot and a 7-DoF KUKA LWR 4+ robot (operating in impedance control) to provide visualization in an interactive surgeon-assisted mode and tool operation during autonomous mode of operation [103]. An improved version of this system, the RONNA G3 robotic system, consisted of two industrial 6-DoF robotic arms mounted on mobile carts, an optical tracking system known as RONNAstereo for patient localization and a planning software with localization features for patient registration [104], and was used to perform a brain biopsy on a 45 year old adult without complications [105]. Recently, the fourth generation of this system RONNA G^4 featuring two KUKA Agilus KR6 R900 6-DoF arms was proposed and is undergoing clinical trials [106].

One of the few commercial products that directly addressed hydrocephalus, which is the medical condition tackled in this thesis, is the Medtech ROSA®Brain robotic system (Medtech, Montpellier, France). It consists of a six degree-of-freedom robotic arm with a planning station and haptic feedback. This robot has been successfully used in adults for frameless stereotactic biopsy [107] or deep brain stimulation (DBS) [108, 109] . However, more importantly, from the point of view of this thesis, the ROSA system has been successfully used for a variety of pediatric conditions including hydrocephalus, epilepsy, and subependymal giant cell astrocytoma (SEGA), among various other conditions [110, 111].

The "Evolution 1" robot (Universal Robot Systems, Schwerin, Germany) was a robot specifically designed for high positioning accuracy of endoscopes in micro-neurosurgical procedures. The robot consisted of a Stewart platform (with a positioning accuracy of 20 μm) mounted on a mobile chassis with a serial manipulator for gross pre-positioning of the platform (since the Stewart platform had a small workspace). In 2004, Zimmermann *et al.* attached a rigid ventriculoscope (Aesculap, Tuttlingen, Germany), which is the same one we replicate in this thesis, to the robot and used the system for ETV procedures on six adults suffering from stenosis related hydrocephalus [112]. While there were no complications related to the usage of the robot, the authors were unable to show a drastic difference between the performance of a robotic system over manual operation for a ventriculostomy.

While rigid endoscopes with rigid instruments are typically successful for the ETV surgery by itself, steerable solutions have been suggested for the ETV, when it has to be combined with other procedures such as the choroid plexus cauterization (CPC) [113] or the endoscopic tumor biopsy (ETB) [114]. In [113], the authors combine a manually operated flexible endoscope trocar (Karl Storz Steerable Neuro-Fiberscope) with a two-concentric-tube electrocautery tool. An actuator stage was designed to manipulate the tool and the steerable endoscope remotely. To test the robot, a surgeon participant was tasked with reaching 12 target points on a phantom ventricular model, with 66% and 100% success in two consecutive trials respectively. In [114], the authors propose an algorithmic approach to determine individual tube parameters for a patient-specific neurosurgical tool using concentric tube designs for ETV/ETB procedures. Dupont et al. [115] made use of concentric-tubes based robotic instruments for a steerable endoscope, to extend the workspace of the endoscope (see Fig. 1.6(a)). Recently, Wang *et al.* proposed a novel steerable sheath for single-port neuroendoscopic procedures that make use of precurved superelastic tubes within the working channels of a sheath [116]. Rotating and translating the individual tubes causes deflection of the sheath, i.e. the tubes themselves act as both working channels, and as tendons (see Fig. 1.6(b)). The authors model the system using Cosserat rod theory to model the system as a set of eccentric constrained curved tubes. However, limitations on the number of tool ports, variations in patient ventricular anatomy, and poor visual quality in steerable endoscopes [24] may weaken the performance of such a solution.

The geometric size requirements of tools required in ETV procedures impose con-

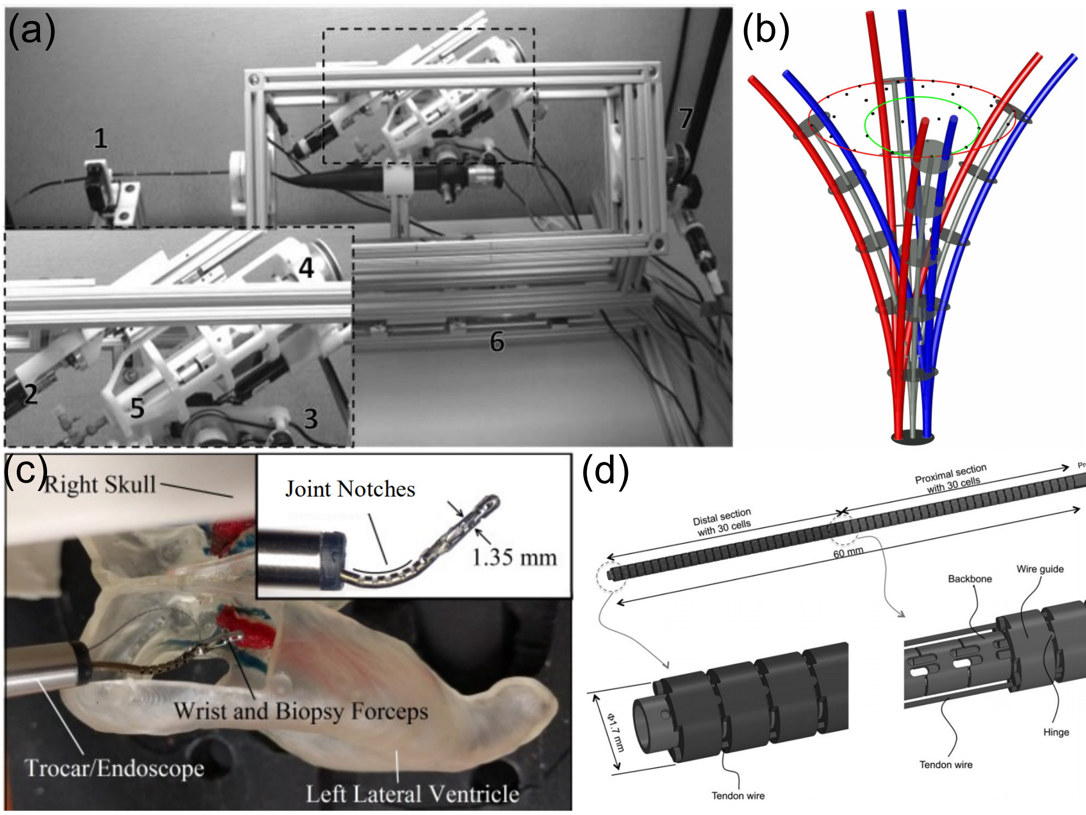

Figure 1.6: (a) Concentric tube robot endoscope tool proposed by Dupont *et al.* ©IEEE 2012 [115], (b) Eccentric constrained curved tubes for a steerable sheath ©IEEE 2019 [116], (c) Unidirectional asymmetric notch joint for a steerable ETV and tumor biopsy tool ©IEEE 2016 [117], (d) Multi-joint steerable tool for intracranial cysts proposed by Kato *et al.* ©IEEE 2015 [118].

straints on the type of joint used to manufacture any robotic tool. The authors in [119, 120] identify several joint types for instruments used in minimally invasive surgeries. In the next chapter, we explore two types of ‘bending flexure joints’ defined in this classification for our robotic neuroendoscope tool. In these joints, the compliance of a bending member created from the body of the instrument itself is used to achieve a bending capability of the joints. The joint motion is then controlled by controlling the stroke of a tendon attached to the bending member. Among meso-scale tendon-driven steerable robots that use bending flexure joints, Eastwood *et al.* [117, 121] propose the design of a steerable tool for neurosurgical applications based on the ‘unidirectional asymmetric notch joint’ design proposed in [122] (see Fig. 1.6(c)). Similarly, a backbone made of symmetric notches machined on both sides of a metal tube is used to form a two joint steerable tool 3.4 mm in diameter and 120 mm in length, for operating on intracranial cysts [123, 118] (see Fig. 1.6(d)). Similar bidirectional symmetric joints have been applied by the authors in [124] to design a 2-DoF robot (capable of achieving *S*-shaped curves) 3.3 mm in diameter and 40 mm in length, to reach lesions in the lateral skull base. Gao *et al.* proposed a 2-DoF solution for the same procedure that makes use of a set of nested nitinol tubes with bidirectional notches machined asymmetrically along the length of the robot [125] (see Fig. 1.7(a)). The robot, which is 6 mm in diameter, has dedicated channels for guiding tendons machined within the walls of the tube. Authors in [126] propose a novel tendon-driven robot with six bending sections that was capable of performing follow-the-leader motion to reach target sites in ETV and ETB procedures (see Fig. 1.7(b)). The robot has an outer diameter of 3.4 mm with a 1.8 mm inner tool channel. The authors demonstrated the capability of the robot to attain *C*-shaped and *S*-shaped curves in phantom anatomical models.

In this thesis, we address the problem of achieving *S*-shaped curves at extremely small diameters using the mechanical properties of bending flexure joints to our advantage.

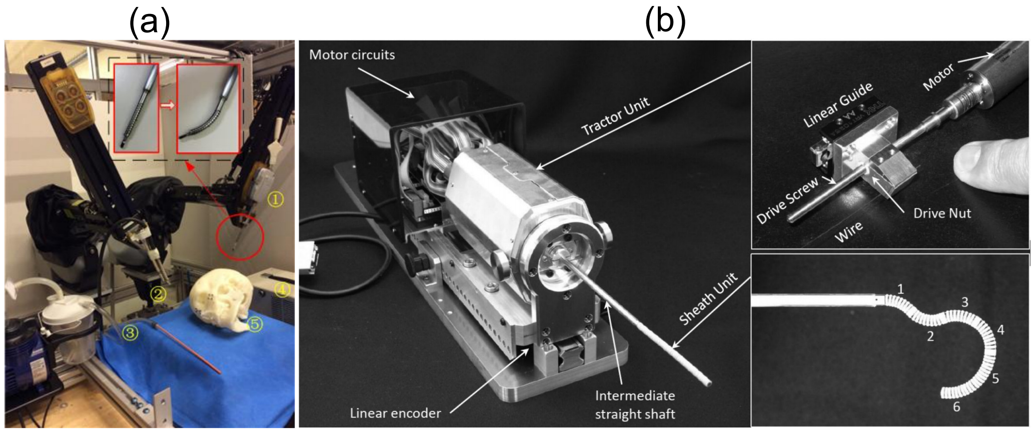

Figure 1.7: Bending flexure joints in neurosurgery: (a) Dexterous continuum manipulator for deep skull base surgery by Gao *et al.* ©IEEE 2016 [125], (b) Tendon- driven 6 segment robot capable of follow-the-leader motion for ETV and tumor biopsy ©IEEE 2020 [126].

1.2.3 Force Sensing in Tendon-driven systems

Tendon-tension is an important feedback modality to measure the state of the robot or to estimate external tip forces in surgical robotics [127, 128]. In this thesis, we therefore explore the design of a miniature force sensor to incorporate into the controllers of our tendon-driven systems.

Strain gauges have been widely used for most force sensors available on the market due to their high linearity. However, these sensors are susceptible to magnetic noise/temperature variation [129] and require a properly designed structure with a skilled surface treatment and bonding technique, which significantly limits the design customization. Therefore various alternative sensing mechanisms employing the Hall effect [130], force-sensitive resistors and quantum tunneling effect [131] have been proposed to fabricate force sensor cost-effectively and replace the expensive conventional sensing mechanisms such as strain-gauges and piezoelectric materials. Among these alternatives, optics-based sensing mechanisms [132, 133, 134, 135, 136, 137, 138, 139, 140, 141, 142, 143, 144, 145, 146, 147] have begun to attract attention, because they provide not only high accuracy, but can also be easily manufactured and customized in a small form factor. Optical sensing has been used to extract uniaxial force information [132, 133, 134, 135, 136, 137, 138, 139,

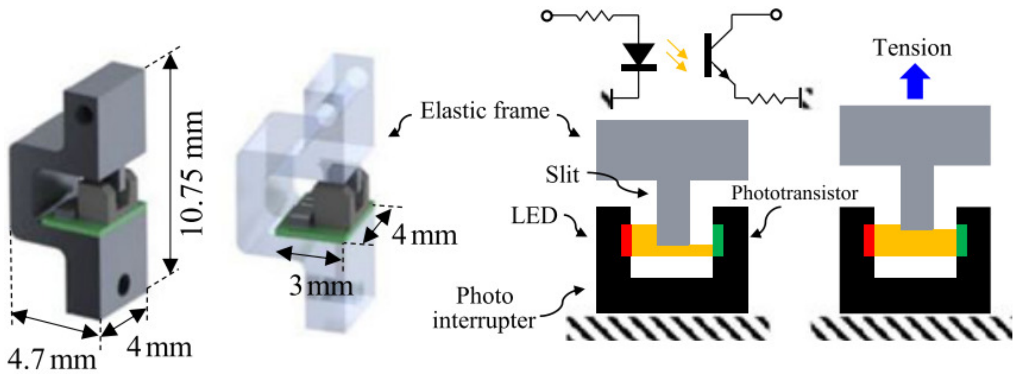

Figure 1.8: Principle of operation of a screen-type optoelectronics-based uniaxial force sensing assembly ©IEEE 2017 [148].

140, 141, 142, 143, 144, 145] or multi-axial tactile information [146, 147] depending on the application. Stress vectors of multiple points or shape of the contact object are estimated by camera-based image analysis, tracking the gradient of specific feature printed on elastic material [147]. Optical fiber based force sensing mechanisms were proposed to measure the force on the complex geometry [143, 144, 145]. Although these optics-based sensing mechanisms significantly expand applicable area in tactile and shape sensing, they require bulky and expensive electronics such as cameras, pulse generators and receivers and have relatively high nonlinearity and hysteresis, which is not suitable for the force feedback system requiring high accuracy. To implement highly accurate and reliable force/displacement sensing mechanisms, optoelectronic components have been employed in the sensor [132, 133, 134, 135, 136, 137, 139, 140, 141, 142]. These mechanisms uses two optoelectronic devices such as an optical emitter and receiver pair. When external load or displacement is applied to the sensor, the optical path between the emitter and receiver changes, thereby varying the output of the sensor (see Fig. 1.8). Depending on the arrangement of the components, the mechanism is categorized as a screen-type [132, 133, 134, 135, 136, 138, 137], reflective-type [139, 140], and direct-type sensor [141, 142]. Given fewer components and simple arrangement of the sensing components, these sensors can provide high accuracy within a compact footprint and have been applied in compact robotic systems [132, 148, 149, 142]. However, these sensing mechanisms have a limited range of high linearity and still require delicate assembly processes to guarantee a high linear output, which eventually increases fabrication cost/time and limits design customization. Furthermore, not only is the output of the emitter (ex., light emitted diode (LED)) significantly affected by electric noise and temperature variation, the output of the receiver (ex., phototransistor) is also distorted by ambient light from the external environment [136, 137]. In [136], the external disturbances were compensated by arrangement of multiple optoelectronic units, but it increases the footprint of the sensor. In [149], disturbance caused by an ambient light was compensated by modulating the input signal; however, it cannot compensate disturbances caused by variations in the LED light.

1.2.4 Shape Sensing in Surgical Robotics

A variety of sensing techniques have been employed to measure the shape of continuum robots in literature [150]. Electromagnetic (EM) tracking [151] utilizes the principle of mutual induction to measure the location and orientation of small EM trackers placed within the tracking volume of a field generator producing an EM field (see Fig. 1.9(a)). EM tracking allows for robust localization of EM trackers without the requirement of the trackers to be in the line-of-sight of the field generator. This, along with the small size of the trackers, high accuracy, and the ease of use makes them very attractive in continuum robotics. However, the accuracy of these EM trackers can be affected in an OR room setting due to the presence of devices such as CT/MRI scanners. Furthermore, the EM field generator must always be placed close to the location of the tracker, making it unusable in cases where this is not possible. Finally, the accuracy of the trackers also decreases as the tracker moves away from a very small volume over the field generator. Another approach to measuring the shape of continuum robots is through imaging modalities such as fluoroscopy making use of the bi-planar C-arm system [152, 153] (see Fig. 1.9(b)). However, the robustness of these techniques and the ability to perform shape recognition in real-time are unclear and need further investigation. Finally, usage of these systems for real-time control is risk

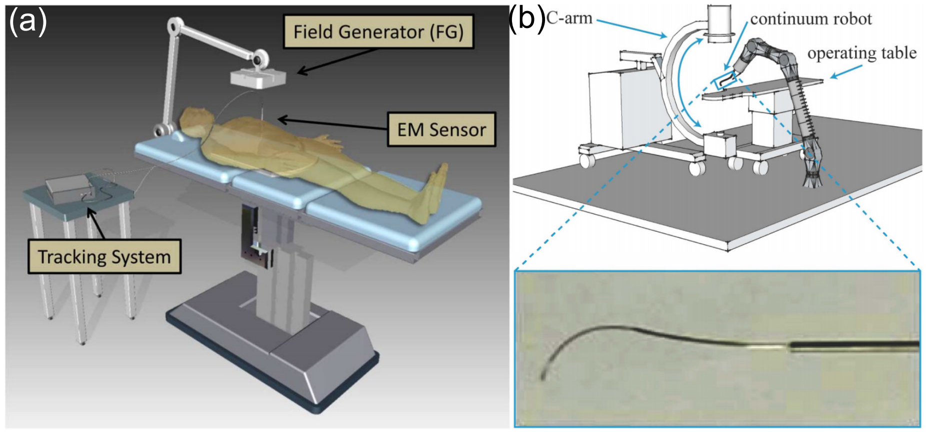

Figure 1.9: Examples of shape sensing systems for minimally invasive surgical continuum robots: (a) Electromagnetic trackers can be tracked with high accuracy by a field generator placed within close proximity ©IEEE 2014 [151] (b) Multi-planar fluoroscopy machines like the C-Arm may be used for shape estimation ©IEEE 2013 [152].

prone due to extensive exposure to radiation and contrast agent overuse.

Fiber Bragg gratings (FBGs) are optical fibers with gratings etched along their lengths in order to modulate the refractive index of the fiber at the location of the gratings, thereby allowing the fibers to reflect light of a specific wavelength [154]. This reflected wavelength is sensitive to changes in axial strain. Therefore, by shifting the neutral axis of the fiber, it can be used to measure bending strain. In [155], the authors present a flexible nitinol needle, constructed using a nitinol wire of diameter 1 mm. This wire has three grooves of 300 μm micromachined along its length such that the grooves are separated from each other by 120° (see Fig. 1.10(a)). Three optical fibers with 4 FBGs each are then attached within each groove. Therefore, the neutral axis of each of the fibers is displaced by this assembly allowing the fibers to measure bending strain, and therefore allowing for 3D shape estimation of the robotic needle. The authors report errors within 1 mm in free space, and approximately 2.2 mm in a phantom tissue experiment.

Another approach followed by the authors in [156], by utilizing curvature sensitivity of gratings etched on D-type optical fibers [157], was to attach two D-type fibers side-by-side along the plane formed by the D-shape cladding (see Fig. 1.10(b)). However, in either of the above cases, the measurable curvature was extremely small and unsuitable for our

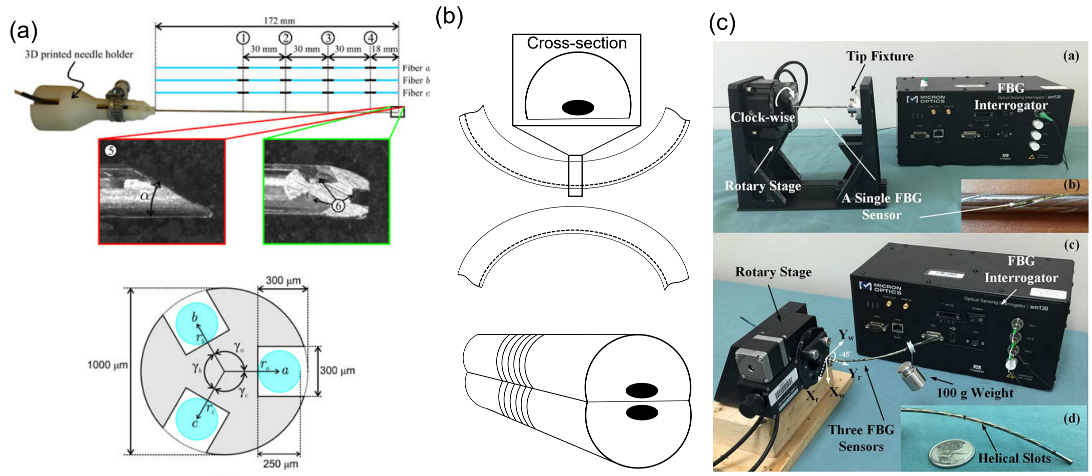

Figure 1.10: Fiber Bragg gratings can be used for shape sensing by offsetting the neutral axis of the sensing assembly: (a) Machining grooves within the body of a needle ©IEEE 2013 [155], (b) Using d-type FBG fibers [156], (c) Helical wrapping of FBG fibers to measure bending and torsion of pre-curved nitinol tubes ©IEEE 2016 [159].

application. For the purpose of our application, where a neuroendoscopic tool is passed through the trocar of a commercially available endoscope, the usage of the endoscope camera for shape reconstruction may be more viable. The authors in [158] propose two pose estimation algorithms, one using a marker-based approach and another marker-less technique that makes use of feature points on the instrument body followed by segmentation techniques to extract a binary image of the instrument. In a realistic setting, the marker-less approach, which utilizes singular value decomposition of the binary image of the instrument to find tip centerline positions, seems most promising. However, these vision based techniques cannot predict shape of the tool, when it is trying to reach targets outside the field-of-view of the endoscope camera. Xu *et al.* make use of a novel helically wrapped FBG sensor design, which is used to measure torsion, curvature and force in a concentric tube robot [159]. The authors engraved three helical patterns in two Nitinol tubes (each) with a wall thickness of 0.5 mm, using a novel three-axis engraving system designed specifically for this operation (see Fig. 1.10(c)). Three FBG fibers are inserted and bonded in these helical grooves such that the fibers helically wrap each tube. As a result of the helical wrapping, the torsion experienced during the operation of the concentric tube robots translates to axial strain along the length of the fibers. Furthermore, this helical wrapping allows the researchers to measure curvature as well as lateral forces with high accuracy. However, it must be noted that this approach can only be utilized for robots with a continuous outer surface (such as concentric tube robots), and may not be directly transferable to bending flexure joints. Furthermore, since bending flexure joints do not require torsion and lateral force measurement, this sensing assembly does not serve the same purpose as that served for concentric tube robots.

Liu *et al.* in [160] manufacture a shape sensing assembly by attaching an FBG fiber with a diameter of 100 μm to two wires of Nitinol that are about 125 μm in outer diameter. The three wires are attached so as to form a triangular cross-section. This offsets the neutral plane of the combination towards the two Nitinol wires, and away from the center of the FBG fiber. However, the composite neutral axis is still very close to the neutral axis of the FBG fiber, thereby reducing the bending strain on the fiber. As a result, the authors are able to measure extremely high curvatures of up to 80 m^{-1} for their 35 mm tendon driven joint with an outer diameter of 6 mm and inner diameter of 4 mm. Two such sensor assemblies are inserted within the walls of this joint by creating channels within these walls along the bending plane of the joint. In [161], the authors further demonstrate the ability of the sensor to be able to measure shape of the robot in the presence of obstacles, such that the curvature of the robot is no longer constant.

In [162], the authors improve upon the design proposed in [160] by packaging the entire sensor assembly (FBG and two Nitinol wires) within a polycarbonate tube, which is then inserted within the walls of their joint. The authors demonstrate that such an assembly successfully allows for large deflection measurement of a tendon-driven joint while improving assembly accuracy and manufacturing capability of such sensors. In [164], the authors propose a novel data-driven method to estimate the tool position using the sensor design proposed in [162]. The authors attach reflective markers to the tip of a 6 mm diameter single degree-of-freedom joint to achieve ground truth 3D position of the tip of the joint.

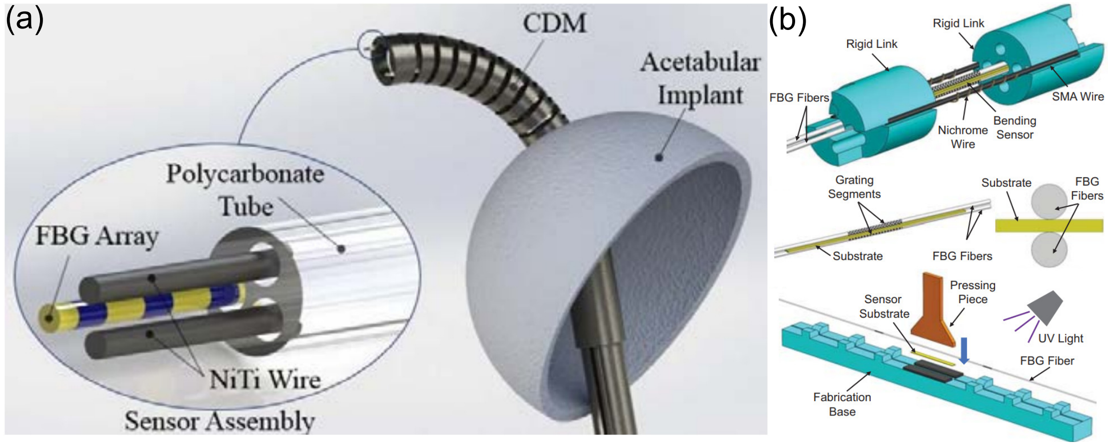

Figure 1.11: Examples of previous work on large deflection FBG-based shape sensing: (a) FBG sensor and two nitinol wires packaged within a polycarbonate tube ©IEEE 2016 [162], (b) FBG fiber bonded to thin nitinol strip ©IEEE 2019 [163].

The joint is also equipped with the sensor assembly described in [162] (see Fig. 1.11(a)). The joint is then actuated to a curvature of 50 m^{-1} from a straight configuration, and optical ground truth data as well as FBG data are simultaneously gathered for training the system. The training dataset is then randomly divided into 70% training and 30% validation data. A linear regression model is then trained using this training data, to identify tip position from raw FBG wavelength information. Finally, the authors compare their data-driven approach to a previously described model-based approach and demonstrate that the data-driven approach is able to significantly reduce tip position error especially at higher curvatures.

Another example of large deflection shape sensing was demonstrated for an SMA-based bending module (used in the 5-DoF catheter previously described and addressed in [73]) capable of measuring curvatures as high as 77.87 m^{-1}. The sensor was designed by bonding an FBG fiber to a thin nitinol strip (which acts as a substrate) with a flexible adhesive (see Fig. 1.11(b)). The sensor output however shows a significant amount of hysteresis and temperature dependence. Temperature-modulation being critical for SMA-driven joints, this can be a significant detriment to the use of FBG-based sensors for SMA-driven joints. In this thesis, we improve upon this design allowing for the measurement of curvatures as high as 145 m^{-1}, approximately two times the previously reported maximum value.

1.2.5 Research Objectives

Navigation of micro-scale guidewires and steerable meso-scale endoscope tools around anatomical obstacles and through tortuous bifurcations is a critical part of minimally invasive surgery. From the literature review, it is clear that miniaturization of steerable catheters and endoscopes has promising implications for minimally invasive cardiovascular and neurosurgical outcomes. The current state-of-the-art solutions lack steerability at the sizes required in interventional cardiology and pediatric neuroendoscopy. Specifically, no solutions exist for steering of micro-scale guidewires with diameters between 0.36 mm - 0.89 mm. Complex maneuvers like follow-the-leader motion, helpful in navigating tortuous vascular bifurcations, have also not been attempted previously at the sizes required for steerable guidewires. While analytical static and kinematics models for small scale joints necessary to build micro-scale and meso-scale robots exist, these models lack the comprehensive study required to control these joints autonomously. Finally, intrinsic large-deflection shape estimation and tendon-force measurement for miniature continuum robot joints is a challenging problem. In the absence of these tools, it is unlikely, that autonomous micro-scale continuum robotics will see application in a wide-spread clinical setting. This work is a preliminary attempt at tackling all of the above problems, namely, a micro-scale robotic guidewire for interventional cardiology, a meso-scale 2-DoF robotic neuroendoscope tool for pediatric neurosurgery, miniature tendon-force sensors for these robots, and intrinsic shape-sensing for the robot joints. Our primary research objective is to design steerable robotic solutions at sizes that are compatible with existing rigid (or non-steerable) solutions on the market today. Therefore, for rapid adoption of the solution, it is necessary that the robotic guidewire must have an outer diameter equal to that of commonly available guidewires (commonly known as O14, O16, or O35 guidewires). Similarly, it is critical that the robotic tool designed for neuroendoscopy be compatible with existing neuroendoscope trocar working channels.

Another major research objective is to incorporate sufficient number of degrees-of-freedom in the joints of our system to perform the tasks critical to the success of surgical procedures. Therefore, the proposed guidewires in this thesis can perform certain maneuvers (like Follow-the-leader motion), that were previously not possible for steerable microcatheters on the market or in previous literature. Similarly, the neuroendoscope to be designed must be able to achieve S-shaped curves and have a handheld controller, such that the clinician can control the bending plane of the S-curve.

Finally, it is critical to move towards autonomous control of the degrees-of-freedom of our robots, to make control of these systems intuitive for clinicians. With this objective in mind, we address the design and validation of various sensors that may be deployed within these robots such that the robot state can be known at all times, and used for closed-loop control of these robots.

1.2.6 Thesis Overview

Chapter 2 outlines the development and taxonomy of micromachined tendon-driven joints for surgical robots. Chapter 3 details the development of a 0.79 mm outer diameter 2-DoF robotic guidewire for peripheral artery diseases. Chapter 4 details the design of a CO-axially Aligned STeerable (COAST) guidewire, a model to determine optimal design parameters, a compact actuation system, and proposes a Jacobian-based control strategy for the same. Chapter 5 proposes a variety of designs for a neurosurgical robot for the endoscopic treatment of pediatric hydrocephalus, while Chapter 6 details energy-based models for the joints of the best design, and a disturbance observer-based control strategy for the same. Chapters 7 and 8 detail the design of miniature tendon-force and intrinsic shape sensing for micro-scale and meso-scale continuum robots, like the ones proposed in this work. Finally, Chapter 9 concludes this thesis.

CHAPTER 2

BENDING FLEXURE JOINTS: A BRIEF TAXONOMY AND EVALUATION

2.1 Tendon-driven Bending Flexure Joints

Tendon-driven robotic minimally invasive catheters or endoscopes usually include joints that involve rolling or sliding motion between two rigid members [165, 166], or exploit the physical compliance of the material to form bending flexural joints [120]. Specifically from the point of view of this thesis, bending flexural joints are constructed by micromachining material from a tubular shaft, thus enabling bending of the tube and creating directional springs [167, 168, 169, 123]. Fig. 2.1 shows the design of three such commonly used flexural joints which are often termed *notch joints*, that are actuated using tendons attached to the distal ends of the joints (see blue lines in Fig. 2.1). A bending member is created by the removal of material in each of the notch joints (see dotted lines in Fig. 2.1(a)-(c)), and actuation of the tendon with a force F_t causes this bending member to deflect, thereby causing the joint to bend. Due to the absence of moving parts, such as in rolling or sliding joints, notch joints are suitable for miniaturization, making them appropriate for the catheters and neuroendoscopes proposed in this thesis.

The bidirectional symmetric notch (BSN) joint [170, 171, 172, 173, 174] (see Fig. 2.1(a)) is obtained by removing material symmetrically on either side of the Y-Z plane creating a bending member symmetrically about this plane. This allows the joint to be deflected on both sides of the Y-Z plane. However, due to the bending member running centrally along the Y-Z plane, the moment arm achieved by the actuating force F_t is low, thereby making this joint very stiff. As a result, the authors in [122, 117] suggest a unidirectional asymmetric notch (UAN) design (see Fig. 2.1(b)) which can achieve a higher moment arm due to the bending member being shifted to one side. Note that both the above

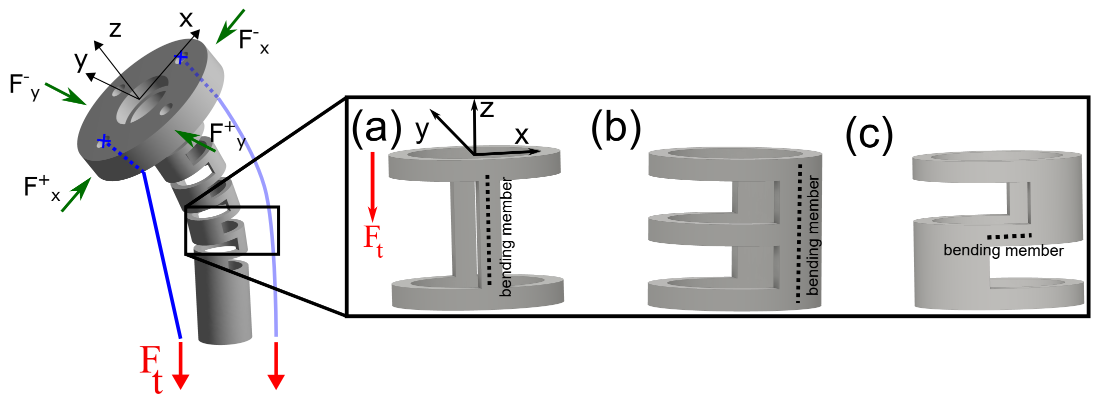

Figure 2.1: Bending flexural joints are designed by creating notches into the body of a tubular shaft. The notch geometries allow us to classify these joints into three types, (a) bidirectional symmetric notch (BSN) joint, (b) unidirectional asymmetric notch (UAN) joint, and the (c) bidirectional asymmetric notch (BAN) joint.

notch geometries, while being stiff to forces applied transverse to the bending plane (Y-Z plane in Fig. 2.1), are compliant in the bending plane (X-Z plane in Fig. 2.1). Therefore, they are susceptible to external forces F_x^+ and F_x^- which may result in undesired deflections. However, unidirectional notch joints cannot resist forces F_x^- by design, while the bidirectional joints can resist these forces by tensioning the appropriate tendons. While the authors in [121] propose the addition of contact-aids to reduce this problem in unidirectional geometries, it cannot be eliminated completely.

In this chapter, we focus on the design-parameters of a type of a flexural notch joint we call the bidirectional asymmetric notch (BAN) joint (see Fig. 2.1(c)) [175, 176, 177, 178]. In comparison to the unidirectional notch joints [121], this joint has notches on both sides of the Y-Z plane (see Fig. 2.1(c)). These notches are arranged asymmetrically about this plane, unlike symmetric notch joints [123], where material is micromachined out on both sides of the Y-Z plane in a symmetric manner. We find that the bending flexibility of the BAN joint is much higher than that of a UAN joint, given the same amount of material removal. This is due to the fact that the bending is dominated by the member created between the two notches of this joint. This phenomenon has been demonstrated in Section 2.4. We note that this additional improvement in flexibility does not excessively affect the

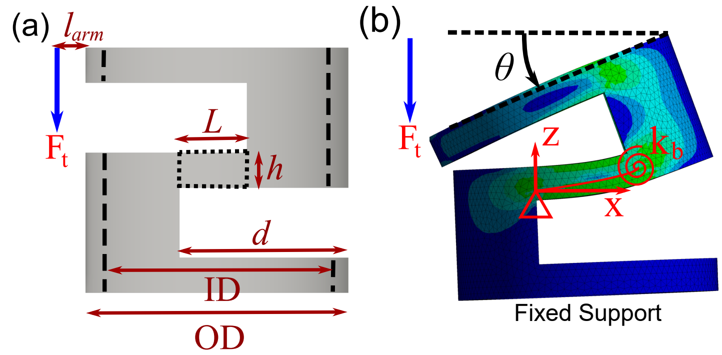

Figure 2.2: (a) Euler beam model used to model forces applied in the bending plane, (b) Finite Element Model of the BAN joint bending primarily due to deflection of intermediate beam.

stiffness of the beam to external forces applied.

We will first generate an Euler beam based bending model for the same, using a Finite Element Analysis (FEA) to guide this model. Finally, we analyze the bending, transverse and axial stiffness of this joint in comparison to the other types of notch joints, since these are the primary forces observed on such joints in a surgical setting. In this section, we provide a model to estimate the bending stiffness of the BAN joint. A simplified schematic is shown in Fig. 2.2(a), where $L = 2d - \mathrm{OD}$ is effective beam length from the left side of the bottom notch to the right side of the top notch, and $l = l_{arm} + (OD - d)$ is the distance from the tendon to the notch. The deformation of the beam, v, due to the tendon tension force, F_t, is governed by the following equation:

$$EIv'' = \frac{F_t}{2}(x + l) \tag{2.1}$$

where E is the elasticity of the tube, $I = \frac{1}{24}(\mathrm{OD} - \mathrm{ID})h^3$ is the second moment of area on the beam, x is the horizontal coordinate originating from the left side of the notch and half of F_t results from the two beams between the notches. By solving (2.1), we get

$$v = \frac{F_t}{2EI}(\frac{l}{2}x^2 + \frac{x^3}{6} + c_1 x + c_2) \tag{2.2}$$

From the FEA, it has been found that the left side of the beam has negligible deflection. Thus, the boundary condition on the left side can be assumed as a fixed end, which yields $c_1 = c_2 = 0$ and

$$v = \frac{F_t}{2EI}(\frac{l}{2}x^2 + \frac{x^3}{6}) \tag{2.3}$$

The bending angle on the right side of the beam is

$$\theta_1 = v(L)' = \frac{F_t}{2EI}(Ll + \frac{1}{2}L^2) \tag{2.4}$$

However, by observation, there is an additional bending angle θ_2 at the connecting position of the beam and the right-side curved wall. A torsional spring model with a stiffness k_b is used here and

$$\theta_2 = \frac{F_t}{2k_b}(L + l) \tag{2.5}$$

Thus, the bending angle of a notch is

$$\theta = \theta_1 + \theta_2 = F_t(\frac{2Ll + L^2}{4EI} + \frac{L + l}{2k_b}) \tag{2.6}$$

2.2 Experiments Performed

In this work, we analyze a finite element model of a single BAN pair, and will use the information gathered from FEM simulations to guide the design of the final robot. All FEM simulations are conducted in ANSYS 18.2 Research Version (ANSYS Inc., Canonsburg,

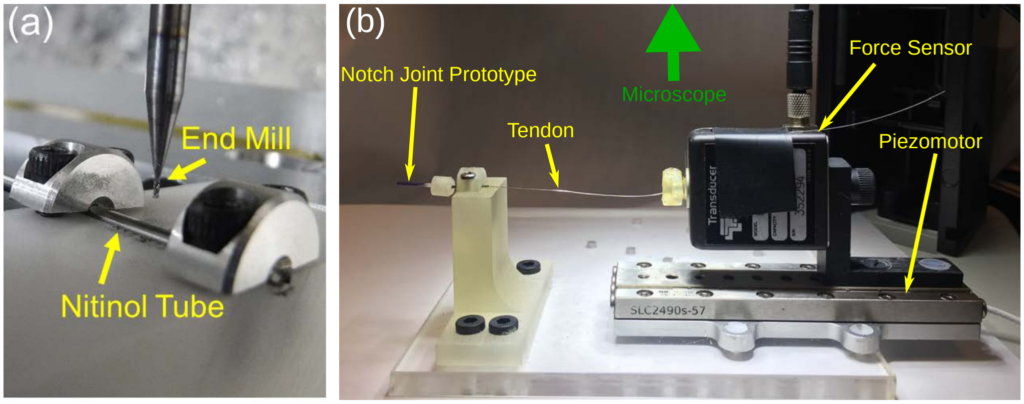

Figure 2.3: (a) Machining setup to manufacture the BAN joints, (b) Experimental setup to measure joint deflection under the application of various forces.

PA, United States). Material properties for Nitinol were taken from literature [121]. We ran a series of simulations, varying the notch geometry varying notch depth d and the height of the bending member h to estimate joint stiffness and torsional stiffness parameters defined in the previous section. A tetrahedral mesh with a mesh density of approximately 0.25×10^6 elements/mm^3 was used to ensure high mesh quality, especially at the notched regions.

Nitinol tubes having outer diameter of 0.8 mm and inner diameter of 0.62 mm (Confluent Medical, CA, United States) were machined on a 3-axis CNC milling machine (Okuma MC-V4020, Okuma America Corporation, NC, United States) with a 200 micron diameter 4 flute end mill (Accupro 62773387, MSC, NY, United States) (see Fig. 2.3(a)). The nominal cutting speed was 157 mm/min and feed rate was 1.27 mm/sec. In order to validate our FEA models, we constructed a compact setup, designed such as to fit on the observation surface of a standard stereo microscope (Leica Camera AG, Wetzlar, Germany) (see Fig. 2.3(b)). A single tendon from the joint to be tested is connected to a piezo-based linear actuator (SmarAct GmbH, Oldenburg, Germany), via a load cell with a maximum load capacity of 5 lbs (Transducer Techniques, CA, United States). Data from the load cell and the microscope are acquired via a 16-bit Analog to Digital Converter (Model 826, Sensoray, OR, United States) and USB respectively. The motor is controlled to provide a step input of 50 μm, while force and encoder data is sampled continuously throughout this time. An

Table 2.1: Set of notch samples tested to validate the FEA and Euler beam models for the bending stiffness of the joint, as well as the torsional stiffness values obtained from each of the FEA simulations.

Sample	Parameters			
	d mm	h mm	k_b	# Trials
S1	0.5	0.15	0.0021	3
S2	0.55	0.125	0.0023	3
S3	0.6	0.15	0.0017	3

image from the microscope is captured periodically once the joint has moved and force data has reached steady state for each step input. A Hough transform computed for each image automatically will provide us with the ground truth for the angle achieved by each joint at each point of time.

In the next section, we validate our Euler beam model for a set of three notch geometries where the dominating bending member is the beam between two notches (see Fig. 2.1(c)), and we follow this with an analysis of a set of UAN and BAN joints to understand the effects of tendon forces in the bending and transverse planes, and axial external forces on each type of joint (see Section 2.4).

2.3 Results

Table 2.1 shows a set of notch samples selected to verify our FEA simulations and Euler beam model. These dimensions were selected such that the intermediate beam was the dominating cause of joint deflection, as assumed in our model in Section 2.1. We can see in Fig. 2.4, that the FE model is able to satisfactorily model the deflection of the BAN joint for small forces and small deflections. Since the total deflection in a robotic tool is caused due to a serial chain of several such joints, this model may be capable of addressing the overall deflection for multiple bidirectional notches.

Next, the ability of the notch joint to be relatively stiff in the plane orthogonal to

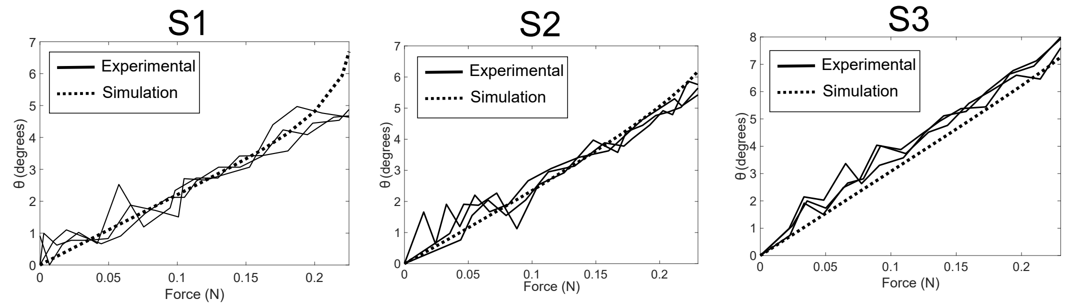

Figure 2.4: Experimental results for each of the dimensions specified in Table 2.1, compared to the FEA simulations for the specific dimensions. Solid lines represent each trial.

the bending plane makes it very desirable for the construction of multi-degree-of-freedom (DoF) robots, because distal tendons can then be routed along the plane orthogonal to the bending plane of the proximal joint. These tendons, when tensioned, will affect any proximal joint only minimally, thereby achieving inter-joint decoupling by design. To this end, we arrive experimentally at a value of notch depth, maximizing flexibility in the bending plane, minimizing flexibility in the transverse plane, without exceeding the ultimate stress that can be applied to the joint. A plot of the tendon tension vs. equivalent (von-Mises) stress in order to achieve complete notch bending, for differing notch depths is shown in Fig. 2.5(a). It can be seen that the ultimate stress of 1070 MPa used in our model is exceeded by notch depths under 500 microns. Therefore, while the usage of these geometries will result in high orthogonal stiffness, they will not be able to achieve complete bending of the notch without breakage.

The tip deflection in the plane orthogonal to the bending plane for various notch geometries is shown in Fig. 2.5(b). Here, it can be seen that joint stiffness decreases with increasing notch depth. We find that the largest ratio of the bending angle vs the tip deflection happens for the depth of 500 microns without any breakage.

2.4 Main Experimental Insights

One of the major insights from the finite element analysis of the BAN joint can be observed in Fig. 2.6. In this figure, we analyze the deformation of each of the three types of joints

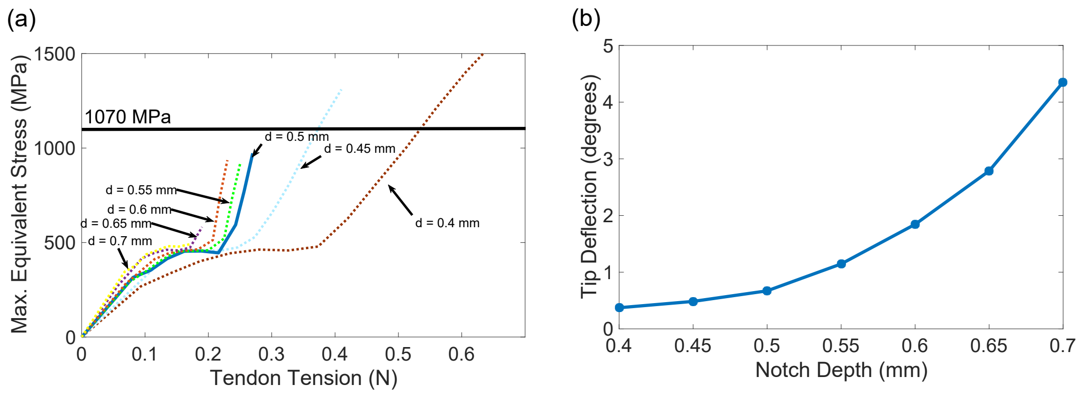

Figure 2.5: (a) Maximum equivalent (von-Mises) stresses seen in a single notch for different tendon tension values and varying geometries, (b) Notch depths vs. tip deflection in the plane orthogonal to the bending plane.

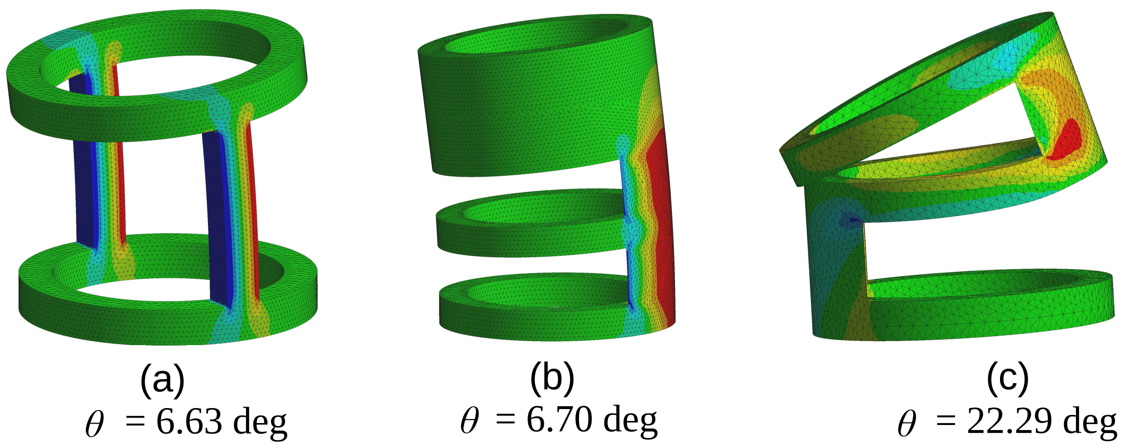

Figure 2.6: The deflection observed in a (a) BSN joint [123], (b) UAN joint [121], and the (c) BAN joint, due to a tendon tension force, $F_t = 0.2$ N, applied at distance, $l_{arm} = 0.19$ mm, from the outer wall of each joint.

that can be used in designing robotic neuroendoscopic tools, under loading from a moment created by tendon tension force, F_t, at a moment arm, $l_{arm} + (\frac{\mathrm{OD}}{2})$. Note that in each case, the bending member is different. In the case of the BSN joint (see Fig. 2.6(a)), these members are the beams created by the remaining wall of the tube after cutting the joint. In the case of the UAN joint (see Fig. 2.6(b)), the bending member is the backbone of the joint, seen by the reddened region to the right of the notches. In our case, the bending portion is both the walls of the uncut portion of each notch as well as the horizontal member that connects the two notches. As a result, the beam that bends in the case of the BAN joint (see Fig. 2.6(c)), may be longer than the ones in the BSN joint or the UAN joint. This results in the higher bending flexibility seen in this type of a joint with the same amount of material removal.

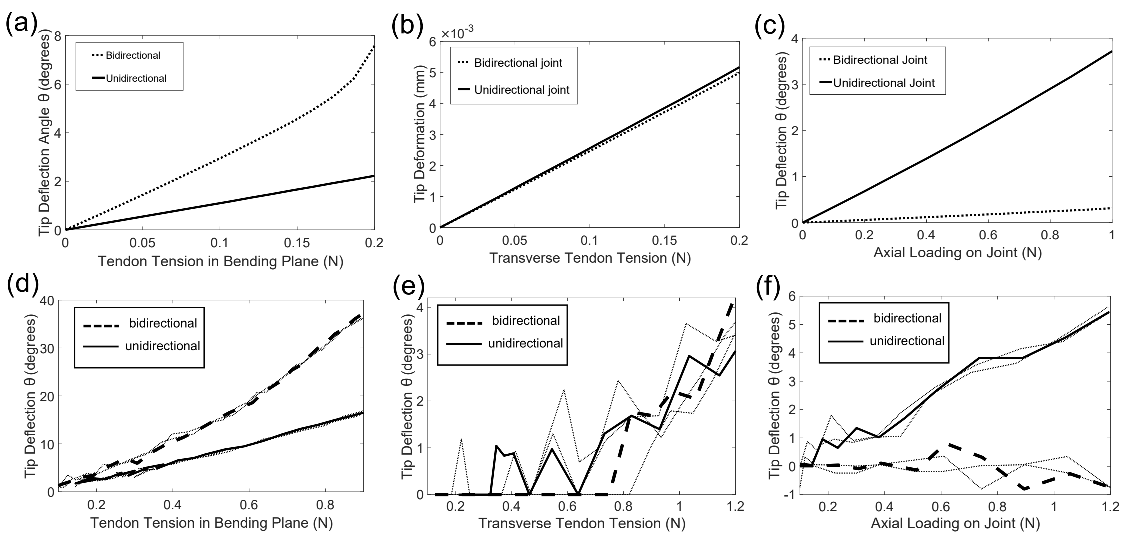

Figure 2.7: Forces applied along the bending plane ((a), (d)), orthogonal to the bending plane ((b), (e)), and axially ((c), (f)) on BAN joint (d = 0.5 mm, h = 0.2 mm) and unidirectional asymmetric joint (d = 0.6 mm, h = 0.2 mm). Figures (a) - (c) indicate FEM results for small loads and small deformations and Figures (d) - (f) indicate experimental results.

Next, we perform an FE analysis for the BAN and UAN joints for small deformations under small loads. These simulations allow us to design a BAN joint to have higher flexibility than the UAN joint in the bending plane, but equivalent stiffness in the direction orthogonal to the bending plane (see Fig. 2.7(a) - (c)). Using the experimental setup described in

Section 2.2, we confirm these simulated results for larger forces and deformations (see Fig. 2.7(d) - (f)) . More importantly, the depth of the cut made to achieve these numbers is much lower (d$_{bidirectional} = 500\ \mu$m) than that seen for the UAN joint (d$_{unidirectional} = 600\ \mu$m). As a result, a better performance can be obtained using a BAN joint, while improving resistance to external axial forces due to the presence of more material in the joint than in the case of the UAN joint (see Fig. 2.7(c), (f)).

CHAPTER 3

TWO DEGREE-OF-FREEDOM ROBOTIC GUIDEWIRE: DESIGN, MODELING AND CONTROL

In Chapter 1, we discussed the necessity of a guidewire in cardiovascular minimally invasive surgical procedures like PVD. In this chapter, we describe a novel design for a robotic guidewire with two orthogonally oriented bidirectional asymmetric notch (BAN) joints, that offer two degrees-of-freedom to the tip of the guidewire. This will provide the physician the ability to navigate at the distal end of the guidewire, to go around a plaque or structures, such as a vessel bifurcation along the path. In other words, this will allow the physician to make tight maneuvers through acute vascular routes, often encountered while navigating in PVD cases. This chapter can be summarized as follows: We begin by introducing the design of the robotic guidewire and the manufacturing process for the same (see Sec. 3.1). In Section 3.2, we present an analysis of the kinematics of the robot, followed by the development of a static model for the notch joint (see Sec. 3.3.1) and the base joint which includes the effects of tendon routing friction (see Sec. 3.3.2). We address the issue of inter-joint load-coupling in Section 3.3.3, and propose a strategy for correcting it in open-loop. Finally, we validate our static model using an observer that estimates shape of the base joint using tendon tension (see Sec. 3.4), and present tracking results for several task space trajectories in Section 3.4.2.

3.1 Design and Construction

The robot presented in this work is tendon driven, and contains two degrees-of-freedom. Each degree-of-freedom is controlled by two tendons that permit the joint to be controlled bidirectionally (BAN joint). Each pair of tendons controlling a joint is attached to the distal end of that joint. As a result, a total of four tendons are routed through the inner lumen

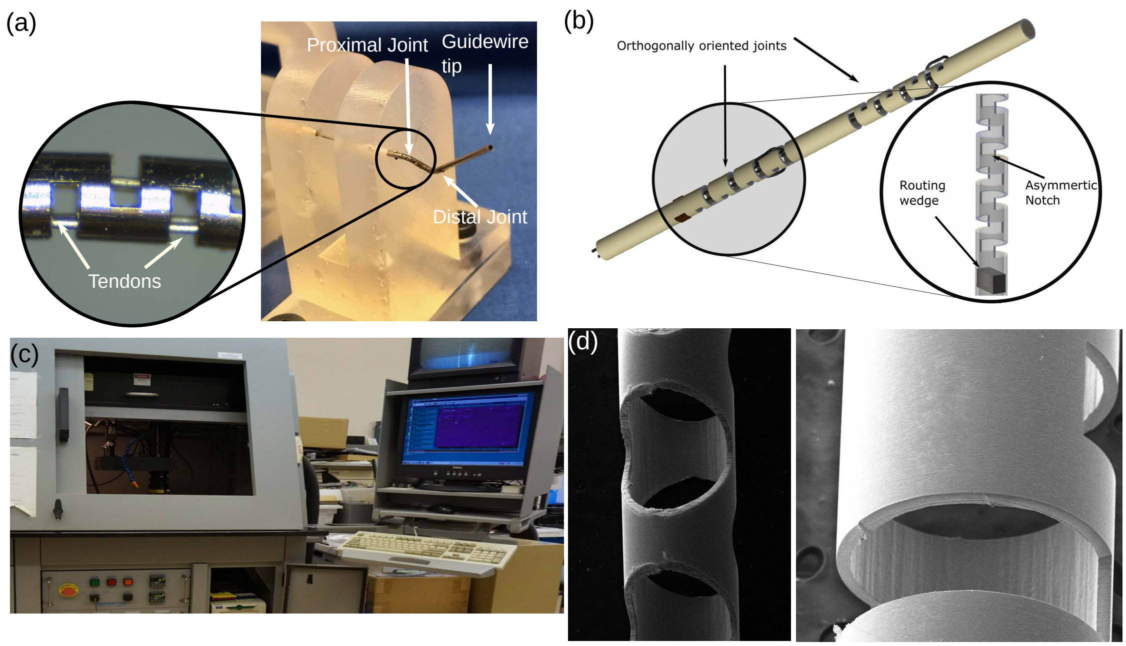

Figure 3.1: (a) The two degree-of-freedom (DoF) robotic guidewire actuated to reach points in 3D workspace. Each joint controlled by two tendons (inset), (b) Schematic of the 2-DoF micro-scale robot using orthogonally oriented notches. The inset shows the schematic of each joint, along with the routing wedge, (c) Nanosecond laser used for micromachining robotic guidewire, (d) SEM images of the femtosecond laser micromachined Nitinol tube show minimal Heat-Affected Zone (HAZ).

of the robot (see Fig. 3.1(a)) The design of the robot is detailed in Fig. 3.1(b). As can be seen in this figure, the robot is constructed from a single tube of Nitinol by micromachining notches into the tube. To manufacture the above designs, Infrared Nanosecond and Femtosecond lasers (Resonetics Corporation, Massachusetts, United States, see Fig. 3.1(c)) were used to cut rectangular notches into a nitinol tube of an outer diameter of 0.78 mm and inner diameter of about 0.62 mm (Confluent Medical, California, United States). The raw nitinol tube is placed in a lathe chuck to permit the rotation of the tube between the etching of joints, thus allowing the finished robot body to be constructed without physically extracting the part from the laser, thus minimizing positioning errors. This setup and the results under a scanning electron microscope are shown in Fig. 3.1(d). As can be seen in the figure, the usage of femtosecond laser pulses minimizes the heat-affected zone (HAZ) around the notches, therefore allowing the micromachining process to occur without accidental treatment of the material. This is not necessarily true for other manufacturing processes such as milling [122] or ablation with a laser of a longer pulse-width.

The creation of notches in the nitinol tube permits the tube to be bent in the plane of the notches, thus creating a joint at the location of the notches (Fig. 3.1(d)). By rotating the tube between joints, we are able to modify the orientation of these joints. For the purpose of this chapter, we rotate the raw tube by $\frac{\pi}{2}$ between joints, thus orienting the joints orthogonal to each other (see Fig. 3.1(a-b)). Finally, nitinol tendons with 0.1 mm diameter (Confluent Medical, California, United States) are manually routed into the tube and the ends bonded to the outer walls of the nitinol tube. We assume that a positive tension is applied to these tendons when they are pulled, and the tendons are incapable of exerting a negative tension on the tube. Also, we make the assumption, that the tendons exert a point force at their attachment point at the inner wall of the tube, and a constant reaction force along the wall of the tube [179].

To minimize coupling between the joints, tendon-driven continuum robots often use a variety of load decoupling strategies. These may include routing the tendons through an inner spine [91] or through individual channels [90, 180]. In our case, we are unable to do either, due to the lack of space in the inner lumen of the Nitinol tube. As a result, we forfeit the notion of complete load-decoupling of the tendons, and instead strive to achieve a 'controlled load-coupling' of the tendons through the inner lumen. This is achieved by inserting a rigid nitinol strip (termed the *routing wedge* in Fig. 3.1(b)). As seen in Fig. 3.1(a), one tendon of the proximal joint and one tendon of the distal joint are routed through each of the two openings of the routing strip. As a result, we achieve a repeatable inter-joint load-coupling in the robot, while keeping the manufacturing cost of the robot low. More complex routing mechanisms would be able to achieve a lower level of load-coupling between the proximal and distal joints, but would result in a longer manufacturing times. In this chapter, we hope to initiate a framework, that helps us easily incorporate our load-coupling into our control strategy.

3.2 Robot Kinematics

In this chapter, we model each asymmetric-notch joint of our underactuated robot as having a piecewise-constant curvature, which enables ease of robot-independent kinematic transformations [181]. In this section we begin by recapping an inverse transformation from the task space of the robot ($\boldsymbol{y}$) to the configuration space parameters ($\boldsymbol{\kappa}$), which is robot independent. Once this transformation is defined, we can move to the actuator space of the robot via a consideration of the statics of the model [90].

The dimensions associated with the kinematics of the robot are defined in Fig. 3.2(a), and the associated frames are denoted in Fig. 3.2(b). We denote the initial (undeformed) length of each notch joint by l_u. When the proximal joint is actuated by the tendon, it deforms by an angle θ. The curvature of this joint is defined as $\kappa_1 = \frac{\theta}{l_u}$, and the homogeneous

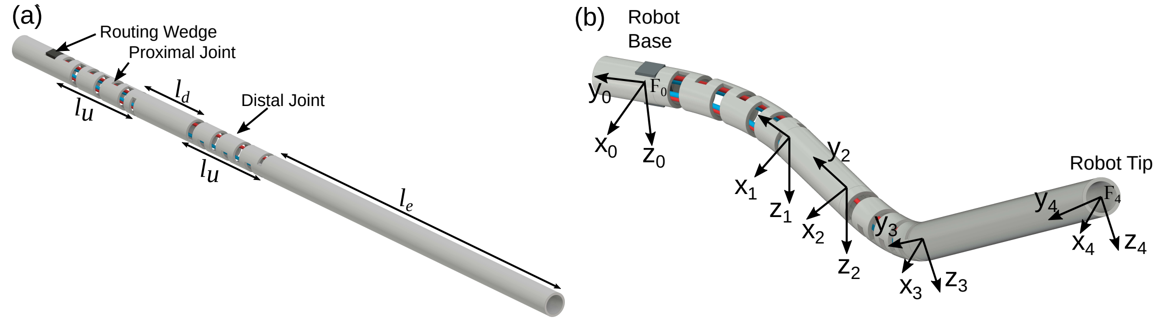

Figure 3.2: Forward kinematic model of a notch joint (a) Undeformed model with joint lengths, (b) Robotic guidewire tip in a deformed state with frames F_0-F_4 attached to the central axis of the robot.

transformation matrix for this joint is given as,

$$B_1^0 = \begin{bmatrix} C_\theta & -S_\theta & 0 & \frac{1-cos\theta}{\kappa_1} \\ S_\theta & C_\theta & 0 & -\frac{sin\theta}{\kappa_1} \\ 0 & 0 & 1 & 0 \\ 0 & 0 & 0 & 1 \end{bmatrix} \tag{3.1}$$

where C and S denote the cosine and sine functions, respectively. Unlike most continuum manipulators that have co-located DoFs, the second degree-of-freedom of our manipulator is located is a certain distance l_d from the Frame 1. This degree-of-freedom allows the robot to move out of the x_0-y_0 plane by an angle φ and its curvature is defined as $\kappa_2 = \frac{\varphi}{l_u}$. Therefore, the final transformation to the base of the robot from the tip can be formulated as follows:

$$B_4^0 = B_1^0.B_2^1.B_3^2.B_4^3 \tag{3.2}$$

where,

$$B_2^1 = \begin{bmatrix} 1 & 0 & 0 & 0 \\ 0 & 1 & 0 & -l_d \\ 0 & 0 & 1 & 0 \\ 0 & 0 & 0 & 1 \end{bmatrix} \tag{3.3}$$

and B_3^2 takes us from Frame 3 to Frame 2,

$$B_3^2 = \begin{bmatrix} 1 & 0 & 0 & 0 \\ 0 & C_\varphi & -S_\varphi & -\frac{sin\varphi}{\kappa_2} \\ 0 & S_\varphi & C_\varphi & \frac{cos\varphi - 1}{\kappa_2} \\ 0 & 0 & 0 & 1 \end{bmatrix} \tag{3.4}$$

Finally, B_4^3 involves a simple translation from Frame 4 to Frame 3, along $-y_3$ by length l_e. Ignoring the orientation at the tip of the guidewire, and assuming a given task-space reference input $[p^0, 1]^T \in \mathbb{R}^4$,

$$\begin{bmatrix} p^0 \\ 1 \end{bmatrix} = B_4^0 \cdot \begin{bmatrix} o^4 \\ 1 \end{bmatrix} \tag{3.5}$$

where $o^4 \in \mathbb{R}^3$ is the origin in the Frame 4. Using the dimensions of our guidewire tip prototype, the workspace of the robot tip is generated and displayed in Fig. 3.3.

For the controller to follow predefined trajectories, we must first define the inverse kinematics of the guidewire. Eq. 3.5 results in the following equations,

$$p_x^0 = l_e \sin\theta \cos\varphi + \frac{\sin\theta \sin\varphi}{\kappa_2} + l_d \sin\theta + (\frac{1 - \cos\theta}{\kappa_1}) \tag{3.6}$$

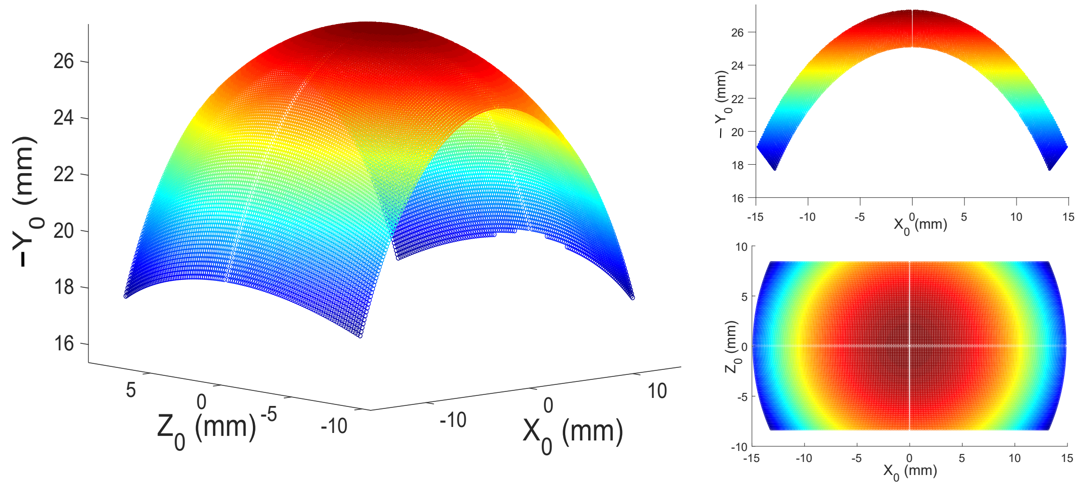

Figure 3.3: Workspace of the robotic guidewire. The joint angles θ and φ can range between $\pm 45°$ and $\pm 30°$ respectively. Joint lengths were measured under a microscope for the above simulations to be $l_u = 4.198$ mm, $l_e = 14.449$ mm, and $l_d = 2.916$ mm.

and subsequently,

$$p_z^0 = -l_e \cdot \sin\theta + (\frac{\cos\varphi - 1}{\kappa_2}) \tag{3.7}$$

The two unknowns θ and φ, and therefore, the curvatures (κ_1, κ_2) can be derived numerically using the above equations [182, 183]. We assume that the initial values of the joint angles are $\theta_{initial} = \arctan(\frac{p_x^0}{2l_u+l_d+l_e})$ and $\varphi_{initial} = \arctan(\frac{p_z^0}{l_u+l_e})$, so that $\theta_{initial} \leq \theta$ and $\varphi_{initial} \leq \varphi$, and increment joint angles until we converge upon the correct values. We use this approach to arrive at the robot curvature for our control system discussed in Section 3.4.

3.3 Robot Static Modeling

In addition to the geometric kinematics discussed above, a sufficient understanding of each notch joint comprising the robot must be developed. This includes a mapping from the joint curvature to the tension applied at the base of the joint. Traditionally, a mapping from the configuration space (κ) to the actuator space parameters ($\mathbf{u}$) is considered. However, in our case, we notice that there is a large variance introduced in this relationship by extremely

Algorithm 1 Robot independent inverse kinematics

Input:
$p = [p_x^0, p_y^0, p_z^0]^{\mathrm{T}}$
ϵ_t
Output:
$\kappa = [\kappa_1, \kappa_2]^{\mathrm{T}}$
Method:
$\theta_{est} = \arctan(\frac{p_x^0}{2l_u + l_d + l_e})$
$\varphi_{est} = \arctan(\frac{p_z^0}{l_u + l_e})$
while $error < \epsilon_t$ **do**
    $p_{est} = B_4^0.o^4$
    $error = p_{est}[2] - p_z^0$
    $\varphi_{est} = \varphi_{est} - G \cdot error$
while $error < \epsilon_t$ **do**
    $p_{est} = B_4^0.o^4$
    $error = p_{est}[0] - p_x^0$
    $\theta_{est} = \theta_{est} + G \cdot error$
$[\kappa_1, \kappa_2]^{\mathrm{T}} = \frac{1}{l_u}[\theta_{est}, \varphi_{est}]^{\mathrm{T}}$

small changes in the tendon path through the lumen of the tube especially at the point where it is bonded to the wall of the nitinol tube. On the other hand, the tension-curvature relationship is more repeatable and consistent, and we will derive the same in this section. For this set of trials, we consider only the case of a single tendon routed straight to distal end of the base joint of the robot.

3.3.1 Moment-Curvature Relationship

The bending angle of the notch joint results from the deformation of each notch that is formed by two tubes and a curved wall, as shown in Fig. 3.4(a). The total joint curvature κ can be approximated by superposition of bending angles of all tubes in the notch, which indicates a linear relationship between the curvature κ and tendon force P:

$$\kappa = d \cdot E_b \cdot P \tag{3.8}$$

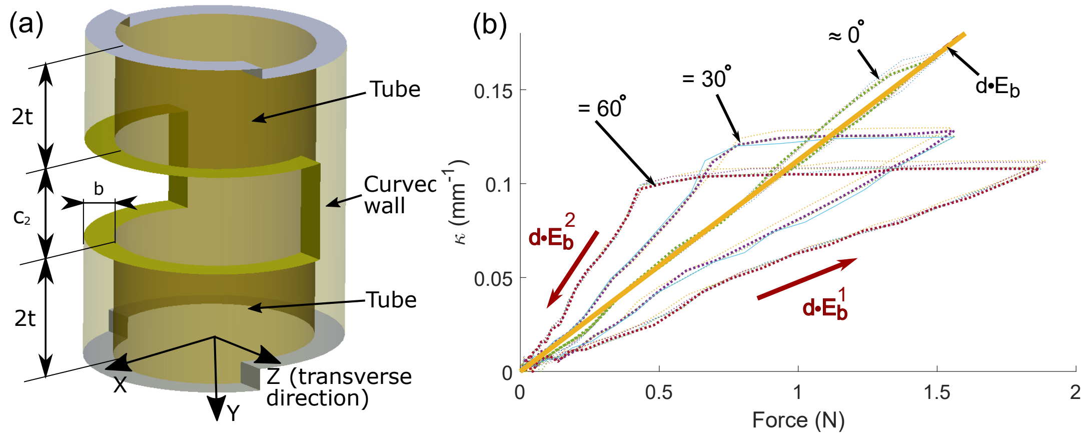

Figure 3.4: (a) Schematic of a single notch in a BAN joint, (b) Hysteresis seen in the τ vs. κ relationships for various values of wrapping angle (α) helps in estimating coefficient of friction (μ) and the bending elasticity (E_b) of the base joint.

where E_b can be defined as the bending elasticity of the joint [179]. Although the analytical model can provide a theoretical explanation about the bending behavior of the notch joint (and which will be developed in future chapters of this thesis), an accurate value of E_b can be estimated from experiments presented in this chapter.

3.3.2 Friction Effects

The above moment-curvature relations were developed with a setup that was designed assuming negligible friction effects. However, in a realistic situation, where two tendons are attached to the notch joint, and are not directly routed to the attachment point, we would see the effects of friction in this relationship. Due to the small diameter of the robot and the tendons controlling the robot, tendon tension can be measured only at the attachment point of the tendons to the actuators. As a result, friction must be incorporated into the moment-curvature relationship defined above. We use a Coulomb friction model to estimate the relationship between the measured tendon tension (τ) and the tension applied at base of the notch joint (T),

$$\tau = T \cdot e^{\mu \cdot \alpha \cdot \mathrm{sgn}(v)} \tag{3.9}$$

where μ is the coefficient of friction of the routing channel, α is the wrapping angle and v is the tendon velocity. Therefore, the relationship between the sensed tension and the joint curvature is given by,

$$\kappa = E_b \cdot \frac{d \cdot \tau}{e^{\mu \cdot \alpha \cdot \mathrm{sgn}(v)}} \tag{3.10}$$

The hysteresis in Fig. 3.4(b) for differing values of wrapping angle displays a linear τ - κ relationship for both positive and negative values of v. The slopes of these linear curves can therefore be expressed as $\Gamma_b(v, \alpha) = \frac{d \cdot E_b}{e^{\mu \cdot \alpha \cdot \mathrm{sgn}(v)}}$. For the hysteresis loop of angle α, we therefore can define two slopes E_b^1, and E_b^2, as displayed in Fig. 3.4(b). Assuming $E_b^1 = \frac{d \cdot E_b}{e^{\mu \cdot \alpha}}$ and $E_b^2 = \frac{d \cdot E_b}{e^{-\mu \cdot \alpha}}$.

Since the slopes E_b^1, E_b^2 are known, we can extract the value of E_b as

$$E_b = \frac{\sqrt{E_b^1 \cdot E_b^2}}{d} \tag{3.11}$$

We can see in Fig. 3.4(b), that for various wrapping angles, this value of joint bending elasticity (E_b) stays constant. As we specified previously, each joint of the robot has two tendons attached to its distal end for bidirectional control. As a result, we will have two wrapping angle values (α_1, α_2) associated with the base joint of the robot.

3.3.3 Coupling Effects

Due to the tendon routing described previously, distal tendons impart a moment on the proximal joint, causing an inter-joint load-coupling [90] to exist by design. In the absence of such coupling, actuating the distal joint without any actuation of the proximal joint should only cause the tip of the robot to move in the y_0-z_0 plane. As a result, a projection of the robot tip on the x_0-z_0 plane should result only in motion along the z_0 axis. However, we observed that a projection of the robot tip on the x_0-z_0 plane results in motion along both the axes (see Fig. 3.5(a), $x = 0$ mm). This phenomenon was also noted when the

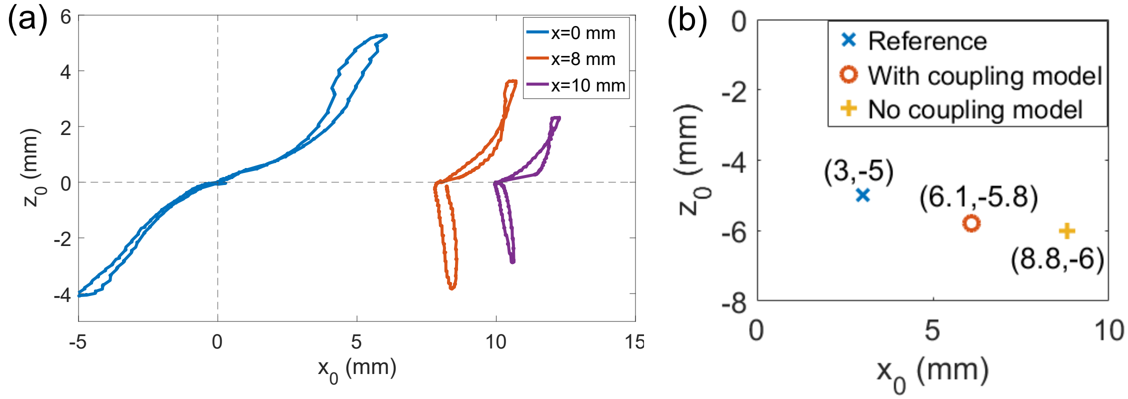

Figure 3.5: (a) Coupling seen between the two DoFs of the guidewire tip on actuating the distal joint with three offsets $x_0 = 0$ mm, $x_0 = 8$ mm and $x_0 = 10$ mm provided to the proximal joint, (b) Controller adjusting for coupling minimizes the steady state error in 2-DoFs.

proximal joint was pre-bent to a non-zero value of joint angle ($\theta \neq 0$) (see Fig. 3.5(a), $x = 8$ mm and $x = 10$ mm). This clearly shows, that pure actuation of the distal joint also causes additional bending in the proximal joint. To model the inter-joint coupling, we modify Eq. 3.8 as follows:

$$\underbrace{\begin{bmatrix} \kappa_1 \\ \kappa_2 \end{bmatrix}}_{\kappa} = d \cdot \underbrace{\begin{bmatrix} 1 & 1 \\ 0 & 1 \end{bmatrix}}_{C} \cdot \underbrace{\begin{bmatrix} E_b & 0 \\ 0 & E_b \end{bmatrix}}_{E_{bending}} \cdot \underbrace{\begin{bmatrix} T_1 \\ T_2 \end{bmatrix}}_{T} \tag{3.12}$$

where T_i is the tension applied at the base of the joint i. This relationship can be used to place the tip in the 2-DoF space, as shown in Fig. 3.5(b). A coupling model improves the steady-state error in 2-DoFs, where the Euclidean norm of the error decreases from 6.1 mm to 3.2 mm. This approach can be used for a more complete model of the coupling effect, and address problems like load-decoupled closed-loop control and path planning.

3.4 Control System

In this section, we initiate the design of a controller to take advantage of the moment-curvature relationship defined previously to control the base joint of the robot. For the

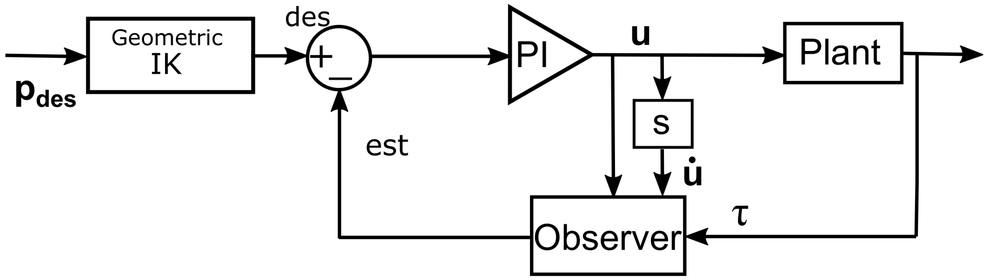

Figure 3.6: Closed loop control system to perform position control on the guidewire base-joint-space variables.

purpose of this chapter, we define the task space as the x_0-z_0 plane (while the operational space [184] of the robot is still $\mathbb{R}^6$). The proposed controller for this task space trajectory control of the robot tip is shown in Fig. 3.6. Consecutive points along a trajectory in the x_0-z_0 plane are provided as input (p_{des}) to the Geometric Inverse Kinematics algorithm defined in Section 3.2. This computation results in a desired curvature κ_{des}, that is then compared with the output of an observer that outputs the most recent state estimate κ_{est}. A PI controller for the actuator displacement is designed as $\mathbf{u} = K_p e + K_i \int edt$, where $e = (\kappa_{des} - \kappa_{est})$.

3.4.1 Observer Design

The Observer Block in Fig. 3.6 is designed to use the moment-curvature relationships to estimate the shape of the robot. Using the friction model defined in Section 3.3.2, we design a piecewise linear observer that uses the following relationships to estimate the base joint curvature $\kappa_{est}[\mathrm{n}]$ at the n^{th} discrete time step,

$$\kappa_{est}[\mathrm{n}] = \begin{cases} d \cdot \Gamma_{piecewise}(\mathbf{u}, \dot{\mathbf{u}}, \mathrm{n}) \cdot \tau[\mathrm{n}], \text{ if } \mathrm{sgn}(\dot{\mathbf{u}}[\mathrm{n}]) \\ \qquad\qquad\qquad\qquad = \mathrm{sgn}(\dot{\mathbf{u}}[\mathrm{n}-1]) \\ \kappa_{est}[\mathrm{n}-1], \text{ else if } \tau[\mathrm{n}] \in [\tau_{min}, \tau_{max}] \\ d \cdot \Gamma_{piecewise}(\mathbf{u}, \dot{\mathbf{u}}, \mathrm{n}) \cdot \tau[\mathrm{n}], \text{ else.} \end{cases}$$

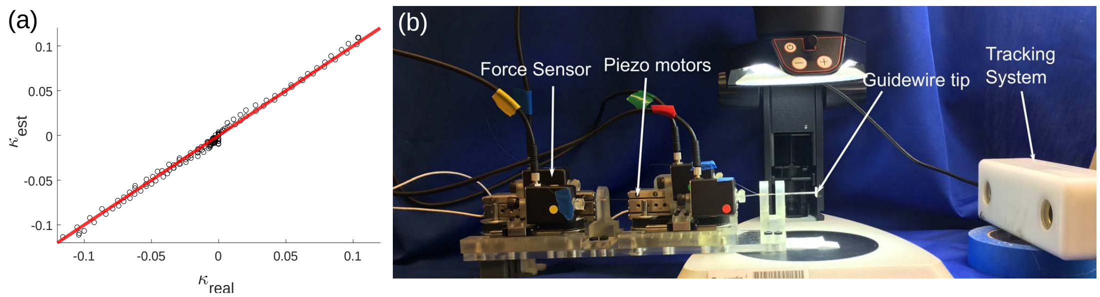

Figure 3.7: (a)Plot of Ground Truth curvature (κ_{real}) vs. the estimate curvature by our observer(κ_{est})), sampled during a set of random trajectories provided to the system. R^2 value for the estimate value of curvature was found to be 99.29%., (b) Antagonistic motion based controller hardware to test tracking accuracy. A tracker connected to the end of the guidewire prototype helps track the tip position in the $x_0 - z_0$ plane.

Here, $[\tau_{min}, \tau_{max}]$ which is the range of forces, for which the hysteresis curve plateaus is computed at each point in time. Also, the bending elasticity function $\Gamma_{piecewise}(\mathbf{u}, \dot{\mathbf{u}}, \mathrm{n})$ is different from the term Γ_b defined previously, and can be defined as follows:

$$\Gamma_{piecewise}(\mathbf{u}, \dot{\mathbf{u}}, \mathrm{n}) = \begin{cases} \Gamma_b(\alpha_1, \dot{\mathbf{u}}), & \text{if}\, \mathrm{sgn}(\mathbf{u}[\mathrm{n}]) > 0 \\ \Gamma_b(\alpha_2, \dot{\mathbf{u}}), & \text{else} \end{cases}$$

Where α_i is the wrapping angle of the tendon that is currently engaged. We tested our observer by providing a set of random trajectories to the system while sampling the curvature under a microscope at several points (see Fig. 3.7(a)). Using this observer, a satisfactory estimate of the base joint curvature in either direction is obtained, and may be used as feedback in our control system.

3.4.2 Tracking Performance

To test our controller, we constructed the compact setup shown in Fig. 3.7(b). Each joint of the robot has two tendons bonded to its distal end, which on the actuator side terminate at an antagonistic transmission which uses a single piezo-based linear actuator (SmarAct GmbH, Oldenburg, Germany). The transmission consists of a timing-belt and pulley arrangement that enables antagonistic motion of the two tendons in effect, similar to the ones used in

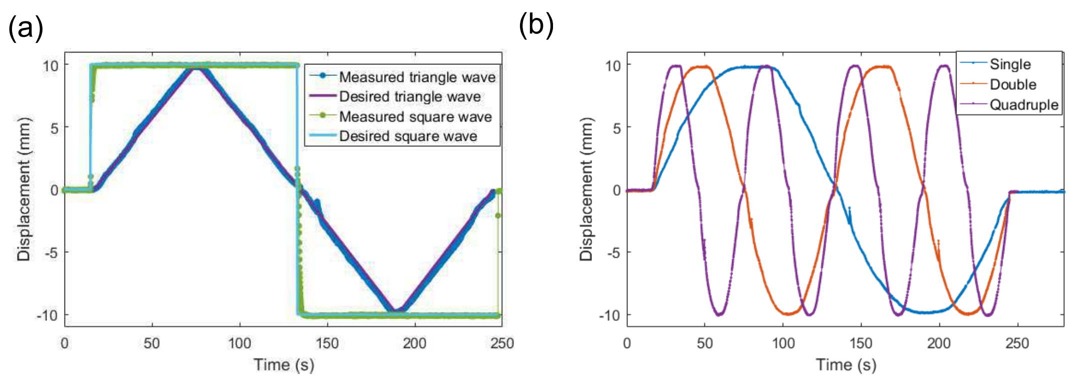

Figure 3.8: (a) Tracking results of the base joint for sinusoidal, triangular and square reference inputs on the x_0 axis, (b) Tracking results for sinusoids of varying frequencies.

previous robotic catheter controllers [182]. Each tendon is bonded to the transmission via a load cell with a maximum load capacity of 5 lbs (Transducer Techniques, California, United States). The data from the force sensor, an encoder and the microscope are acquired via a 16-bit ADC (Model 826, Sensoray, Portland, United States) and UART respectively. An image processing algorithm that uses Hough transforms automatically provides us with the ground truth for the base joint curvature at each point of time. Lastly, a marker is attached to tip, and a stereoscopic camera (MicronTracker H40, Toronto, Ontario, Canada) tracks the end of the guidewire prototype in the x_0-z_0 plane.

Next, we provided three types of input profiles (sinusoidal, triangular and square trajectories) in task space to the base joint controller. The time period of each input type was varied from 50 secs - 250 secs. Fig. 3.8(a)-(b) illustrates that the PI controller defined previously is able to track the input profiles closely, with negligible steady state error for each step input. Furthermore, it is also able to track at speeds often seen in a surgical environment.

3.5 Conclusions

In this chapter, we presented a novel robotically actuated 2-DoF guidewire tip, with the ability to deliver tension to two orthogonal degrees-of-freedom. We also introduced the design and manufacturing process for such an active guidewire and analyzed the statics and kinematics of the joints that constitute the robot. We demonstrated a control strategy for the base joint of the robot taking advantage of the statics model. While this robot demonstrates precise control of individual degrees-of-freedom for joints with fixed lengths, it cannot execute any follow-the-leader motion strategies that are critical for catheters to navigate around tortuous anatomy. In the next chapter, we address this major shortcoming of the 2-DoF guidewire with a novel mechanism known as the Co-axially Aligned Steerable (COAST) mechanism that allows for follow-the-leader motion at scales smaller than those addressed in this chapter.

3.6 Acknowledgement

The author would like to thank Dr. Xuefeng Wang for part of the contents of this chapter.

CHAPTER 4

CO-AXIALLY ALIGNED STEERABLE (COAST) GUIDEWIRE: DESIGN, MODELING, AND CONTROL

In the last chapter, a tendon-driven robotic guidewire design was proposed, analyzed and evaluated. Similar other tendon-driven catheters and guidewires have been proposed in literature previously [78, 79, 185]. However, all of these designs have a fixed joint length or a discrete set of joint lengths. This does not permit the clinician to vary the bending length (and therefore, the curvature) of the guidewire according to the vessel geometry, making it difficult for the guidewires to cross tortuous anatomy without kinking or breakage. Furthermore, these designs do not perform any sort of follow-the-leader (FTL) motion making it challenging for the guidewire to navigate into acute anatomical paths such as the aortic bifurcation, or around the aortic arch. The notion of follow-the-leader mechanisms has been around for decades, with the first mention of an FTL-like mechanism known as the 'active endoscope' introduced by Ikuta *et al.* in 1988 [186]. This mechanism was designed using five antagonistic-SMA joints and had an outer diameter of 13 mm, and executed what the authors called 'shape control'. This control strategy was a first attempt to actively control the body of the catheter to follow a certain path, without using an anatomical wall as a passive guide to the robot. Similarly, cable-driven mechanisms have been proposed to execute follow-the-leader motion (also commonly known as 'snakes') extensively. For example, the

HARP (Highly Articulated Robotic Probe) was able to execute follow-the-leader mechanism by using two tubes called 'snakes' whose stiffness was controllable [187, 188]. Using a series of motors to control three outer tendons, one central tendon and two feeders for each snake, the authors could execute FTL motion successfully. The large outer diameter of HARP-like tendon-driven FTL robots have made it possible to use these robots only in specific types of cardiovascular procedures [189].

Mechanisms such as concentric tube assemblies allow the curvature and bending angle of the robot to be varied with increasing joint length [190, 191]. These robots are designed by arranging several precurved SMA tubes within each other. By rotating and translating each of the individual tubes, the position and orientation of the distal ends of the robots can be controlled. In some very specific cases, concentric tube robots can execute follow-the-leader (FTL) motion [192, 193, 194]. However, this requires precurvature selection and a specific actuation sequence which may not be trivial. Furthermore, concentric tube robots suffer from instabilities arising from the presence of multiple minimum energy states [195]. This often results in the robot 'snapping' from one minimum energy state to another during operation, which may be dangerous to the procedure. The authors in [196] suggest a way to avoid this problem by micromachining notch structures within the individual tubes. However, the precurved nature of the tubes is retained, which results in a coupling between the joint lengths and bending angle of the robot, i.e. the bending length and the bending angle of concentric tube robots cannot be individually controlled.

In this chapter, we propose a tendon-driven 'COaxially Aligned STeerable (COAST)' guidewire robot that can simultaneously and independently control the bending angle and the length of the bending segment, thereby executing follow-the-leader motion at its distal bending segment. Finally, the entire robot assembly can be miniaturized to a total outer diameter of 0.40 mm. These characteristics make the COAST mechanism extremely suitable for use as a micro-scale steerable robotic guidewire. The guidewire is capable of advancing its distal end through complex vasculature of varying curvatures with minimal interaction and support from the vessel walls. Therefore, the proposed study can implement a vascular intervention procedure with a single COAST guidewire navigation without any replacement to alternative guidewires, which may significantly reduce the operational time and effort.

This chapter is organized as follows: We first summarize the mechanical designs in Section 4.1 for the COAST guidewire robot (Section 4.1.1) and the compact actuation mechanism (Section 4.1.2), along with a characterization of the roll motion component of the mechanism (Section 4.1.3). Section 4.2 details the mechanical models developed for different aspects of the COAST guidewire; starting with a large deflection curved beam bending model for the notched tubes (Section 4.2.1), curvature-stiffness modeling for coaxially combined notched tubes (Section 4.2.2), followed by a friction-based static and kinematic model for the actuated robot that relates curvature to required tendon stroke (Section 4.3.1). In Section 4.4, we develop the forward kinematics model (Section 4.4.1) and a Jacobian-based inverse kinematics model (Section 4.4.2) for the guidewire robot to generate actuator inputs, given an FTL trajectory. A control scheme is presented involving feedforward and feedback blocks to compensate for actuator space errors (Section 4.4.3), and the method is implemented for the COAST robot to perform FTL motion in free space (Section 4.4.4) and within 3D printed vasculature phantoms (Section 4.4.5). Finally, we present our conclusions in Section 4.5.

4.1 Mechanism and Design

4.1.1 COAST Mechanism and Actuation Module

To implement the 'follow-the-leader' motion with limited DoFs in the compact space required for a guidewire, the COAST robot has coaxially aligned three layered structure consisting of inner, middle, and outer tubes (see Fig. 4.1(a)). The inner tube is made of stainless steel and has a regular cylindrical cross-section with an inner channel, while the middle and outer tubes are nitinol tubes with notch patterns micromachined along the

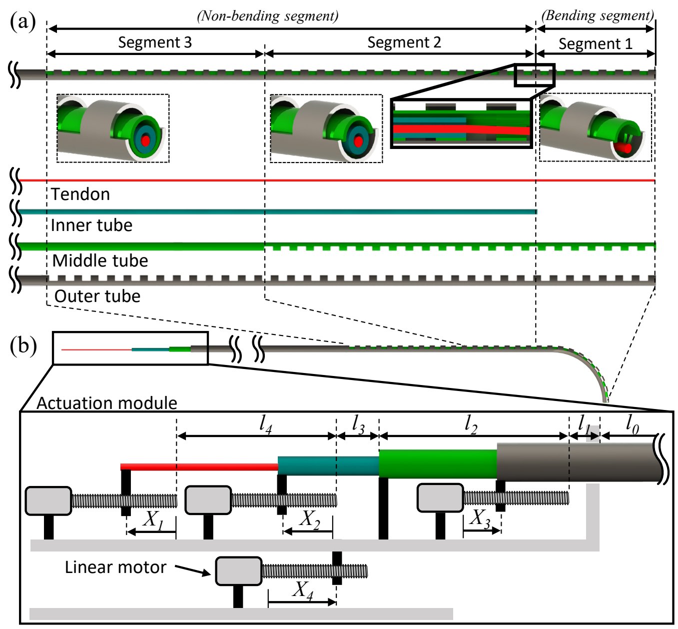

Figure 4.1: (a) Schematic of the coaxially aligned steerable (COAST) guidewire robot with the various tubes used in the assembly, (b) Schematic of the actuation module used to control the tendon and coaxial tubes.

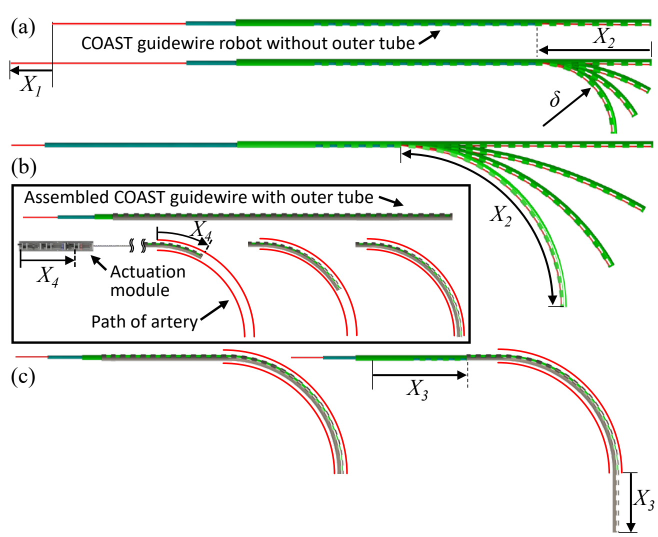

Figure 4.2: (a) Controlling the tendon stroke (X_1) and joint length (X_2) allows for variable curvature, (b) Controlling X_1 and X_2 while advancing the actuation module (X_4) allows for follow-the-leader motion, (c) outer tube advanced individually (X_3) to go further into a target vasculature, while retaining the curvature at the location of the vessel tortuosity.

lengths of each tube. These notches are unidirectional asymmetric notch joints such as the ones proposed in [122, 197]. Each of the tubes has suitable dimensions so that they can respectively slide within each other. To avoid collision/interference between the notches on the middle and outer tube, there is a 180 degree phase difference in the notches. A tendon passes through the inner tube and is connected to the distal end of the middle tube. Depending on the relative positions of each tube and notch pattern, the proposed structure is divided into three segments (i.e., segments 1-3 in Fig 4.1(a)). In segment 1, the notch pattern on the middle tube decreases its second moment of area and shifts its neutral axis to the un-notched side, which increases compliance as well as the moment arm of the tendon. In segment 2, however, introducing the stainless steel inner tube increases the second moment of area of the combined structure, resulting in a significant increase in the stiffness of segment 2 as well as decrease of the moment arm. Lastly, only the outer tube retains its notch patterns in segment 3, which contributes to an increased stiffness of segment 3. Therefore, the proposed structure has three segments with varying stiffness and can be largely classified into bending (i.e., segment 1) and non-bending segments (i.e., segments 2 and 3) depending on the relative position of the inner tube.

The proposed coaxially aligned tubes and tendon are connected to an actuation module (see Fig. 4.1(b)). The tendon, inner tube, and outer tube, are connected to linear motors respectively, while the middle tube is fixed to the actuation module itself. Therefore, the actuation module has three control variables: X_1, X_2, and X_3, corresponding to tendon stroke, relative distance between the inner and middle tubes, and displacement of the outer tube respectively. In addition, we can rotate and translate the actuation module itself, using control variables ψ and X_4 respectively. Therefore, totally, we have five controllable variables in the system:

$$\begin{bmatrix} \psi \\ X_1 \\ X_2 \\ X_3 \\ X_4 \end{bmatrix} = \begin{bmatrix} \text{Actuator Stage Roll Angle} \\ \text{Tendon Stroke} \\ \text{Bending Segment Length} \\ \text{Outer Tube Displacement} \\ \text{Actuator Stage Displacement} \end{bmatrix}$$

Given the control variables, the proposed mechanism can form the shape of any arc within geometric constraints, since X_1 and X_2 control the curvature and arc length of bending segment, respectively (see Fig. 4.2(a) - details are introduced in Section 4.3). Therefore, the bending segment can follow the curved path of the vasculature, which is a function of the curvature and arc length by controlling X_1 and X_2 as well as feeding the actuation module (X_4), which leads to a follow-the-leader motion during guidance along a curved path (see Fig. 4.2(b)) without any passive support from the vasculature wall. Finally, the outer tube can slide and proceed further along the curved middle tube (see Fig. 4.2(c)); It can provide a stable passage for the middle tube to reach proper locations as an introducer sheath, while retaining the curvature at the location of the curved path. This entire procedure can then be repeated at the next curved path to reach the final target location. The proposed mechanism therefore provides easy insertion of the guidewire into tortuous vasculature without replacement of guidewire, thereby significantly reducing the procedure time. Therefore, effectively, the COAST guidewire features two modes of operation:

- Follow-The-Leader (FTL) motion: FTL motion can be achieved by controlling X_1, X_2 and X_4 simultaneously at any roll angle ψ.
- Feed-Forward (FFw) motion: The outermost tube can be individually advanced (by actuating X_3) to further displace the distal tip of the robot while retaining the current curvature along the body of the robot.

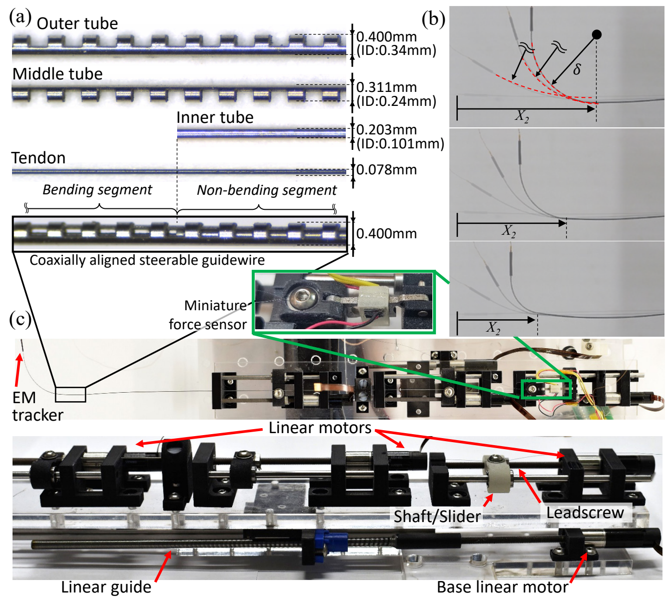

Figure 4.3: (a) Coaxial tubes and dimensions, (b), Demonstration of COAST achieving various curvatures at different arc lengths (X_2) (c) Actuation stage showing individual linear motors to control the COAST guidewire.

A first test-bench COAST guidewire prototype was constructed and assembled as shown in Fig. 4.3. The outer and middle tubes are made using superelastic nitinol for high bending capability and their notch patterns are fabricated on a femtosecond laser (WS-Flex Ultra-Short Pulse Laser Workstation, Optec, Frameries, Belgium). The tendon is also made of nitinol for ease of insertion through the tubes and ease of attachment. Finally the inner tube is stainless steel, since it has a higher stiffness than nitinol. The tube and tendon diameters are indicated in Fig. 4.3(a). The outer tube, the inner tube, and the tendon are connected to linear motors (Maxon Precision Motors, MA, United States, resolution $\approx 2.8\ \mu$m) and generate linear motion, sliding on each surface (see Fig. 4.3(c)). Through the motor strokes, we can control the tendon displacement (X_1) and the bending joint length (X_2), thereby achieving variable curvatures at several bending joint lengths (see Fig. 4.3(b)). The entire actuation stage is installed on the base stage with a linear guide and actuated by a base linear motor (to control X_4). The tendon is connected to a miniature force sensor [198] to measure the tendon tension.

Table 4.1: Specifications of the COAST guidewire prototype.

Items	Outer tube	Middle tube	Inner tube	Tendon
Total length (mm)	242	253.1	269.5	388.68
Length of the notched section (mm)	112.8	75.0	-	-
Outer diameter, $2r_o$, (mm)	0.480	0.36	0.254	0.076
Inner diameter, $2r_i$, (mm)	0.400	0.300	0.239	-
d (mm)	0.424	0.243	-	-
h (mm)	0.315	0.315	-	-
c (mm)	0.285	0.285	-	-
Young's modulus (GPa)	42.6	42.6	200	53.965

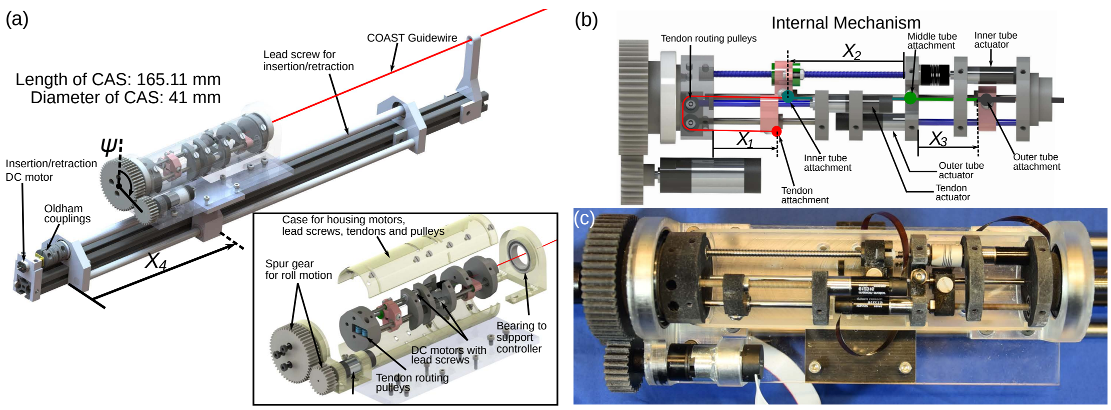

Figure 4.4: (a) Assembled and exploded (inset) view of the CAS for the COAST guidewire and the driving unit shows the DC motor and lead screw arrangement that enables the entire setup to be compact, (b) Inner mechanism of the CAS and control variables for individual tubes, (c) Image of inner mechanism

.

4.1.2 Compact Actuation System (CAS)

The preliminary actuation stage of Fig. 4.3 is then replaced by a compact actuation stage (CAS). The outer and middle tubes are micromachined using a femtosecond laser (WS-Flex Ultra-Short Pulse Laser Workstation, Optec, Frameries, Belgium) from a stock tube of superelastic nitinol (elastic modulus, E = 40-45 GPa). The inner tube is made from AISI 304 stainless steel due to its added stiffness (E_{inner} = 200 GPa). The dimensions of the tubes are indicated in Table 4.1. The tendon is a superelastic nitinol tendon with an elastic modulus of 53.965 GPa (see Fig. 4.11(c)). Notch parameters on both tubes (specifically notch depth, d, and lengths of the notched sections) were selected to ensure that the guidewire can traverse angles typically found in adult aortic bifurcations (35° $\pm$ $11.1°$ [199]). High accuracy measurements for d, h and c are performed using the focusing lens in the femtosecond laser. The tubes and the tendon are attached to the CAS (see Fig. 4.4(a)), which is a compact cylindrical structure of length 165.11 mm and diameter 41 mm. The CAS is fixed onto the actuator stage, which is advanced/retracted using a DC Motor (Pololu Robotics and Electronics, NV, United States) with a 380:1 gear ratio and 110 mNm nominal torque, attached to a lead-screw (OD: 3/8 in, pitch: 40 rev/in) and linear-bearing rails (McMaster-Carr®, GA, USA) (indicated by X_4 in Fig. 4.4(a)). Rolling motion (indicated by ψ in Fig. 4.4(a)) is achieved with a DC motor (Maxon Precision Motors, MA, United States) with a 141:1 gear ratio and 297.5 mNm nominal torque via a spur gear assembly (gear-ratio 1:2, see Fig. 4.4(a)). The cylindrical case is attached to the larger spur gear at one end, and rests on two ball bearings at either end of the case. An exploded view of the cylindrical actuator assembly is shown in Fig. 4.4(a)(inset). The outer and inner tubes and the tendon are actuated by DC motors with a 16:1 gear-ratio and nominal torque of 9.968 mNm (Maxon Precision Motors, MA, United States) with a lead screw assembly, while the middle tube is attached to an intermediate disk and is rigidly connected to the actuator stage itself. In each case, the lead-screws are supported on either end by locating and non-locating bearings to account for radial and axial misalignment. The attachment points for all the tubes and the tendon, as well as the control variables for the tubes ($X_1 - X_3$), are indicated in Fig. 4.4(b). The whole assembly is made compact by ensuring that the individual DC motor bodies do not add to the length of the stage. This is achieved by overlapping each motor body with the lead screw of another degree-of-freedom. For example, the DC motor corresponding to the inner tube actuation coincides axially with the location of the lead screw for the outer tube and vice versa (see Fig. 4.4(c)). Similarly, the tendon is routed using two pulleys (see Fig. 4.4(a)(inset) and 4.4(b)) to reverse the direction of the tendon stroke (wrapping angle for the routing assembly is $\alpha = \pi$). This causes the

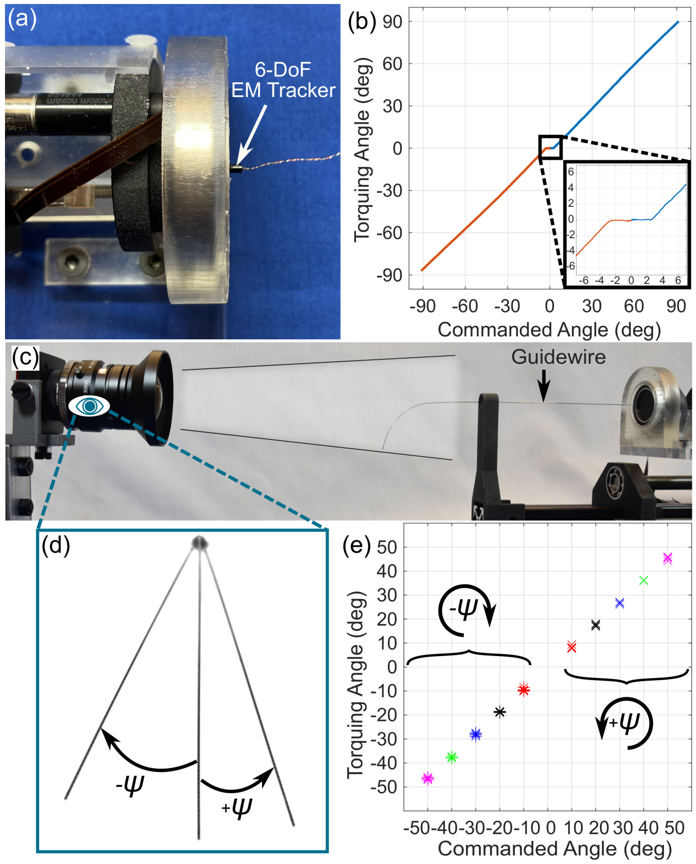

Figure 4.5: (a) EM tracker attached to the CAS for characterizing roll motion component, (b) Achieved vs. commanded torquing angle plot for 0° to $\pm 90^\circ$ (inset: dead bands for both trials indicating backlash), (c) Experimental setup for characterizing roll motion with COAST guidewire assembled in the CAS, (d) Camera perspective view of torqued guidewire configurations, and (e) Achieved vs. commanded torquing angle plot for assembled guidewire case.

tendon stroke to overlap with the stroke of the motor controlling the inner tube, thereby further reducing the size of the compact actuation system. This tendon routing and motor arrangement minimizes the controller stage length while increasing the overall stroke of the lead-screws in comparison to the actuation module. Furthermore, the cylindrical structure ensures that the motor assembly mass is distributed consistently around the axis of the spur-gear assembly, thereby further reducing the load on this degree-of-freedom.

4.1.3 Validation of Torquing Motion

To characterize the motion and backlash of the torquing components, we use a 6-DoF EM tracker (Aurora®, Northern Digital Inc., Ontario, Canada) affixed to the front portion of the CAS body as shown in Fig. 4.5(a). For two separate experimental trials, ramped control inputs of $0°$ to $90°$ and $0°$ to $-90°$ respectively, are given, and the roll angle from the EM tracker is acquired. Fig. 4.5(b) shows the resulting torquing angle of the CAS vs. the commanded input angle for the two trials. We observe a maximum error of $\pm 3°$ which is attributed to machining limitations and imperfect mating of the spur gears. For both trials, we observe initial dead bands of $2.5°$, as shown in Fig. 4.5(b)(inset), which is estimated as the backlash resulting from torquing motor housing and space between the teeth of the spur gears. Validation of torquing with the COAST guidewire assembled in the CAS is performed with a CMOS Camera (Zelux™ 1.6 MP, Thorlabs Inc., NJ, United States), with the camera facing the distal end of the guidewire as shown in Fig 4.5(c). The guidewire is actuated such that the camera view consists of a line, which rotates around a pivot point as the CAS is torqued. This view, as seen by the camera, is shown in Fig. 4.5(d), with the actuated and torqued guidewire configurations superimposed. A set of five trials was performed for each commanded angle of $\{\pm 10°, \pm 20°, \pm 30°, \pm 40°, \pm 50°\}$ and the resultant torquing angles are acquired by comparing the slopes of the lines due to the torqued configurations with the $\psi = 0°$ line. Fig. 4.5(e) shows the plot of the torquing angles vs. the commanded input angles for the guidewire assembled case. The error between the two angle values is found to increase for higher torquing angles, with a maximum of $\pm 4.5°$ for the commanded input of $\pm 50°$. In addition to the machining and backlash, the errors are also inferred to be due to the weight of the actuated tip, which applies counter-moment resulting in torsion of the guidewire body.

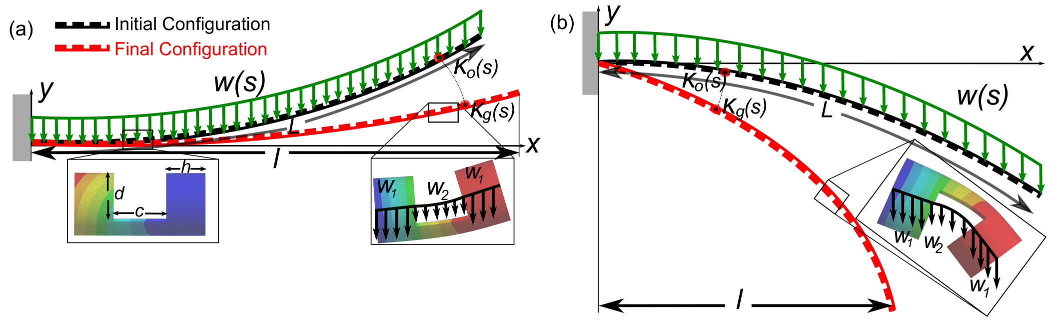

Figure 4.6: Curved micromachined beam with gravity induced large deflections for (a) positive and (b) negative initial curvatures.

4.2 Mechanical Model

4.2.1 Large Deflection Curved Beam Bending

We begin by considering the case of a single notched tube (either the outer or middle tube) with notch depth, d, notch width, c, and n notches in the joint (see Fig. 4.6(a)). Furthermore, r_o and r_i are the outer and inner radii of the tube respectively and unidirectional asymmetric notch pattern micromachining creates a cross-section of area $(A_o - A_i)$ at the notches. The laser micromachining also results in a machining-induced pre-curvature in the tubes. The direction of this pre-curvature corresponds to the direction of the notch pattern in the bending plane and its magnitude is a function of the depth, d, of the rectangular notches. We assume that in the absence of any external loading (including gravity effects), this curvature is constant across the entire length of the beam and is indicated by $\kappa_o(d) = 1/R_o(d)$ (where $R_o(d)$ is the radius of curvature). This is a reasonable assumption, since the machining parameters stay constant throughout the length of the tube, and hence, pre-curvatures are distributed equally along this length (the notch depth d is dropped from the terms $\kappa_o(d)$ and $R_o(d)$ in the remainder of this section for brevity). Therefore, individual tubes in the COAST mechanism behave like pre-curved slender cantilever beams of length L under gravity loading (see Initial Configurations, indicated by the black-colored beams in Fig. 4.6). Gravity induced loading results in a non-trivial deformation of these pre-curved beams (see Final Configurations, indicated by red-colored beams in Fig. 4.6) and this deformation is highly dependent on the initial configuration of the cantilever beam. This loading may be assumed as a distributed load, $w(s)$, with a fixed direction (along the negative $y-$axis in Fig. 4.6(a)-(b)) which is a piecewise function of the path of this pre-curved cantilever beam:

$$w(s) = \begin{cases} w_1 & s \in ((n-1)(h+c), nh+(n-1)c] \\ w_2 & \text{otherwise} \end{cases} \tag{4.1}$$

where, $w_1 = \pi\rho g(r_o^2 - r_i^2)$ and $w_2 = \rho g(r_o^2 - r_i^2)\cos^{-1}(\frac{d-r_o}{r_o})$ (see Fig. 4.6(insets)). Here, $\rho = 6450\,\text{kg/m}^3$ is the density of nitinol, $E = 45\,\text{GPa}$ is the elastic modulus of superelastic nitinol in its austenite phase, $g = 9.81\,\text{m/s}^2$, $d \geq r_o$ is the depth of the rectangular notches, c is width of each notch, h is the separation between two notched sections and $n = 1, 2, \ldots, N$, is a variable representing the notch number. The notch parameters, $\{d$, h, $c\}$, are assumed to be uniform throughout the length of the notched sections of the tubes. Similarly, the second moment of area $I(s)$, which is also a function of the path variable, can be defined as follows:

$$I(s) = \begin{cases} \frac{\pi}{4}(r_o^4 - r_i^4) & s \in ((n-1)(h+c), nh+(n-1)c] \\ (r_o^4 - r_i^4)\frac{(\phi + \sin\phi)}{8} - \frac{8\sin^2\left(\frac{\phi}{2}\right)(r_o^3 - r_i^3)^2}{9\phi(r_o^2 - r_i^2)} & \text{otherwise} \end{cases} \tag{4.2}$$

where, $\phi = 2\arccos\left(\frac{d-r_o}{r_o}\right)$. Also, the location of the neutral axis of our notched tube is given as follows:

$$\bar{y}_j(d, r_o, r_i) = \frac{4\sin\left(\frac{\phi}{2}\right)(r_o^3 - r_i^3)}{3\phi(r_o^2 - r_i^2)} \tag{4.3}$$

The beam deformation equation in Cartesian coordinates for large deflections of a pre-curved beam is given as follows:

$$\kappa_g(x) = \frac{\frac{d^2y}{dx^2}}{[1 + (\frac{dy}{dx})^2]^{3/2}} = \frac{1}{R_o} - \frac{M(x)}{EI(x)} \tag{4.4}$$

The integral approach introduced in [200] is used to determine the governing equations for our beam:

$$\frac{ds}{dx} = \frac{1}{\sqrt{1 - H^2(x)}} \tag{4.5}$$

$$\frac{dy}{dx} = \frac{H(x)}{\sqrt{1 - H^2(x)}} \tag{4.6}$$

where $H(x) = \int_0^x (\frac{1}{R_o} - \frac{M(x)}{EI(x)})dx$. This is a variant of the method proposed in [200] for curved beams with path-varying cross-sections and loads. For a given projected final length of the curved beam (onto the x-axis), l, the total length of the beam can be determined by integrating Eq. (4.5) (see Fig. 4.6). By searching the projected length, l, until $|s(l) - L| < \epsilon_{err}$, we arrive at the final solution for the path of the beam under gravity loading. The search space and the computation time can be reduced from the monotonicity of $s(l)$ with respect to l [200]. Here, ϵ_{err} is a normalized error margin. Once the final projected length, l, of the beam is known, Eq. (4.6) can be solved to determine the final Cartesian coordinates of the beam. Since the distributed load and second moments of area ($w(s)$ and $I(s)$) are given as a function of path, s, which is a function of loading w, we divide the load ρg into N_{load} equal steps [201]. At each load step, $j = 1, 2, \ldots, N_{load}$, the path information of the previous load step (solution to Eq. (4.5)) and the current load are used to determine shear forces and bending moments [201]:

$$V^j(x) = \int_x^l w^j(x^{j-1})dx \tag{4.7}$$

$$M^j(x) = \int_x^l V^j(x)dx \tag{4.8}$$

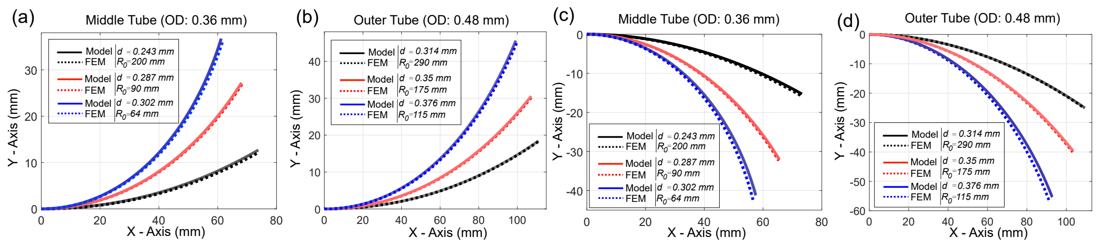

Figure 4.7: Validation of the curved beam bending model in ANSYS for (a-b) positive pre-curvatures and (c-d) negative pre-curvatures for stainless steel tubes with $N = 1$ and varying r_o, d, and R_o values.

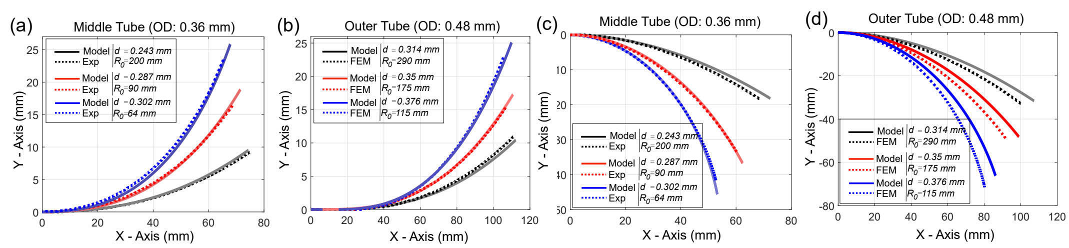

Figure 4.8: Validation of the curved beam bending model for experimental data with (a-b) positive pre-curvatures and (c-d) negative pre-curvatures for tubes with varying $N = \{125, 188\}$, r_o, d, and R_o values.

The moment, thus approximated, is used to determine $H^j(x)$ in Eqs. (4.5-4.6). A similar procedure is used to approximate $I^j(x)$ (second moment of area of the current load step) from Eq. (4.5) and $I(s^{j-1})$. First, we validated our large-deflection curved beam model with finite element simulations in ANSYS® 18.2 for stainless steel ($E = 200\,\text{GPa}$) beams with a single long notch ($N = 1$). The numerical integration for $H(x)$, Eq. (4.5), and $s(l)$ for various values of l at each load step were computed on a 20 core Intel® Xeon® Processor using the parallel processing toolbox in MATLAB® R2020b. The tube dimensions (r_o, r_i, d, R_o, and L) were varied to match the outer and middle tubes. In each case, we observe that the numerical model (Eq. (4.6)) accurately predicts the final shape of the curved beam for both positive and negative initial curvatures (see Fig. 4.7). We then proceed to test our model experimentally for outer and middle tubes sampled with varying notch parameters (see Fig. 4.8). We observe that the model successfully estimates the shape of the beams for all middle tube samples and all outer tube samples with positive curvatures (see Fig. 4.8(a)-(c)). We find that the model begins to deviate from the experimental results for

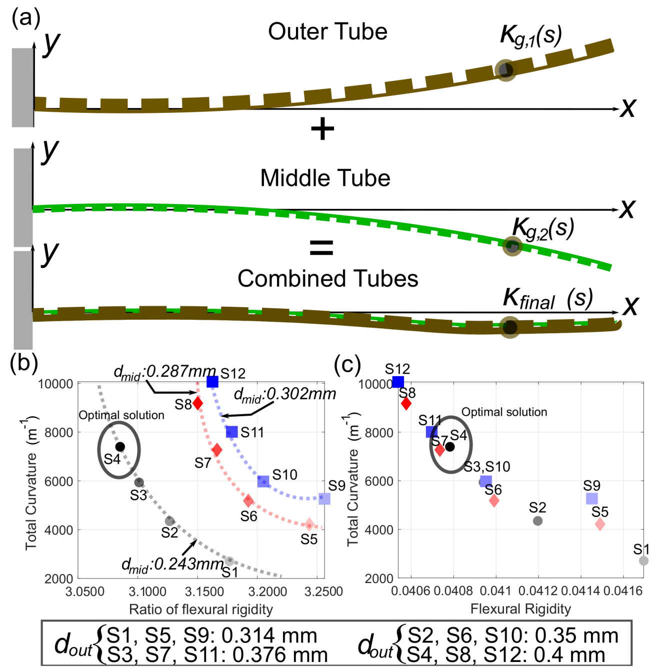

Figure 4.9: (a) Combined beam bending behavior of the outer and middle nitinol tubes, (b) Graph of Flexural Rigidity ratios of the outer to the middle tube vs. total curvature in the combined tube samples, (c) Graph of Flexural Rigidity vs. total combined curvature. Depths of the middle and outer tubes are given by d_{mid} and d_{out} respectively.

outer tubes with negative pre-curvatures (see Fig. 4.8(d)). We hypothesize that this may be due to the machining tolerances that especially affect higher deformations of initially pre-curved notched beams when the pre-curvatures are in the direction of the distributed force (gravity).

4.2.2 Combined Tube Optimization

When the COAST mechanism is assembled completely, the final pre-curvature of its bending segment is determined by the pre-curvatures, moments and the flexural rigidity of the individual beams comprising the assembly, primarily the outer and middle tubes (see Fig. 4.9(a)). We use a modified version of the method proposed in [202] to achieve the final curvature of the tube as follows:

$$\kappa_{final}(s) = [\sum_{k=1}^{N_t} E_k I_i(s)]^{-1} [\sum_{k=1}^{N_t} M_k(s) + E_k I_k(s) \kappa_{g,k}(s)] \tag{4.9}$$

where $N_t = 2$ is the number of micromachined tubes in our mechanism and individual curvatures $\kappa_{g,k}(s)$ are obtained from Eqs. (4.4) and (4.5). Note, that unlike [202], gravity has a significant contribution to the final shape of the pre-curvature and leads to large deflections in the individual tubes. As a result, this term cannot be ignored and is incorporated in our updated model. Finally, $\kappa_{final}(s)$ is a piecewise function of s, much like $\kappa_g(s)$, $I(s)$, and $w(s)$, due to varying cross-sections. Therefore, the total pre-curvature in any given telescoping combination of outer and middle tubes will be considered and is given by $\int_{s=0}^{L} |\kappa_{final}(s)|$.

Fig. 4.9(b)-(c) are plots of 12 samples (S1, S2,. . . , S12) of coaxially combined middle and outer tube pairs. The plot displays the ratios of the flexural rigidity of the outer-tube to that of the middle tube ($\int_{s=0}^{L} I_{out}(s) / \int_{s=0}^{L} I_{mid}(s)$) vs. the total pre-curvature ($\int_{s=0}^{L} |\kappa_{final}(s)|$) for each sample. Furthermore, Fig. 4.9(c) represents a graph of flexural rigidity of the samples ($\int_{s=0}^{L} I_{out}(s) + I_{mid}(s)$) vs. the total pre-curvature in the samples. We observe that sample S1 has the lowest predicted pre-curvature, but suffers from relatively higher dominance of the outer tube in comparison to sample S4, which demonstrates lowest rigidity ratio (see Fig. 4.9(b)). In fact, sample S1 demonstrates the highest total flexural rigidity and hence may be unsuitable for a guidewire application due to the risk of vascular perforation (see Fig. 4.9(c)). We therefore select samples S3 and S4 as our best samples with relatively low rigidity and yet minimal pre-curvatures. In the remainder of this chapter, we will use sample S4 with $d_{mid} = 0.243$ mm and $d_{out} = 0.4$ mm as the middle and outer tube notch depths respectively.

4.3 Kinematics Modeling

In this section, we first derive the relationship between the tendon stroke (X_1), the desired curvature (κ), and bending joint length (X_2).

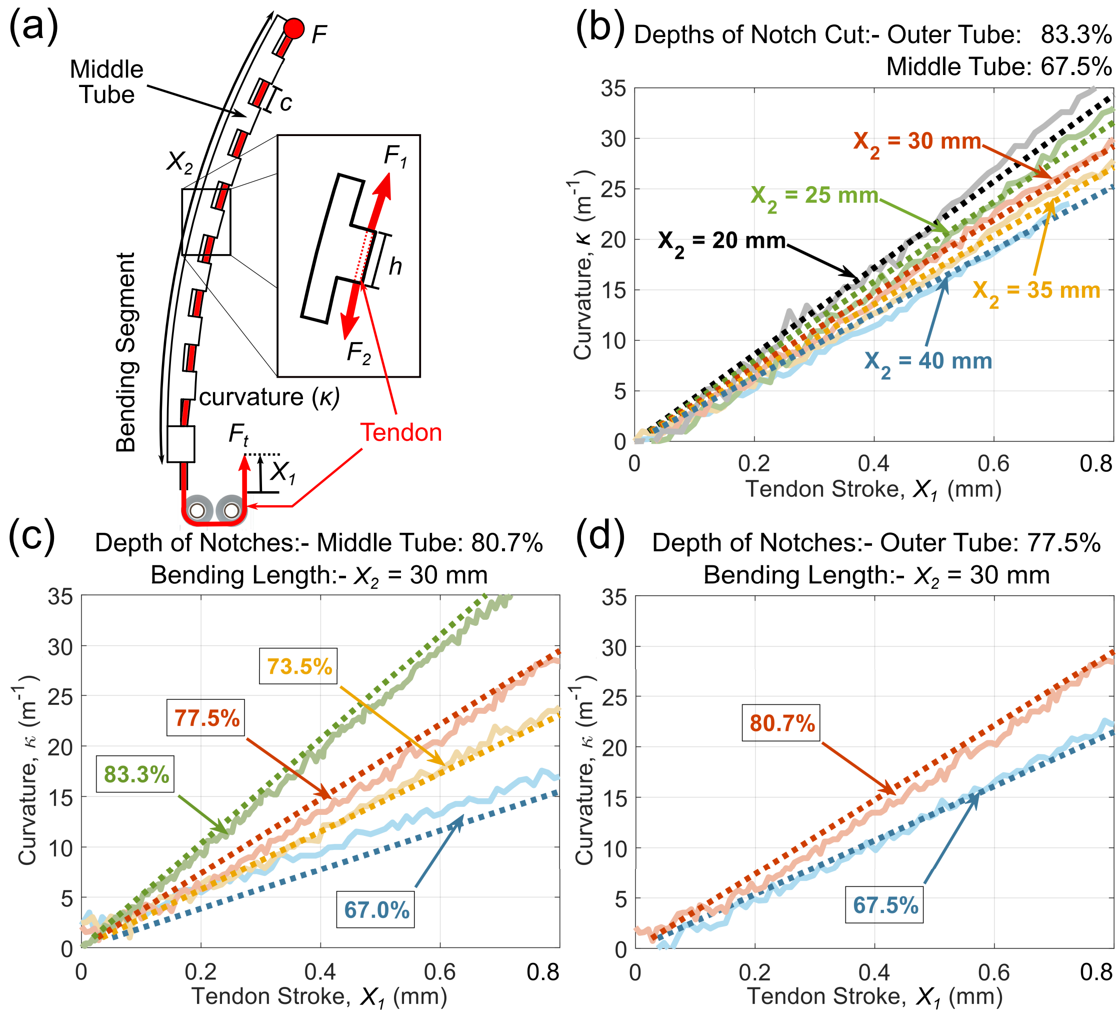

Figure 4.10: (a) Schematic of guidewire bending segment showing forces at the tip (F), and the actuator (F_t); Plots showing variation of curvature (κ) vs. tendon tendon stroke (X_1) in joint loading case: (b) varying bending lengths (X_2) for sample S4, (c) varying outer tube's notch depths for constant middle tube and bending length, and (d) varying middle tube's notch depths for constant outer tube and bending length. Solid and dashed lines indicate experimental and modeled data, respectively.

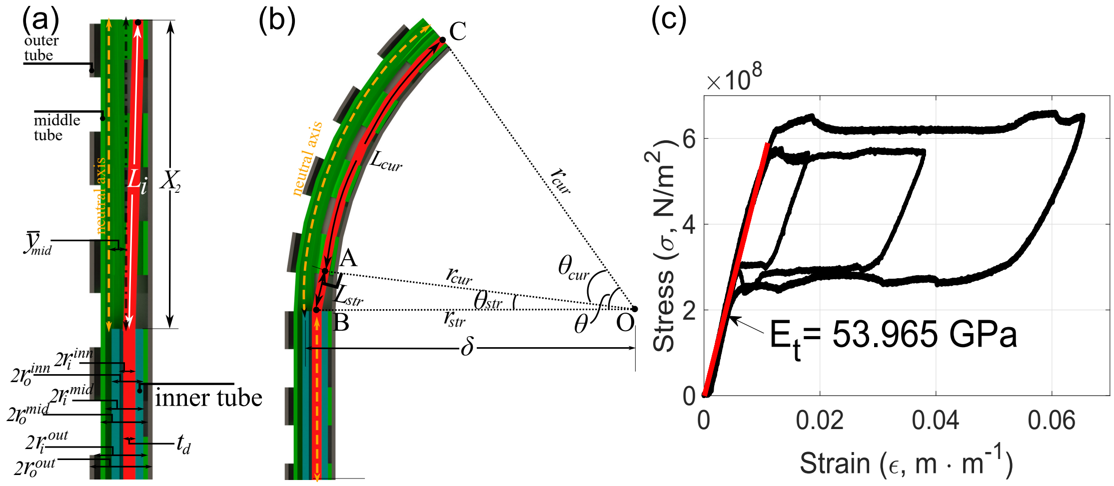

Figure 4.11: (a)-(b) The coaxial tube structure geometry in the straight configuration and with curvature $\kappa = (\frac{1}{\delta})$, (c) Stress-strain curve for the Nitinol tendon.

4.3.1 Joint Kinematics

A simplified schematic of the COAST guidewire is shown in Fig. 4.10(a), where the notched joint represents the bending segment (only middle tube shown) and a shortened tendon. The tendon stroke (X_1) required for a desired curvature (κ) at a certain bending segment length (X_2) is derived as:

$$X_1 = \underbrace{\Delta L^{kin}(\kappa, X_2)}_{\text{Geometric term}} + \underbrace{\frac{\sigma_t L_{total}}{E_t}}_{\text{Tendon elongation}} \tag{4.10}$$

$$= \Delta L^{kin}(\kappa, X_2) + \frac{F_t L_{total}}{\pi E_t r_t^2} \tag{4.11}$$

Tendon elongation is the dominant term in this relationship, and it depends on the stress in the tendon, given by $\sigma_t = F_t/(\pi r_t^2)$. Here, F_t is the tendon tension at the actuator (see Fig. 4.10(a)), $r_t = 38\,\mu$m is the tendon radius, $L_{total} = 388.68$ mm is the undeformed total tendon length (from its attachment point on the actuator to the guidewire tip). Let us first derive the expression for the geometric term, $\Delta L^{kin}(\kappa, X_2)$ above. A schematic of the bending portion of the robot along with the various lengths and radii of the tubes is shown in Fig. 4.11(a). The tendon diameter is indicated as $t_d = 2r_t$. The initial length of the tendon in this straight configuration is given by $L_i(X_2){=}\sqrt{r_{off}^2{+}X_2^2}$. Here, $r_{off}{=}(r_o^{inn}{-}r_i^{inn})$, is the offset between the inner tube and the middle notch joint. This is the length at which the joint begins to bend and is therefore critical to eliminate any slacking of the tendon at any stage. As the bending segment of the guidewire bends to a certain curvature κ, the inner wall of the middle tube forms an arc of angle θ with center 'O' (see Fig. 4.11(b)). As a result, the path of the tendon through the middle tube can be divided into two portions. The straight portion of the tendon, denoted by line segment $\overline{\text{AB}}$ in Fig. 4.11(b), runs from the inner wall of the inner tube and intersects the bending portion of the middle tube at point 'A' such that the line $\overline{\text{AB}}$ is tangential to the bending curve at point 'A'. The second portion, denoted by arc AC in Fig. 4.11(b), bends with the middle tube, running along the inner wall of the middle tube with radius, r_{cur}. Furthermore, $\bar{y}_{mid}(d^{mid}, r_o^{mid}, r_i^{mid})$ (derived in Eq. (4.3) and abbreviated as $\bar{y}_{mid}$ in future references) is the location of the neutral axis of the notched section of the middle tube in its central coordinate frame. From geometry, we observe that the triangle formed by the straight portion of the tendon, ΔOAB, is a right angled triangle, where $\overline{\text{OB}} = r_{str} = (\delta{-}\bar{y}_{mid}{-}r_i^{mid}{+}r_o^{inn}{-}r_i^{inn}{+}r_t)$, and $\overline{\text{OA}} = r_{cur} = (\delta - \bar{y}_{mid} - r_i^{mid} + r_t)$. Furthermore, $\delta = (\frac{1}{\kappa})$ is the radius of curvature of the middle joint. The length of the straight portion of the tendon is then given as $L_{str} = \sqrt{r_{str}^2 - r_{cur}^2}$. The interior angle θ_{str} between the sides $\overline{\text{OA}}$ and $\overline{\text{OB}}$ is given as $\theta_{str} = \arccos(r_{cur}/r_{str})$ and the length of the curved portion of the tendon is: $L_{cur} = r_{cur}(\theta - \theta_{str})$. Finally, the tendon displacement needed for the target geometry combination of (κ, X_2) is given as follows:

$$\Delta L^{kin}(\kappa, X_2) = L_i(X_2) - (L_{str} + L_{cur}). \tag{4.12}$$

We assume that primarily, friction losses occur from the pulleys in the CAS and tendon-notch interactions. Accounting for these losses as in [203, 122], the tendon tension can be expressed in terms of the bending moment applied to the joint tip as:

$$F_t = e^{\mu\alpha \mathrm{sgn}(v)} \eta^{L_N \mathrm{sgn}(v)} \frac{M_t}{\Delta y_t} \tag{4.13}$$

where M_t is the applied moment by the tendon, Δy_t is the moment arm of the tendon at the distal end of the robot, $\mu = 0.2965$ is the coefficient of friction of the pulleys in the CAS, while $\eta = 1.0063$ is the friction loss occurring due to cable interactions with the notch edges (such that $F_2 = \eta F_1$ in Fig. 4.10(a)(inset)). Furthermore, $L_N = (X_2 N_{mid})/L_{mid}^{notch}$ is the total length of the notch walls in contact with the tendon (N_{mid} and L_{mid}^{notch} being the number of notches and the length of the notched section for the middle tube, respectively). Substituting Eq. (4.13) in Eq. (4.11), and relating applied tension, F_t, to the curvature, κ, (using the Euler beam model proposed in [204]) the joint kinematics model is completed as follows:

$$X_1 = \Delta L^{kin}(\kappa, X_2) + e^{\mu\alpha \mathrm{sgn}(v)} \eta^{L_N \mathrm{sgn}(v)} \frac{E(I_{out} + I_{mid}) L_{total}}{\Delta y_t \pi E_t r_t^2} \kappa \tag{4.14}$$

where E is the elastic modulus of the tubes, E_t is that of the tendon (derived experimentally in Fig. 4.11(c)), and I_{mid} and I_{out} are the second moments of area of the middle and outer tubes, respectively. We validate the kinematics model for different pairs of outer and inner tubes with bending lengths varying as X_2={20,25,30,35,40} millimeters. The CMOS camera is used to image the deflection of the bending section by setting the imaging plane parallel to the plane of bending. The curvature (κ) of the bending segment is extracted from the acquired images and plotted against the tendon stroke (X_1), for different values of the bending segment length (X_2), as shown in Fig. 4.10(b) for the tube pair selected from Section 4.2.2. The model is observed to be in agreement with the experimental results. We observe some initial deviation for the bending lengths $X_2 > 25$ mm. This non-linearity is attributed to the high compliance of the outer tube as a result of high notch depth. Fig. 4.10(c) also shows the variation of the $X_1 - \kappa$ relation when the notch depths for only the outer tube are varied. Similarly Fig. 4.10(d) shows the $X_1 - \kappa$ relation when the notch depths for only the middle tube are varied. Eq. (4.14), hence, also models the variation of notch depth for the individual tubes as seen in these figures.

4.4 Control and Experiments

4.4.1 COAST Robot Forward Kinematics

We now define a Forward Kinematics (FK) map for the COAST guidewire robot, and use an analytical Jacobian to map the actuator space ($\boldsymbol{q}$) of the robot to the task space ($\boldsymbol{x}$). We consider frames $\{F^i\},\ i = \{0, 1, 2, 3, 4, 5\}$, shown in Fig. 4.12(a) for the robot joints, and use product of exponentials to define the transformation from the tool-frame, $\{F^5\}$, to the base-frame, $\{F^0\}$. The transformation between the base-frame and tool-frame of the unactuated guidewire robot is given by:

$$g_{st}(0) = \begin{bmatrix} 1 & 0 & 0 & 0 \\ 0 & 1 & 0 & 0 \\ 0 & 0 & 1 & L_{0,5} \\ 0 & 0 & 0 & 1 \end{bmatrix} \tag{4.15}$$

where $L_{0,5}$ is the constant distance measured between the CAS exit and the distal tip of the robot. In this work, as in our previous chapters, we assume a constant curvature bending characterized by κ. The bending length is defined by X_2 and bending angle is then given as $\theta = \kappa X_2$. The remaining joint parameters are defined as the actuator stage displacement, X_4, and the roll (torquing) angle, ψ. The assumed constant curvature bend can be represented geometrically as a chord as shown in Fig. 4.12(b). The tangent angles of the chord are defined as half of the bending angle whereas the change in length, θ_d, is

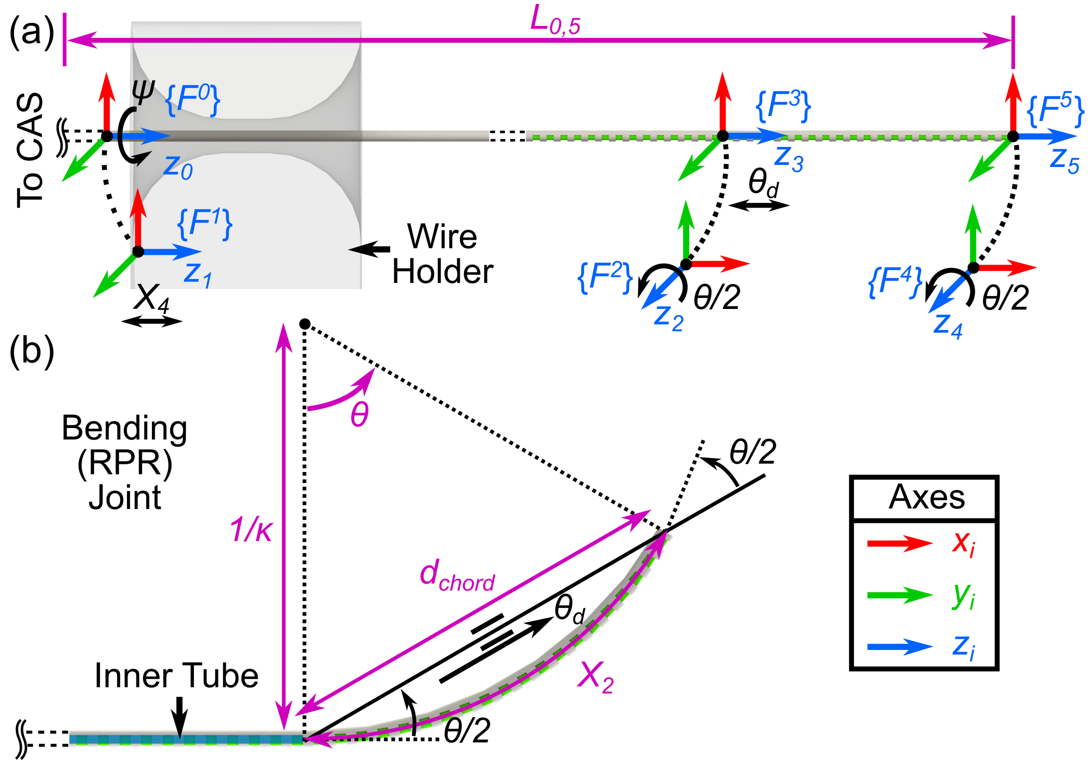

Figure 4.12: Schematic of (a) unactuated COAST guidewire showing the coordinate frames $\{F^0\}$-$\{F^5\}$ (x, y and z axes shown with red, green and blue arrows, respectively), and (b) bending joint at guidewire tip considered as a serial RPR manipulator.

defined as the difference between chord and arc length given by:

$$\theta_d = d_{chord} - X_2 = \frac{2X_2 sin(\theta/2)}{\theta} - X_2 \tag{4.16}$$

Thus, the bending joint can be modeled as a revolute-prismatic-revolute (RPR) joint with parameters $\theta/2$, θ_d, and $\theta/2$ shown in frames $\{F^2\}$, $\{F^3\}$, and $\{F^4\}$ respectively.

The twist for joint i is defined as $\xi_i = \begin{bmatrix} v_i & \omega_i \end{bmatrix}^T$, where ω_i is the unit angular velocity of the joint as expressed in the fixed frame, and $v_i = -\omega_i \times q_i$, for q_i being the position vector of the origin of frame $\{F^i\}$ [205]. The twist for a prismatic joint is defined as $\xi_j = \begin{bmatrix} v_j & 0 \end{bmatrix}^T$, where v_j is the unit velocity of the origin of the frame $\{F^j\}$ affixed to the prismatic joint. The angular velocities and the position vectors of the frames for the revolute joints are given as:

$$\omega_1 = \begin{bmatrix} 0 \\ 0 \\ 1 \end{bmatrix} \; \omega_3 = \begin{bmatrix} 0 \\ 1 \\ 0 \end{bmatrix} \; \omega_5 = \begin{bmatrix} 0 \\ 1 \\ 0 \end{bmatrix}$$
$$q_1 = \begin{bmatrix} 0 \\ 0 \\ 0 \end{bmatrix} \; q_3 = \begin{bmatrix} 0 \\ 0 \\ L_{0,5} - X_2 \end{bmatrix} \; q_5 = \begin{bmatrix} 0 \\ 0 \\ L_{0,5} \end{bmatrix} \tag{4.17}$$

The linear velocities for the frames affixed to the prismatic joints are given as:

$$v_2 = \begin{bmatrix} 0 \\ 0 \\ 1 \end{bmatrix} \; v_4 = \begin{bmatrix} 0 \\ 0 \\ 1 \end{bmatrix} \tag{4.18}$$

The resultant twists for each joint are given by:

$$\xi_1 = \begin{bmatrix} 0 \\ 0 \\ 0 \\ 0 \\ 0 \\ 1 \end{bmatrix} \xi_2 = \begin{bmatrix} 0 \\ 0 \\ 1 \\ 0 \\ 0 \\ 0 \end{bmatrix} \xi_3 = \begin{bmatrix} -(L_{0,5} - X_2) \\ 0 \\ 0 \\ 0 \\ 1 \\ 0 \end{bmatrix}$$
$$\xi_4 = \begin{bmatrix} 0 \\ 0 \\ 1 \\ 0 \\ 0 \\ 0 \end{bmatrix} \xi_5 = \begin{bmatrix} -L_{0,5} \\ 0 \\ 0 \\ 0 \\ 1 \\ 0 \end{bmatrix} \tag{4.19}$$

The forward kinematics of the robot are given through the product of exponentials:

$$g_{st}(\Theta) = e^{\hat{\xi}_1 \psi} e^{\hat{\xi}_2 X_4} e^{\hat{\xi}_3 \frac{\theta}{2}} e^{\hat{\xi}_4 \theta_d} e^{\hat{\xi}_5 \frac{\theta}{2}} g_{st}(0) \tag{4.20}$$

The full forward kinematics mapping is given by:

$$g_{st}(\Theta) = \begin{bmatrix} C_\psi C_\theta & -S_\psi & C_\psi S_\theta & C_\psi \frac{1-C_\theta}{\kappa} \\ S_\psi C_\theta & C_\psi & S_\psi S_\theta & S_\psi \frac{(1-C_\theta)}{\kappa} \\ -S_\theta & 0 & C_\theta & \frac{S_\theta}{\kappa} + L_{0,5} - X_2 + X_4 \\ 0 & 0 & 0 & 1 \end{bmatrix} \tag{4.21}$$

where S and C denote the sine and cosine functions respectively. The position, $\boldsymbol{p} = (p_x, p_y, p_z)$, of the guidewire tip is given by the fourth column, while the orientation of the tangent vector at the tip, $\boldsymbol{t} = (t_x, t_y, t_z)$, is given by the third column of the matrix $g_{st}(\Theta)$. The task space is hence defined by $\boldsymbol{x} = [p_x \; p_y \; p_z \; t_x \; t_y \; t_z]^T$. We make a note here that the FFw motion (X_3) is treated as an additional feature of the COAST guidewire mechanism and not included in the kinematic mapping. The actuator space hence consists of the inputs $\boldsymbol{q} = [\psi \; X_1 \; X_2 \; X_4]^T$. Modeling and control with X_3 as input for trajectories involving FTL-inaccessible targets will be included in our future work.

4.4.2 Jacobian Model

Given a constant curvature trajectory, the actuator input required to achieve the desired trajectory is estimated using the Jacobian pseudo inverse ($J^\dagger$). We begin with the mapping of the actuator input velocity vector $\dot{\boldsymbol{q}} = [\dot{\psi} \; \dot{X}_1 \; \dot{X}_2 \; \dot{X}_4]^T$ onto the task space velocity vector $\dot{\boldsymbol{x}} = [\dot{p}_x \; \dot{p}_y \; \dot{p}_z \; \dot{t}_x \; \dot{t}_y \; \dot{t}_z]^T$.

$$J(\boldsymbol{q})\dot{\boldsymbol{q}} = \dot{\boldsymbol{x}} \tag{4.22}$$

where $J(\boldsymbol{q})$ is the analytical Jacobian matrix formed by the partial derivatives $\partial\boldsymbol{x}/\partial\boldsymbol{q}$.

The FK map $g_{st}(\Theta)$ (Eq. (4.21)) does not show the direct dependence of the trajectory on the actuator variable X_1. To obtain the kinematics pertaining to X_1, we consider the time derivative of the kinematic model (Eq. (4.14)):

$$\dot{X}_1 = \frac{\partial X_1}{\partial X_2}\dot{X}_2 + \frac{\partial X_1}{\partial \kappa}\dot{\kappa} \tag{4.23}$$

Hence, Eq. (4.23) allows us to compute the rate of change of tendon stroke, X_1, in terms of rates of change of bending length, X_2, and the curvature, κ. We then redefine the actuator space as $\boldsymbol{q'} = [\psi\ X_2\ X_4]^T$ and $J(\boldsymbol{q'})$ as:

$$J(\boldsymbol{q'}) = \begin{bmatrix} -S_\psi \frac{1-C_\theta}{\kappa} & C_\psi S_\theta & 0 \\ C_\psi \frac{1-C_\theta}{\kappa} & S_\psi S_\theta & 0 \\ 0 & C_\theta - 1 & 1 \\ -S_\psi S_\theta & \kappa C_\psi C_\theta & 0 \\ C_\psi S_\theta & \kappa S_\psi C_\theta & 0 \\ 0 & -\kappa S_\theta & 0 \end{bmatrix} \tag{4.24}$$

A full column rank Jacobian matrix results in an overdetermined system. To obtain the Inverse Kinematics (IK), we consider a general least squares solution to Eq. (4.22), resulting in the left pseudo inverse, $J^\dagger$, and the solution for $\dot{\boldsymbol{q}}'$ is:

$$\dot{\boldsymbol{q}}' = J^\dagger \dot{\boldsymbol{x}}, \text{ where } J^\dagger = (J^T J)^{-1} J^T \tag{4.25}$$

The obtained $\dot{\boldsymbol{q}}'$ vector is then integrated to find the inputs ψ, X_2, and X_4 as functions of time. Using Eq. (4.23) $\dot{X}_1$ is integrated similarly to find X_1. This completes the solution for $\boldsymbol{q} = [\psi\ X_1\ X_2\ X_4]^T$ for a given constant curvature trajectory. Typical trajectories encountered by the guidewire robot within vasculature may be sectioned into successive

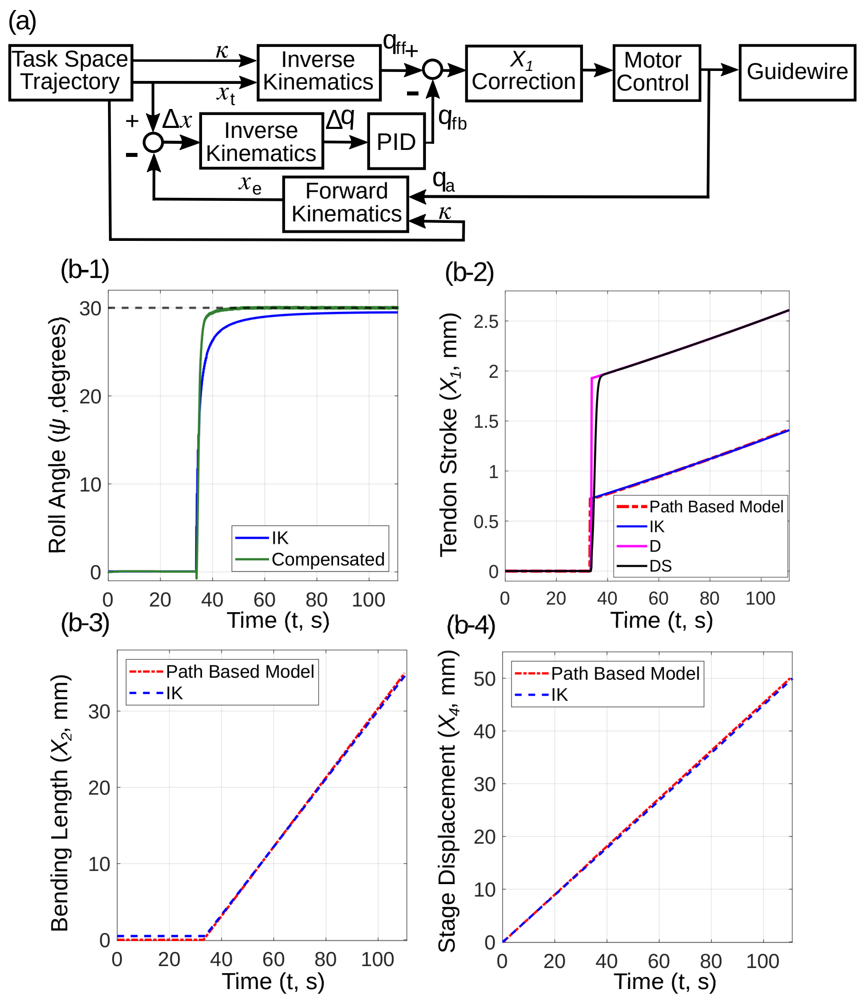

Figure 4.13: (a) Task space trajectory control block diagram, and plots showing variation of (b-1) ψ, (b-2) X_1, (b-3) X_2, and (b-4) X_4 for trajectory $T_{1,30^\circ}$.

pairs of constant curvature paths which may be preceded by straight paths. For the straight path of a trajectory section, the Jacobian matrix $J(\boldsymbol{q'})$ loses rank, however, an analytical solution for the joint space is easily determined, resulting in the above IK solution only being applied for the curved paths of the trajectory.

4.4.3 Jacobian Control Implementation

The control scheme for tracking a task space trajectory, $\boldsymbol{x_t}$, is shown in Fig. 4.13(a). The feedforward term, $\boldsymbol{q_{ff}}$, is computed directly from the IK solution (defined in Section 4.4.2), while the feedback term, $\boldsymbol{q_{fb}}$, is generated by an inverse Jacobian control scheme [206].

Since both the FK and IK maps rely on the path's curvature at a given time, the trajectory also feeds the precomputed curvature, κ, into each block. The feedback controller maps the estimated task space error, $\Delta \boldsymbol{x}$, to a joint space error, $\Delta \boldsymbol{q}$, with the same least squares IK solution. This is then passed through a PID controller to generate the feedback term. The least squares IK solution for X_1, X_2 and X_4 show negligible error when compared to the path-based control implemented in [204], while ψ is observed to show a notable joint error. This can be seen from Fig. 4.12 (b-1)-(b-4) where the IK solution tracks a path-based control closely. While PID gains can be applied to each joint variable, in this thesis, we apply non-zero gains only for ψ to reach the desired trajectory.

The kinematics model (Eq. (4.14)) does not account for the deadband associated with tendon stroke, X_1. This results in the IK solution producing an initial stroke length that is less than that needed to initiate bending during the transition from the straight to the curved paths of the trajectory. To compensate for this, an offset, q_{1D}, which is experimentally determined from the curvature-tendon stroke tests, is added at the transition phase for X_1. The sudden increase in X_1 at the transition may result in breaking of the tendon, so the input is smoothed by scaling with the result of a sigmoid function that is shifted by a chosen δt from the start of the transition phase. The final commanded tendon stroke, q_{1DS}, sent to the actuator is given by:

$$q_{1DS} = \frac{q_{1ff} + q_{1D}}{1 + e^{-(t - \delta t)}} \tag{4.26}$$

The result of deadband correction and smoothing are displayed in Fig.4.12(c-2), denoted by D and DS respectively. Once generated, the combined feedback and feedforward joint space commands are sent to the motor control plant, which includes a PID controller and a Disturbance Observer [207], and finally to the motors.

4.4.4 Free Space Implementation

The aforementioned control scheme is implemented for the COAST guidewire robot assembled in the CAS. We generate three sets of trajectories, each beginning with an initial

Table 4.2: Trajectory parameters and tracking results.

Trajectory	Straight Path	Curved Path		Measured Radius	Final Tip Error
	a (mm)	δ_g (mm)	$\theta°$	δ_m (mm)	$\Delta\varepsilon$ (mm)
$T_{1,0^\circ}$	15	22.24	90	24.05	8.46
$T_{2,0^\circ}$	15	35.33	60	33.44	3.26
$T_{3,0^\circ}$	15	70.67	30	92.82	4.29

straight path, characterized by distance, a, followed by a constant curvature path defined by its radius of curvature, δ_g, and bending angle, θ (see Fig. 4.14(a)). Each trajectory, $T_{i,\psi}$, is traversed with a FTL motion by the robot, first in the base plane ($\psi = 0°$), and then in torqued plane ($\psi \neq 0°$). The experimental torquing angle for each $T_{i,0^\circ}$-$T_{i,\psi}$ pair is acquired by computing best fit planes using Singular Value Decomposition (SVD) of the recorded trajectory coordinates. The defined trajectories ($T_{i,0^\circ}$) and executed tip motion in the base plane are shown in Fig. 4.14(b-1)-(b-3). The defined trajectories and executed tip motion for torqued planes ($\psi \neq 0°$), along with the estimated torquing angles , are shown in Fig. 4.14(c-1)-(c-3). Significant deviations in the actual tip positions and the generated trajectories are observed in the curved path and we see a shift at the transition between the straight and curved paths for the trajectories, especially for those with larger curvatures. As addressed in our previous work, these are attributed to inter-segment coupling, which would be partially compensated when traversing constrained vasculature. At the transition phase, a trajectory offset to compensate for this coupling is shown for each $T_{i,0^\circ}$ to estimate the final position error of the tip, $\Delta\varepsilon_i$ (values shown in Table 4.2 for the desired path parameters, a, δ_g, and θ, measured radius of curvature, δ_m, and the tip position error, $\Delta\varepsilon_i$). Further deviations, specifically in the torquing angle, result due to mechanical backlash in the torquing gears (as discussed in Section 4.1.3), as well as the weight of the EM tracker and the connecting wire, which apply a moment at the tip and deflect the robot from the intended trajectory. The deviation worsens for higher commanded torquing angles as the connecting wire interferes with torquing motion at the tip by resisting the motion or inducing vibrations. The results of planar tracking for the trajectory $T_{1,0^\circ}$ (parameters specified

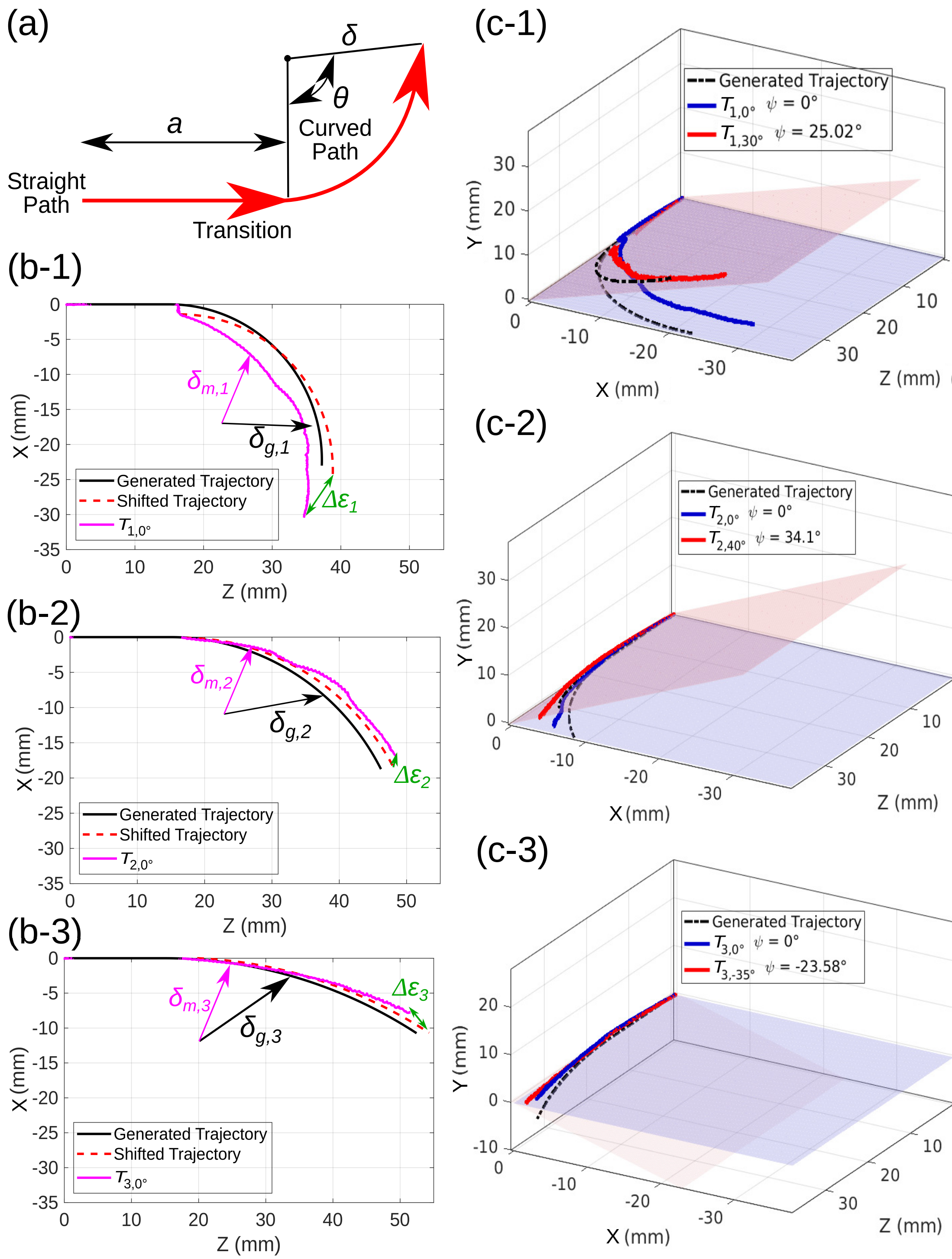

Figure 4.14: (a) Schematic showing a general trajectory with straight and curved path parameters; Generated, executed and coupling compensated trajectories (b-1) $T_{1,0^\circ}$, (b-2) $T_{2,0^\circ}$, and (b-3) $T_{3,0^\circ}$; Generated and executed trajectories, and best fit planes for (c-1) $T_{1,0^\circ}$ (blue), $T_{1,30^\circ}$ (red), (c-2) $T_{2,0^\circ}$ (blue), $T_{2,40^\circ}$ (red), (c-3) $T_{3,0^\circ}$ (blue), $T_{3,-35^\circ}$ (red)

in Table 4.2, namely $a = 15\,\mathrm{mm}$, $\delta_g = 22.24\,\mathrm{mm}$, and $\theta = 90°$) with a single CMOS camera without and with the EM tracker are shown in Fig. 4.15(a) and Fig. 4.15(b), respectively, where we show the error of the guidewire tip position, $\Delta\varepsilon$, and the measured radius of curvature, δ_m. In the trial without the EM tracker, the guidewire was visually observed

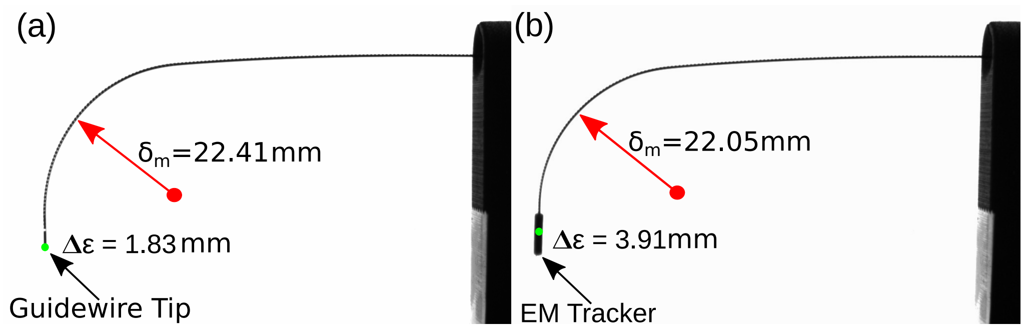

Figure 4.15: Images of trajectory $T_{1,0^\circ}$ executed (a) without and (b) with the 5 DoF EM tracker.

to be parallel to the camera at all times, resulting in significantly less error than that shown in Table 4.2 for $T_{1,0^\circ}$ (where all of the measured data was with the EM tracker attached to the guidewire tip). The same trajectory carried out with the EM tracker attached results in visually obvious out-of-plane motion potentially caused by interference with the sensor's connecting wire. It is important to note that due to the variability of the EM tracker wire motion in free space when the EM tracker is attached to the guidewire tip, we observe a different error in Fig. 12(b) ($\Delta\varepsilon = 3.91\,\mathrm{mm}$) compared to the data for the same desired trajectory, $T_{1,0^\circ}$, in Table 4.2 ($\Delta\varepsilon = 8.46\,\mathrm{mm}$). Hence, from the results above, we are unable to draw any quantitative conclusions regarding the EM tracker's full influence on the guidewire's tip position error. Given the invasive nature of the EM sensor system on the final tip position error, multiple camera-based imaging systems will be considered in our future work, as an alternative to track the guidewire tip and characterize the motion of the robot.

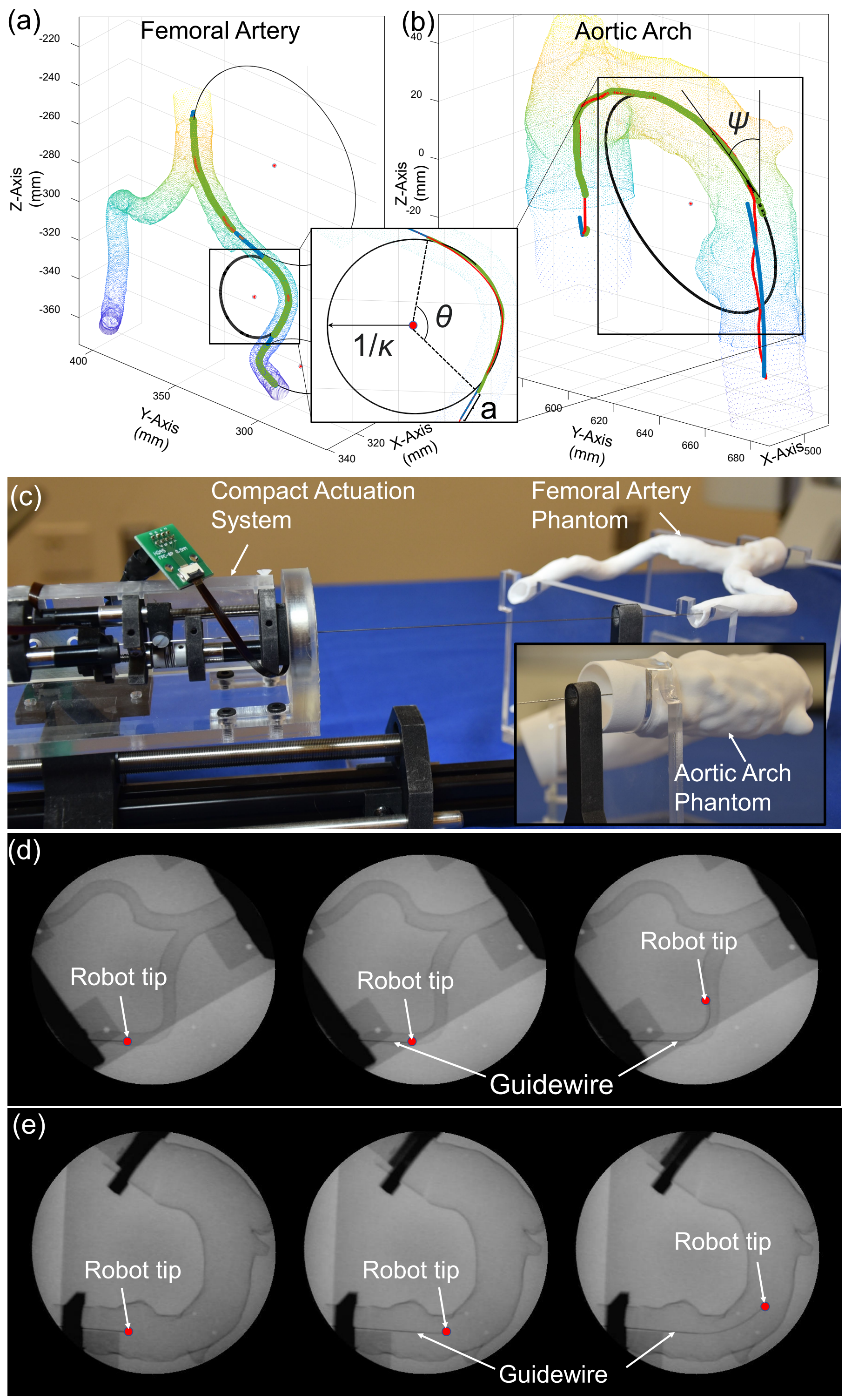

Figure 4.16: Extraction of curvatures from vascular centerlines for the (a) femoral artery and (b) aortic arch; (c) Experimental setup; Experimental results shown by fluoroscopy images of guidewire motion for (d) a curve in the femoral artery, and (e) aortic arch.

4.4.5 Tests in Phantom Anatomy

To demonstrate the feasibility of the COAST guidewire in 3D-vasculature, we consider two vascular sections: 1) a highly tortuous segment of the femoral artery, and 2) the initial curvature of an aortic arch (see Fig. 4.16(a)-(b)). We use the Vascular Modeling Toolkit (vmtk) to segment each of these blood vessels from anonymized CT data and extract vascular centerlines [208]. We then approximate the centerline points with a cubic spline, for which we compute the Menger curvature at each triad of points along the spline. We identify areas of constant curvature by thresholding the curvature along the centerline length. For a vascular segment of constant curvature, κ_i, we use singular value decomposition to find the normal to the plane of bending (n_i). This process is then repeated for all the curved and straight portions of the centerline approximation. The torquing angle, ψ, is calculated by finding the angle between normal vectors of consecutive bending planes (see Fig. 4.16(b)). We then project all the points of a given constant curvature section, i, onto the bending plane corresponding to $N(n_i)$. Finally, we use the Gauss-Newton method to solve a non-linear least-squares problem iteratively and compute the best fitting circle to the projected points. The start and end of the curved centerline are projected on the best fitting circle, and the angle between these points is determined (see θ in Fig. 4.16(a-b)(inset)). Similarly, the length of the centerline between two consecutive curved segments is used to determine pre-curvature offsets (see a in Fig. 4.16(a-b)(inset)). Finally, the combined set of parameters $\{a_i, \kappa_i, \theta_i, \psi_i\}$ is used to determine the constant curvature trajectory input to the Jacobian model (described in Section 4.4.3).

To observe the guidewire within the phantom models, we use the OEC 9800 Plus C-Arm System (GE Healthcare®, Chicago, USA) in which images are acquired using an Orion HD (Matrox™, Dorval, Canada) frame-grabber in tandem with the MATLAB® Image Acquisition Toolbox (MathWorks™, Natick, USA). 3D-printed phantom models of the aortic bifurcation and aortic arch (Formiga P110 Velocis SLS printer, Bavaria, Germany) are placed under the C-Arm system with the guidewire positioned near the start point of each phantom vasculature (see Fig. 4.16(c) and 4.16(c)(inset)). The execution of paths in the femoral artery and aortic arch can be seen in Fig. 4.16(d) and Fig. 4.16(e), respectively. The guidewire adequately tracks the generated trajectories, as shown in Fig. 4.16(d) and 4.16(e). A non-invasive X-ray imaging system for real-time tracking and control of the robot when the robot is within vasculature will be considered in our future work.

4.5 Conclusions

In this chapter, a CO-axially Aligned STeerable (COAST) robot guidewire robot was proposed, analyzed, and utilized to achieve three dimensional follow-the-leader motion with Jacobian Control. The COAST robot consists of two micromachined nitinol tubes, a single steel inner tube and a nitinol tendon that are coaxially aligned for decoupled control of bending angle and bending length of the distal tip. A modified integral approach for non-uniform curved beams with large deflections is proposed and validated to estimate the pre-curvatures in the individual micromachined tubes of the COAST robot. Using these individual tube pre-curvatures and a combined deformation model for the telescoping micromachined tubes, the total pre-curvature in the COAST distal tip can be estimated. Then the geometric properties of micromachining can be optimized for high compliance and low pre-curvatures. For this optimized distal tip design, a new compact actuation system (CAS) is proposed that allows 3D follow-the-leader motion capabilities for the guidewire robot. A forward kinematics model and joint-space kinematic model including tendon friction are proposed and used for a overdetermined Jacobian matrix for the robot. The left pseudo inverse of the Jacobian matrix is then used for task space trajectory control of the guidewire robot to perform follow-the-leader motion in three dimensions. The Jacobian based control approach is demonstrated for a COAST guidewire robot prototype with the compact actuation system in free space and within phantom vasculature.

4.6 Acknowledgements

The author would like to thank Mr. Achraj Sarma, Mr. Timothy J. Brumfiel, and Dr. Seokhwan Jeong for part of the contents of this chapter.

CHAPTER 5
ROBOTIC PEDIATRIC NEUROENDOSCOPE: DESIGN AND KINEMATICS ANALYSIS

5.1 Introduction

Pediatric hydrocephalus (HC) is a relatively common condition among infants, with rates varying from 0.4 to 3.2 cases in 1000 live births (with higher rates estimated in developing countries) [209]. Traditionally, hydrocephalus is treated by the means of a shunt, an implanted plastic tubing that diverts the CSF from the brain to other body cavities. A minimally invasive procedure called Endoscopic Third Ventriculostomy (ETV) is attractive in comparison to the shunting procedures because it obviates the need for a foreign body implantation and its associated long-term maintenance [22, 23]. In this procedure, CSF flow is diverted among various brain compartments, by creating a hole at the floor of the third ventricle, thereby allowing the CSF to bypass any anatomical blockages. Typically, ETV is performed using a rigid endoscope to be deployed along a linear trajectory from the insertion point on the scalp to the target site. Frequently used rigid scopes such as the MINOP endoscope (Aesculap Inc., PA, United States) or the OI HandyPro endoscope (Karl Storz SE & Co. KG, Tuttlingen, Germany) have hollow cylindrical working channels between 1 mm - 2.2 mm in diameter [24]. Rigid tools, such as a scissors, grasper or an electrocautery probe may be inserted through these channels. The endoscopes are equipped with high resolution wide-angle cameras and other cylindrical channels for irrigation and suction. More tools can also be inserted through these additional channels for bimanual manipulation of the target site. In the often distorted ventricular anatomy associated with hydrocephalus, however, finding such a linear trajectory while avoiding blood vessels and structures is non-trivial. One possible solution involves a flexible, steerable endoscope [33]. However,

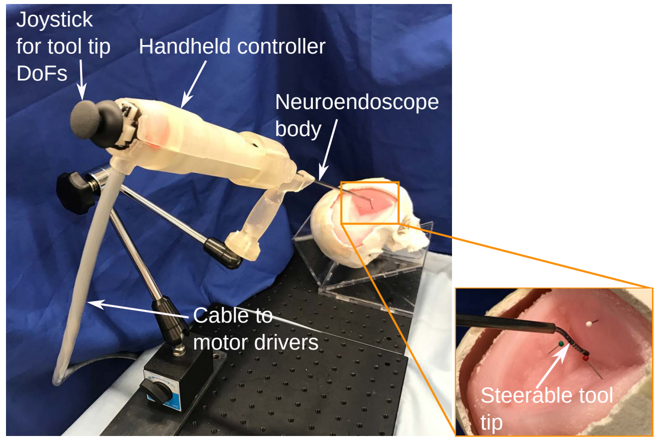

Figure 5.1: Handheld controller with a joystick for a steerable two degree-of-freedom neuroendoscope tool tip (inset) for the endoscopic third ventriculostomy (ETV) procedure.

steerable/semi-rigid endoscopes suffer from the problem of lower video resolution [24], a steeper learning curve for the clinicians and limited availability of flexible tools that are compatible with such an endoscope. Alternatively, one may choose to keep the rigid endoscope and its associated advantages, but design a tool that is steerable and flexible at its tip once it is deployed through the shaft of the rigid endoscope. In this chapter, we will look into the design and kinematic analysis of such a robotic tool and a controller for the same (see Fig. 5.1). To direct our design process, we arrive at the following set of requirements for such a robotic tool.

Requirements for Robotic Neuroendoscope:

1. The tool must be compatible with existing rigid endoscopes, i.e. it should pass through the working channels of these endoscopes.

2. The controller for the tool should be ergonomic and easy to handle, preferably handheld in nature. (While this requirement is not quantifiable and will not guide the design of the robotic tool tip itself, it will define the design of the handheld controller for the robot.)

3. Maximum visibility of every portion of the tool is desired within the endoscope field of view [210].

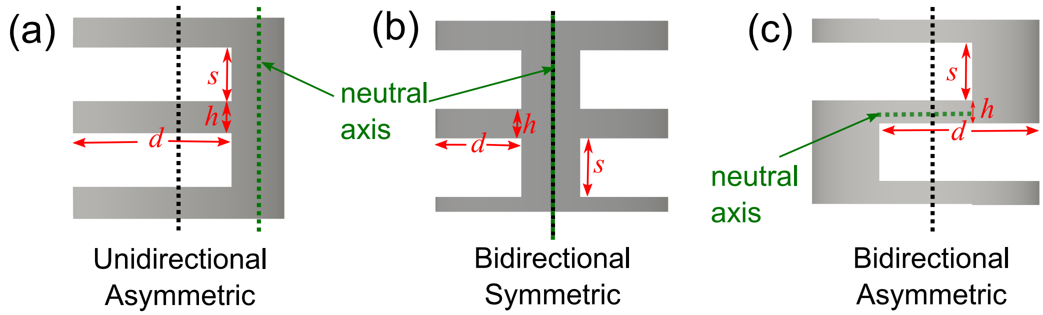

Figure 5.2: Types of bending flexural joints. Notch depth (d), distance between consecutive notches (h) and notch height (s) define the bending properties of each joint as well as the location of neutral axis of the bending element in each joint type.

4. The tool tip can be manipulated so that it can be orthogonal or at an angle to the tissue that is to be manipulated.

5. Bimanual triangulation capabilities [210].

The first requirement imparts a size constraint on the diameter of the proposed robotic tool. In this work, we focus on designing tools for the MINOP endoscope. Since the working channel of the MINOP scope is 2.2 mm in diameter, the maximum outer diameter of our robotic tool was selected to be 2 mm. This constraint severely limits the mechanism that may be used to drive the joints of the robot. To achieve a high bending curvature with a small tube diameter, we make use of a type of joint known as the bending flexural joint [119, 120] to build our robot. Bending flexural joints are tendon driven continuum joints, constructed by selectively micromachining away material from a tube of a superelastic material such as Nitinol, thereby making the tubular structure more compliant in a plane determined by the pattern of the machining. Typically, bending flexural joints may be classified into bidirectional symmetric notch (BSN) [173, 168], unidirectional asymmetric notch (UAN) [122, 117, 121], or bidirectional asymmetric notch (BAN) [177, 175, 178] joints depending upon the pattern of notches cut into a tube of Nitinol (see Fig. 5.2 and Chapter 2). In this work, we make use of the asymmetric notch joints (UAN and BAN) as the bending members in our robotic tool body. These joints are defined by the notch depth (d), the spacing between consecutive notches (s) and the height of each notch (h)

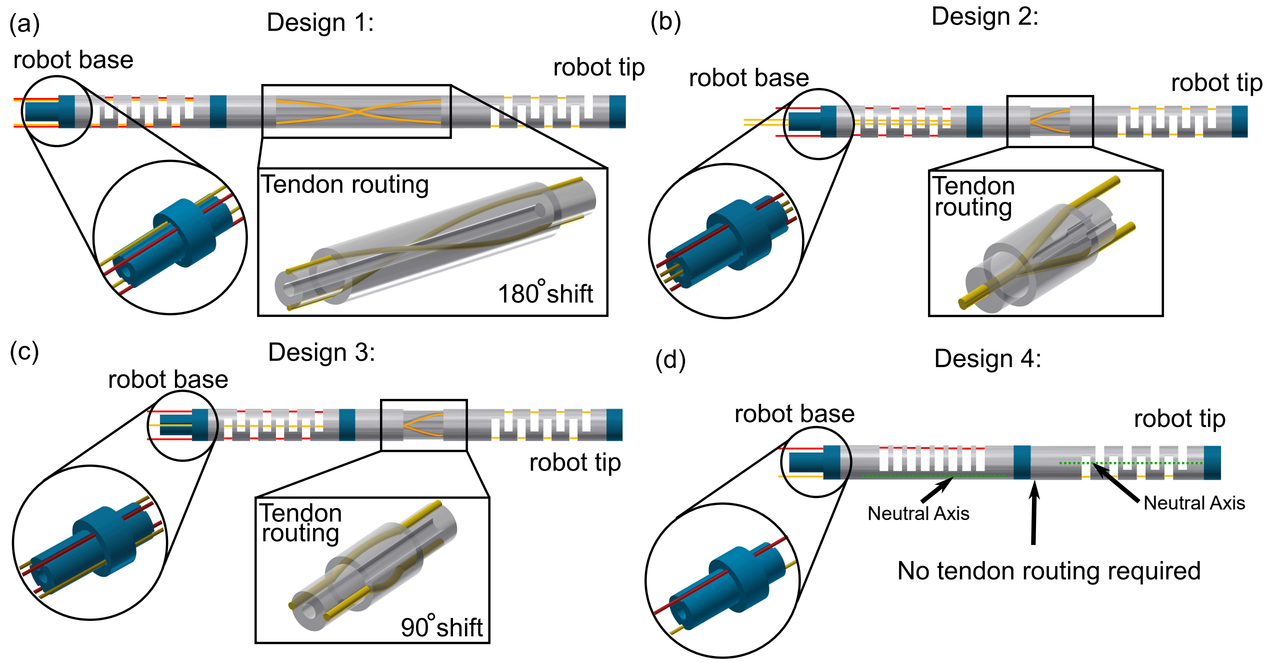

Figure 5.3: Four possible designs for neuroendoscope tip (see Fig. 5.1 (inset)) are analyzed in this work. (a)-(c) The first three designs, differ from each other in the manner in which distal tendons (indicated by yellow lines) are routed through the body of the tip, (d) This design uses properties of two types of bending flexural joints to achieve decoupling in the 2-DoFs.

(see Fig. 5.2). The next requirement takes into consideration the actual operating room environment that these operating tools will be used in. Typically, two surgeons are involved in these procedures: one surgeon controls the endoscope, the other manipulates various tools deployed through the working channel of this endoscope. The back ends of these tools are handheld and provide ease of insertion/retraction as well as rolling the tool bodies inside the endoscope's working channel [25]. Therefore, the dimensions of the handheld tool controller must be comparable to existing tool controllers. The surgeons typically extend the tip of the tool to approximately 1-1.5 inches (24.5 mm-38.1 mm) from the distal end of the scope towards the target. If the target is unreachable from this distance, the entire endoscope itself is moved closer to the target. Therefore it may be beneficial for the undeformed length of the robotic tool tip to be under 1.5 inches (< 38.1 mm) for ease of use from the point-of-view of the operating clinician. The third requirement is to maximize joint flexibility of the tool while ensuring visual observation of the tool at all times and this

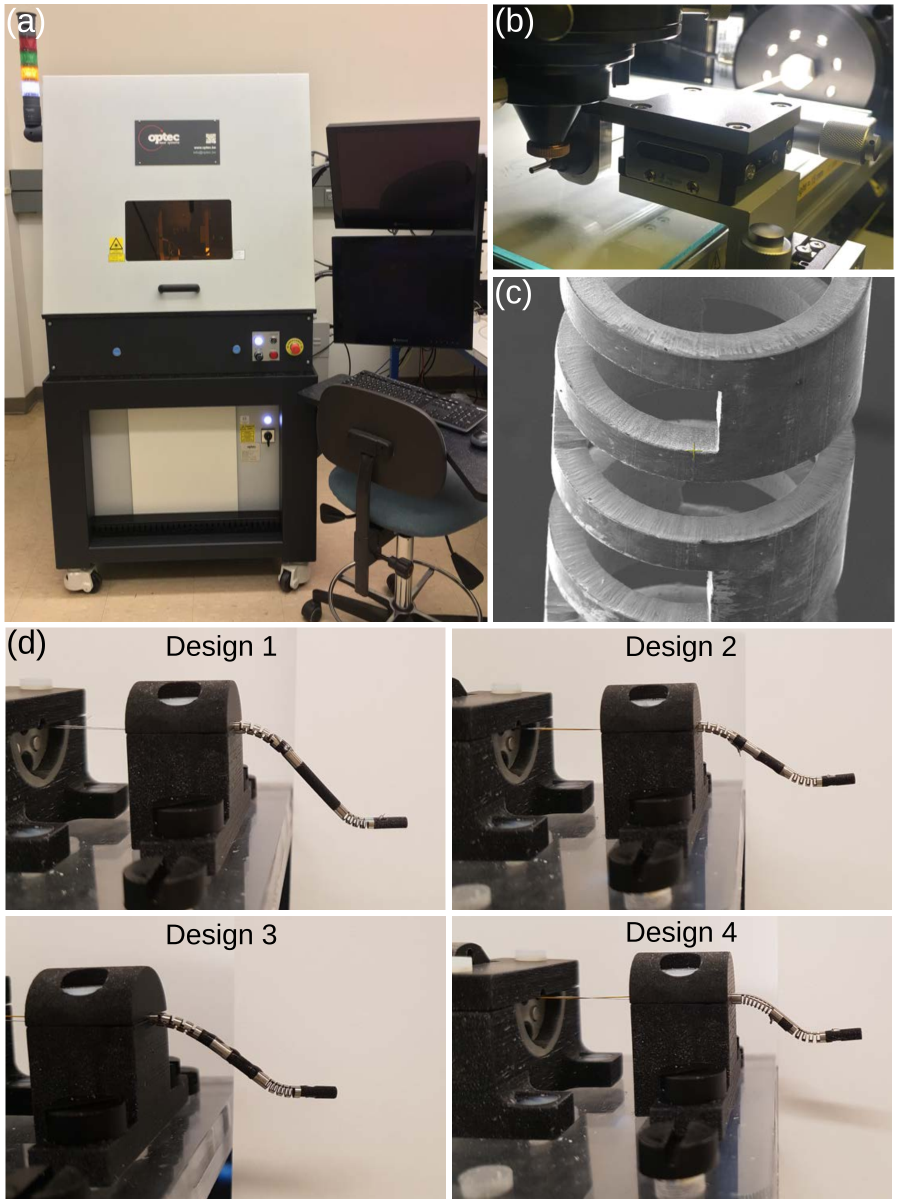

Figure 5.4: (a) Femtosecond laser (Optec Laser S.A., Frameries, Belgium) used to manufacture bending joints of the robot, (b) Laser cutting of tube segments using a nitinol tube in a lathe stage, (c) Bending flexural joint samples under scanning electron microscope imaging reveal a lack of any heat affected zones (HAZ), (d) The four proposed designs in Fig. 5.3, manufactured using femtosecond laser micromachining and 3D printed connectors, and finally assembled with tendon routing.

constraint has been addressed in Section 5.3.1.

Authors in [114] converged upon a single degree-of-freedom (DoF) joint of length $\sim$30 mm passing through a rigid segment (which was the endoscope) with an additional rolling degree-of-freedom possible at the base of the steerable joint. The curvature of this joint was derived using a path planning technique to reach several targets in an ETV/ETB (Endoscopic Third Ventriculostomy and Endoscopic Tumor Biopsy) procedure. However, the authors did not take into account any of the above requirements of a tool of this nature. A single segment joint would fail the fourth and fifth requirements from a robotic tool due to the lack of joints. Furthermore, the authors proposed a concentric tube robot, where the curvature and joint lengths of the steerable tip are coupled [211]. As a result, adding more degrees of freedom to the tip would increase the already lengthy tool tip exceeding the length requirements of such a tip. To meet all of our requirements, it is important for the robot to have at least 4 degrees-of-freedom (DoFs). In addition to insertion/retraction and rotation of the robotic tool within the endoscope, it is important for the robot to have two DoFs in a single plane so as to form an *S*-shaped curve (see Fig. 5.1 (inset)), thereby allowing orthogonality to the ventricle floor and bimanual triangulation capabilities. In a previous chapter (see Chapter 2), we demonstrated and compared the properties of bending flexural joints of sub-millimeter diameters with finite element model simulations and experiments. We demonstrated that for an equivalent joint length and notch depth, the bending plane compliance of BAN joints (see Fig. 5.2(b)) is significantly higher than the other types of joints, without losing transverse plane stiffness significantly. In [212], we utilized this property of BAN joints to design a 2-DoF robotic tool for the ETV procedure (similar to 'Design 3' in this work) with a handheld controller for the same. However, the length of this robotic tool ($\approx$ 2 inches) did not satisfy the length requirements discussed above. Furthermore, we observed a certain degree of inter-joint coupling in the bending and transverse planes, which is further analyzed in this chapter. We will describe the design and kinematic analysis of possible robotic tip candidates conforming to all of the above requirements. These new designs propose and compare four possible solutions to inter-joint decoupling in meso-scale tendon-driven robotic tools at these sizes with more than one degree-of-freedom. We further propose a miniaturized version of a handheld controller for our robotic tools in comparison to that proposed in [212], that conforms with the controllers for tools currently used in ETV procedures.

This chapter can be summarized as follows: In Section 5.2, we propose four designs for a 2-DoF robotic tool body (see Section 5.2.1) and the design of a corresponding handheld controller for the same (see Section 5.2.2). Next, we quantify some of the requirements stated above and generate kinematic models and joint limits for the robot thus designed in Section 5.3. Finally, we validate our kinematic model, propose a control loop including a disturbance observer for the handheld controller to reliably adhere to this model and finally compare our robotic tool designs with respect to this application in Section 5.4.

5.2 Robot Design

5.2.1 End-Effector Design and Manufacturing

To achieve the requirements stated in Section 5.1, we consider four types of designs for the robot tip (see Fig. 5.3). Each of these designs is capable of achieving two degrees-of-freedom in a single bending plane to achieve the desired *S*-shaped curves. Furthermore, all designs make use of bending flexural joints to achieve bending. The designs differ from each other in the type of tendon routing strategies used and the type of flexural joints used to achieve bending. The tendon routing strategies have been selected with a view to achieve a predictable inter-joint coupling model for each design.

Designs 1-3 in Figs. 5.3(a)-(c) make use of BAN joint geometries (see Fig. 5.2(c)) for *both* their proximal and distal joints, while Design 4 (see Fig. 5.3(d)) makes use of a UAN and a BAN joint for the proximal joint and the distal joint, respectively. BAN joints are highly compliant in their bending plane and can accommodate two tendons to be controllable in either direction. Therefore, for designs 1-3 (which involve two BAN joints), a total of 4 tendons are required to control all the joints. In Design 1, any notion of minimizing inter-joint coupling is relinquished by routing one proximal and one distal tendon close together along the proximal joint's bending plane (see circular inset in Fig. 5.3(a)). The proximal tendons are terminated at the end of the proximal joint. Furthermore, an intermediate section termed the *tendon phase shifter* routes each distal tendon by $180°$. This routing is done so that applying tension to a distal tendon will naturally exert bending moments on the proximal joint due to friction and normal forces on the proximal joint wall. However, the bending achieved in the proximal joint will be in the *opposite direction* as that achieved in the distal joint, thereby achieving the required *S*-shaped curve. The bending curvature of the proximal joint may then be further controlled by applying tension to tendons of the proximal joint. In theory, the two joints in this design should be fully controllable in either directions with this method. However, in practice, due to the high coupling between the joints and the additional tendon routing requirement, this type of a design may require high forces for distal joint control and decoupling. Furthermore, the $180°$ tendon phase shifter increases the total length of the joint to about 1.2 inches (30.48 mm).

Designs 2-3 try to minimize inter-joint coupling by design, similar to [91]. In Design 2, the distal tendons are routed along the central axis of the proximal joint. While this distal tendon routing may be effective in reducing inter-joint coupling in comparison to Design 1, it is not completely eliminated [91]. Furthermore, due to the limited lumen diameter available along the central axis of the robot ($\leq 0.5\ mm$), passing more than two tendons through this central lumen may result in inter-tendon friction, resulting in unpredictable motion. Therefore, this design becomes unusable in scenarios where a third tendon to control a scissors/grasper at the tool tip may have to be passed through the inner lumen of the tool body. To address this issue, the distal tendons may be routed along the transverse plane of the proximal joint, as is proposed in Design 3 (see the circular inset in Fig. 5.3(c)). The transverse plane is defined as a plane orthogonal to the bending plane of the proximal

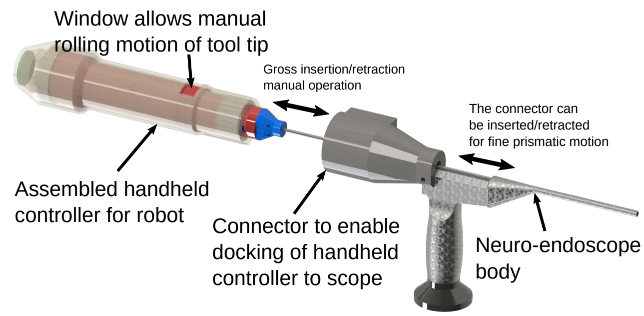

Figure 5.5: The handheld controller can be inserted into standard neuroendoscopes such as the MINOP (shown above), via a connector. By changing the connector, one can insert the tool into any endoscope, thereby making it accessible to a variety of commercial solutions.

joint intersecting with the bending plane along the axis of the undeformed proximal joint. This design exploits the property of BAN joints to offer significantly higher stiffness in the transverse plane in comparison to the bending plane [213]. By routing tendons anywhere on this plane, we can achieve similar decoupling properties as Design 2. The added advantage is that this type of routing creates enough room along the central lumen of the robot to pass any cables/electrodes that control the tool that may be attached to the tip of the robot. However, this design may result in a slight amount of uncontrollable motion along the transverse plane, which may not be permissible. Both Designs 2 and 3 use a compact tendon routing strategy, that limits the length of the robotic tip (beyond the MINOP scope) to be under 1 inch (0.99 in and 0.95 in for Designs 2 and 3, respectively) as discussed in Section 5.1.

Finally, Design 4 uses a combination of the joints discussed earlier in this section. The proximal joint is constructed using a UAN flexural joint (see Fig. 5.2(a)) controlled by a single tendon (see red line in Fig. 5.3(d)). This tendon allows the joint to be flexed in one direction, as demonstrated in [122, 117, 121]. Unlike the BSN joint, the neutral axis of this joint is displaced to one side of the tube (see dotted green line in Fig. 5.2(a)) and the bending stiffness is much higher when tension is applied along the neutral axis. Unlike previous work, we take advantage of the displaced neutral axis of the UAN joint to route a secondary distal tendon along this neutral axis. The distal joint is a BAN joint (see Fig.

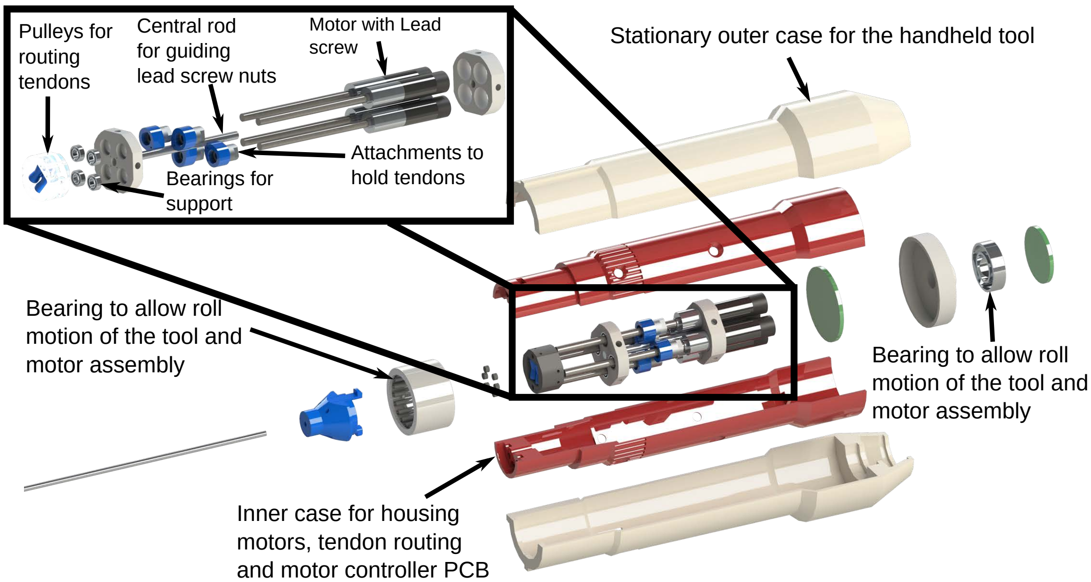

Figure 5.6: Exploded view of the handheld controller for the pediatric neuroendoscope and the driving unit shows the DC motor and lead screw arrangement that enables the entire setup to be compact (overall diameter is 31 mm).

5.2(c)) due to its additional bending plane compliance in comparison to the UAN joint for the same joint length [213]. This use of a BAN joint allows this joint to be flexed to a very high curvature with small tendon tension, thereby also reducing the effect of this tendon tension on the proximal joint. This design also does not need any tendon routing segments, which makes the length of the robot tip even smaller at 0.64 inches (16.26 mm) and yet capable of achieving high joint angles with low coupling. Furthermore, both proximal and distal joint can be fabricated in Design 4 at the same time (unlike other designs, which have to be assembled after machining), which decreases assembly error and effort. We anticipate this design to have limitations similar to UAN proximal joints in resisting external forces applied in uncontrollable bending directions [121]. Furthermore, routing any cables associated with tool-control along the central axis of the proximal joint will always cause it to deflect.

For all designs, we manufacture a set of notch joints with dimensions listed in Table 5.2, using laser micromachining (see Fig. 5.4(a)). A Nitinol tube of 1.93 mm outer diameter (OD) and 0.22 mm wall thickness is ablated by femtosecond laser pulses of spot size

6 μm, while being translated and rotated by a platform including a lathe stage (see Fig. 5.4(b)). The resulting finished notch joint displays minimal heat affected zone (HAZ) due to the small pulse duration allowing the superelastic properties of the nitinol to be retained even after micromachining (see Fig. 5.4(c)). All the aforementioned designs are manufactured as separate units that are assembled together using 3D printed routing members (Projet 5600, 3D Systems, South Carolina, United States), except Design 4, which is manufactured as a single unit in which the 3D printed routing members are inserted after laser processing. Nitinol tendons of diameter 0.13 mm are then routed towards the ends of the proximal and distal joints for each design passing through the routing members. The completely assembled designs from Fig. 5.3 are shown in Fig. 5.4(d). Note, that unlike other continuum robots with larger outer diameters that make use of dedicated tendon routing channels throughout their lengths [177, 126], the wall thickness of the Nitinol tubing used in these robots does not allow for channels to be created within these walls. As a result, for each joint, the routing of tendons occurs at the base and the end of each joint using the 3D printed routing members. Within the length of the joint itself, the tendon paths are not constrained (as can be seen in Fig. 5.2 and Fig. 5.4(d)).

5.2.2 Handheld Controller Design

In section 5.1, we saw that the controller for operating the robotic tool tip must be in the range of existing devices used with commercially available endoscopes in terms of its size. As a result, we have designed a controller module that has a diameter of 32 mm and length 178.85 mm, making it very comparable to the size of existing products. Furthermore, the controller is easily able to dock itself into a connector module that interfaces with the MINOP neuroendoscope (see Fig. 5.1 and Fig. 5.5). This connector has a female socket that slides onto the neuroendoscope allowing for fine control of the tool tip position and the capability to be secured to the scope by a set screw for hands-free operation. The outer sheath of the controller also has a window for the clinician to be able to roll the entire motor and robot assembly along its central axis, to achieve yet another degree-of-freedom that is already available in existing devices. An exploded view of the controller is shown in Fig. 5.6. As described previously, all the joints for the aforementioned designs are tendon driven. All tendons are controlled by prismatic actuation achieved by DC motors with lead screws. Individual joint tendons are routed via a pulley arrangement to a single DC motor, thereby requiring two motors per joint (for Designs 1-3). Since all of the designs we plan to analyze require 2-4 tendons, we allow room for up to four DC Motors of diameter 8 mm (Maxon Precision Motors, MA, United States) with lead screws of length 50 mm and pitch 0.5 mm. All four lead screws are mounted with nuts that hold the tendons which are resting on a single central rod. This rod prevents the nuts from rotating, thereby causing them to slide along the length of this rod achieving prismatic motion. This entire motor and lead screw assembly is resting on two bearings at either end of the controller and is placed in an inner housing (denoted by a red colored case in Fig. 5.6). These bearings therefore allow the housing to be rotated along the central axis of the entire cylindrical assembly allowing for the previously described rolling motion. A controller that takes disturbances from varying tensions from the different joint stiffness and friction from tendon routing into consideration and compensates for the same, is implemented in Simulink (The Mathworks Inc., Natick, MA, United States) and is described further in Section 5.4.1. A single cable is routed from the handheld controller to the motor drivers that receive motor commands from the control system with disturbance compensation (see Fig. 5.1).

5.3 Robot Kinematic Modeling

5.3.1 Justification for robot joint limits

In section 5.1, we highlighted the minimum requirements for a robotic tool for pediatric hydrocephalus from the point of view of an operating clinician. In this section, we refine the constraints previously defined, into clear kinematic constraints for the robot workspace. We begin by defining a general *robot-independent* kinematic model of our 2-DoF robotic

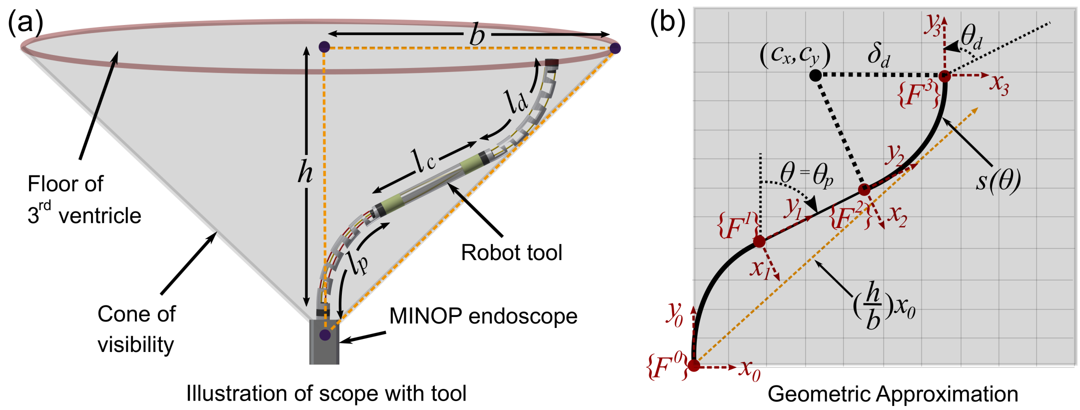

Figure 5.7: (a) From clinical requirements, we must design a robotic tool that is always within the cone of visibility of the clinician's endoscope, (b) These clinical requirements impart a geometric constraint on the maximum angle achievable by the base joint of the robot.

tool body [181]. This kinematic model will help us set constraints on the bending angles of our robot. This model will assume 1) constant curvature for each joint bending and 2) insignificant axial compression of the joint during bending.

Let us consider a 2-DoF robotic tool body, extending out of a neuroendoscope such as the MINOP, with a cone of visibility parameterized by its height (h) and radius (b) (see Fig. 5.7(a)). Since the surgeon typically docks the tip of the endoscope around 1.5 inches (38.1 mm) from the floor of the third ventricle (as stated in Section 5.1), we inspected the MINOP endoscopic camera and found corresponding values of h and b for these conditions. Next, we define the length of the proximal joint to be l_p, the length of the distal joint to be l_d and the connecting segment between the two consecutive joints is l_c. The values of these lengths will vary with the design and the tendon routing strategies involved in the connecting segments. The bending angle of the proximal joint and distal joint are θ_p and θ_d, respectively. We attach frames $\{F^0\}$, $\{F^1\}$, $\{F^2\}$ and $\{F^3\}$ as shown in Fig. 5.7(b). The homogeneous transformation matrix that expresses frame $\{F^1\}$ with respect to frame

$\{F^0\}$ is given by:

$$A_1^0 = \begin{bmatrix} C_{\theta_p} & S_{\theta_p} & 0 & \delta_p(1 - C_{\theta_p}) \\ -S_{\theta_p} & C_{\theta_p} & 0 & \delta_p S_{\theta_p} \\ 0 & 0 & 1 & 0 \\ 0 & 0 & 0 & 1 \end{bmatrix} \tag{5.1}$$

Here, $\delta_p = \left(\frac{l_p}{\theta_p}\right)$ is the radius of curvature for the proximal joint.

Similarly:

$$A_2^1 = \begin{bmatrix} 1 & 0 & 0 & 0 \\ 0 & 1 & 0 & l_c \\ 0 & 0 & 1 & 0 \\ 0 & 0 & 0 & 1 \end{bmatrix} \tag{5.2}$$

describes a point in frame $\{F^2\}$ with respect to frame $\{F^1\}$. Now, the second joint of the robot can be assumed to be an arc of length l_d of a circle of radius δ_d and center located at $p_c^2 = [-\delta_d, 0, 0, 1]^T$. In the frame $\{F^0\}$, this center is found as $p_c^0 = [c_x, c_y, 0, 1]^T$ and is given by:

$$p_c^0 = A_1^0 A_2^1 p_c^2 \tag{5.3}$$

The third requirement for the proposed tool (discussed in Section 5.1) limits the workspace of the tool to the cone of visibility of the endoscopic camera (see Fig. 5.7(a)), which constrains the proximal joint angle. Similarly, the fourth and fifth requirements impart a minimum constraint on the distal joint. For the tool tip to be perfectly orthogonal, the condition, $\theta_d = -\theta_p$, holds true and for triangulation to be feasible, $\theta_d < -\theta_p$, must be true. Since our robot consists of two joints with parallel bending axes, both joints bend in the same plane. Therefore, let us investigate the cross-section of this cone of visibility

Table 5.1: The maximum possible proximal angle θ_p for each of the proposed designs in Section 5.2.1. For each design, we assume joint J5 from Table 5.2 with $l_p = 6$ mm to be the proximal joint and joint J4 ($l_d = 4.9$ mm) to be the distal joint.

	Design 1	Design 2	Design 3	Design 4
l_c (mm)	18.2	14.4	13.4	5.3
θ_p (degrees)	34.82	35.71	36.01	40.8

in this *bending plane*, which is simply a line parameterized by its slope $m_c = \frac{h}{b}$ (see Fig. 5.7(b)). Therefore, the equation of the circle corresponding to the arc of the second joint defined in $\{F^0\}$ at the points of intersection with the line $y_0 - m_c \cdot x_0 = 0$ corresponding to the cone of visibility is given by:

$$\left(x_0^2 - c_x^2\right) + \left((m_c x_0)^2 - c_y^2\right) - \delta_d^2 = 0 \tag{5.4}$$

This quadratic equation in x_0 takes the form $ax_0^2 + bx_0 + c = 0$ and will have a single solution only at the maximum feasible θ and therefore, when $b^2 - 4ac = s(\theta) = 0$ has a single solution for θ.

Therefore, any solution $\theta_p = \theta$ such that $s(\theta) = 0$ (such that $\theta_d = -\theta_p$) has a single solution is the maximum feasible solution given the geometric constraints. The values of these maximum feasible θ_p values for all of our proposed designs are specified in Table 5.1.

5.3.2 Joint Kinematic Model

Next, we perform a *robot-dependent* kinematic analysis for the BAN joints used as building blocks in our four proposed designs. This analysis will provide a relationship between joint angles (θ) and tendon displacement (ΔL) [181]. This analysis provides insight into how much the actuating motor must translate to achieve a certain joint curvature and is important for controlling any multi-DoF robotic tool body designed using these joints. As noted in a previous chapter and our previously published work [213], the beams created between

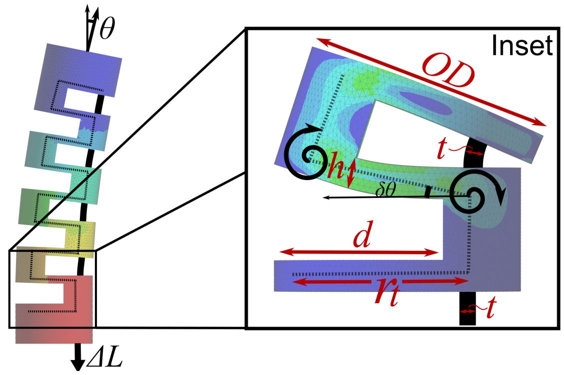

Figure 5.8: Skeleton model for kinematic analysis of the BAN joint that defines the relationship between the bending angle, θ, and tendon displacement, ΔL. This relationship is a summation of the bending of individual beams created from two consecutive notches and therefore depends on the number of notches and notch geometry (inset).

consecutive notches dominate the bending properties of the joint. Therefore, the joint parameters that play an important role in defining joint kinematics are: beam thickness, which depends on its outer and inner diameter (OD and ID respectively), notch depth (d), beam height (which is the same as the spacing between two notches, h), tendon diameter (t) and number of notches (N) (see Fig. 5.8 (inset)). We observe that the ΔL - θ relationship depends mainly on two terms, the purely kinematic term and the tendon elongation term (which is affected by joint statics).

$$\Delta L = \underbrace{f(\theta, N, d)}_{\text{kinematic term}} + \underbrace{\epsilon(\theta, d, h, N)}_{\text{tendon elongation term}} \tag{5.5}$$

To provide a theoretical analysis of the kinematic term, we consider a skeleton model of the joint (see Fig. 5.8). In this model, we assume that each beam stays rigid and that bending occurs due to rotary joints located at the corners of the horizontal and vertical members of the model. An equal amount of differential bending angle, $\delta\theta$, is assumed to occur at each notch and the total bending angle of the joint (θ) is assumed to be the summation of all these individual contributions. Therefore, $\delta\theta = \left(\frac{\theta}{N}\right)$.

The 'kinematic term' in Eq. (5.5) is given by:

$$f\left(\theta, N, d\right) = N \cdot r_t \cdot sin(\delta\theta) \tag{5.6}$$

Here, $r_t = d - \frac{(OD-ID)}{2} - \frac{t}{2}$, approximates the length of the bending beam member between the two notches (see Fig. 5.8 (inset)).

We see that in the above equation, the beam height (h) does not play any role and it does not contribute directly to the joint kinematics. However, varying this term greatly affects joint statics, thereby affecting the tendon elongation required to achieve a certain θ. While in some previous work, tendon elongation is assumed to be insignificant, we find that it greatly affects continuum robots with small beam radii, since θ is significantly sensitive to ΔL variations for such systems. In this chapter, we approximate $\epsilon\left(\theta, d, h, N\right)$ in a data-driven manner and denote it as follows:

$$\epsilon\left(\theta, d, h, N\right) = E_{tendon} \cdot F_{tendon}(\theta, d, h, N) \tag{5.7}$$

where the tendon compliance, E_{tendon}, and tendon tension, $F_{tendon}(\theta, d, h, N)$, are measured experimentally. F_{tendon} is severely dependent on beam height (h) and number of notches (N) and therefore causes a significant effect on the ΔL - θ relationship even for notches with the same notch depth (d), as will be seen in the next section.

5.4 Results

5.4.1 Controller Design

The proposed handheld controller was designed to employ various robot joints with different stiffness. This will cause a change in the relationship between ΔL and $\Delta\theta$ (denoted by the plant $G_3(s)$ in Fig. 5.9(a)). Therefore, the disturbance load, τ_d imposed on the motor by the bending stiffness of the robot joints has non-consistent value, and the system cannot

Table 5.2: The set of notch joint samples tested to validate the bending and transverse stiffness of each of the bi-directional asymmetric notch joints.
In each case the notch height (termed s in Fig. 5.2) is 0.5 mm.
[1] Joint 'J6' is a UAN joint.

Sample	Parameters				
	N	d mm	h mm	$f(\theta, N, d)$ coefficients	# Trials
J1	12	1.2	0.15	54.9164	3
J2	12	1.4	0.15	48.5623	3
J3	12	1.5	0.15	42.4740	3
J4	12	1.6	0.15	38.7463	3
J5	8	1.2	0.3	(8.6792,14.8569)	3
J6 [1]	8	1.6	0.15	36.3664	3

have a consistent control performance with general feedback control loop. It may result in an overshoot or non-constant steady state error in the final position of the surgical tool tip leading to trauma or a decrease in the overall accuracy.

To achieve precise and robust position control, a feedback control loop including a PID controller and a disturbance observer (DOB) [214] was implemented (see Fig. 5.9(a)). In this system diagram, the following are some key transfer functions:

- k_i: control input (u) - current (i) relationship,
- G_1: current (i) - motor torque (τ) relationship,
- G_2: motor torque (τ) - motor stroke (ΔL) relationship.

We assumed that $G_1(s)$ has constant value due to the relatively fast electrical dynamics than that of the mechanical system, and $G_2(s)$ is designed to be a second-order system. The linear stroke of the motor (ΔL), which is measured by the encoder (334910, Maxon Precision Motors, MA, United States) is fed back to the loop, and the control error, e is used as the input of the PID controller, producing the PID control input, u_C. Then, the DOB loop estimates the disturbance torque, τ_d, in the form of the control input, $\hat{u}_d$ and is derived as follows:

$$\hat{u}_d = \left(u - \Delta L k_{i.n}^{-1} G_{1.n}^{-1} G_{2.n}^{-1}\right) Q \tag{5.8}$$

where $k_{i.n}$, $G_{1.n}$ and $G_{2.n}$ are the nominal forms of the functions, k_i, G_1 and G_2, respectively, which are characterized with the system identification toolbox (MATLAB 2016b, The Mathworks Inc., Natick, MA, United States) by measuring the real response of the functions with respect to the chirp signal input. Here, Q is a second-order low-pass filter (i.e., $Q(s) = w_c^2/(s^2 + 2w_c s + w_c^2)$, w_c is cut-off frequency) for the causality and the system stability. Then, $\hat{u}_d$ is added to u_C resulting in the final control input, u:

$$u = u_C + \hat{u}_d \tag{5.9}$$

Now, the relationship between u_C and ΔL is derived from the block diagram (see Fig. 5.9(a)):

$$\Delta L = \left[\left(u_C + \hat{u}_d\right) k_i G_1 - \tau_d\right] G_2 \tag{5.10}$$

By combining Eqs. 5.8, 5.9 and 5.10, we can derive the following transfer function between ΔL, u_c, and τ_d:

$$\Delta L = \frac{G}{1 + [G G_n^{-1} - 1]Q} u_c - \frac{[1 - Q]G_2}{1 + [G G_n^{-1} - 1]Q} \tau_d \tag{5.11}$$

where $G = k_i G_1 G_2$ and $G_n = k_{i.n} G_{1.n} G_{2.n}$. Since $Q \approx 1$ under the cut-off frequency, w_c, Eq. 5.11 becomes $\Delta L \approx G_n u_C$, which means that the effect of the disturbance, τ_d is compensated, and the entire plant operates as the nominal plant, G_n. Therefore, the control response always follows the response of the nominal model (G_n) according to the designed PID controller, regardless of external disturbance (τ_d) or change of plant (G).

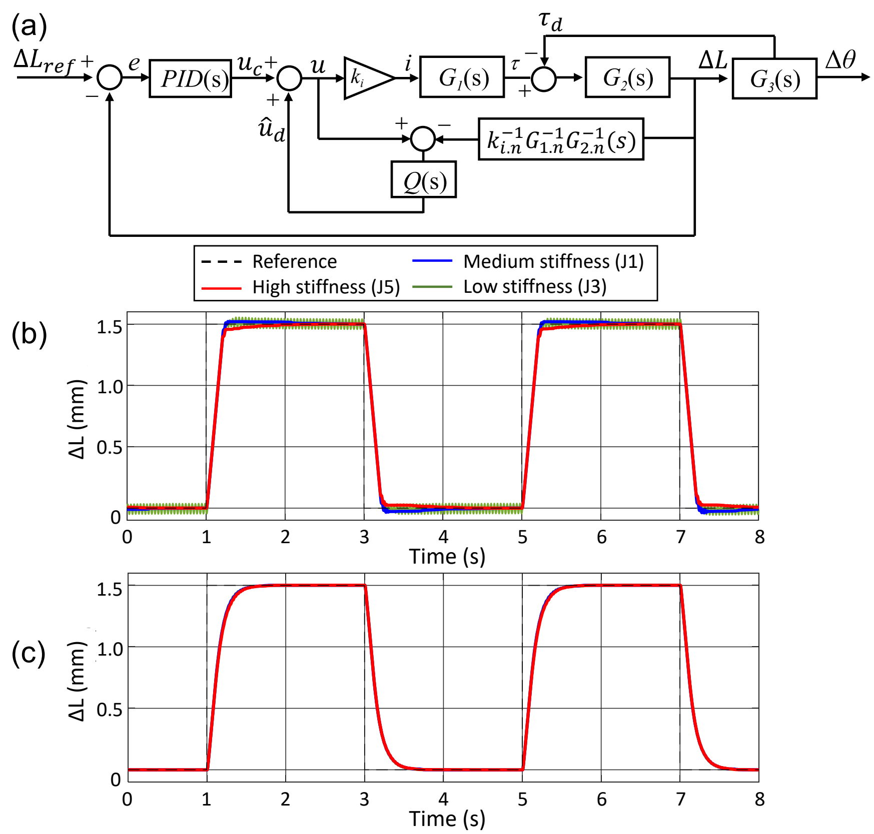

Figure 5.9: (a) A lower level of control loop consisting of PID and disturbance observer. (b) the control performance without a disturbance observer. (c) the control performance with a disturbance observer.

To validate the performance of the proposed control loop, several joints having different stiffness (i.e., J1, J3 and J5 in Table 5.2) were attached to the actuator. The gains of the PID controller (for e.g. [P:1.2, I:3, D:0.02]) were tuned based on the stiffest of the tested samples, J5, to have zero overshoot and settling time < 1s. Fig. 5.9(b) shows that each joint sample has a different control response with overshoot, or chattering. Thus, the PID controller cannot provide a consistent control performance. On the other hand, the DOB results in PID controller always having a consistent control result regardless of external conditions (see Fig. 5.9(b)). As a result, we can expect an equivalent control performance for all the tested joints in the presence of varying stiffness, resulting in an accurate ΔL with respect to the ΔL_{ref} and stable joint movement to validate our kinematics models.

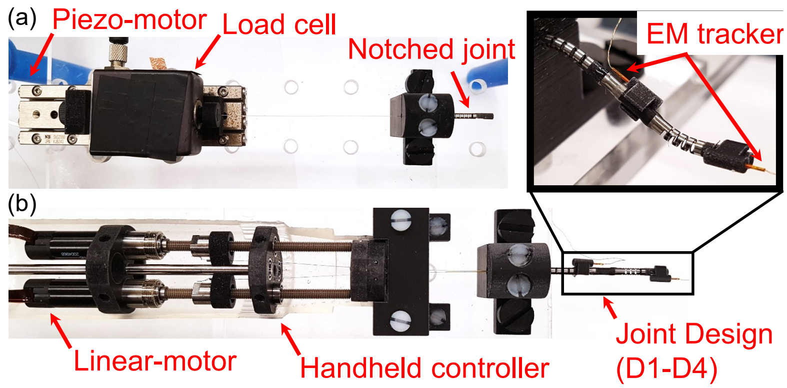

Figure 5.10: (a) Experimental setup with a load cell mounted on a piezomotor to measure joint kinematics, (b) Experimental setup to measure inter-joint coupling for each of the proposed designs. (inset) EM Trackers located at the tip of each joint help to measure bending and transverse plane deflection.

5.4.2 Kinematics Validation

To validate the kinematic model derived in the section 5.3.2, we construct six asymmetric notch joints (J1 - J6) with varying geometric parameters (see Table 5.2). Note that joints J1-J5 are BAN joints for which, we derived the kinematics relationship in Section 5.3.2, while joint J6 is a UAN joint, for which we refer the reader to the relationship defined in [122]. Each of these samples are tested by attaching a single tendon from the joint tip to a piezomotor (SmarAct GmbH, Oldenburg, Germany) through a load cell with a capacity of 5 lbs (Transducer Techniques, CA, United States) (see Fig. 5.10(a)). The load cell measures the tendon tension F_{tendon}, while the piezomotor causes a linear displacement in the tendon (ΔL). A 5-DoF Electromagnetic (EM) Tracker (Northern Digital Inc., Waterloo, Ontario, Canada) is attached to the tip of each joint prototype to measure joint angles. The tensile stress of the tendon used for all notch and robot designs was measured and used to compute strain values to measure the tendon elongation term $\epsilon\left(\theta, d, h, N\right)$ from the tendon tension using an Instron 5965 Universal Testing System (Instron, Norwood, MA, United States). Fig. 5.11(a) shows the results of our kinematic analysis for all the joints tested. As can be seen in the figure, this relationship is linear for highly compliant joints J1-J4. Furthermore, as notch depth (d) increases from J1-J4, the slope of the function $f\left(\theta, N, d\right)$ decreases from Eq. (5.5), thereby requiring larger tendon displacement (ΔL) for an equivalent $\Delta\theta$. However, this is valid only for joints of comparable joint stiffness. Joint J5, which has the same notch depth as Joint J1 should have the same value of $f(\theta, N, d)$ and therefore an equivalent kinematic relationship in the absence of tendon elongation term ϵ. However, the tendon elongation dominates this relationship for J5, while J1 is highly compliant and therefore less susceptible to the $\epsilon(\theta, d, h, N)$ term. This can be seen clearly in Fig. 5.11(b), where the red solid line indicates the kinematic term for J1 and J5, while the dotted lines indicate the estimated value including additional tendon elongation (red dotted line for J1 and green dotted line for J5) . Similarly, J4, which displays the highest compliance also displays a slight amount of tendon elongation that may be compensated to successfully model the complete joint kinematics (dotted line in Fig. 5.11(c)). Finally, for the UAN joint 'J6', to be employed in Design 4 (see Fig. 5.3(d)), we employ the method applied by the authors in [122] to arrive at a theoretical value for the ΔL-θ relationship (solid line in Fig. 5.11(d)) added to the tendon elongation term defined previously to model the kinematics of this joint successfully (dotted line in Fig. 5.11(d)).

5.4.3 Multi-joint Design Comparisons

Finally, using the handheld controller (described in Section 5.2.2) and the controller described in the previous section, we perform a comparison of the four robot tool body designs described in Section 5.2.1. The experimental setup used for these comparisons is very similar to the one used in Section 5.4.2. However, in this case, each design prototype was attached to the end of the handheld controller (see Fig. 5.10(b)) and an EM tracker was attached at the end of each DoF of each design to measure bending angles in both the bending and transverse planes. For designs 1-3, joint J5 (see Table 5.2) was used for the proximal joint due to its high stiffness in the bending and transverse planes, while joint J4 (see Table 5.2) was used as the distal joint due to its high compliance. For design 4, the proximal joint (termed the joint 'J6' in Table 5.2) was designed to have a stiffness compa-

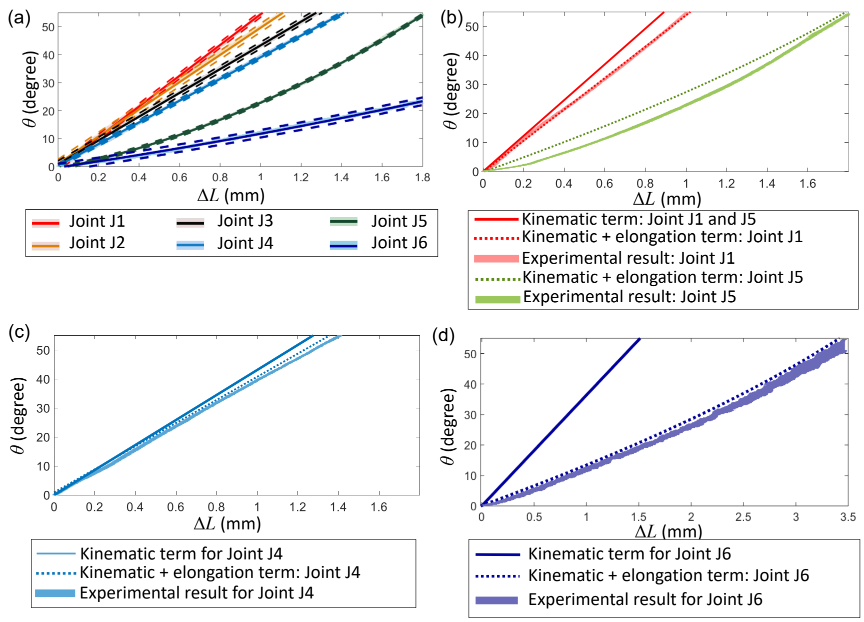

Figure 5.11: (a) The experimental relationship between ΔL and θ for all the samples listed in Table 5.2, (b) Comparison between the theoretical value for the kinematics of Joints J1 and J5 (solid red line), and the corresponding values including tendon elongation compensation (dotted red and green lines), (c) Joint J4 theoretical value compared with experimental results and tendon elongation compensation, (d) Joint J6 theoretical value computed from [122] compared with experimental results and tendon elongation compensation.

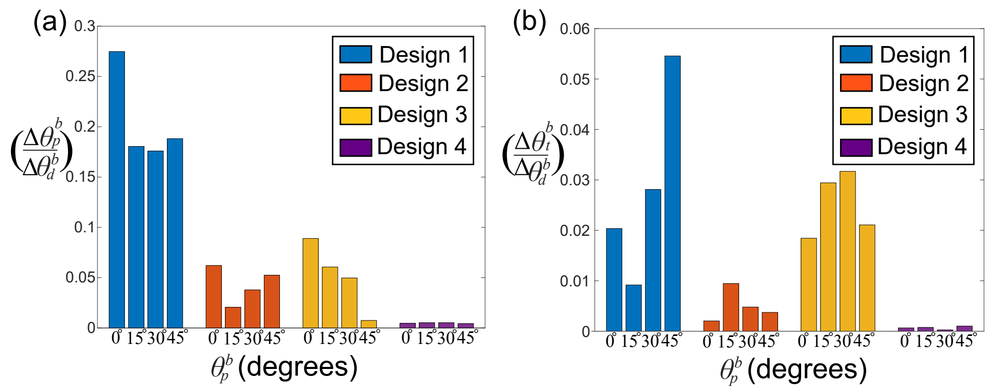

Figure 5.12: (a) Bending plane and (b) transverse plane inter-joint coupling for each of the designs proposed in Section 5.2.1.

rable to joint J5 and joint J4 was used as the distal joint. To evaluate the joint decoupling effect, the proximal joint was actuated to a certain angle $\theta_p^b = \{0°, 15°, 30°, 45°\}$ and the distal joint angle (θ_d^b) was varied continuously from $0° - 45°$ (i.e., $\Delta\theta_d^b = 0° - 45°$). The effect of this on variations of the proximal bending angle ($\Delta\theta_p^b$) and proximal transverse angle ($\Delta\theta_p^t$) was measured for each design.

The results of these trials are shown in Fig. 5.12(a) - (b). In these figures, we measure the *bending-plane* coupling as the mean of the ($\Delta\theta_p^b/\Delta\theta_d^b$) ratio and the *transverse-plane* coupling as the mean of the ($\Delta\theta_p^t/\Delta\theta_d^b$) ratio over 400 data points collected at regular intervals over the range of θ_d^b. Interestingly, we note that in both the bending and the transverse planes, the coupling in Design 1 exceeds that of any other design. High values of the ratio $\Delta\theta_p^b/\Delta\theta_d^b$ are expected due to the nature of tendon routing along the bending plane and can be compensated by antagonistic proximal tendon actuation. However, due to the nature of routing in this design, we observed that slight mismatches in assembling the two degrees of freedom result in larger *transverse-plane* coupling ($\Delta\theta_p^t/\Delta\theta_d^b$), which cannot be eliminated in this design. On the other hand, we find that Design 4 displays the least amount of coupling in the bending and transverse planes. The resistance to *bending-plane* coupling is primarily due to the distal joint tendon being routed along the neutral axis of the proximal joint. Moreover, we believe that the ability to manufacture this design as a single unit results in a high degree of alignment of the two degrees-of-freedom, thereby reducing *transverse-plane* coupling. While this design proves to be the best in terms of inter-joint coupling, it lacks full bidirectional controllability by design (as discussed in Section 5.2.1) and may not be feasible for all surgical procedures. Lastly, we find that Designs 2 and 3 are comparable in their coupling along the bending-plane. However, as expected, the *transverse-plane* coupling for Design 3 is slightly larger, since the distal tendons are routed along the transverse plane of the proximal joint. Therefore, Design 2 serves as a better design for applications where the inner lumen of the tool is not required for routing tool-tip tendons (such as electrocautery applications). On the other hand, for applications where the tool may require a tendon to be passed through the inner lumen of the tool body, Design 3 achieves comparable performance without blocking the inner lumen of the tool body.

5.5 Conclusions

In this chapter, we propose the requirements of a minimally invasive robotic tool tip for commercially available neuroendoscopes used in ETV procedures to treat pediatric hydrocephalus. Following this, we propose four different designs making use of unidirectional and bidirectional asymmetric notch joints and varying tendon routing strategies for this 2-DoF robotic tool tip. We conclude that a design that makes use of a stiff unidirectional notch joint as the proximal joint and a highly compliant distal joint using bidirectional asymmetric notch design proves to achieve the desired joint angles while keeping inter-joint coupling at a minimum. The disadvantages of this type of a design can be eliminated with the use of the other proposed designs that make use of the bidirectional joint's ability to resist transverse and axial direction forces for tendon routing. We also propose a kinematic model that relates bending angle for our bidirectional notch joints to the linear tendon displacement required to achieve this angle. While joint kinematics are predictable for the compliant joints, we find that joint statics and tendon elongation prove to be a dominant factor of this relationship for stiffer joints. Furthermore, due to the small radius of the tool body, the bending angle is highly sensitive to tendon displacement which is highly susceptible to noise, such as poor tendon-motor connections and tendon-joint connections. Therefore, we believe that a statics based model to predict bending angle and a controller using tendon tension as feedback is essential for autonomous operation of such a tool. In the following chapters, we will work on the design of a small-scale force sensor to measure tendon tension and incorporate this into the handheld controller design. Incorporating this into the current design and using the analysis of this chapter to design a decoupled 2-DoF tool body, we hope to achieve a high level of autonomy in the control of our robotic tool.

5.6 Acknowledgements

The author would like to thank Ms. Nancy Deaton and Dr. Seokhwan Jeong for part of the contents of this chapter.

CHAPTER 6

ROBOTIC PEDIATRIC NEUROENDOSCOPE: MODELING AND CONTROL

6.1 Introduction

In the previous chapter, we proposed four designs for our neuroendoscopic tool body, with various levels of inter-joint coupling in the bending and transverse planes of the robot [215]. In this chapter, the design demonstrating the lowest inter-joint coupling is selected and integrated with a newly proposed inner spine for enhanced decoupling performance. A detailed static analysis of this design is introduced in this chapter: namely a loading and unloading static model for the unidirectional asymmetric notch (UAN) joint, which is one of the joints of the robot. Previous work [122, 117] does not address the unloading cases, which are different from the loading scenario, due to the material induced hysteresis observed in superelastic nitinol. Both loading and unloading models are critical for any closed loop force-based control of a robotic tool that makes use of these joints. In this chapter, we have proposed and validated a static model for the bidirectional asymmetric notch (BAN) joint which also constitutes the distal joint of the robot. Since BAN joints do not exhibit large enough stresses to induce superelasticity, the loading and unloading models for this type of joint remain the same.

This chapter also proposes a force-based control strategy to address sources of significant error for tendon-driven robots that arises from unpredictable tendon slack [179]. Errors in the amount of slack can result in errors in the joint angle and tip configuration. This problem is even more significant as the outer diameter of the tendon-driven robot is reduced. Furthermore, manufacturing errors leading to a backlash in the gears of the lead-screws used to actuate the tendons of the robot can also significantly affect tracking performance. These can result in significant positioning errors. These mechanical uncertainties and dis-

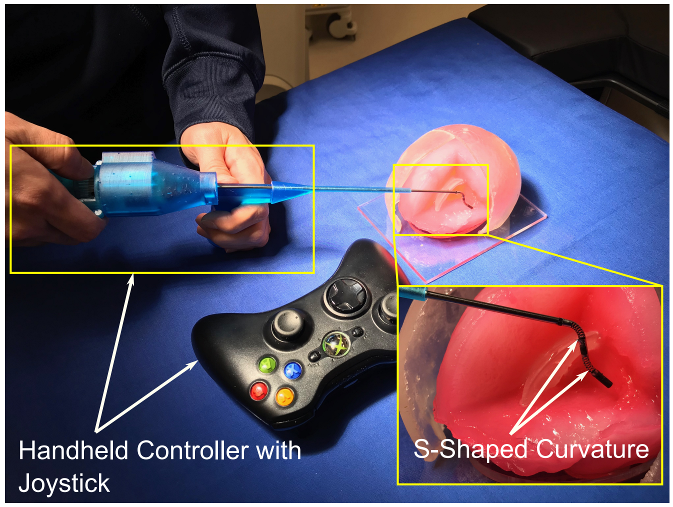

Figure 6.1: The proposed robotic endoscopic tool and handheld controller with a phantom brain ventricular model.

turbances are minimized by introducing force-based joint control. A disturbance observer is used in conjunction with the designed controller to provide stable control performance.

This chapter can be summarized as follows: We reiterate the design of the meso-scale 2-DoF robotic tool and experimental setup to validate joint decoupling in Section 6.2. In Section 6.3, we introduce static models for both joints of the 2-DoF robotic tool, with a static model including hysteresis in Section 6.3.1 for the proximal joint followed by a model and finite element analysis for the distal joint in Section 6.3.2. Finally, we introduce a disturbance observer-based force controller (Section 6.4.1) and implement a hysteresis compensator based on the joint static model (Section 6.4.2) followed by validation (Section 6.4.3) and discussion of the controller performance in Section 6.5.

6.2 Robot Design

6.2.1 Tool Design

The proposed robotic tool (see Figs. 6.2(a),(b-1)) consists of two bending flexure joints that allow the tip to be flexed in a single plane in opposite directions to form an *S*-shaped curve. The two joints are manufactured by micromachining a single tube of superelastic nitinol

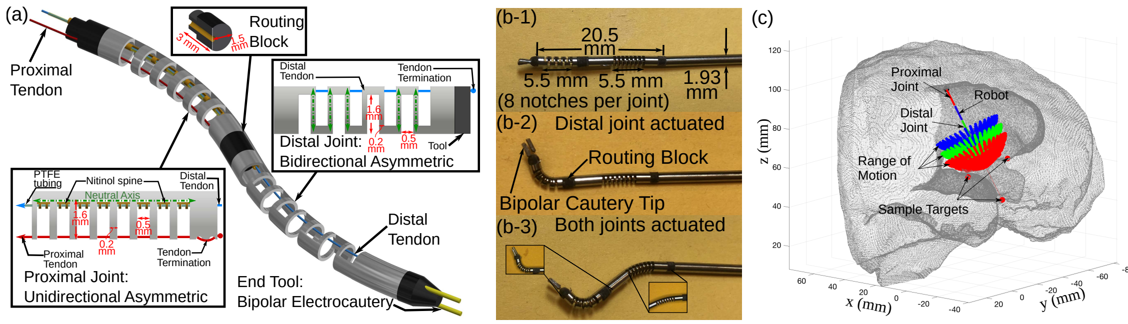

Figure 6.2: (a) The proposed 2-DoF robotic tool uses a combination of the UAN and BAN joints for the joints and a routing block for tendon routing (routing block is rotated by 180° about its longitudinal axis in the inset for clarity); (b-1) The robotic tool is in a straight configuration when both the proximal and distal tendons are relaxed, (b-2) Distal tendon actuation demonstrating decoupling, (b-3) S-shaped configurations can be achieved by applying tension to both tendons; (c) Range-of-motion (ROM) of the tool tip in a software ventricular mockup.

material of outer diameter (OD) 1.93 mm and thickness 0.22 mm. The stock metal tube is secured in a lathe stage and micromachined using a femtosecond laser (Optec Laser S.A., Frameries, Belgium) while being rotated and advanced by the lathe stage. The usage of a femtosecond laser minimizes the heat-affected zone created around the micromachined area of the tube. Since the superelastic properties of nitinol are affected by temperature, such a manufacturing process ensures a stable and repeatable set of prototypes for our static analysis. Using this micromachining process, we generate the notch patterns required for creating compliance in the nitinol tube at the proximal and distal joints. A larger notch is created between the two joints to house a tendon-routing block (see Figs. 6.2(a),(b-2)). Thus, both the joints of our robotic tool are micromachined from a single tube of nitinol as a single unit. This greatly reduces misalignment caused from assembly errors in the manufacturing process [215]. We note that for meso-scale robots, misalignment can be a severe cause of error for multi-DoF robots. Minimizing the number of discrete components to be assembled significantly improves the controllability of the robotic tool without errors arising from misalignment, friction, and other sources. The notch pattern of the tube determines the bending properties of the joint. We use this phenomenon to our advantage in the design of our robotic tool. The proximal joint of the tool is constructed by creating notches along one direction of the bending plane allowing the tube to be flexed in the same plane. The joint thus created is called a UAN joint (see Fig. 6.2(a)(inset)). A single tendon (which is a nitinol wire of diameter 130 μm) is routed from the base of this joint and fixed to the end of the joint (see red-colored tendon in Fig. 6.2(a)). Tendon fixturing is done by micromachining two circular holes (diameter $\approx$ 150 μm) at the end of the joint and weaving the tendon in these two holes. A groove is machined in the outer wall of the tube between these two holes to ensure that the tendon is flush with the outer wall as it weaves in and out of the notches. Finally, a knot is tied at the end of the tendon and this knot is soldered such that the knot diameter exceeds the termination holes, thereby securing the tendon in place. By tensioning the tendon, the UAN joint can be flexed in the direction of the notches. The distal joint is created by micromachining asymmetric notches along both directions of the bending plane [175]. This allows the distal joint to bend in two directions and this joint is therefore termed the BAN joint (see Fig. 6.2(a)(inset)). However, in this work, the distal joint is controlled in a single direction by a single tendon to minimize the inter-joint coupling problems seen in meso-scale robots (see blue-colored tendon in Fig. 6.2(a)). The distal tendon is terminated at the end tool (Bipolar Electrocautery tool in Fig. 6.2(a)), by soldering a knot at the end of the tendon such that the distal end of the tendon cannot pass through the 3D-printed fixture that also holds the end tool. The proximal and distal tendons allow the robotic tool to be actuated in different directions of the same bending plane individually, thus making the *S*-shaped curve possible (see Fig. 6.2(b-3)). A 3D-printed separator block (Projet 5600, 3D Systems, South Carolina, United States) called the 'routing block' is inserted in the space between the two joints (see Fig. 6.2(a),(b-2)). The distal tendon is passed through the proximal joint via a *nitinol spine*. This spine is a nitinol tube (OD = 0.41 mm, thickness = 0.08 mm) micromachined with unidirectional asymmetric notches along the proximal bending direction (see Fig. 6.2(a)) and a PTFE tube attached to the inner wall of the tube to minimize friction. This nitinol spine helps in joint decoupling and also allows intrinsic shape sensing modalities or tool cables to be routed through it [207]. In effect, the nitinol tube in the spine acts as a pure extension spring capable of bending in a single plane. Therefore, the entire spine arrangement is similar to a miniature Bowden cable, capable of transmitting mechanical pulling forces directly to the distal joint of the robot. Fig. 6.2(c) indicates the range-of-motion (ROM) analysis of the robotic tool. We observe that it is capable of reaching a large volume within the ventricular cavity. In our previous work [215], we have demonstrated that a previous iteration of this design successfully covers the visible portion of the ventricular cavity which is critical for an ETV procedure.

6.2.2 Joint Decoupling and Validation Setup

The choice of different types of bending flexure joints for each of the joints of the robotic tool is deliberate. We have demonstrated in the past [213] (see Chapter 2), that the BAN joint can achieve a higher bending compliance for the same amount of material removal (or joint length) compared to the UAN joint. The tendon force required in bending the distal joint to a given angle is therefore much lower than the force required to achieve the same angle with the proximal joint (as will be evident in the next section). This allows us to control the distal joint to a high curvature without imparting significant forces on the proximal joint, thereby minimizing inter-joint coupling by design. The routing block and the micromachined spine ensure that the distal tendon is always routed close to the neutral axis of the proximal joint (see green dotted-dashed line in Fig. 6.2(a) (inset)). Actuating the distal tendon, therefore, causes a negligible moment (since the moment arm is negligible) to be applied on the proximal joint, thereby effectively further decoupling the two joints.

To evaluate decoupling in the robotic tool introduced in this section (as well as the static models and the controller introduced in Sections 6.3 and 6.4), we designed the experimental setup shown in Fig. 6.3(a). The robotic tool and joint prototypes were fixed in a 3D-printed vice. A 5-DoF electromagnetic (EM) tracker (Northern Digital Inc., Waterloo, Ontario, Canada) was attached to the tip of each prototype to be tested, to measure joint angles and

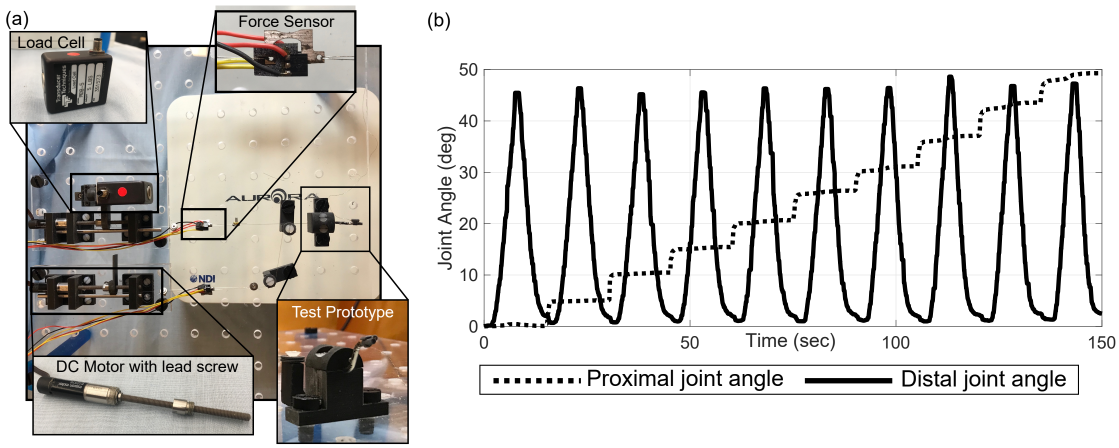

Figure 6.3: (a) Experimental setup to test joint decoupling; (b) The distal joint actuated to $\approx 45^\circ$ for various values of proximal joint angles to demonstrate decoupling.

robot tip position. The free ends of the two tendons were attached to a DC motor (0.5 W, ∅ 8 mm, Maxon Precision Motors, MA, United States) with a lead screw of length 50 mm, pitch 0.5 mm, and maximum feeding force of 22 N, via a photointerrupter-based miniature force sensor [216]. To calibrate and validate the force sensor data, a load cell with a load capacity of 5 lbs. (Transducer Techniques, CA, United States) was also attached to one of the DC motors via a linear rail. This load cell was also used to validate all the static models proposed in this work. All the analog data was acquired with a digital-analog acquisition board (PCIe-6321, National Instruments, TX, United States).

To demonstrate the decoupling performance of this robotic tool design, the distal joint was actuated approximately between 0° to 45° in an open-loop manner, while the proximal joint was held constant from approximately 0° to 50° in 10 discrete steps with the help of the EM tracker. These maximum joint angle limits were selected since they are higher than the required joint angles for this design for a potential ETV procedure [215]. The proximal joint was first incremented with a step input of $\approx 5^\circ$, followed by distal joint actuation. Two EM trackers were used in the setup described above to measure both joint angles simultaneously. Fig. 6.3(b) demonstrates that the proximal joint remains steady at the commanded position at all times during the distal actuation. We observe that for proximal joint angle values of approximately 45°, a coupling of $\leq 1^\circ$ is observed when the distal joint reaches its maximum value. However, for this application, this coupling can be considered minimal and the robotic tool can be assumed to be effectively decoupled.

6.3 Robot Modeling

We use Castigliano's theorems to derive the relationship between bending angle (θ_n) and tendon tension (F_n) for each of the joints of the robotic tool ($n = \{1, 2\}$). In the previous sections, we have described the design of the tool, which makes use of different notch geometries for each of the joints of the tool. Therefore, the bending member employed for the flexion of the proximal joint ($n = 1$) varies significantly from the bending member employed in the BAN joint forming the distal joint ($n = 2$). As a result, the static model employed for each of these joints also takes these differences into account. In each case, we try to express this model in the form: $F_n = S_n(\theta_n)$, where θ_n is the input to the model and F_n is the corresponding output. The static function $S_n(\theta_n)$ is later used in the controller in Section 6.4 to generate tendon tension references for the controller.

6.3.1 Proximal Joint

As described in Section 6.2.1, the proximal joint is formed from a set of N asymmetric unidirectional notches cut into a nitinol tube of outer and inner radii, r_o and r_i, respectively. The asymmetrical notches result in the neutral axis of the tube being pushed by a distance, $\overline{y}$, from the center of the tube (O_t in Fig. 6.4(a)) and is given as follows:

$$\overline{y} = \frac{4\left(r_o^3 \sin^3(\phi_o) - r_i^3 \sin^3(\phi_i)\right)}{3\left(r_o^2\left(2\phi_o - \sin 2\phi_o\right) - r_i^2\left(2\phi_i - \sin 2\phi_i\right)\right)} \tag{6.1}$$

where r_o and r_i are the outer and inner radii of the tube respectively and $\phi_o = \arccos\left(\frac{d-r_o}{r_o}\right)$ and $\phi_i = \arccos\left(\frac{d-r_o}{r_i}\right)$ are the angles at O_t created due to the micromachining (see Fig. 6.4(a)) [122]. Furthermore, d is the notch depth, which is selected so that maximum proximal joint stiffness could be achieved, given a maximum allowable feeding force (~22 N) of the actuator for the proximal joint tendons. We assume piecewise constant curvature approximation (PCCA), which assumes that the total deflection of the proximal joint angle (θ_1, created at the center, O_j in Fig. 6.4(a)) is distributed equally along all the notches. Each of these unidirectional asymmetric notches deflects by an angle, $\frac{\theta_1}{N}$ (with center, O_n, in Fig. 6.4(a)(inset)), due to force F_1 applied by the tendon of diameter, $t_d = 0.13$ mm (see Fig. 6.4(a) (inset)). This force causes a moment, $M_1 = F_1 L$, to be applied to the backbone of the joint, which is the segment of the tube left over after the etching of the notch. Here, $L = (r_i - \frac{t_d}{2}) + \overline{y}$ is the moment-arm of the applied tendon tension. The direction of the applied force F_1 plays a significant role in the static relationship of the joint. We term the positive force gradient (ΔF_1) created during tendon pulling as the 'tendon loading' phase and negative (ΔF_1) created during tendon releasing as the 'tendon unloading' phase. Depending on the direction of the application of force (i.e., tendon loading/unloading), the static relationship observed between tendon tension F_1 and bending angle θ_1 differs significantly due to the large hysteresis in F_1-θ_1 relationship. This hysteresis is caused by two sources:

1. Nitinol material characteristics,

2. Friction due to the tendon-notch contact.

Therefore, the F_1-θ_1 relationship is given as follows:

$$F_1 = \begin{cases} S_{1.up}(\theta_1) & \text{if } \Delta F_1 \geq 0 \\ S_{1.down}(\theta_1) & \text{else} \end{cases} \tag{6.2}$$

Even though this relationship is expressed differently in each case (loading/unloading), we use the same principle to arrive at the value of F_1. As a result, we express both the above functions as $S_1(\theta_1)$ for brevity. Castigliano's first theorem is used to compute F_1 as follows

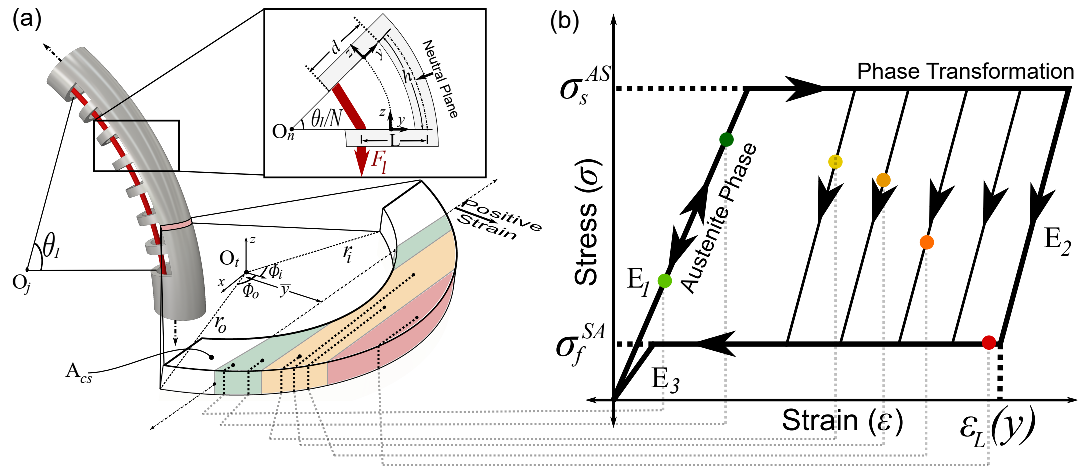

Figure 6.4: (a) Flexion of the UAN joint under tendon tension (inset) results in a gradient of strains along the y-axis on either side of the neutral plane; (b) Any discretized point along the cross-sectional area, A_{cs}, can be mapped on to a point on the nitinol stress-strain graph in superelastic state exhibiting hysteresis.

[122]:

$$F_1 = S_1(\theta_1) \tag{6.3}$$

$$= \frac{1}{\eta^{2N} L} \frac{\partial U(\theta_1)}{\partial \theta_1} \tag{6.4}$$

where $\eta = 0.985$, is a friction loss parameter arising from interaction between each of the $2N$ notch edges at the joint and the tendon; and is derived experimentally. Furthermore, $U(\theta_1)$ is the total strain energy in the joint and it is defined as follows:

$$U(\theta_1) = Nh \int_{A_{cs}} \int_0^{\epsilon} \sigma(e)\, de\, dA \tag{6.5}$$

where A_{cs} is the cross-sectional area of each notch of height h and $\sigma(e)$ is the stress at each point of the area along the y-axis (see Fig. 6.4(a)). To estimate the stress corresponding to each point of the bending segment, we inspect the stress-strain curve for superelastic nitinol (see Fig. 6.4(b)). Nitinol exhibits stress-induced phase transformations at temperatures above its austenite phase transformation temperature. At this temperature, during loading, nitinol exhibits a linear elastic region with slope E_1 until phase transformation is initiated at a strain value: ($\frac{\sigma_s^{AS}}{E1}$). During transformation to the martensite phase, the curve demonstrates an upper plateau region until complete transformation to the martensite phase. In this work, we model the austenite and transformation phases for nitinol and not the martensite phase. Therefore, during loading, i.e. when the tendon is pulled and $\Delta F_1 \geq 0$, the stress function $\sigma(\epsilon)$ is defined as follows:

$$\sigma(\epsilon) = \begin{cases} E_1 \epsilon(\theta_1, y) & \text{for } \epsilon(\theta_1, y) \leq \frac{\sigma_s^{AS}}{E_1} \\ \sigma_s^{AS} & \text{for } \epsilon(\theta_1, y) > \frac{\sigma_s^{AS}}{E_1} \end{cases} \tag{6.6}$$

where $\epsilon(\theta_1, y) = \frac{\theta_1(y-\overline{y})}{Nh}$ is the strain, which is constant for all points at a distance, y. During unloading, i.e. when the tendon is released and $\Delta F_1 < 0$, the stress curve follows a hysteresis curve from a point of maximum strain to a lower plateau region (having stress σ_f^{SA} as seen in Fig. 6.4(b)) with a constant slope E_2. This plateau region continues until a strain value: ($\frac{\sigma_f^{SA}}{E_3}$), at which point the austenite phase is regained for further unloading. We assume this phase to have an elastic modulus, E_3. In this work, we assume $E_1 = E_2 = E_3 = 55$ GPa, $\sigma_s^{AS} = 800$ MPa, and $\sigma_f^{SA} = 275$ MPa where these values are obtained experimentally. Therefore, during unloading, each location along the y-axis follows a different stress-strain trajectory entirely based on the value of θ_1 at which unloading began.

The value of strain along the y-axis at the beginning of the unloading process is given by:

$$\epsilon_s^{SA}(y) = \epsilon(\theta_1^{max}, y) \tag{6.7}$$

where, θ_1^{max} is the joint angle at which unloading began.

Primarily, for each point along the y-axis, the stress-strain curve during unloading can be divided into two regions based on the $\epsilon_s^{SA}(y)$ and therefore, the stress can be given as follows

$$\sigma(\epsilon) = \begin{cases} \sigma_{lin}(\epsilon) & \text{for } \epsilon_s^{SA}(y) \leq \frac{\sigma_s^{AS}}{E_1} \\ \sigma_{nl}(\epsilon) & \text{for } \epsilon_s^{SA}(y) > \frac{\sigma_s^{AS}}{E_1} \end{cases} \tag{6.8}$$

where $\sigma_{lin} = E_1\epsilon(\theta_1, y)$ is the linear portion of the curve (austenite phase of nitinol), where no hysteresis is observed in the stress value. For the sections of the backbone experiencing strain values larger than $(\frac{\sigma_s^{AS}}{E_1})$ at maximum bending curvature θ_1^{max}, hysteresis will be observed as the tendon tension is lowered (i.e., unloading). These sections of the nitinol backbone have already entered the transformation from austenite to martensite phase (the superelastic plateau region) and the value of stress in these regions is given as follows:

$$\sigma_{nl}(\epsilon) = \begin{cases} \sigma_2(\theta_1, y) & \text{for } \epsilon(\theta_1, y) > \epsilon_L(y) \\ \sigma_f^{SA} & \text{for } \frac{\sigma_f^{SA}}{E_3} \leq \epsilon(\theta_1, y) \leq \epsilon_L(y) \\ E_3\epsilon(\theta_1, y) & \text{for } \epsilon(\theta_1, y) < \frac{\sigma_f^{SA}}{E_3} \end{cases} \tag{6.9}$$

where $\sigma_2(\theta_1, y) = E_2(\epsilon(\theta_1, y) - \epsilon_L(y)) + \sigma_f^{SA}$ is the linear region with slope E_2 (see Fig. 6.4(b)). Furthermore, $\epsilon_L(y) = \epsilon_s^{SA}(y) - (\frac{\sigma_s^{AS} - \sigma_f^{SA}}{E_2})$ is the strain at which phase transformation to austenite phase (lower plateau region) resumes during unloading (see Fig. 6.4(b)). Using Eqs. (6.8) and (6.9) in Eq. (6.5), we can compute the total strain energy $U(\theta_1)$ of the proximal joint for the section of the backbone experiencing positive strain. Similarly, this process is then repeated for the portion of the backbone experiencing negative strain and the strain energy of that portion is added to $U(\theta_1)$. Finally, the value of F_1 can be obtained using Eq. (6.4).

To validate our model, we manufactured two samples of the proximal joint with N=8, h=0.5 mm, and $d = \{1.6, 1.7\}$ mm. The experimental setup used to measure tendon tension, motor stroke and joint angle is the same as the one described in Section 6.2.2. Numerical integration (MATLAB 2018b, The Mathworks Inc., Natick, MA, United States) was

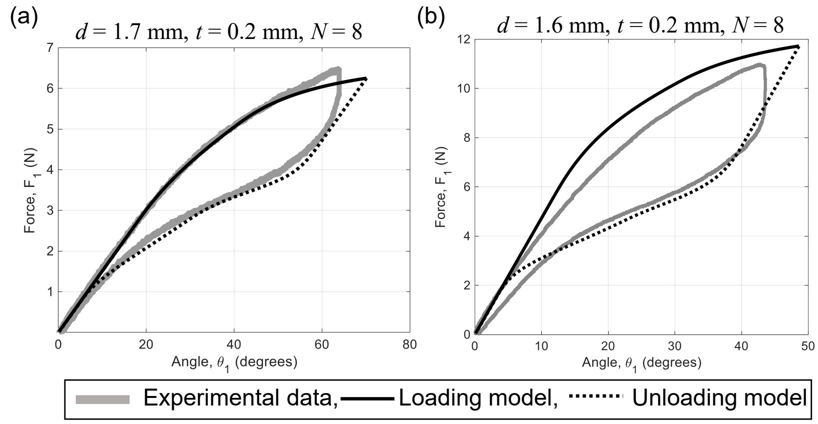

Figure 6.5: The analytical model incorporating hysteresis successfully replicates experimental results for the F_1-θ_1 relationship (demonstrated for two samples with varying depths).

used to compute $S_1(\theta_1)$ from Eq. (6.4). Fig. 6.5 and the RMSE values in Table 6.1 show that the proposed model accurately replicates the experimental result of the sample joints. We observe that for d=1.7 mm, the model is unable to fit the data for values of joint angles greater than $\theta_1{\approx}60°$ (see Fig. 6.5(a)). We believe that this is due to some of the portions of the backbone entering the unmodeled martensite region of the nitinol stress-strain curve. Similarly, the model slightly overestimates the loading tendon tension for d=1.6 mm (see Fig. 6.5(b)). Next, using this model and the force feedback controller (detailed in Section 6.4) for the sample with d=1.7 mm, we observed the bending angle of the proximal joint for a linear reference input, θ_{ref}=$\{0°\text{- }15°\text{- }0°, 0°\text{- }30°\text{- }0°, 0°\text{- }45°\text{- }0°, 0°\text{- }60°\text{- }0°\}$. The corresponding force trajectories, F_{ref} with respect to θ_{ref} are generated using:

1. The model without hysteresis, $S_{1.up}$ (proposed in [122]),

2. the value computed using Eq. (6.2).

The results of this experiment are in Fig. 6.6. For all values of θ_{ref}, our model (solid line in Fig. 6.6) closely follows θ_{ref}, in comparison with the model not incorporating hysteresis (dashed line in Fig. 6.6). Furthermore, for smaller joint angle region (such as a linear input reference reaching $15°$, see Fig. 6.6(a)), the solid line and dashed lines match exactly, meaning that the entire backbone stays in the austenite region throughout

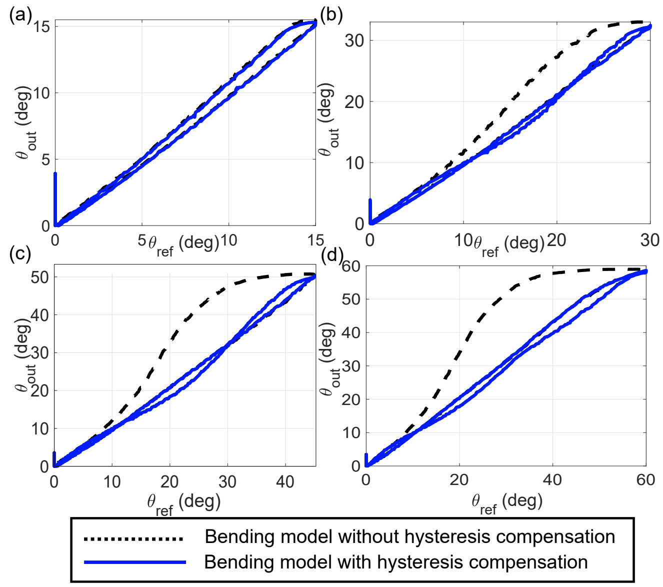

Figure 6.6: For a triangular reference angle of $\theta_{ref} = \{0°\text{- }15°\text{- }0°, 0°\text{- }30°\text{- }0°, 0°\text{- }45°\text{- }0°, 0°\text{- }60°\text{- }0°\}$, a model compensating material induced hysteresis is able to correctly identify and reduce material induced hysteresis.

the loading/unloading process without the hysteresis. The residual hysteresis in Fig. 6.6(a) is expected to come from the unmodeled friction factors between the tendon and joint. Thus the model is successfully capable of estimating the amount of hysteresis present for any given θ_{ref} trajectory.

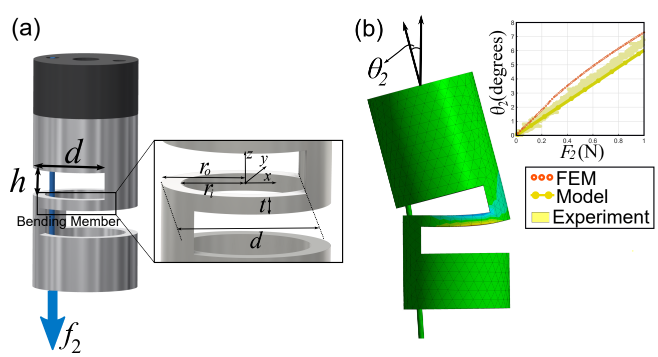

Figure 6.7: (a) Sample of a two-notch BAN joint with a tendon applying tension f_2 and corresponding geometric parameters (inset); (b) finite element model of the two-notch joint with results compared with experimental data and analytical model (inset).

6.3.2 Distal Joint

In the case of the distal joint, the dominant source of bending is the beam between two consecutive notches in the joint [178, 213] (indicated by 'Bending Member' in Fig. 6.7(a)). As can be seen in the stress concentration derived using finite element modeling for a two-notch distal joint sample (see Fig. 6.7(b)), the vertical walls experience negligible stresses and do not contribute to significant joint flexion and therefore, can be ignored in our model. Our model assumes that the entire distal joint consisting of N notches is a serial chain of $(N - 1)$ *elastic links*. Each *elastic link* in turn, consists of two curved beams between two consecutive notches connected in parallel as a combination of two elastic *bending members*. Therefore, the deflection of a single *bending member* under tendon tension f_2 must be analyzed first. This member is modeled as a curved beam created due to two consecutive notches of notch depth d and height h made in a tube of outer and inner radii r_o and r_i, respectively (see Fig. 6.7(a) (inset)). The distance between two consecutive notches is $(h + t)$, where t is shown in Fig. 6.7(a) (inset). The curved beam, therefore, has height t, thickness $(r_o - r_i)$ and length $2(d - r_o)$. A model of the curved beam with respect to the center of the tube is shown in Fig. 6.8(a). The central angle created by this beam at the center of the tube is indicated by φ. The beam is assumed to be fixed at one end, while the tendon tension f_2 is statically equivalent to a force moment pair f_2-M_2 at the free end, where f_2 is a downward acting force and a moment M_2 of magnitude $f_2 L_2$ (with a direction pointing out of the page). Here, $L_2 = d - (r_o - r_i) - (\frac{t_d}{2})$ is the moment arm for the force f_2. Unlike the proximal joint, we cannot assume a uniform bending across the entire length of the bending member and therefore, the analysis used for the proximal joint cannot be directly applied to this bending member. On the other hand, the distribution of the applied tendon tension across the bending member can be calculated and acts as the input to our model. This applied force-moment pair f_2-M_2 results in a bending moment along the y-axis (see Fig. 6.8(a), (b)), causing a bending of the joint. To measure this value, we consider cross-sections of the beam parallel to the y-z plane along

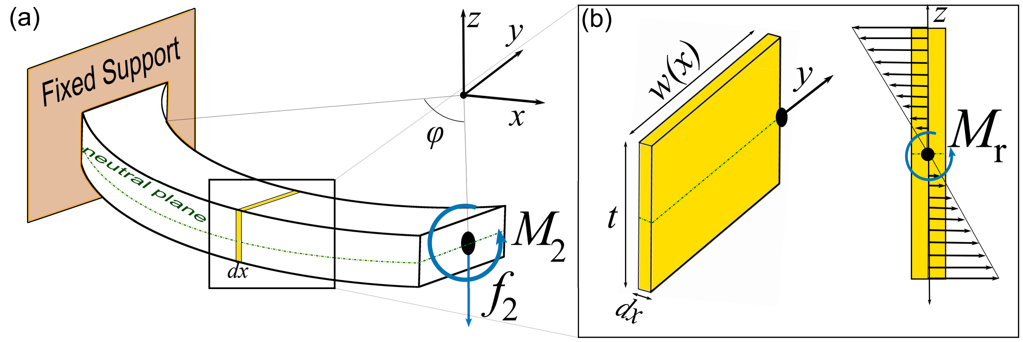

Figure 6.8: (a) Bending member modeled as curved beam with f_2-M_2 applied at the free end; (b) Resulting moment M_r at rectangular cross-section of beam model results in linear gradient along z-axis.

the length of the beam. Such a cross-section will have a height of t, thickness dx, and width $w(x) = \sqrt{r_o^2 - x^2} - \sqrt{r_i^2 - x^2}$ which varies with x (see Fig. 6.8(b)). Application of the force f_2 and moment M_2 at a cross-section at any point x results in a moment at the cross-section given by:

$$M_r(x) = M_2 - f_2 \cdot (d - r_o - x) \tag{6.10}$$

The stress distribution resulting from $M_r(x)$ along the z-axis at every cross-section is shown in Fig. 6.8(b) and is given by:

$$\sigma_{yy}(x, z) = \frac{M_r(x)z}{I_y(x)} \tag{6.11}$$

where the second moment of area with respect to the y-axis $I_y(x) = t^3 w(x)/12$. Now, the total strain energy across the beam is given by:

$$U = \frac{1}{2} \int_{V_{beam}} \sigma_{yy}(x, z)\epsilon_{yy}\, dV \tag{6.12}$$

$$= \frac{1}{2} \int_{V_{beam}} \frac{\sigma_{yy}(x, z)^2}{E(\sigma_{yy})}\, dV \tag{6.13}$$

Unlike in the case of the proximal joint, we assume that $\epsilon_{yy} = \sigma_{yy}(x,z)/E(\sigma_{yy})$, for all values of σ_{yy}. In the case of the distal joint, $E(\sigma_{yy})$ is expressed as a piecewise linear function, which is slightly different from Eq. (6.6):

$$E(\sigma_{yy}) = \begin{cases} E_{d2} & \text{for } \sigma_{yy}(x,z) < \sigma_{dl} \\ E_{d1} & \text{for } \sigma_{dl} \leq \sigma_{yy}(x,z) \leq \sigma_{du} \\ E_{d2} & \text{for } \sigma_{yy}(x,z) > \sigma_{du} \end{cases} \tag{6.14}$$

where, σ_{dl} and σ_{du} are minimum and maximum values of the stress respectively, for which the bending member is in the austenite phase. In our case, σ_{dl}=-800 MPa (for negative stresses) and σ_{du}=800 Mpa (for positive stresses) are used. For these stresses, we denote the Young's modulus as E_{d1}. In the superelastic phase, we denote the Young's modulus as E_{d2}. From Eq. (6.11) and Eq. (6.13), we obtain:

$$U = \frac{1}{2}\int_{V_{beam}} \frac{M_r(x)^2 z^2}{E(\sigma_{yy}) I_y^2(x)}\, dV \tag{6.15}$$

$$= \frac{1}{2}\int_{-(d-r_o)}^{(d-r_o)} \int_{-\frac{t}{2}}^{\frac{t}{2}} \frac{M_r(x)^2 z^2 w(x)}{E(\sigma_{yy}) I_y^2(x)}\, dz\, dx \tag{6.16}$$

Also, by Castigliano's second theorem, the bending angle θ_{beam} is defined as follows:

$$\theta_{beam} = \frac{\partial U}{\partial M_2} = \frac{\partial U}{\partial M_r} \tag{6.17}$$

Similarly, the total displacement of a point at the tip of the beam is given by:

$$\Delta_{beam} = \frac{\partial U}{\partial f_2} \tag{6.18}$$

First, we validate our model for curved beams of various materials and dimensions with a finite element model of the same. Curved beams of various materials and dimensions were modeled in ANSYS 18.2 (Ansys Inc., Canonsburg, PA, United States) and compared with

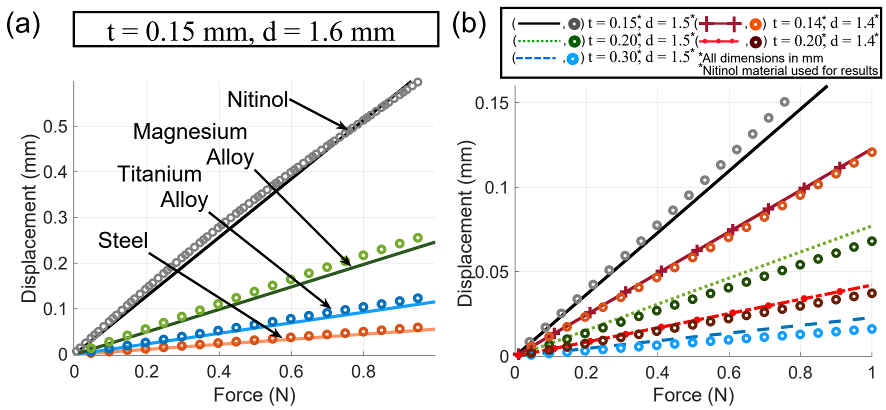

Figure 6.9: Analytical estimation of beam tip displacement (Δ_{beam}) vs. applied force (f_2) for our curved beam model (solid lines), in comparison to finite element model performance (circular points) for: (a) varying material parameters, (b) varying geometric parameters.

our analytical results (see Fig. 6.9). This analysis proves that the proposed model for the curved beam consisting of the distal joint is valid under varying geometric and material considerations. Next, we use the derived curved beam model to model the BAN joint. For each pair of notches in the joint, a pair of two such curved beams is created by the notching. These two beams are modeled as a set of elastic members connected in parallel and a BAN joint with N notches has $(N-1)$ such parallel members. These $(N-1)$ members are assumed to be a serial chain of elastic members. Therefore, the bending angle, θ_2, of the complete joint with N notches is given by:

$$\theta_2 = \frac{(N-1)}{2}\theta_{beam} \tag{6.19}$$

Note that θ_{beam} is a bending angle for the single bending member under the influence of force, f_2, derived in Eq. (6.17).

Furthermore, the tendon tension F_2 incorporating the tendon friction loss is the same as defined for the proximal joint (with the only difference being that a tendon encounters friction from N notch edges) and is given by $F_2 = (1/\eta^N)f_2$, where $\eta = 0.985$ (same as that in Eq. (6.4)) is defined as the friction loss parameter arising from tendon interaction with every notch edge. To validate our static model, we use the same setup as that

Table 6.1: RMSE values for statics models.

Joint Type	Parameters				
	t (mm)	d (mm)	h (mm)	Notches	RMSE
Proximal Joint	0.2	1.6	0.5	8	0.6163 N[a]
					0.9355 N[b]
	0.2	1.7	0.5	8	0.1587 N[a]
					0.0771 N[b]
Distal Joint	0.2	1.325	0.5	2	1.4111°
		1.425			1.1952°
		1.525			0.5035°
		1.625			0.7294°
		1.725			1.0176°
	0.15	1.6	0.5	2	1.1766°
	0.2				0.9634°
	0.225				0.2680°
	0.25				0.2112°
	0.32				1.0253°
	0.2	1.6	0.5	2	0.2619°
				4	0.9705°
				8	4.7619°
				12	1.8848°

[a] Loading model given by $S_{1.up}(\theta_1)$ in Eq. (6.2).
[b] Unloading model given by $S_{1.down}(\theta_1)$ in Eq. (6.2).

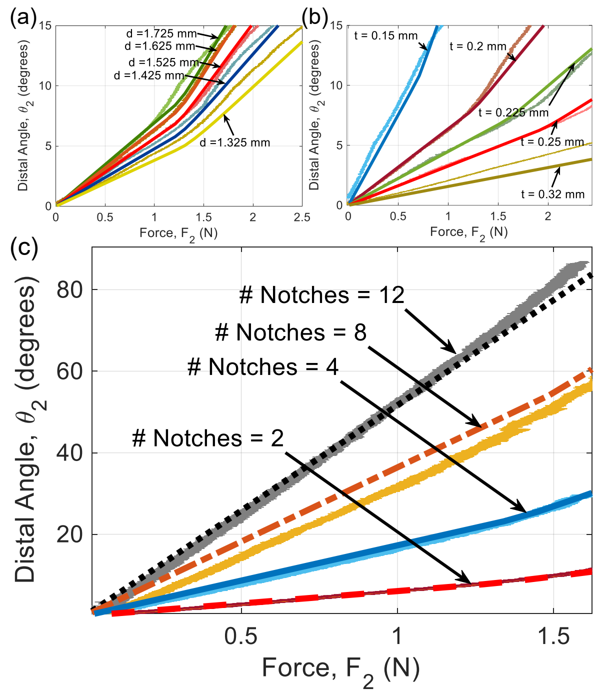

Figure 6.10: F_2-θ_2 relationship for: (a) Five samples with $N = 2$ and varying depths, d; (b) Five samples with $N = 2$ and varying beam height, t; (c) Samples with $d = 1.625$ mm, $t = 0.2$ mm, and varying number of notches, N. Three trials were conducted for each case.

described in Section 6.2.2. A total of ten samples with $N = 2$ and varying depths and thicknesses were tested to validate the model for the case of a single pair of parallel curved beams. Five samples with $N = 2$, $t = 0.2$ mm, $d = 1.325$ mm - 1.725 mm (in increments of 0.1 mm), and five samples with $N = 2$, $d = 1.625$ mm, $t = 0.15$ mm-0.32 mm were manufactured with the femtosecond laser, following which the dimensions were measured under a microscope. Next, four samples with depth $d = 1.6$ mm, height $t = 0.2$ mm, and varying notches ($N = \{2, 4, 8, 12\}$) were tested using the setup. The results from these trials are seen in Fig. 6.10 and Table 6.1. The material parameters for our analytical model ($E_{d1} = 24.3$ GPa, $E_{d2} = 15$ GPa, $\sigma_{dl} = -800$ MPa, $\sigma_{du} = 800$ MPa) are derived from these experimental results. We observe that the analytical model successfully estimates joint flexion and the serial chain assumption holds well for the operating range of joint angles. One interesting observation is that the bending modulus ($E_{d1} = 24.3$ GPa) in the distal joint is significantly different from the proximal joint (65 GPa). However, the finite element

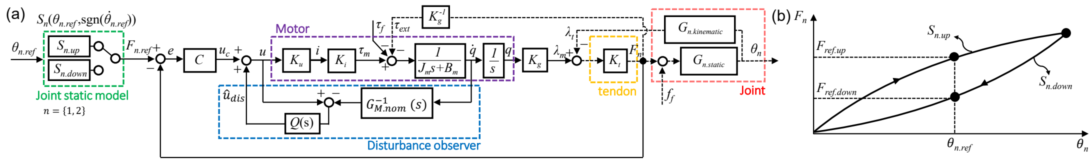

Figure 6.11: (a) A controller system with the proposed joint static model to compensate the systersis. (b) Hysteresis relationship between joint angle and force.

model for the $N = 2$ case modeled using the experimental material properties successfully estimates experimental and analytical values (see Fig. 6.7(b) (inset)), thereby confirming the estimates for these parameters. We believe that this large difference may be a result of the observed anisotropy of nitinol [217, 218, 219, 220], or due to changes occurring from the laser micromachining of the notches. Previous work has tested biaxial anisotropy of nitinol for tension/torsion [218], and the high sensitivity of nitinol elastic modulus to the orientation of rolling direction [220]. This phenomenon has not been demonstrated for the bending loads tested in this work; we will investigate this anisotropy for nitinol in our loading cases in our future work. We have mentioned previously (see Section 6.2.1) that the distal joint is highly compliant in comparison to the proximal joint, given the same number of notches and joint lengths. For $N = \{8, 12\}$, the joint is able to achieve a high bending angle at a significantly lower tendon tension than in the case of the proximal joint with $N = 8$ (see Figs. 6.5 and 6.10(c)). This indicates that even at the highest curvature, the stresses applied to the individual bending members remain small, resulting in the entire bending member remaining in the austenite phase on the nitinol stress-strain curve. On the other hand, for the samples with $N = 2$ (see Figs. 6.10(a)-(b)), the slope of the F_2-θ_2 relationship curves slightly upwards for higher forces indicating that certain portions of the bending member begin to undergo phase-transformation in the stress-strain curve (see upper plateau region in Fig. 6.4(b)). This model, which incorporates this non-linearity (see Eq. (6.14)), correctly estimates this change. Similarly, due to this lack of material induced hysteresis for the distal joint (where $N = 8$), the equations for the Young's modulus (see Eq. (6.14)) need not be as complex as the one for the proximal joint (see Eqs. (6.6) and

(6.8)), which greatly simplifies the relationship for the loading/unloading cases. Therefore, we approximate the F_2-θ_2 relationship for our robotic tool's distal joint (which has the same properties as the $N = 8$ curve in Fig. 6.10(c)) as a linear function of the bending angle θ_2 and use the same for our controls model in Sec. 6.4.

6.4 Control Algorithm

6.4.1 Design of Force controller

To achieve joint-space control based on the proposed static models by controlling tendon force precisely, following relationships between tendon force, motor stroke and joint angles (see Fig. 6.3(a)) can be derived and expressed as system block diagram (see Fig 6.11(a)):

$$F_n = K_t(\lambda_m - \lambda_t) \tag{6.20}$$

$$\theta_n = G_{n.static}(F_n) \tag{6.21}$$

$$\lambda_t = G_{n.kinematic}(\theta_n) \tag{6.22}$$

where K_t, λ_m, and λ_t are the spring constant of the nitinol tendon, motor stroke (at the tendon attachment point), displacement of another end of the tendon connected the joints, respectively. The elongation of the tendon is represented as $(\lambda_m - \lambda_t)$, which generates tendon tension. $G_{n.static}$ and $G_{n.kinematic}$ are the static and kinematic relationships for each joint between F_n-θ_n and θ_n-λ_t, respectively. With the given system diagram, a force feedback loop was implemented. The joint static models S_n derived in Section 6.3 provide a reference force $F_{n.ref}$ corresponding to the desired reference angle $\theta_{n.ref}$ and it is fed into a force feedback loop with the measured force from the force sensor. Finally, the linear motor implements feedback control, actuating the tendon with a proportional-integral (PI) controller, C (see Fig. 6.11(a)).

In the proposed tendon-based mechanism, the high transmission ratio of the lead screw and the gearbox generates high friction, τ_f, and tendon slack results in a sudden change of the external load, τ_{ext}, imposed on the motor (i.e., dotted line connected to the K_g^{-1} block in Fig. 6.11(a) may conditionally exist). These disturbances may cause unstable force control performance. In the proposed control loop, therefore, C was used in conjunction with a disturbance observer (DOB) to attain a robust acceleration control, which increases stability and robustness of the force controller [221]. The DOB makes use of measured angular velocity, $\dot{q}$, obtained from the encoder of the motor and control input, u, and calculates the estimated disturbance, $\hat{u}_{dis}$ with the inverse of the nominal plant of the motor, $G_{M.nom}^{-1}$ (see the Disturbance Observer block in Fig. 6.11(a)). Q is a low-pass filter to satisfy system causality. In the designed control loop, K_u, K_i, J_m, B_m, K_s, and K_g represent the control constant, the torque constant, the motor inertia, motor viscous friction constant, and the transmission ratio which includes the gearbox and the lead screw. Furthermore, e, u_c, i, τ_m, and f_f are the control error, the original control input, motor current, motor torque, and the friction between the tendon and the joints.

6.4.2 Hysteresis Compensator

As seen in Fig. 6.5, the proposed proximal joint has a large hysteresis in the force-angle relationship due to the characteristics of superelastic nitinol, resulting in large angular differences in the force loading/unloading curve. In this section, two control schemes are presented to show the effectiveness of model-based control and hysteresis compensation: 1) The joint static model without the hysteresis model and 2) The joint static model with the hysteresis model.

Case I : To achieve θ_{ref}, the loading case model $S_{n.up}$ from Eq. (6.2) (see Fig. 6.11(b)) is only considered as the joint static model S_n. F_{ref} generated from $S_{n.up}$ is fed into the designed force feedback controller. This can provide exact force reference profiles for the loading case and avoid the complex modeling to calculate the unloading model, $S_{n.down}$, inducing the hysteresis curve (see Fig. 6.4(b) and Eq. (6.9)).

Case II : The joint static model $S_n(\theta_{ref})$ includes both static models for loading ($S_{n.up}$) and unloading ($S_{n.down}$) cases (see Eq. (6.2)). It generates $F_{ref.up}$ or $F_{ref.down}$ as a force reference to achieve the θ_{ref} depending on the loading/unloading cases (see Fig. 6.11(b)). Therefore, the final output force considering the force difference in the hysteresis curve is applied to the joint, achieving the desired θ_{ref} as shown in Fig. 6.5.

6.4.3 Validation

In **Experiment 1** (see Fig. 6.12(a)), we generated sinusoidal joint angle references ($\theta_{n.ref}$) for both the proximal and distal joints to validate the performance of the hysteresis compensation control discussed above in Sections 6.4.1 and 6.4.2. For the reference trajectories, $\theta_{1.ref}$ was initially varied between $0°$ to $45°$ while $\theta_{2.ref}$ was held at $0°$. Next, $\theta_{2.ref}$ was varied while $\theta_{1.ref}$ was held at $0°$. Lastly, both $\theta_{1.ref}$ and $\theta_{2.ref}$ were varied simultaneously. For the control of the proximal joint, Case I and Case II were used in each trial. On the other hand, only Case I was used for the distal joint control since entire bending portion of the distal joint stays within the austenite phase of nitinol and does not experience any material induced hysteresis as discussed in Section 6.3.2.

In **Experiment 2** (see Fig. 6.12(b)), the kinematic-based control scheme [215] was used for both proximal and distal joints to validate the effectiveness of the force-based control. In the experiment, each joint followed the same joint reference trajectories used in Experiment 1; however, tendons were intentionally offset with 0.3 mm interval in each trial to simulate tendon slacking.

In **Experiment 3** (see Fig. 6.13), the same force control schemes used in Experiment 1 were employed, but the references had a variable amplitude to evaluate our decoupling design in various joint configurations. Detailed analysis of control performance for each experimental trial will be discussed in the next section.

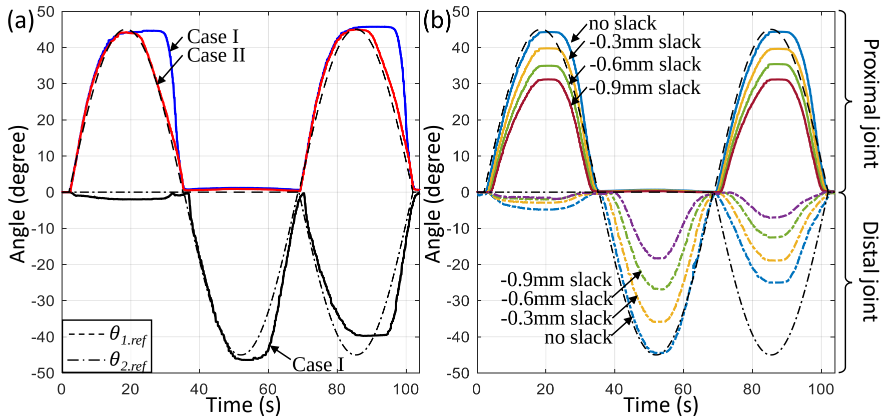

Figure 6.12: (a) Control experiment with the proposed force-based control schemes. (b) Control experiment with the kinematic- control scheme.

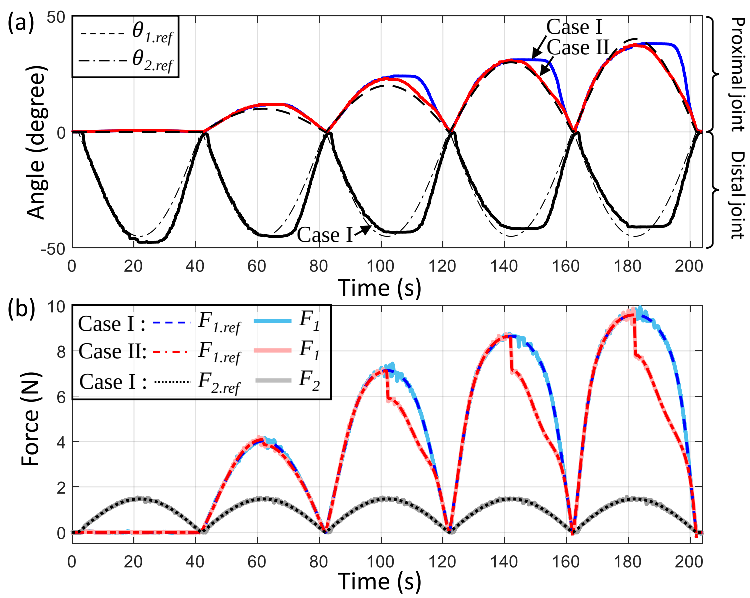

Figure 6.13: (a) Experiments on sinusoidal reference tracking for the proximal and distal joints with the proposed control algorithms. (b) Force references and corresponding measured forces generated by the proposed joint static model.

6.5 Results

Root mean square error (RMSE) of the reference tracking control results from the Experiments 1 and 2 are summarized in Table 6.2. From Experiment 1, we observed that in the case of the proximal joint, the model incorporating $S_{1.up}$ and $S_{1.down}$ performs the best (i.e., Case II in Section 6.4.2. see solid red line in Fig. 6.12(a)). $S_1(\theta_{ref})$ provides an $F_{1.ref}$ profile considering both loading/unloading cases and compensates most of the hysteresis, resulting in consistent control performance. The basic model including only $S_{1.up}$ (i.e., Case I. see solid blue line in Fig. 6.12(a)) performs the worst since the model completely fails to follow the reference trajectory during the unloading phase. This indicates that a hysteresis based model is critical for any control to be performed on a UAN joint. In the case of the distal joint, Case I (solid black line in Fig. 6.12(a)) shows a reasonable tracking performance in the loading phase, however, the error increases in the unloading phase although the distal joint is assumed not to have hysteresis (as discussed in Section 6.3.2). We believe that this error is caused by unmodeled friction factors in the unloading phase since the current friction model does not consider any Coulomb friction model at each bending angle of each joint. Additionally, the force-angle relationship of the distal joint is more sensitive than that of the proximal joint due to its low stiffness. For better control performance, a more precise friction model will be investigated in our future work. Additionally, there is almost no coupling between the two joints ($< 2°$). When the distal and proximal joints are moved simultaneously, the distal joint showed a slight increase of error due to the curved shape of the proximal joint increasing the friction. However, the RMSE is much smaller than using kinematic control (see Fig. 6.12(b) and Table 6.2), since force control is ideally not affected by kinematic changes. The result of Experiment 2 (see Fig. 6.12(b)) shows that even a small amount of displacement offset (<1 mm) causes a large error, which implies that sub-millimeter tendon slacking potentially caused by mechanical connections, wear, and gear backlash may result in extremely poor control performance. The slack sig-

Table 6.2: RMSE of the joint angles depending on the control schemes.

Force-based control			**Kinematic-based control**		
Condition	Bending joint		Condition	Bending joint	
	Proximal	Distal		Proximal	Distal
Case I	7.48°	4.34°	No slack	3.00°	8.68°
Case II	1.87°	-	-0.3mm slack	3.85°	12.33°
-	-	-	-0.6mm slack	6.34°	16.62°
-	-	-	-0.9mm slack	8.77°	20.16°

nificantly increases when the two joints move simultaneously since the path of the distal tendon slightly changes. This slacking problem is critical for pure kinematic control and force-based control is free from this issue. From Experiment 3 (see Fig. 6.13(a)), it is observed that the distal joint tracks its reference trajectory with small error under various conditions of the proximal joint angle. Fig. 6.13(b) shows the force references and the corresponding measured tendon forces for the proximal and distal joints with the control schemes of Case I and Case II. Finally, we believe that the kinematic-based joint control is simple and easy to implement, but does not provide a reliable control performance in highly coupled systems. The proposed model-based force control can provide an alternative way to implement precise joint control, avoiding problems caused by hysteresis, tendon slacking, and inter-joint coupling.

6.6 Conclusions

In summary, this chapter describes the modeling and control of a 2-DoF meso-scale steerable robotic instrument body with an OD of 1.93 mm that may be used as a tool for a commercially available neuroendoscope. The instrument makes use of two sub-types of tendon-driven bending flexure joints and uses their bending properties to achieve controllable joint-space motion while minimizing inter-joint coupling by design. The proximal joint of the robotic tool demonstrates hysteresis in the relationship between its joint angle and the applied tendon tension. We model the entire static model for this joint, including loading/unloading hysteresis. We conclude that this model of the joint, coupled with a disturbance observer-based controller is successfully capable of tracking varying types of reference joint angle trajectories.

6.7 Acknowledgements

The author would like to thank Dr. Seokhwan Jeong and Mr. Kent Yamamoto for part of the contents of this chapter.

CHAPTER 7

FORCE SENSING FOR TENDON-DRIVEN ROBOTS

7.1 Introduction and Motivation

Over the last several decades, the field of robotics has seen rapid improvements in novel actuation, transmission mechanisms, and control algorithms [222]. At the same time, compact and high precision force and displacement sensors have became essential to implementing precise and dexterous feedback control performance [222, 223, 224]. In particular, robotic hands [225, 226, 227, 228, 229, 149, 148] and medical devices [143, 144, 230, 231] such as robotically steerable handheld endoscopic tools [232] require high precision force sensors with miniaturized dimensions depending on their actuation/transmission mechanisms in a compact form factor. However, the cost of these sensors drastically increases as the dimensions of the sensor are miniaturized, increasing the cost of the total system.

In this chapter, we propose a new design of an optics-based dual-screen type sensor providing: 1) a wide range of highly linear output and 2) a reliable output robust to external disturbances and manufacturing errors in a cost-effective and compact package. A novel model of the optical relationship between the emitter and the receiver, which has not been derived in previous research, is proposed and used for the design process. A new sensor design and signal acquisition mechanism are introduced to increase the linearity and compensate the disturbances caused by both the LED and the ambient environment.

This chapter is organized as follows: In Section 7.2, the optical model of the screen-type sensor is introduced. A new sensor design to increase the linear range of the output is presented in Section 7.3. A signal acquisition mechanism and corresponding electric circuit to decrease external disturbances are presented in Section 7.4. An implementation of the proposed sensor mechanism is introduced in Section 7.5 and discussion and conclusion is

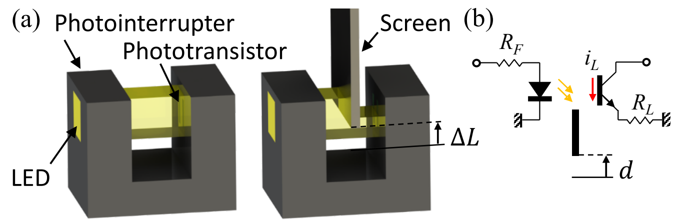

Figure 7.1: (a) Simplified illustration of PT-based force/position sensing mechanism. (b) Electrical circuit demonstrates the relationship between d and i_L.

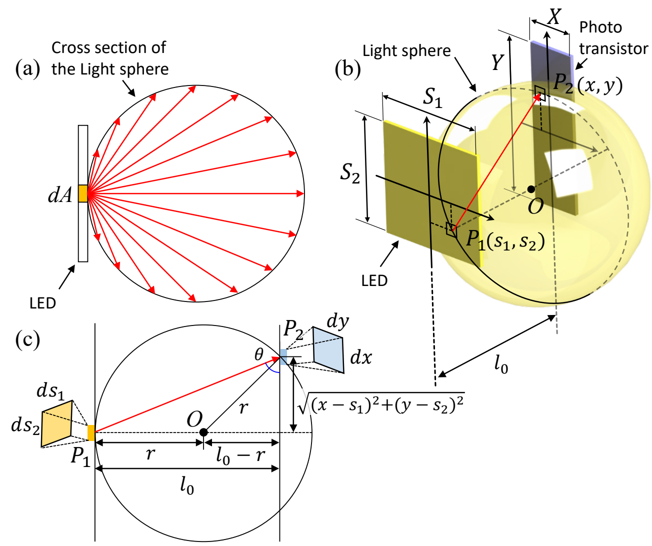

Figure 7.2: (a) Lambertian distribution of light assumes constant radiant intensity I on a sphere emitted from infinitesimal LED area dA, (b) Optical relationship between the LED and PT surfaces in 3D, (c) 2D slice of the plane consisting of points P_1, P_2, and O indicates geometric relationships between emitting and receiving areas.

provided in Section 7.6.

7.2 Modeling

7.2.1 Modeling of the Photointerrupter

In this section, models of the geometric and optical characteristics of photointerrupter are presented prior to the sensor design. To implement the screen-type sensor, a conventional photointerrupter module consisting of an LED and a phototransistor (PT) has been used (see Fig. 7.1(a)). In the module, the LED and the PT are facing each other, and one screen is placed between them. The light (i.e., photons) emitted from the LED strikes the base of

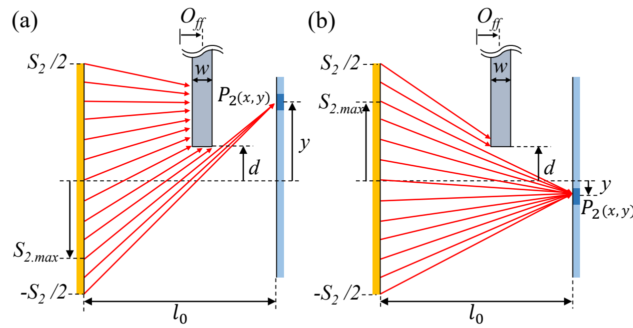

Figure 7.3: Path of the incident light entering the infinitesimal area on the PT and change of $S_{2.max}$ when (a) $y \geq d$ and (b) $y < d$. The screen has width, w, and is placed at a vertical distance, d, away from the horizontal centerline and has an offset, O_{ff}, from the vertical centerline.

the PT causing an electric current, i_L, to pass through the PT (see Fig. 7.1(b)). If the screen blocks a portion of the light path, it decreases the total amount of the radiant flux entering the PT, Φ_{tran}. As a result, the vertical displacement of the screen, d, changes i_L. The vertical displacement, d, can be indirectly estimated by measuring the voltage applied to the resistor R_L since Φ_{tran} is linearly proportional to i_L. This principle has been employed in the optics-based displacement sensors or force sensors [132, 133, 134, 135, 136, 137] to implement a compact and cost-effective sensing mechanism. However, the relationship between d and Φ_{tran} has not been explored through detailed modeling and has been assumed to be linear. This simplifying assumption may increase the nonlinearity of the sensor output and thereby lead to decrease in the accuracy of the sensor. Therefore, detailed optical and geometric relationships have to be analyzed for reliable sensor performance.

In this work, a single LED is not approximated as a point source of light with a spherical light distribution, but rather a lambertian distribution [233]. In a lambertian distribution, the photons are emitted from the infinitesimally small area dA on the surface of the LED and the radiant intensity, I, is uniform on the surface of the light sphere in the direction of incidence of light (see Fig. 7.2(a)).

Fig. 7.2(b) shows the optical and geometric relationship between the LED and the PT. On the surface of the LED, the photons are emitted from the infinitesimally small area located at P_1 and enter the infinitesimally small area located at P_2 on the PT side; P_1 and P_2 have (s_1, s_2) and (x, y) coordinates on 2-D plane of each surface, respectively. Fig. 7.2(c) represents a geometric relationship of the incident light path on the 2-D plane including P_1, P_2, and the origin of the light sphere O. Then, the radiant intensity I normal to area P_2 is expressed as follows:

$$
\begin{aligned}
I(s_1, s_2, x, y) &= \frac{\Phi_{Total}}{4\pi r^2} sin(\theta) && (7.1)\\
&= \frac{\Phi_{Total}}{4\pi \left(\frac{l_0^2+(x-s_1)^2+(y-s_2)^2}{2l_0}\right)^2} sin(\theta) && (7.2)
\end{aligned}
$$

where Φ_{Total} is the total radiant flux on the spherical surface of the light emitted by infinitesimal area dA, r is radius of the light sphere, and l_0 is the distance between the LED and the PT (see Fig. 7.2(c)).

From the geometric relationship, Φ_{tran} can be derived as an integral of the area of the LED and the PT and is given by:

$$
\Phi_{tran} = \int_{A_2} \int_{A_1} I(s_1, s_2, x, y)\, dA_1\, dA_2 \tag{7.3}
$$

$$
\begin{aligned}
A_1 &= \{(s_1, s_2) | -S_1/2 \leq s_1 \leq S_1/2, -S_2/2 \leq s_2 \leq S_2/2\}\\
A_2 &= \{(x, y) | -X/2 \leq x \leq X/2, -Y/2 \leq y \leq Y/2\}
\end{aligned}
$$

Here S_1 and S_2, and X and Y are the widths and heights of the LED and the PT respectively.

To implement the screen-type optical sensor, a screen is placed between the LED and PT (see Fig. 7.3). The screen has a width, w, and is located a vertical distance, d away from the horizontal centerline and has an offset, O_{ff}, from the vertical centerline middle of the LED and PT. This screen should be made of metal or covered with thin metal foil to completely block the incident LED light. In Fig. 7.3, the screen blocks the path of the

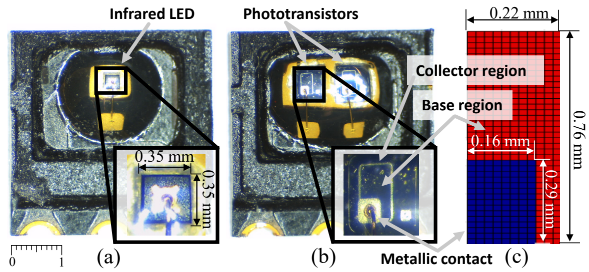

Figure 7.4: (a) Microscopic image of (a) the LED and (b) the PTs embedded in the PT module (EE-SX1321, OMRON). (c) The estimated base area of the PT based on both microscopic observation and the data driven approach.

light, resulting in change of the maximum bound, $S_{2.max}$, of the integral area on the LED surface A_1. Therefore, we can redefine the effective integral area based on the geometrical relationship in Fig. 7.3 as follows:

$$A_1 = \{(s_1, s_2)| - S_1/2 \leq s_1 \leq S_1/2, -S_2/2 \leq s_2 \leq S_{2.max}\} \tag{7.4}$$

where $S_{2.max}$ is defined as follows:

$$S_{2.max} = \begin{cases} \frac{y(l_0+w+2O_{ff})-2l_0d}{w-l_0+2O_{ff}} & \text{if } y \geq d \\ \frac{y(l_0-w+2O_{ff})-2l_0d}{-w-l_0+2O_{ff}} & \text{if } y < d \end{cases} \tag{7.5}$$

Note, the light path has different boundary condition depending on the relative position of y and d (see Fig. 7.3(a) and (b)). As a result, the geometrical parameters change the integration area A_1, resulting in change of Φ_{trans} (see Eq. (7.3)). A simulation and experiment for the derived model will be introduced in following section.

7.2.2 Simulation and Experiment

To verify the proposed model, geometric parameters of the PT module were measured and simulated with the derived model. Figs. 7.4(a) and (b) show microscopic images of the infrared LED and the PTs, respectively, that is present in the photointerrupter module (EE-SX1321, OMRON). The dimension of the LED was measured at 0.35 mm x 0.35 mm from

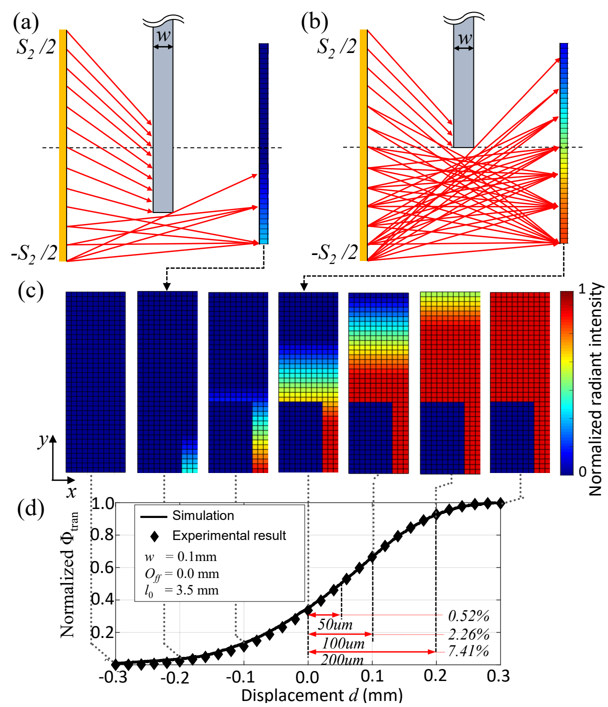

Figure 7.5: (a) As the screen is lowered, almost no light reaches the receiver surface, (b) As the screen is raised, the amount of light reaching the PT base increases, (c) Normalized intensity received at several discrete values of screen height, d, and (d) Experimental data for single screen-type optical setup validates our model.

the microscopic image (S6D, Leica, Germany) with 6 μm resolution, while the base region of the PTs do not have an exact rectangular shape due to the metallic contact node at the junction of the emitter region (see Fig. 7.4(b)). The effective base area (see Fig. 7.4(c)) is estimated based on both microscopic observation (see Fig. 7.4(b)) and a data driven approach. The derived model with the measured geometric parameters was compared with experimental results (see Fig. 7.5). Detailed experimental setup will be described in Section 7.3.3. Fig. 7.5(a) and (b) show a typical geometric arrangement of the screen-type optical sensor. It shows the path of the incident light between the LED and PT, resulting in different radiant intensity, I, according to screen position, d, on the surface of the PT (see Fig. 7.5(c)). The color of the surface represents a relative amount of I on a unit area of the PT, which is simulated from the derived model at $w = 0.1$ mm, $O_{ff} = 0$ mm, and $l_0 = 3.5$ mm. Therefore, Φ_{trans} can be obtained by Eq. (7.3).

Fig. 7.5(d) shows normalized Φ_{trans} from the simulation and the experimental result with the same geometric condition. They match with R^2-value of 0.9989, which implies that the derived optic model exactly represents the nature of the mechanism. The area of the metallic contact node is excluded from the integration of radiant intensity, I, and hence results in a slight offset and asymmetry of the output, which is also represented by the derived model and experimental result. The above illustrates that our derived model closely mimics the optical and geometric characteristics of a single LED and PT-based screen-type sensor. Using this derived model, a new sensor design will be introduced in next section.

7.3 Design of the Sensor

As shown in Fig. 7.5(d), the output of the sensor has a very narrow high linear range (< 50 μm). The narrow linear range may decrease the signal-to-noise ratio and resolution of the sensor, thereby making it difficult to implement a small size force sensor requiring a large deformation displacement due to low stiffness. Furthermore, precise positioning of

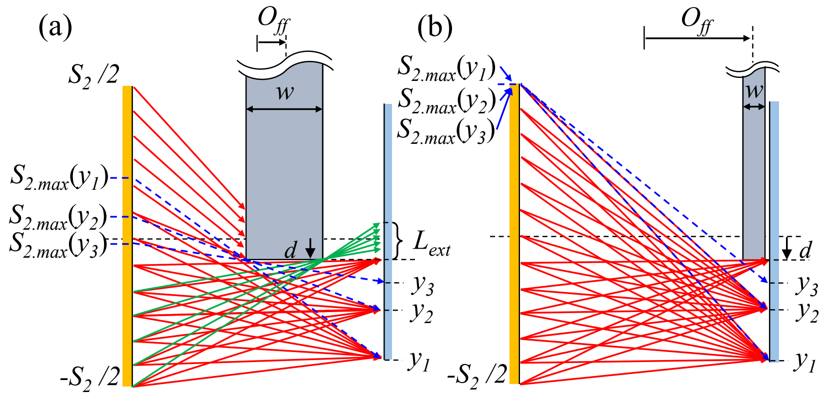

Figure 7.6: (a) For lower values of O_{ff} and higher values of screen width, w, $S_{2,max}(y)$ and L_{ext} are sources of nonlinearity; (b) By maximizing O_{ff} and minimizing w, we can reduce both sources.

the screen in this linear range is extremely difficult during manual assembly of the sensor, given the size of the sensor. Machining error and misalignment during assembly may disturb the precise screen positioning, which eventually decreases the linearity of the sensor and this was identified as a limitation in prior work [137, 135]. In this section, several design parameters are investigated to find an optimal arrangement of the sensor assembly to increase the linear range. It will be verified with the derived model and corresponding experiments.

7.3.1 Arrangement of the screen

In the screen-type sensing mechanism, the fundamental assumption is that d linearly changes the exposed area of the PT, which finally causes a linear variation in Φ_{tran}. Therefore, Φ_{tran} becomes linearly proportional to d. However, the light is not emitted from the LED as a straight line as discussed earlier, which increases nonlinearity in the conventional screen-type sensor. In Fig. 7.6(a), the blue arrows represent $S_{2.max}$ (defined in Eq. (7.5)) for each y, and it changes significantly with d, *i.e.*, each unit area of PT at y (i.e., P_2 in Fig. 7.2(c)) does not have a constant integration area A_1. Furthermore, small amount of the light enters the PT surface over d (see the green line in Fig. 7.6(a), denoted as L_{ext}), resulting in additional increase of the sensor output. Therefore, $S_{2.max}$ and L_{ext} are considered as nonlinear

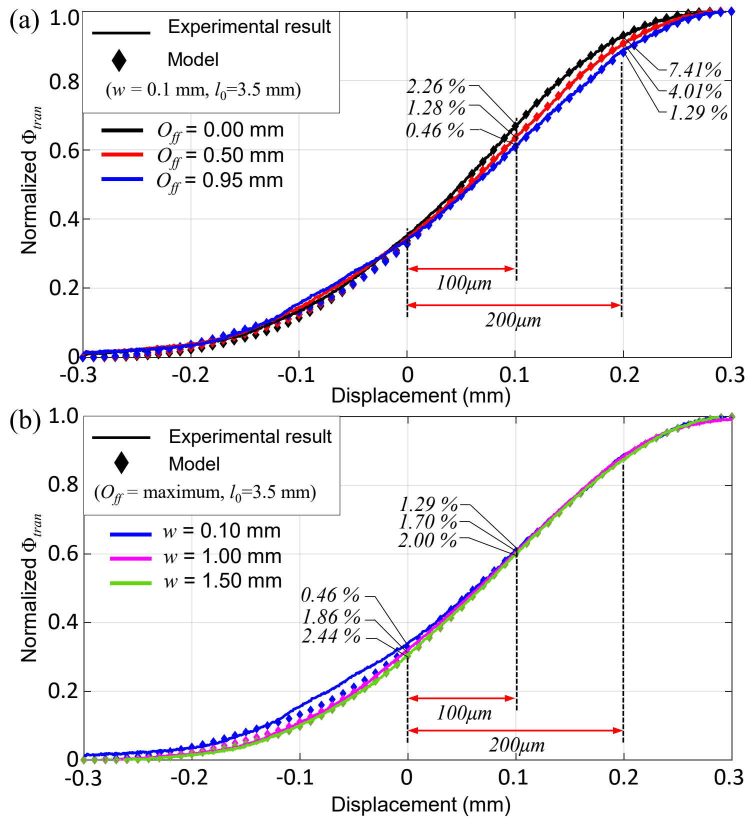

Figure 7.7: The experimental results of the normalized Φ_{tran} in a single-screen sensor and the results of corresponding model when (a) the screen-offset, O_{ff} is set to be variable, and (b) screen width, w is set to be variable.

factors and must be constant and minimized, respectively, to increase the linearity between d and Φ_{tran}. Based on parametric study of the derived optical model in previous chapter, we found that O_{ff} and w are dominant variables to compensate the aforementioned nonlinear factors. Several simulations with O_{ff} and w were conducted and compared with experimental data.

Figs. 7.7(a) and (b) show simulation and experimental result when O_{ff} is set to be variable at $w = 0.1$ mm and w is set to be variable at maximum O_{ff}, respectively. The simulation and corresponding experimental results show same tendency, indicating that the nonlinearity of the output decreases as O_{ff} increases and w decreases; when $w = 0.1$ mm and $O_{ff} = 0.95$ mm, nonlinearity of the output decreases to 1.29% from 7.41% in range of 200 μm, and decreases to 0.46% from 2.26% in range of 100 μm. Therefore, the screen should be close to the PT side as much as possible by maximizing O_{ff}, and then w should be minimized, which decreases L_{ext} and makes $S_{2.max}$ have a near constant value for majority of the range of y (see Fig. 7.5(b)).

Thus, we can reduce the nonlinear factors and increase the linearity of the sensor by considering the derived optical model, while previous research has not explored the detailed sensor design based on the optical model.

7.3.2 Dual-screen arrangement

Although the proposed screen arrangement shows high linear output (see Fig. 7.7), the linearity is still sensitive and largely affected by the range of the screen displacement. For example, the linearity significantly decreases if the screen is not precisely placed at the middle of the PT. In this section, a novel dual-screen arrangement is presented to increase the linear range of the proposed sensing mechanism in the presence of assembly errors resulting from misalignment of the screen placement.

As shown in Fig. 7.8(a), an additional screen is added to the existing screen arrangement (i.e., single-screen), and the two screens together (which is called 'dual-screen' setup)

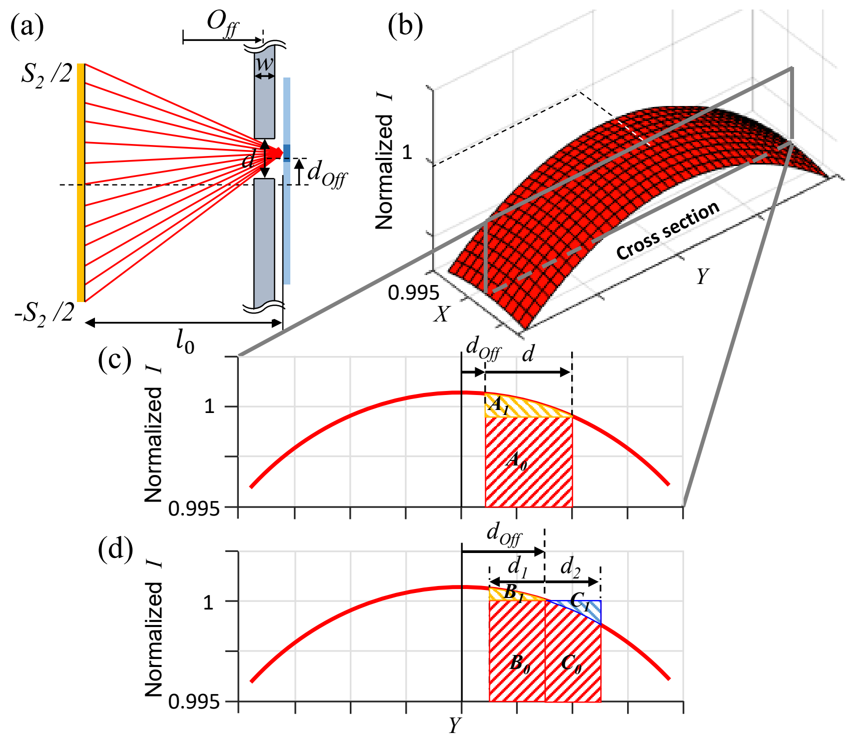

Figure 7.8: (a) Novel dual-screen arrangement uses two screens and displacement, d, is the distance between screens, while d_{Off} represents assembly errors; (b) Normalized radiant intensity, I, over the entire PT area has a nonlinear curved distribution. Normalized I w.r.t. Y-axis on the 2-D plane for (c) the single-screen arrangement and (d) the dual-screen arrangement.

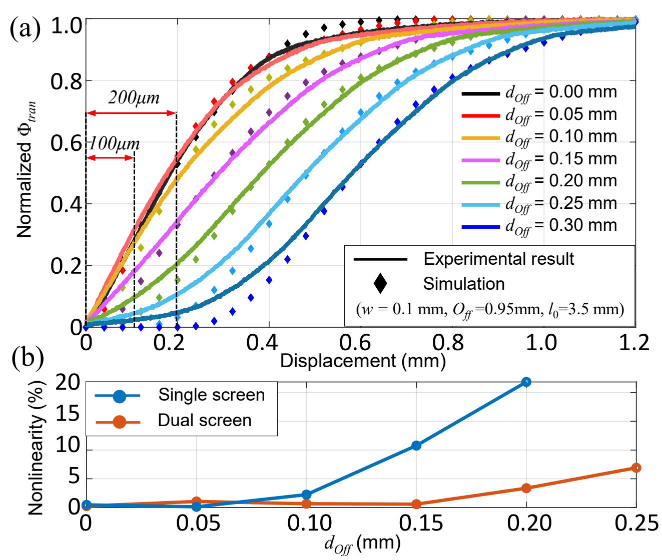

Figure 7.9: (a) Normalized Φ_{tran} received by the dual-screen setup for various values of d_{Off} shows high linearity; (b) Dual-screen can achieve lower nonlinearity than that of the single-screen in wide range of d_{Off}.

perform the same function of blocking the path of the light. The relative gap between the screens therefore represents the displacement d, and d_{Off} represents the offset of the screen from the center-line of the sensor. d_{Off} may represent errors in assembling the sensor, which may result in the screens not meeting exactly at the center of the PT. In the single-screen setup, this d_{Off} represents any assembly errors that would result in the screen not being exactly placed in the middle of the PT.

This dual-screen arrangement can increase the linearity and the linear range of the sensor output (see Fig. 7.8(b)-(d)). Fig 7.8(b) shows normalized radiant intensity, I, on the surface of the PT (except the metallic contact area in Fig. 7.4(c)) and the distribution of I has a curved surface due to the optical relationship between the LED and the PT. Fig. 7.8(c) shows a cross-section of this curved surface, and the area under the curve (hatched area in Fig. 7.8(c)), which depends on varying d, is proportional to the output of the single-screen. Due to the curved surface, this area includes A_1 in addition to the linear portion A_0, which increases nonlinearity of the output. The proposed dual-screen arrangement can compensate this nonlinear area as shown in Fig. 7.8(d). When the upper and lower screen are displaced by d_1 and d_2 respectively, corresponding nonlinear areas B_1 and C_1 (yellow and blue hatched area in Fig. 7.8(d)) are compensated by each other. Therefore, the output of the dual-screen arrangement would result in a smaller nonlinearity than that of the single-screen.

To verify our hypothesis, the dual-screen arrangement was implemented with the experimental setup (see Fig. 7.10, presented in Section 7.3.3) at $w = 0.1$ mm and $O_{ff} = 0.95$ mm. The simulation and the corresponding experiment results (see Fig. 7.9(a)) show normalized Φ_{tran} of the sensor with various d_{Off}. Fig. 7.9(b) represents the nonlinearity of single-screen and dual-screen setups (over a 100 μm range) over increasing values of d_{Off} and it shows that the dual-screen has lower nonlinearity than that of the single-screen over the entire feasible range of d_{Off}. Therefore, high linearity over a higher range of d_{Off} can be achieved with rearrangement of the screen position and dual-screen configuration.

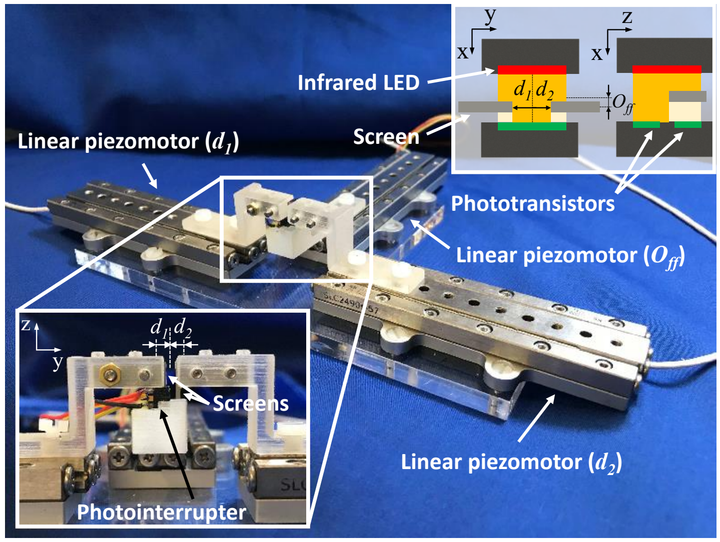

Figure 7.10: Experimental setup. Three piezomotor based assembly to mimic the single/dual screen arrangements allows for fine control of each screen and variations in screen offsets.

7.3.3 Experimental Setup

To measure output of the sensor, an experimental setup was implemented with three linear piezomotors (SmarAct GmbH, Oldenburg, Germany) (see Fig. 7.10). The piezomotors operate with a 0.7 μm position interval and approximately 10 nm encoder resolution. Two of the piezomotors face each other and move linearly along a common axis, while the third piezomotor is mounted such that its linear track moves perpendicular to this axis. Two screens may be connected to the two piezomotors that face each other, allowing us to adjust the gap between the screens to mimic the dual-screen setup introduced above. The photointerrupter module is placed on the third pieozomotor and it adjusts O_{ff}. The sensor outputs were measured with analog to digital conversion of the data acquisition board (Model 826, Sensoray, Portland, United States).

7.4 Disturbance Compensation Algorithm

In the previous section, we discussed increasing the linear range of the single-screen setup by modifying the screen placement (by optimizing w and O_{ff} values) and introducing a

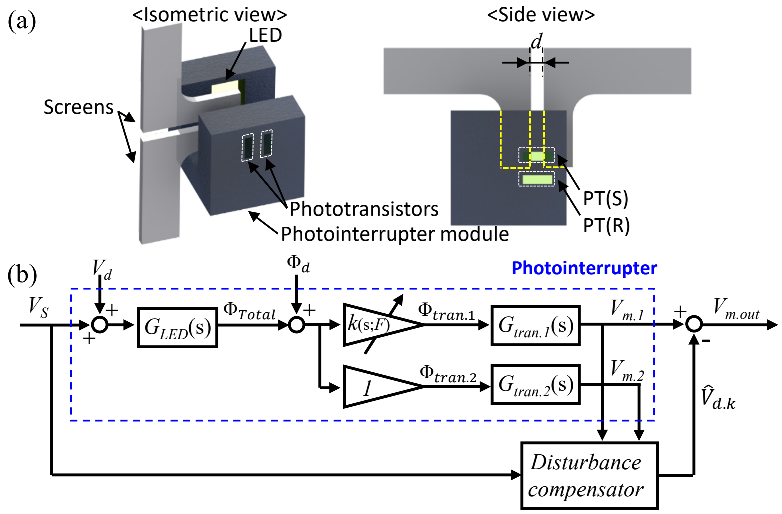

Figure 7.11: (a) Proposed novel dual-screen setup with dual PT module; (b) Block diagram of the proposed signal acquisition mechanism including dual-PT to compensate the external disturbances.

novel dual-screen arrangement to maximize the linear range in the presence of assembly errors. However, the proposed sensing mechanism still entirely relies on the light emitted from the LED. Therefore, change of temperature, ambient light around the sensor, and electric noise significantly affect the efficiency and output of the LED, which disturbs the sensor output which is a common problem in optics-based sensors [136, 137, 134, 135]. In this section, a novel dual-PT signal acquisition mechanism is presented to reduce these disturbances, and the corresponding electric circuit will be introduced.

7.4.1 Dual-phototransistor Setup

To compensate the disturbances from the external environment, we employed a dual-PT assembly as a signal acquisition mechanism as shown in Fig. 7.11(a). It consists of one infrared LED as a light emitter and two PTs as light receivers in a single photointerrupter module (EE-SX1321, OMRON). The first PT (see PT(S) in Fig. 7.11(a)) measures change of incident light passing through the screens, while the second one (see PT(R)) measures total amount of light emitted from the LED without the screens. Each acquired signal is used as an output and reference, respectively, and their common noise can be compensated.

The corresponding system block diagram can be represented as Fig. 7.11(b) (blue dotted box). V_S is a supply voltage to the LED and V_d is a voltage disturbance from the electric noise. Φ_{Total} is the total light flux emitted from the LED, and Φ_d is disturbance caused by light flux from the external light source and degradation of the LED efficiency. $\Phi_{tran.1}$ and $\Phi_{tran.2}$ represent light flux entering the first and second PTs, respectively. $k(s;F)$ is transfer function between Φ_{total} and $\Phi_{tran.1}$, which is resulted from the light blocking of the screen and is function of applied force, F. $V_{m.1}$ and $V_{m.2}$ are the output voltages of the PTs (i.e., PT(S) and PT(R), respectively). $G_{LED}(s)$, $G_{tran.1}(s)$ and $G_{tran.2}(s)$ are transfer functions of the LED and each of the PTs, respectively. To simplify the model, we can assume that this disturbance in flux, Φ_d, manifests itself within the term, V_d. Thus, the noise from electric and light sources is expressed as a single disturbance variable, V_d, and it is included in the sensor outputs $V_{m.1}$ and $V_{m.2}$ in the form of noise. If the noise can be observed and compensated from $V_{m.1}$, we can, in theory, achieve pure sensor output only affected by F. The estimated disturbance voltage, $\hat{V}_d$, and dual-screen transfer function, $\hat{k}(s;F)$, can be estimated from the sensor outputs as follows:

$$\hat{V}_d = V_{m.2}{G_{tran.2}}^{-1}{G_{LED}}^{-1} - V_S \tag{7.6}$$

$$\hat{k} = \frac{V_{m.1}}{V_{m.2}}\frac{{G_{tran.1}}^{-1}}{{G_{tran.2}}^{-1}} \tag{7.7}$$

Then, assuming that $G_{tran.1}$ and $G_{tran.2}$ are identical as G_{tran}, an estimate of the noise caused by external disturbances, $V_{d.k}$, is given as follows:

$$\hat{V}_{d.k} = \hat{V}_d\hat{k}G_{LED}G_{tran.1} = V_{m.1} - V_S G_{LED} G_{tran}\frac{V_{m.1}}{V_{m.2}} \tag{7.8}$$

Finally, $\hat{V}_{d.k}$ is calculated in the disturbance compensator block (see Fig. 7.11(b)) and subtracted from $V_{m.1}$ resulting in noise compensated sensor output, $V_{m.out}$, which is expressed

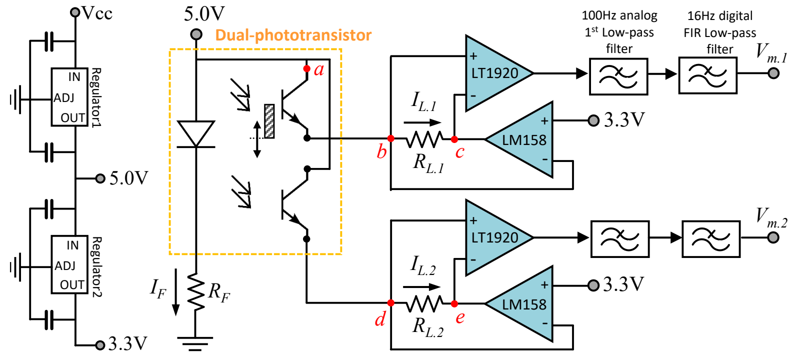

Figure 7.12: Schematic of dual-PT signal processing circuit. An operational amplifier regulates collector-emitter voltages for both transistors, while instrumentation amplifies the voltage drop across $R_{L.1}$ and $R_{L.2}$.

as follows:

$$V_{m.out} = V_{m.1} - \hat{V}_{d.k} = V_S G_{LED} G_{tran} \frac{V_{m.1}}{V_{m.2}} \tag{7.9}$$

Experimental results with the proposed dual-transistor setup will be presented in the following section 7.4.3.

7.4.2 Electric circuit

The current output of the photointerrupter has a high linear relationship with, Φ_{tran} when the collector-emitter voltage of the PT V_{CE} has constant value. To satisfy this condition, an electric circuit was designed as shown in Fig. 7.12. The current of the LED is limited to I_F by the resistor, R_F. When a 5 V supply is provided to the photointerrupter, operational-amplifiers (LM158 in Fig. 7.12), added to each output of the PTs maintain the voltage of point b and d at 3.3 V, which always keeps the voltages applied to each PT constant as 1.7 V (i.e., voltage between a and b, and a and d. 5 V-3.3 V=1.7 V) in a negative-feedback manner. Therefore, the current passing through each PT, $I_{L.1}$ and $I_{L.2}$ become linearly proportional to $\Phi_{tran.1}$ and $\Phi_{tran.2}$, respectively, and they are estimated with instrumental-amplifiers by measuring the voltage difference across resistors $R_{L.1}$ and $R_{L.2}$, respectively.

In the signal acquisition, first-order analog low-pass filters with 100 Hz cut-off are used

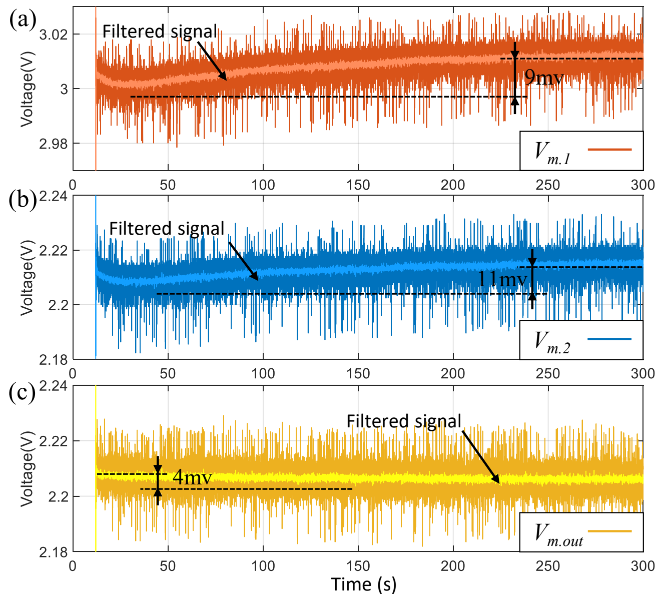

Figure 7.13: Output signals of the dual-PT circuit at constant room-temperature : (a) $V_{m.1}$; (b) $V_{m.2}$; (c) $V_{m.out}$

for anti-aliasing and their outputs were acquired by the data acquisition board (NI 6321, National Instruments) in digital form. Lastly, finite impulse response digital filters with 16 Hz cut-off are used for noise reduction and produce final outputs ($V_{m.1}$ and $V_{m.2}$ in Fig. 7.12)

7.4.3 Experimental results

To verify the performance of the disturbance compensator and the electric circuit, the experimental setup (see Fig. 7.10) was used with the dual-photointerrupter system and corresponding electric circuit. The first PT was fully open and the second one was partially closed by the screens using the final assembly shown in Fig. 7.15(a).

Fig. 7.13 shows experimental result of $V_{m.1}$, $V_{m.2}$ and compensated output $V_{m.out}$ in no load condition for 300 seconds. It is observed that both $V_{m.1}$ and $V_{m.2}$ are affected by common noise in a low frequency band (0-2 Hz), and there is a voltage overshoot immediately after V_S is applied to the sensor. On the other hand, $V_{m.out}$ was immediately stabilized without the overshoot and the noise. For the low-pass filtered signal with cut off frequency

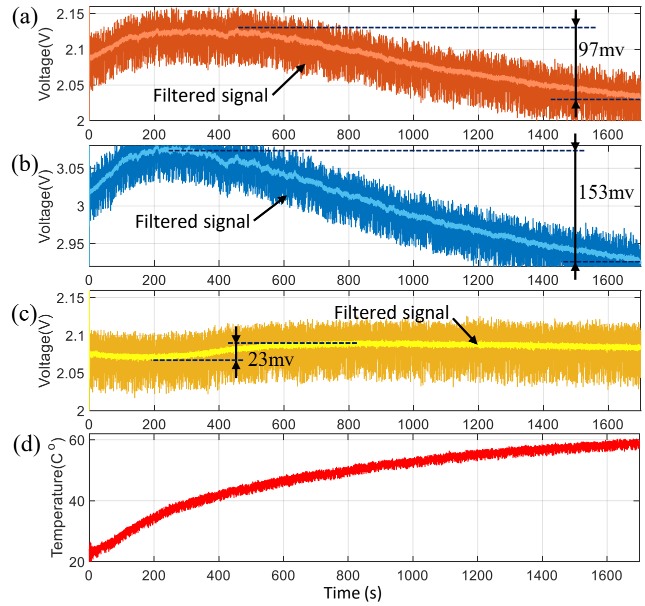

Figure 7.14: Output signals of the dual-PT circuit at varying ambient temperatures for: (a) $V_{m.1}$; (b) $V_{m.2}$; (c) $V_{m.out}$; (d) Variation of ambient temperature. $V_{m.out}$ shows relatively small variation to ambient temperature.

Table 7.1: Experimental results of the dual-PT

Experimental condition	**Items**	$V_{1.out}$	$V_{m.out}$
No load condition	Standard deviation	0.89mV	0.67mV
	Maximum deviation	9.0mV	4.0mV
No load condition with temperature variation	Standard deviation	11.5mV	4.5mV
	Maximum deviation	97mV	23mV

of 16 Hz (see Fig. 7.12), the standard deviation of the signal decreases to 0.67 mV from 0.89 mV, and the maximum deviation decreases to 4 mV from 9 mV, which eventually increases the resolution of the sensor output and provides stable feedback performance.

Fig. 7.14 shows the experimental results in no load condition with temperature variation. The entire experimental setup was installed in a forced convection oven and the ambient temperature was increased to 60°C from room temperature for 1700 seconds. $V_{m.1}$ and $V_{m.2}$ significantly fluctuate with temperature due to variation of the LED efficiency, while $V_{m.out}$ showed relatively small variation. For the low-pass filtered signal, the standard deviation of the signal decrease to 4.5 mV from 11.5 mV, and the maximum deviation decreases to 23 mV from 97 mV. In the two experiments, the proposed signal acquisition

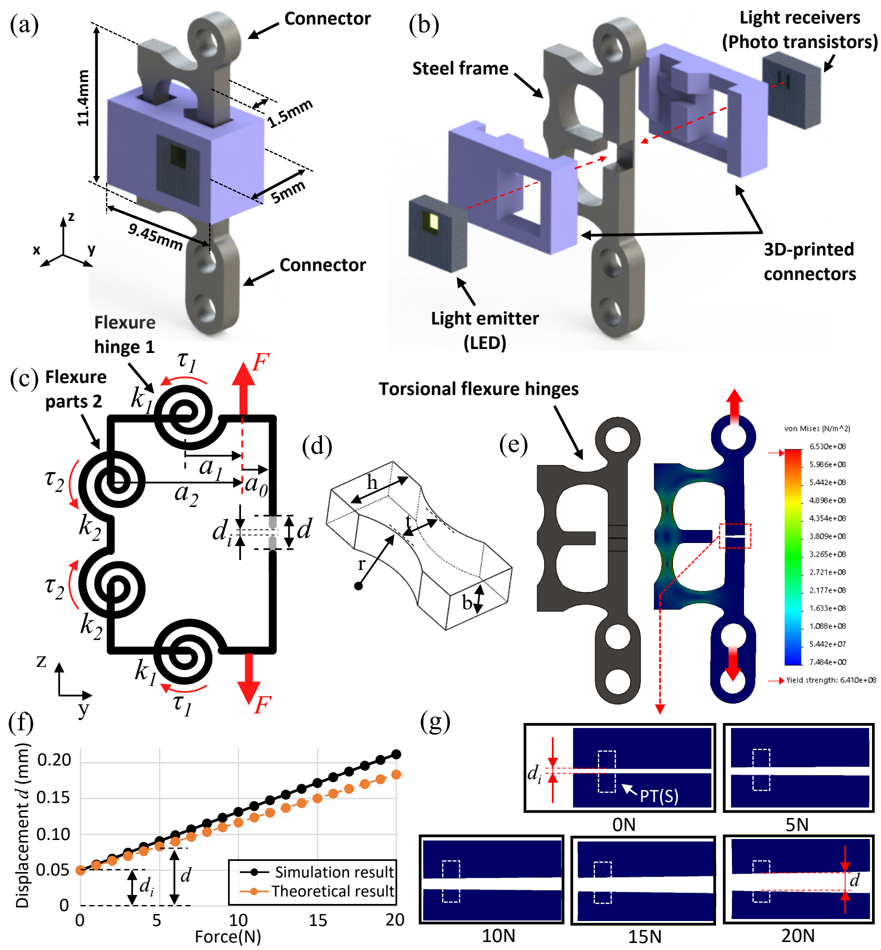

Figure 7.15: (a) Assembled dual-screen/dual-PT-based force sensor; (b) Exploded view of assembly; (c) Simplified torsional-spring model for steel frame (see Table 7.2 for details); (d) Schematic of the hinge joint. (e) FEM model of the steel frame (f) d-F graph from simulation and theoretical result; (g) Distance, d between the screens from the simulation.

mechanism including the compensator and the electric circuit effectively reduced the disturbances imposed on the sensor, which may increase the resolution of the output. The results are summarized in Table 7.1.

7.5 Implementation of the Force Sensor

7.5.1 Design of force sensor

To implement a force sensor with the proposed dual-screen and the dual-PT, the sensor was designed as shown in Fig. 7.15. The designed sensor consists of a steel frame (AISI4140),

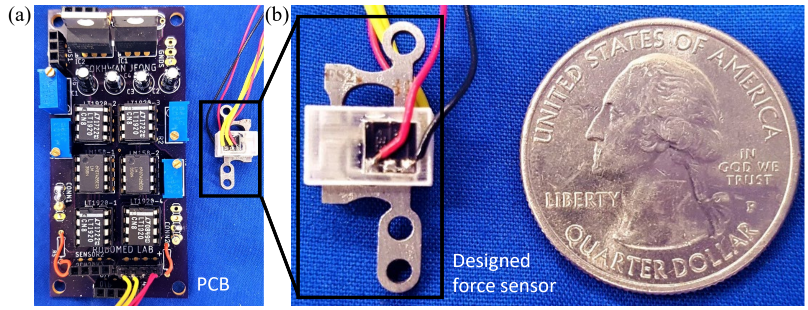

Figure 7.16: The entire dual-screen, dual-PT sensor assembly involves: (a) a signal processing circuit and (b) the steel frame with 3D-printed connectors holding the photointerrupter and screen setup.

3D-printed connectors, two screens and the photointerrupter having dual-PTs, and they are assembled in one module as shown in Figs. 7.15(a) and (b). The steel frame consists of four torsional flexure hinges and a thin slit in the middle of the frame. This slit blocks one of the two photo-transistors thereby implementing the dual-screen mechanism in the dual-PT assembly. The steel frame can be easily fabricated with electric discharge machining (EDM) or milling, since it has a simple 2D planar shape and the slit also can be formed with the EDM or laser micromachining. Finally, 3D-printed connectors are assembled on the steel frame with UV glue (ClearWeld Quick Setting Epoxy, J-B Weld).

Fig. 7.15(c) shows simplified schematic of the steel frame including torsional flexure hinges. When an external force, F, is applied to the frame, the hinge parts are deformed and that generates a gap between the screens, d. Then, the relationship between d and F is derived as follows (see Fig. 7.15(c)):

$$d = 2F\left[a_1(a_0 + a_1)/k_1 + a_2(a_0 + a_2)/k_2\right] + d_i \tag{7.10}$$

where k_1 and k_2 are torsional coefficients of the flexure parts 1 and 2, respectively. Terms a_1 and a_2 are the distances between each flexure part and the axis of the force, respectively; a_0 is distance between the axis and a position on the screen where PT(S) is located. d_i is an initial gap between the screens when the frame is undeflected and $F = 0$; Depending on direction of the applied force in various applications, the screen can be designed with different d_i, taking into consideration the linear range of the dual-screen array (e.g. Pure tensile force: $d_i \leq 50$ μm, pure compression force: $d_i \approx 200$ μm, and both tensile/compression force: $d_i \approx 100$ μm). It is assumed that the rotation angles of the flexure parts due to the external force, F, are negligible.

To implement the torsional flexure parts, a circular hinge design was employed, which can be modeled as a 1-degree of freedom rotational compliant joint. The torsional coefficient, k_n (n=1,2), is expressed as follows [234]:

$$k_n = 2Eb_n{t_n}^{5/2}/9\pi{r_n}^{1/2} \quad (n = 1, 2) \tag{7.11}$$

where E is Young's modulus of the steel frame and b_n, t_n and r_n are geometric parameters of each hinge (see Fig. 7.15(d)). For applications in micro-scale medical devices such as tendon-driven steerable surgical tools or guidewires [232], d_i was designed to 50μm for tension measurement and maximum allowable force was set to 20N. Using Eq. 7.10, 7.11 and finite element analysis (Solidworks 2018, Dassault Systems) (see Fig. 7.15(e) to (g)), the steel frame was designed so that d has 200 μm distance under the maximum allowable force (i.e., 20 N), which keeps the screen in the high-linearity range of the dual-screen setup (see Fig. 7.9(a)). Both simulation and theoretical result (see Fig. 7.15(f)) show that d has a high linearity (∼99.8%). Design parameters of the sensor are summarized in Table 7.2, and Fig. 7.16 shows an implemented force sensor and printed circuit board for the signal acquisition proposed in Section 7.4.

7.5.2 Experimental results

Due to the observed high linearity of the sensor, it can be calibrated with a reference force sensor (MDB-5, Transducer Techniques, California, United States) using a first order linear transformation. After that, the linearity and hysteresis of the force sensor were measured with a tensile loading and unloading test as shown in Fig. 7.17(a). The designed force

Table 7.2: Design parameters of the sensor

Items	Specification
Maximum allowable force (F)	21N
Maximum screen displacement (d)	200μm
Torsional coefficient (k)	9,019 mNm/rad
Dimension	11.4mm$\times$9.45mm$\times$5mm
Distance between elastic parts and the screen (a)	a_0 = -0.38mm a_1 = 2.5mm, a_2 = 5.25mm
Young's modulus of the frame (E)	205GPa
Hinge width (b)	$b_1 = b_2$ = 1.5mm
Hinge thickness (t)	t_1 = 0.9mm t_2 = 0.85mm
Hinge cutting radius (r)	r_1 = 3.06mm r_2 = 2.5mm

Table 7.3: Performance of the force sensors

Screen type		Items				
		Volume	Non-linearity	Hysteresis	Accuracy	Repeat-ability
Dual-screen		0.54 cm^3	1.08 %	0.83 %	99.58 %	99.85 %
Single-screen	[134]	2.06 cm^3	-	1.48 %	99.48 %	99.91 %
	[137]	0.24 cm^3	1.85 %	1.19 %	96.15 %	-
	[149]	39.6 cm^3	1.11 %	0.84 %	97.65 %	-

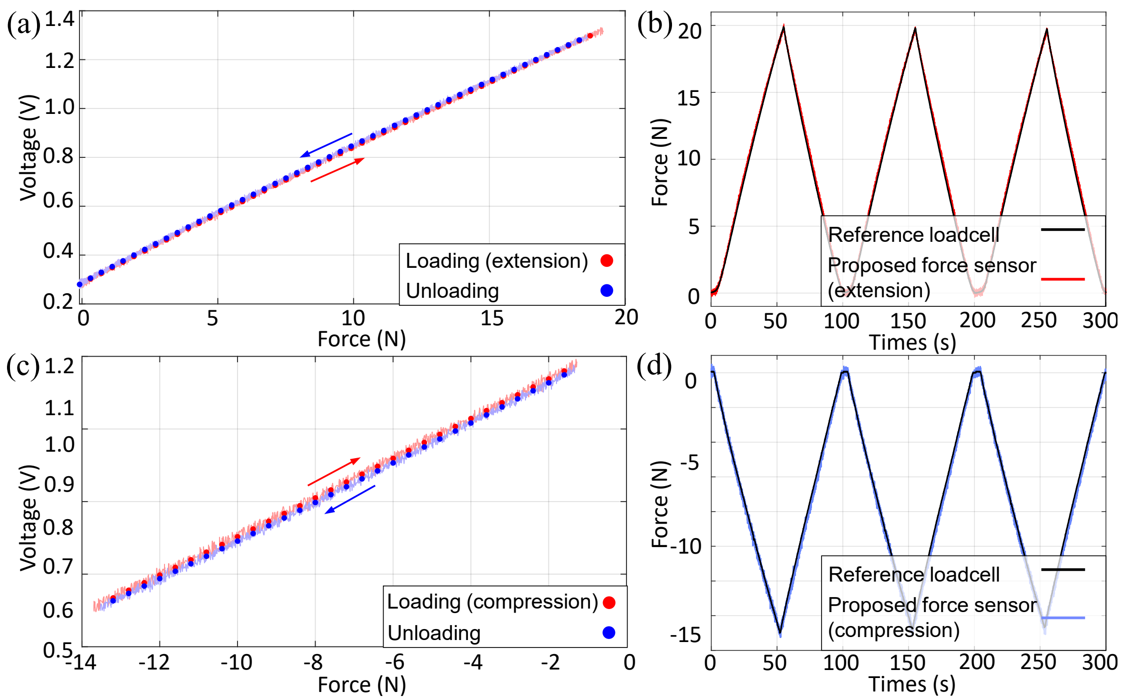

Figure 7.17: (a) Tensile loading/unloading experiment for identification of linearity and hysteresis and (b) Triangular wave signals from the proposed force sensor and the reference load cell; (c)-(d) Same experimental results for compressive loading/unloading condition.

sensor was serially connected to the reference force sensor and a linear actuator (Maxon Precision Motors, MA, United States), and an axial force was applied to the both sensors by actuating the linear motor. Based on the loading/unloading test, the output of the designed sensor was calibrated with a first order least square linear fitting. To measure its repeatability, the loading/unloading test was repeated 30 times under same experimental setup with 0.04 Hz. The experimental test shows 1.08% nonlinearity, 0.83% hysteresis and 99.58% accuracy (refer to [134] for the definitions of these terms). Considering its compact dimension, the proposed sensor shows the most effective performance compared to that of the miniaturized single-screen type force sensors in previous studies (see Table 7.3). Furthermore, such high sensor performances can be maintained over a wide range of assembly errors in the form of d_{Off} (see Fig. 7.9(b)) while external noises are reduced by the disturbance compensator. Fig. 7.17(b) shows triangular signals from the designed sensor and reference sensor, respectively, and they exactly match with R^2-value of 0.9958. The

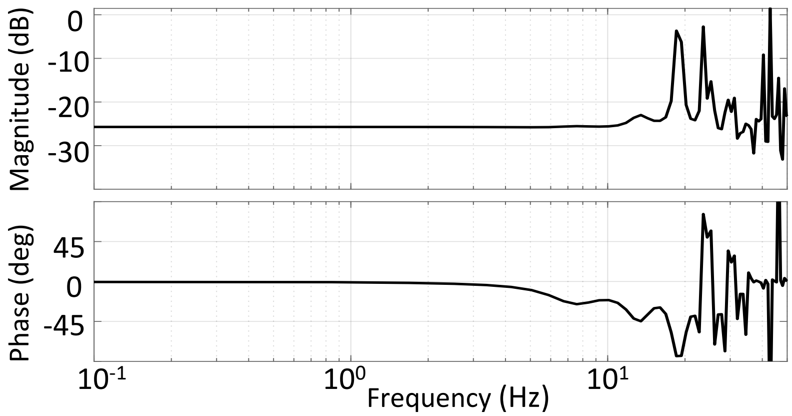

Figure 7.18: Bode plot demonstrating the frequency response to a chirp input

experimental results are summarized in Table 7.3. Interestingly, a higher nonlinearity was observed for the same tests under compressive loading/unloading (see Fig. 7.17(c) and (d)). It can be caused by inherent misalignment/slip of axis of the compressive forces applied at each end of the sensor while the axes of the tensile forces are passively aligned. This issue can be resolved by additional mechanical components such as linear guider/slider.

To validate the sensor response in dynamic condition, a chirp input signal varying from 0.1 Hz to 15 Hz was generated by the linear motor and the signal from the reference load cell was used as an input. Fig. 7.18 shows a frequency response of the proposed force sensor and the force sensor showed a consistent response up to the frequency ($\sim$15Hz).

7.6 Conclusions

In this chapter, we propose the design of a novel miniaturized force sensor which displays a highly linear output over a wide range that is robust to external noise and can be manufactured in a cost-effective manner. The force sensor uses a photointerrupter with a screen-type sensing mechanism to measure applied forces. A lambertian model of the LED allows for a more accurate representation of the light sensed by the PTs present in the photointerrupter. This model further allows us to optimize the screen width and offsets to maximize the linearity of the sensor output. Further, we propose a dual-screen setup, that allows for robustness towards manufacturing and assembly errors resulting in misplacement of the individual screens. These design factors allow the sensor to have more customizable compact design that be easily extended to a multi-axial assembly. We prove the efficacy of our dual-screen setup in the presence of artificially introduced errors in the assembly in the form of offset, d_{Off}. Finally, we also account for any sources of electrical noise, ambient lighting noise and temperature variations in the environment of the sensor by proposing a dual-PT assembly that estimates and minimizes any such sources of noise in real-time.

The compact size of this sensor allows us to incorporate the sensor in any compact robotic systems for micro-scale robotic surgical tools, and can be employed for single or multi-dimensional force perception and precision feedback control.

7.7 Acknowledgement

The author would like to thank Dr. Seokhwan Jeong for leading the research in this chapter.

CHAPTER 8

LARGE DEFLECTION FBG-SHAPE SENSOR FOR MICRO-SCALE AND MESO-SCALE ROBOTS

Fiber Bragg grating (FBG) sensing is a promising technology where gratings etched into a fiber reflect light at a wavelength that correlates with the space between gratings and thus, the strain of the fiber. FBG fibers have been previously studied for shape sensing in various applications. Liu *et al.* have developed an FBG bending sensor by attaching a fiber to two nitinol wires and routing the assembly through the walls of their continuum robot [160]. This design was later improved to insert the fiber and wires through the lumen of a polycarbonate tube, bonding them at the ends, and has been tested up to a curvature of 66.7 m^{-1} [162]. Furthermore, it was implemented in the optimization-based control of a 6 mm diameter continuum manipulator [235]. However, this method requires a channel to guide it along the length of the robot which is not always available in the micro-scale and meso-scale robots under consideration in this thesis. Our laboratory has previously developed large deflection FBG sensors that can measure similar curvatures for larger robots [236, 163]. Other groups have also worked with FBG bending sensors, but their maximum reported curvatures are less than 14 m^{-1} [237, 155, 156]. Therefore, shape-sensing is still an open problem in small scale continuum robots with large deflections. This chapter presents an FBG-based bending sensor design to provide accurate large deflection sensing for micro-scale and meso-scale continuum robotic tools with a maximum measured curvature of 145 m^{-1}.

This chapter is organized as follows: Section 8.1 describes the assembly of the FBG fiber within bending flexure joints with diameters equivalent to those seen for the guidewire robot and neuroendoscope robot. Section 8.2 introduces two models for this sensor assembly: A model to estimate joint curvature from FBG fiber strain (Section 8.2.1) and a

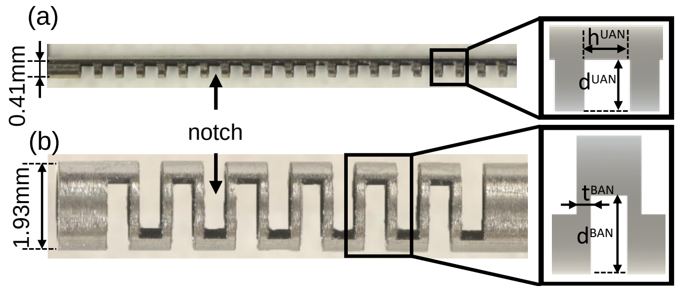

Figure 8.1: Tendon-driven bending flexure joints: (a) Micro-scale UAN joint and the notch parameters defining its bending properties (inset), (b) Meso-scale BAN joint and the notch parameters defining its bending properties (inset).

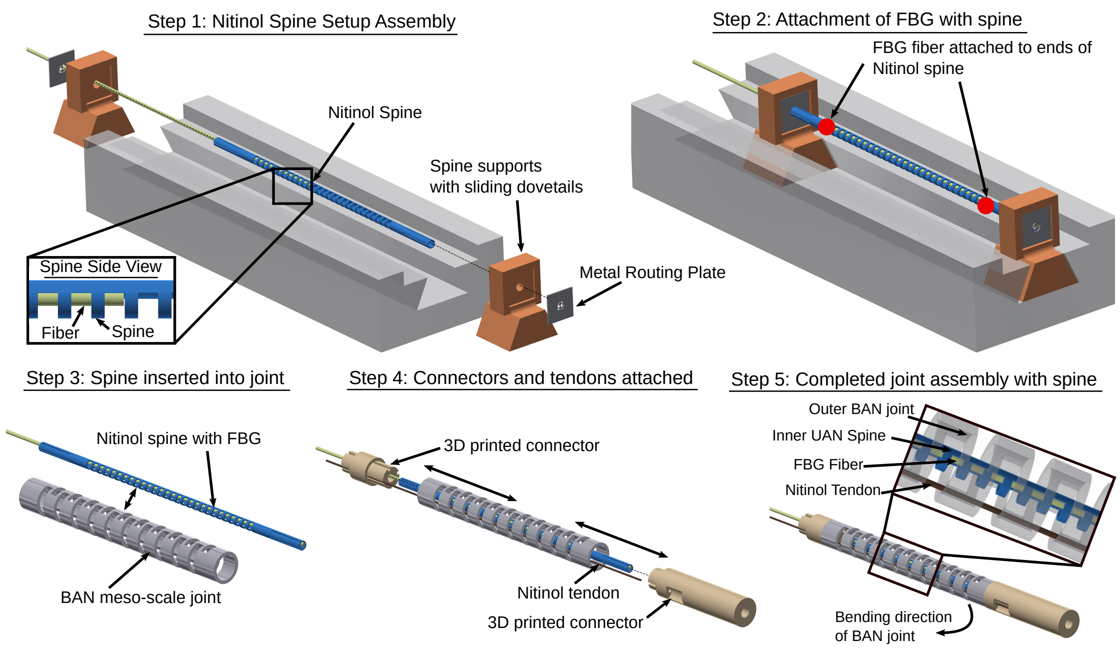

Figure 8.2: Steps to affix the FBG fiber within a spine for the meso-scale BAN joint.

relationship between tendon tension and joint curvature for the meso-scale joint (Section 8.2.2). Finally, in Section 8.3 we demonstrate the feasibility of this sensing technique by implementing a Kalman filter based observer that takes into account the FBG strain and tendon tension to estimate the meso-scale robot's joint angles.

8.1 Shape Sensor and Joint Assembly

As a recap, the tendon-driven joints explored in this thesis are called bending flexure joints [119, 120]. The joints employed in the micro-scale robotic guidewire (see Chapter 4) are termed unidirectional asymmetric notch (UAN) joints [122, 121] (see Fig. 8.1(a)) while the meso-scale neuroendoscopic robotic tool consists of bidirectional asymmetric notch (BAN) joints [177, 175, 178] (see Chapters 5 and 6).

Bending flexure joints allow for high joint curvatures at small joint lengths (each joint length in our case is 12 mm). However, due to the low wall thickness of the nitinol tubes used for machining these joints, explicit tendon routing channels cannot be machined into the walls of the tube. This lack of space in the robot also limits the options for the placement of FBG fibers in each joint to measure joint deflection. Unlike the authors in [162], the tendons and FBG fibers cannot be routed in dedicated channels within the walls of the tube. The fibers are therefore routed along the central lumen of the bending flexure joints. Furthermore, since FBG fibers cannot measure pure bending strain and can *only* measure axial strain, the neutral axis of the sensor assembly must be shifted away from the central axis of the joint. Authors in [162, 160], solve this problem by attaching two nitinol wires to a single FBG fiber, thereby adding an offset to the neutral axis of this sensor-wire assembly. However, this design is too large to fit in the central lumen of our micro-scale robot and tendons for tool control must be routed with the sensor through the central lumen of our meso-scale robot, which may affect an unprotected fiber. Hence, this is not a feasible solution.

In this section, we will first address each of these problems for the meso-scale robot joint and then proceed to modify the solution for the joint of the micro-scale guidewire.

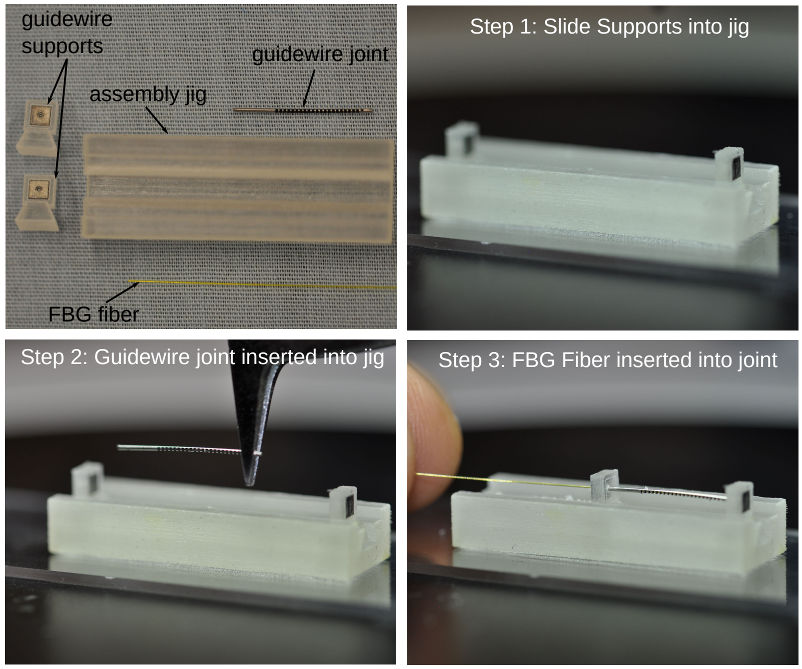

Figure 8.3: Assembly process for inserting the FBG fiber into the joint of a robotic guidewire with an outer diameter of 0.41 mm.

8.1.1 Meso-scale joint assembly

Fig. 8.2 shows the steps to assemble an FBG fiber inside the meso-scale BAN joint. A central 'spine' for the entire robot is created (shown in blue in Fig. 8.2) by micromachining a *passive* UAN joint from a nitinol tube of OD 0.57 mm and ID 0.44 mm. This 'spine' can run along the central axis of the entire joint. To assemble the fiber within the spine, the spine is first placed in a jig, held in place at both ends with a set of supports with sliding dovetail joints (see Step 1 in Fig. 8.2). Each of these spine supports has a metallic routing plate embedded in it. The routing plate is also micromachined using a femtosecond laser from a sheet of nitinol approximately 0.08 mm in thickness. This plate has slots to ensure the correct orientation of the spine, as well as holes to hold the FBG fiber in place. Once the spine is held in place by the supports and oriented correctly using the plate, the fiber is inserted via the hole inside the metal routing plates of the supports at both ends of the spine. The fiber used is a Draw Tower Grating (DTG) based fiber (FBGS International NV, Geel, Belgium) of diameter 195 μm with a single grating of length 8 mm. Glue (ClearWeld Quick Setting Epoxy, J-B Weld, Atlanta, United States) is then applied through the two slots micromachined on either side of the notches to attach the fiber to the ends of the spine (see Step 2 in Fig. 8.2) such that the grating is located in the middle of the spine. The glue is allowed to cure overnight with the assembly held in place by the jig. Next, the spine is extracted from the jig and inserted into the meso-scale BAN joint of the robot (see Step 3 in Fig. 8.2). The spine, along with the joint, is held in place by two 3D printed connectors at each end of the joint (see Step 4 in Fig. 8.2). A single tendon is routed to the distal end of the meso-scale joint during this assembly, allowing the control of the active robot joint. The passive UAN spine is oriented such that it bends in the same direction as the meso-scale BAN joint (see Step 5 (inset) in Fig. 8.2) Therefore, when the tendon is actuated, the robot and the spine-fiber assembly are assumed to have similar curvatures (see Section 8.2.1). It is important to note that the fiber will always run along the back wall (the side of the joint without the notches) of the spine due to the specific placement of the neutral axis of the UAN joint regardless of where the two ends of the fiber are glued around the inner circumference of the spine (see Section 8.2.1 for more details).

8.1.2 Micro-scale joint assembly

Fig. 8.3 shows the steps to assemble an FBG fiber inside the micro-scale UAN joint. The process is similar to the assembly of the spine for the meso-scale BAN joint described above. The guidewire is manufactured by using a femtosecond laser to micromachine a 12 mm long UAN joint from a nitinol tube of OD 0.41 mm and ID 0.24 mm. Two routing plates are also micromachined and placed on the sliding supports of the assembly jig (see Step 1 in Fig. 8.3). The guidewire is inserted in the supports and oriented so that when the FBG is placed, it will run along the un-notched side of the UAN joint of the guidewire (see Step 2 in Fig. 8.3). The FBG fiber used has a diameter of 160 μm with a single grating of length 8 mm (Technica Optical Components, Atlanta, United States). Due to the small difference between the ID of the guidewire and the OD of the FBG fiber, only a single hole for the fiber can be cut in the routing plate, requiring that the guidewire be visually aligned under a microscope. The FBG fiber is pushed through the routing plates and the guidewire joint such that the gratings on the fiber lie entirely inside the joint and at the middle of the joint (see Step 3 in Fig. 8.3). Once the alignment of the guidewire and fiber is confirmed, a light adhesive tape is gently placed over the ends of the fiber to ensure that they remain pressed against the un-notched wall of the guidewire and to prevent the fiber from shifting during the glueing process. Glue is applied through the two slots on either side of the notches to attach the fiber to the un-notched wall at the ends of the guidewire joint. The entire assembly rig is then flipped so that the notches face upward and the still liquid glue will not occlude the inside of the guidewire. Once the glue has cured overnight, the guidewire joint is removed from the assembly rig and two 50 μm nitinol tendons are routed from the proximal end to where they are pulled out of a slot on the notched side at the distal end of the guidewire. The distal ends of the two tendons are tied together, tension is applied and they are glued in place to the outer wall of the joint.

8.2 Joint and Fiber Models

In this section, we model the relationship between the deflection of the joint and the obtained strain in the FBG fiber for the meso-scale and micro-scale bending flexure joints. For the meso-scale robot, we used a BAN joint, where the FBG fiber is routed through the center of the joint via a central spine. In our previous work [175], we have demonstrated the feasibility of using tendon forces as feedback for shape-estimation for BAN joints. However, the addition of a central spine changes the static model of the BAN joint which must also be modeled.

8.2.1 Micro/Meso-scale Robot: Strain-Joint Angle Relationship

In FBG sensors, the axial strain (ϵ) in the fiber-core causes a change in the wavelength of light reflected back by the fiber ($\Delta\lambda$). Two different types of FBG sensors were used for the two scales of robots tested in this work. For the meso-scale joints of the neuroendoscope robot tool, Draw Tower Gratings (DTGs) with an outer diameter (D_{DTG}) of 195 μm are used. For the micro-scale guidewire, FBG fibers manufactured with a smaller outer diameter (D_{FBG}) of 160 μm were used. For DTG fibers, the relationship between the change in wavelength ($\Delta\lambda$) and the axial strain (ϵ) of the DTG fiber is given by the manufacturer (FBGS International NV, Geel, Belgium) as follows:

$$\ln(\frac{\lambda_1 + \Delta\lambda}{\lambda_1}) = k_{\epsilon.1}\epsilon + S_{T.1}\Delta T + S_{T.2}\Delta T^2 \tag{8.1}$$

where ΔT is the change in temperature relative to the value upon initialization of the measurements. Also, $\lambda_1 = 1579$ nm is the nominal wavelength of the DTG fiber, $k_{\epsilon.1} = 0.772$ is the strain sensitivity and $S_{T.1} = 6.37 \times 10^{-6}$ and $S_{T.2} = 7.46 \times 10^{-9}$ are the temperature sensitivities provided by the manufacturer. For standard FBG sensors, the governing equation for the $\Delta\lambda$-ϵ relationship is as follows [162]:

$$(\frac{\Delta\lambda}{\lambda_2}) = k_{\epsilon.2}\epsilon + S_{T.3}\Delta T \tag{8.2}$$

Here, the constants $k_{\epsilon.2} = 1.2$ pm/$\mu\epsilon$ and $S_{T.3} = 10$ pm/°C are intrinsic characteristics of the fiber and $\lambda_2 = 1550$ nm is the nominal wavelength of the FBG provided by the manufacturer (Technica Optical Components, Atlanta, United States). Temperature variation can be accounted for using the governing equation for the fiber or by introducing a second, reference grating below the joint that is unattached to the guidewire wall so that it is not strained by changes in curvature. Since this work is performed in a controlled laboratory environment, the temperature is assumed to be constant ($\Delta T = 0$) and hence the change in wavelength is only related to strain. In the case of the meso-scale bending flexure joints considered in this work, the sensing fiber is contained within a spine which itself is a passive UAN joint. In the case of the robotic guidewire, the robot's joint itself acts as the spine in which the fiber is fixed. We denote the outer and inner radii of these spines as r^{spine}_{outer} and r^{spine}_{inner} respectively (see Fig. 8.4(a)). Also, the depth of the unidirectional asymmetric notches in the spine is denoted as d_{spine}. The distance between the neutral plane and central axis of the spine is given as y^{spine}_{na} and is a function of the cross-sectional area A^{spine} [122] (see Fig. 8.4(b) (inset)). A^{spine} is a function of r^{spine}_{outer}, r^{spine}_{inner}, and d_{spine}. Furthermore, the location of the neutral axis of the FBG from the same central axis (see black dashed-dotted line in Fig. 8.4(a)) is given as follows:

$$y^{fiber}_{na} = r^{spine}_{inner} - (\frac{D_{fiber}}{2}) \tag{8.3}$$

As previously defined, $D_{fiber} = \{D_{DTG}, D_{FBG}\}$ is the outer diameter of the fiber used in each case (DTG or FBG). In the case of each of the joints in this chapter, we ensure that the D_{fiber} and d_{spine} are selected such that $y^{fiber}_{na} < y^{spine}_{na}$. This ensures that the fiber is always undergoing compression when the spine is curved and will always rest along the back wall of the UAN joint (the side of the joint without the notches). The neutral axis of the composite structure composed of the fiber and spine is then given by:

$$y^{composite}_{na} = \frac{E^{spine}A^{spine}y^{spine}_{na} + E^{fiber}A^{fiber}y^{fiber}_{na}}{E^{spine}A^{spine} + E^{fiber}A^{fiber}} \tag{8.4}$$

Here, $A^{fiber} = \pi D^2_{fiber}/4$ is the cross-sectional area of the fiber (see Fig. 8.4(b)), while $E^{spine} = 75$ GPa and $E^{fiber} = 70$ GPa are the Young's modulus for the spine and fiber respectively [160]. Furthermore, the distance of the fiber from this composite neutral axis is given by $\Delta y_{na} = (y^{composite}_{na} - y^{fiber}_{na})$. The strain along the fiber (ϵ) for spine angle θ (see

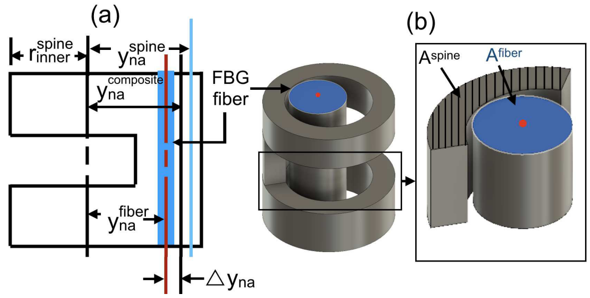

Figure 8.4: Micro/Meso-scale Robot Joints: (a) Schematic of the neutral axes of the spine, the FBG fiber, and the composite structure, (b) Schematic of the notch and integrated fiber.

Fig. 8.5) is then given as follows:

$$\epsilon = \frac{\theta \cdot \Delta y_{na}}{L_\theta + \theta \cdot y_{na}^{composite}} \tag{8.5}$$

Here L_θ is the length of the FBG at the joint angle of θ, estimated as $L_\theta = (y_{na}^{fiber} + 1/\kappa)\theta$, where κ is the curvature. Substituting this value of strain, ϵ, in Eqs. (8.1) and (8.2), we can get the θ-$\Delta\lambda$ relationship for the micro-scale (UAN) joint as follows:

$$\Delta\lambda = \frac{k_{\epsilon.2} \cdot \lambda_2 \cdot \theta \cdot \Delta y_{na}}{L_\theta + \theta \cdot y_{na}^{composite}} \tag{8.6}$$

For the meso-scale joint, this relationship is given as follows:

$$\Delta\lambda = \lambda_1 \cdot e^{\left(\frac{k_{\epsilon.1} \cdot \theta \cdot \Delta y_{na}}{L_\theta + \theta \cdot y_{na}^{composite}}\right)} - \lambda_1 \tag{8.7}$$

It is worth mentioning that y_{na}^{fiber} and y_{na}^{spine} are the most critical factors that affect the axial strain of the fiber. Since y_{na}^{spine} is located inside the back-wall of the spine, the minimum distance between y_{na}^{fiber} and y_{na}^{spine} depends on the wall thickness of the spine. In the current design, the fiber is always compressed when the tendon is been pulled. Any machining of the nitinol tube for attaching the FBG fiber on the spine changes the y_{na}^{spine} and hence the sensitivity of the sensor assembly. To evaluate the model derived in Eqs. (8.6)-(8.7), we conducted experiments on the guidewire (UAN) and neuroendoscope (BAN) joints.

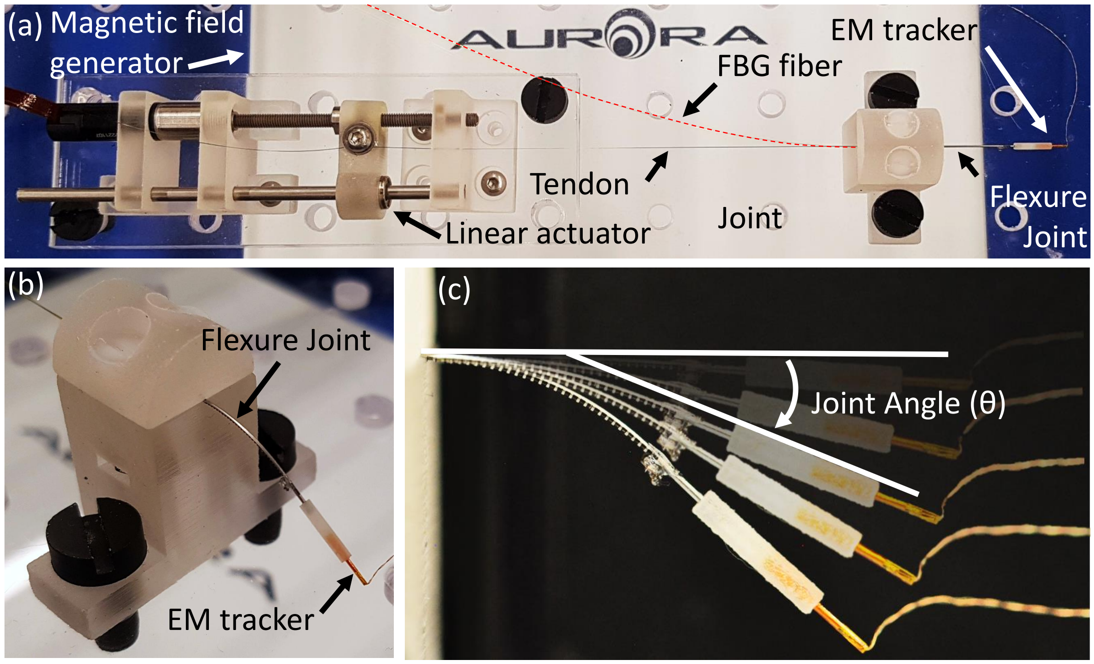

Figure 8.5: Experimental setup for sensor validation.

The experimental setup is shown in Fig. 8.5. For each test, a DC motor with a lead screw (Maxon Precision Motors, MA, United States) was attached to the tendon for the UAN/BAN joint with the FBG sensor assembled inside. The θ-$\Delta\lambda$ relationship has been tested on one micro-scale UAN joint (see joint J1 in Table 8.1) and one meso-scale joint (see joint J2 in Table 8.1). An electromagnetic (EM) tracking system (Northern Digital Inc. Medical Ontario, Canada) was used to record the true bending angle of each sample. Figure 8.6(a)-(b) illustrates the comparison between the modeled θ-$\Delta\lambda$ relationship and the experimental data. For the joint loading case, we find the model has an R^2-value of 0.991 for the micro-scale (UAN) joint and 0.996 for the meso-scale (BAN) joint. Note that while the ϵ-$\Delta\lambda$ relationship is non-linear for the DTG fiber in the meso-scale joint (see Eq. (8.1)), it demonstrates a high degree of linearity over its operating range ($\epsilon \leq 7\%$). As a result, the R^2-value is reported for this case to maintain consistency. However, we observe hysteretic behavior in the experimental data during unloading of the joints (see Fig. 8.6(a)-(b)). As a result, for the joint unloading case, we have lower R^2-values of 0.886 for the micro-scale (UAN) joint and 0.962 for the meso-scale (BAN) joint. This hysteresis effect is addressed

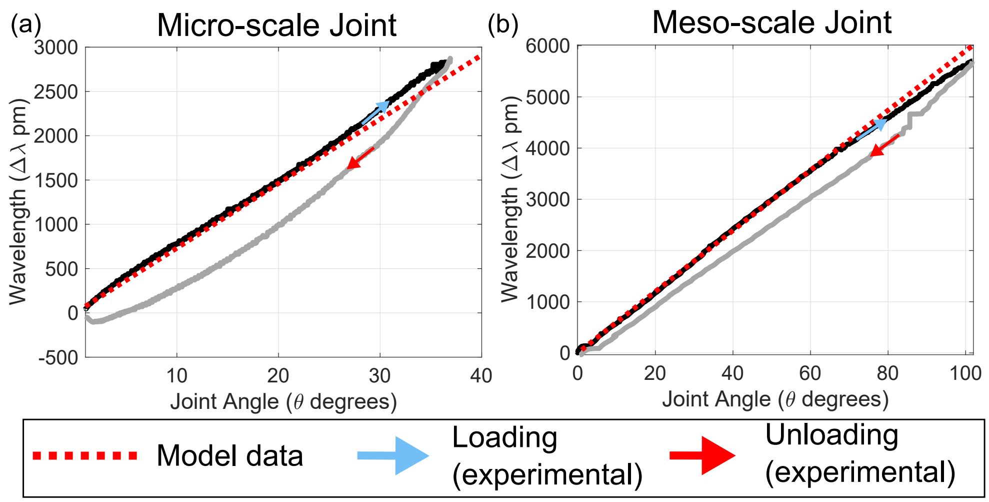

Figure 8.6: Comparison between the Joint Angle (θ)-Wavelength Shift ($\Delta\lambda$) model (during joint loading) and the experimental data demonstrating hysteresis in the (a) Micro-scale joint, (b) Meso-scale joint.

for the meso-scale robot in Section 8.3.

8.2.2 Meso-scale Robot: Spine-Joint Static Relationship

To arrive at a static relationship for the spine-joint assembly of the meso-scale joint, we made two assumptions:

1. The stiffness of the FBG fiber is negligible in comparison to that of the joint and the spine and therefore it is not considered in the development of the static model of the joint,

2. Joint statics are affected by bending moments, tendon friction, and pure compression forces. However, in these joints, pure compression is insignificant in comparison to the bending and friction forces and is not incorporated into our model.

Fig. 8.7(a) shows an FEM simulation (Solidworks 2018, Dassault Systems) of a BAN joint, spine and nested joint including a spine inside of the lumen of the BAN joint. Because the neutral axes of the BAN joint and the spine are on the same plane but not statically connected as a single body, the total moment applied on the nested joint by the tendon (M^{total}) can be stated as a superposition of the moments applied to the joint (M^{joint}) and

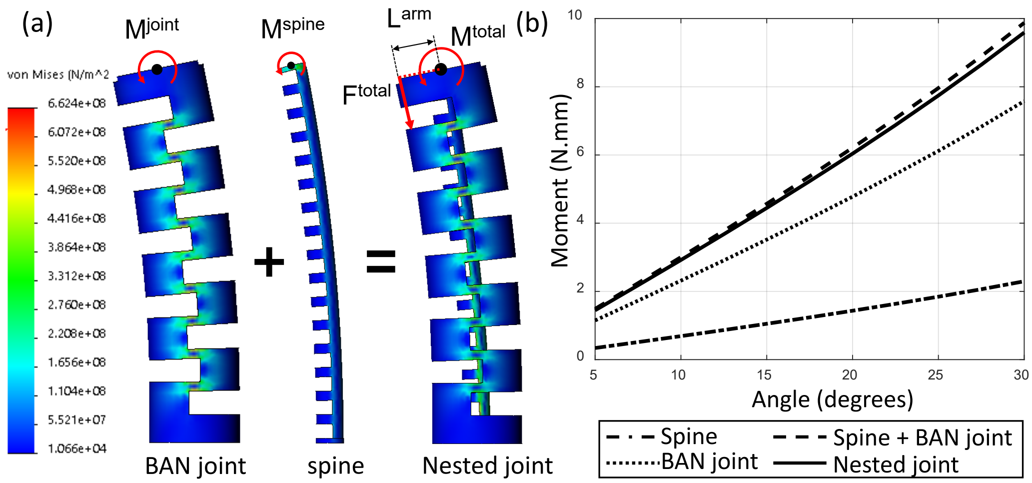

Figure 8.7: (a) The nested joint model in FEM simulation and (b) FEM result.

spine (M^{spine}): $M^{total} = M^{joint} + M^{spine}$. These moments are applied to the FEM model, and the model validates this moment superposition relationship (see dashed line in Fig. 8.7(b)). Here $M^i = F^i L_{arm}$ is the moment applied on the joint, the spine or the joint-spine combination due to the tendon tension F^i, where $i = \{joint, spine, total\}$. Since the moment arm ($L_{arm}$) is the same for all three cases, we can represent this equation as follows:

$$F^{total} = F^{joint} + F^{spine} \tag{8.8}$$

For the outer BAN joint, the outer radius of the tube (r_o^{BAN}), depth of the notches (d^{BAN}), and the thickness of the segment between two consecutive notches (t^{BAN}) are the parameters defining the statics (see Fig. 8.1(b)). From [212], a BAN joint is modeled as a serial chain of N bidirectionally asymmetric notches. Using Castigliano's second theorem:

$$\theta = \frac{(N-1)}{2} \frac{\partial U(t^{BAN}, d^{BAN})}{\partial M^{notch}(F^{joint}, d^{BAN}, r_{outer}^{BAN})} \tag{8.9}$$

where N is the total number of notches in the joint, $U(t^{BAN}, d^{BAN})$ is the strain energy across the bending section for a single pair of notches, and $M^{notch}(F^{joint}, d^{BAN}, r_{outer}^{BAN})$ is

Table 8.1: The set of samples tested to validate the spine-joint static model.
[a] J1 is unidirectional asymmetric notch joint in micro-scale robot (Guidewire) .
[b] J2 and J3 are bidirectional asymmetric notch joints in meso-scale robot (Neuroendoscope).
[c] are the R^2-values for the θ-$\Delta\lambda$ model developed in Section 8.2.1.
[d] are the RMSE values for the θ-F^{total} model developed in Section 8.2.2.

Sample	Parameters					
	t (mm)	d (mm)	h (mm)	Notches	R^2-value[c] -	RMSE[d] (N)
J1[a]	-	0.27	0.3	28	0.991	-
J2[b]	0.2	1.09	-	20	0.996	0.071
J3[b]	0.2	1.20	-	20	-	0.077

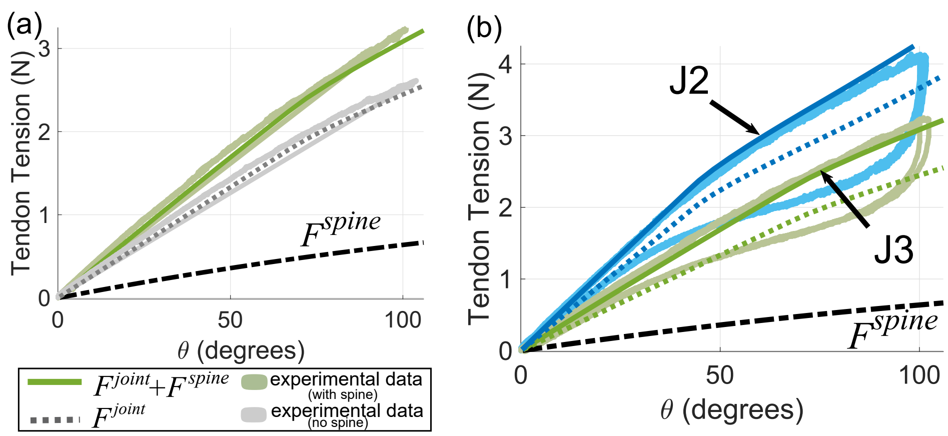

Figure 8.8: (a) For the joint 'J3' in Table 8.1, the gray and green colored solid lines allow us to estimate F^{spine}, (b) Bidirectional asymmetric notch joints with spine containing a single FBG fiber (joints J2 and J3 in Table 8.1).

the moment applied on the single pair of notches due to the tendon tension F^{joint}. Using Eq. (8.8), we can find the tendon tension required to achieve the bending angle (θ) for any BAN joint.

To find the θ-F^{spine} relationship, we make use of joint loading experimental data from joint 'J3' in Table 8.1. The experimental setup of Fig. 8.5 is used, replacing the micro-scale guidewire joint with the larger meso-scale BAN joint 'J3' with and without the FBG sensor assembly. A second order polynomial fit is generated to approximate the θ-F^{total} and θ-F^{joint} relationships (see Fig. 8.8(a)). Using Eq. (8.8) and these polynomial approximations of experimental data, we can arrive at the θ-F^{spine} relationship. This relationship can then be applied to a model of joint 'J2' (see dotted blue and green lines in Fig. 8.8(b) generated using Eq. (8.9)) to arrive at an accurate model for the joint behavior with the spine (see solid blue line in Fig. 8.8(b)). Therefore, the effect of the sensor assembly on the statics of the meso-scale robot joint can be effectively modeled (RMSE values for joints 'J2' and 'J3' are 0.071 N and 0.077 N respectively). However, as seen in Fig. 8.8(b), the model holds only for the case of joint loading. A significant amount of hysteresis is observed in the θ-F^{total} relationship during the unloading of the joint. This hysteresis results from the material properties of the nitinol material used to manufacture the BAN joint. Superelastic nitinol demonstrates hysteresis in its stress-strain relationship as it transitions between its austenite and martensite phases. We compensate for this hysteresis in the next section.

8.3 Meso-scale Robot: Joint State Estimation

In the case of the micro-scale guidewire joint, FBG sensing is the only feasible modality available to estimate the shape of the guidewire other than imaging. Tendon force or displacement proves to be unreliable in this case due to varying tendon-sheath friction forces as the guidewire traverses through the patient's vasculature towards the target. However, for tools with a fixed sheath length (such as the meso-scale robotic neuroendoscope), tendon force too (F^{total}) can be an effective feedback mechanism to estimate robot joint state. However, since the forces required for controlling meso-scale BAN joints can be ≤ 4 N (see Fig. 8.8(a)-(b)), the noise in the force sensor can result in significant error in our estimation. We demonstrate in this section, that shape sensing using the FBG fiber assembly, combined with the tendon force information can significantly improve the performance of an observer estimating joint state (θ) for the meso-scale joint.

First the hysteresis observed in the θ-$\Delta\lambda$ relationship (see Section 8.2.1) and the θ-F^{total} relationship (see Section 8.2.2) must be effectively modeled and compensated. In this work, we use a Preisach model to estimate the hysteresis in our sensor response [238].

This model was adopted due to its ability to estimate intermediate hysteretic loops and relatively low computational costs. In its continuous form, the Preisach model estimates any hysteretic system as a function of infinite hysteretic binary switches (usually switching between '0' and '1'):

$$\hat{\theta}(t) = \iint_{\alpha \geq \beta} \mu(\alpha, \beta) \gamma_{\alpha,\beta}[x(t)] d\alpha d\beta \tag{8.10}$$

Here $x(t)$ and $\hat{\theta}(t)$ are the input and output of the Preisach model at state t respectively. In our case, the input ($x(t)$) can either be FBG wavelength shift ($\Delta\lambda$) or tendon force (F^{total}), while the output ($\hat{\theta}(t)$) is the estimated value of true joint angle (θ). The hysteretic switches mentioned earlier are denoted by the function $\gamma_{\alpha,\beta}$, where α and β are the switching limits of each switch in the input ($x(t)$) space.

In this work, we use the method used by the authors in [239], to discretize and map the Preisach model into a linear framework and estimate 'Preisach weights' by using a linear regression. For each of our models, we begin by first discretizing the input space into N_p equal sections and defining $(N_p)^2$ switches over the entire Preisach plane. The Preisach model may then be described as $F = \Gamma \cdot \mu(\alpha, \beta)$. Here, $F = [f(1), f(2), ..., f(m)]^T$ is the output of the discretized model for m samples and Γ is a matrix consisting of the $(N_p)^2$ columns of Preisach switches in each of its m rows. $\mu(\alpha, \beta)$ is the 'Preisach weight' to be learned for each of our models. Following this, a number of sinusoidal inputs of varying amplitudes and constant frequency (0.05 Hz) are applied to the system. The tendon force (F^{total}), FBG wavelength shift ($\Delta\lambda$) and true joint angle (θ) values are collected for training our discrete Preisach model. Therefore, from each of our sensors that measure $\Delta\lambda$ and F^{total}, hysteresis in the sensor response can be modeled to generate estimates of true joint angle (θ). We denote these estimates together as $\hat{\theta} = [\hat{\theta}_\lambda, \hat{\theta}_f]^T$, where $\hat{\theta}_\lambda$ is generated by the Preisach model for the θ-$\Delta\lambda$ relationship and $\hat{\theta}_f$ is generated by the Preisach model for the θ-F^{total} relationship.

An Unscented Kalman Filter (UKF) uses $\hat{\theta}$ to generate an estimate of joint angle, θ^{est} (see Fig. 8.9(a)). A joint angle prediction ($\tilde{\theta}$) is generated by a robot-specific kinematic model [181] of the BAN joint that relates tendon stroke to the joint angle. This prediction is adjusted using the output of the Preisach model ($\hat{\theta}$) to generate an estimate of joint angle, θ^{est}. To demonstrate the effectiveness of the state estimate, we first use only tendon tension (F^{total}) to generate θ^{est}. A set of sinusoids with decreasing amplitudes and a frequency of 0.1 Hz were used as the input signal (denoted by u in Fig. 8.9(a)). There is significant noise in θ^{est} with a higher RMSE of 5.2339 deg when using only tendon tension (see dotted black line in Fig. 8.9(b)). When the Preisach model estimating $\hat{\theta}_\lambda$ is incorporated, the values of θ^{est} generated closely follow the true θ values (RMSE = 1.0833 deg) (see dotted-dashed red line in Fig. 8.9(b)). Using only FBG data ($\hat{\theta}_\lambda$) to generate θ^{est}, we observe a higher RMSE of 1.0839 degrees. To demonstrate the effectiveness of the state estimate in the presence of external tip forces, a foam block was placed in the path of the joint, and a set of sinusoids with decreasing amplitudes and a frequency of 0.05 Hz were used as the input signal (see Fig. 8.9(c)). This shows that the addition of $\hat{\theta}_\lambda$ is robust to the presence of external forces (RMSE = 1.0866 deg), while tendon tension (F^{total}) by itself cannot reproduce θ^{est} correctly (RMSE = 18.2500 deg). This demonstrates the effectiveness of using the FBG sensor assembly introduced in this work in conjunction with force feedback to estimate the state of the joints of our meso-scale robot. The current implementation of the Preisach model using a linear fit is limited in its ability to adapt to changes in hysteresis such as those caused by the dynamic responses of the system and the sensors which will vary under largely different operating speeds. However, this proof-of-concept will be the basis for future development of a robust hysteresis model and its application in controllers for micro-scale and meso-scale robots.

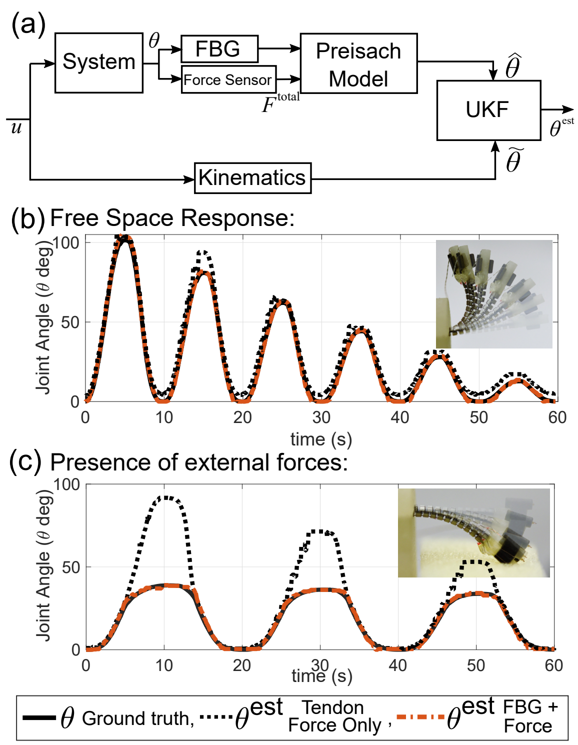

Figure 8.9: (a) UKF based observer for the meso-scale robot involves combining a kinematics model, tendon tension (f) and FBG fiber wavelength ($\Delta\lambda$) to generate joint angle estimate (θ^{est}), (b) Free space response of the observer, (c) Response of the observer in the presence of external tip forces.

8.4 Conclusions

In this chapter, we design and develop a sensor-framework using an FBG fiber to measure the shape of micro-scale and meso-scale continuum robots. To obtain strain in the core of the FBG while it bends, the neutral axis of the FBG fiber was shifted by attaching it within a UAN joint micromachined from a nitinol tube. One advantage of the sensor design is the ability to sense joint bending for small-scale joints, which we demonstrate using a micro-scale joint (OD = 0.41 mm) and a meso-scale joint (OD = 1.93 mm). The design and assembly process of this sensor are described for both scales of joints explicitly. Another advantage is a highly linear and repeatable response which can be explained by the analytical model proposed and validated in this work. One disadvantage of the sensor is a hysteresis pattern observed in the sensor response. However, this may be modeled effectively using a Preisach model. We demonstrate this using a Kalman Filter-based observer to estimate the deflection of the meso-scale joint. This sensor achieves, to the author's knowledge, the highest reported curvature of FBG bending sensors, 145 m^{-1}.

8.5 Acknowledgements

The author would like to thank Ms. Nancy Deaton, Dr. Nahian Rahman, and Dr. Seokhwan Jeong for part of the contents of this chapter.

CHAPTER 9
CONCLUSIONS AND FUTURE WORK

9.1 Contributions

In conclusion, this thesis describes the development of tendon-driven continuum robots at micro-scales and meso-scales. By utilizing the superelastic properties of nitinol, serial joints can be micromachined within tubes of the alloy, allowing for drastic miniaturization. Using serial chains of these joints and efficient tendon routing, a number of multi-DoF steering mechanisms can be designed for guidewires and endoscopy tools at micro- and meso-scales. We demonstrated our ability to achieve complex motions like follow-the-leader motion at micro-scales using co-axially aligned micromachined nitinol tubes. This thesis also presents kinematic and static models for the joints of the proposed robots, using the hysteretic stress-strain properties of superelastic nitinol and incorporating tendon elongation in tendon-driven systems. The development of novel force and shape sensing systems has also been initiated in this body of work. The main contributions of this thesis are as follows:

1) <u>2-DoF Robotic Guidewire:</u> We developed a robotically actuated 2-DoF guidewire tip comprised of joints laser micro-machined into a 0.78 mm ($<$ 2.4 Fr) nitinol tube. Two tendons of outer diameter 0.1 mm were used to control each joint, with tendon routing blocks inserted along the length of the guidewire body for decoupled control of each degree-of-freedom. We presented an analysis of the notch joint used as a building block in the robot and a control strategy for this type of a joint. The experimental results showed that tendon-force is an important observable quantity that can be used as a shape sensing mechanism for this type of a joint in practical control applications. While this robotic guidewire was capable of reaching bifurcations in a 3D workspace without any torsion, the limited joint

length of each robot joint prevented the robot from performing any follow-the-leader motion, required to enter tortuous vascular structures. Following are the major contributions of this work:

- Development of a 2-DoF robotic guidewire with an outer diameter of 0.78 mm, well within the size ranges widely used in minimally invasive surgical procedures.
- Decoupled control of both degrees-of-freedom.
- Tendon force for joint-space control and state estimation of each joint.

2) COAST Robotic Guidewire: To address the follow-the-leader requirement for steerable catheters, we developed a novel COaxially Aligned STeerable (COAST) guidewire robot that is 0.40 mm in diameter demonstrating variable curvature and independently controlled bending length of the distal end. The COAST design involves three coaxially aligned tubes with a single tendon running centrally through the length of robot. The outer tubes are made from micromachined nitinol allowing for tendon-driven bending of the robot at various segments of the robot, thereby enabling variable bending curvatures, while an inner stainless steel tube controls the bending length of the robot. By varying relative positions of the tubes and the tendon by insertion and retraction in the entire assembly, various joint lengths and curvatures can be achieved, which enables a follow-the-leader motion. We introduced a mechanical model that accounts for micromachining-induced pre-curvatures with a goal to identify an optimal tube pair that reduces combined distal tip pre-curvature and correspondingly minimizes abrupt changes in actuated tip position. We modeled the kinematics, statics, as well as the coupling within tubes of the COAST robot and developed a simple controller to control the distal tip of the robot. We also developed a novel compact actuation mechanism for a COAST robot that is capable of executing follow-the-leader motion in tortuous three dimensional vascular pathways. Finally, we experimentally demonstrated the ability of COAST guidewire to accurately navigate through phantom anatomical bifurcations and tortuous anatomy. Following are the major contributions of this work:

- Development of a 0.4 mm robotic guidewire demonstrating variable and independently controllable bending joint angle and length (enabling follow-the-leader motion).
- Compact actuation system for the control of the robot joint, translation and rotation of the entire guidewire.
- Mechanical model development for large-deflection beam bending of pre-curved non-uniform cross-section tubes undergoing gravity loading.
- Identification of optimal tube combination reducing combined distal tip pre-curvature and distal tip flexural rigidity.
- Modeling of kinematics, statics and inter-segment coupling between the tubes of the COAST guidewire.
- Demonstration of follow-the-leader motion in 2D and 3D phantom vasculature.

3) Robotic Neuroendoscope tool: A meso-scale two degree-of-freedom robotic endoscopic tool body for minimally invasive surgeries (MIS) was designed in this work to address hydrocephalus cases. The design of the robotic tool used two tendon-driven joints known as a bending flexure joints (similar to those used in the guidewires) that allow us to control each degree-of-freedom by minimizing inter-joint coupling by design. Pure kinematic modeling and control for these robots does not provide precise control performance due to kinematic uncertainties arising from tendon elongation, tendon slacking, gear backlash, etc. We proposed a static model for each of the joints of the robotic tool that avoids several of these problems. Depending on the direction of tendon tension application, the proximal joint displays considerable hysteresis due to the superelastic material characteristics. We incorporated this hysteresis in our static model. The statics of a highly compliant distal joint was also modeled and validated using finite element analysis and experimental data. Using these models, we developed a control system with a disturbance observer and the proposed static model to provide precise force control and compensate for joint

hysteresis. Following are the major contributions of this work:

- Development of a 1.93 mm 2-DoF robotic endoscope tool with handheld controller.
- Incorporation of superelastic nitinol hysteretic model for the joint-space tendon-force control of robot joints.
- Development of a disturbance observer-based control system for precise force control.

4) Miniature Force Sensor for tendon-driven robots: In previous literature, photointerrupter based force sensors demonstrated a reasonable performance in a cost-effective manner, but had a narrow range of linear output with significant susceptibility to external disturbances. This made it difficult to use these sensors in precision force measurement and feedback control. In this portion of my thesis, we presented a nonlinear optical model that utilized a lambertian distribution for the photointerrupter, which was then used to optimize the design parameters of the sensor. The optimized geometry of the screen and a novel dual-screen arrangement were proposed to increase the linear range of the sensor output. A dual-phototransistor signal acquisition was introduced to compensate the external disturbances and provides robust sensor output. A prototype of the sensor was fabricated in a miniaturized form factor with the ability to measure forces up to 21 N, having 1.08 % nonlinearity, 0.83% hysteresis, and 99.58 % accuracy. The proposed model and sensing mechanisms were experimentally validated and implemented in the neuroendoscope and COAST guidewire controllers. Following are the major contributions of this work:

- Development of a Lambertian distribution based non-linear optical model of a photointerrupter.
- Development of a dual-screen dual-photointerrupter based tendon-force sensor using machining parameters optimized by the non-linear optical modeling.

5) Large Deflection FBG-based shape sensing: We designed and developed a sensor-framework using an FBG fiber to measure the shape of micro-scale and meso-scale continuum robots that can deform to large curvatures. To obtain strain in the core of the FBG

while it underwent deformation, the neutral axis of the FBG fiber was shifted by attaching it within a UAN joint micromachined from a nitinol tube. One advantage of the sensor design was the ability to sense joint bending for small-scale joints, which we demonstrated using a micro-scale joint of the guidewire and a meso-scale joint of the neuroendoscope. The design and assembly process of this sensor were detailed for both scales of joints. Another advantage was a highly linear and repeatable response which can be explained by the analytical model we proposed and validated in this work. One disadvantage of the sensor was a hysteresis pattern observed in the sensor response. However, this may be modeled effectively using a Preisach model. We demonstrated this using a Kalman Filter-based observer to estimate the deflection of the meso-scale joint. This sensor achieved, to our knowledge, the highest reported curvature of FBG bending sensors, 145 m^{-1}. Following are the major contributions of this work:

- Development of a fiber Bragg grating (FBG) and micromachined nitinol tube based shape sensor framework for large deflection continuum joints.
- Development and validation of an analytical model for the sensor response and Preisach model for hysteresis estimation in sensor response.
- Demonstration of hysteresis compensation in the meso-scale robot joint deflecting to 145 m^{-1} in free space and presence of external forces.

9.2 Future Work

While this thesis provides a comprehensive introduction and proof-of-concept development of several novel robots and sensing mechanisms, several topics are left to be addressed in the future. This section presents a brief summary of the potential areas of research that can contribute towards clinical application of the robots discussed in this thesis:

1) The next logical step for the COAST guidewire is the development of a Compact Actuation System (CAS) without a translational stage. A significant degree-of-freedom in the

COAST guidewire is a lead-screw based translational stage (indicated by variable X_4 in the Chapter 4), which drastically increases the length of the CAS. As described in the patent filed for the 2-DoF guidewire [240], preliminary work towards miniaturizing an insertion stage by coiling the guidewire around a rotating drum has been initiated. Adapting this setup for the COAST mechanism actuation will likely improve clinical adoption of this mechanism.

2) Another significant future work is the development of a CO-axially Aligned STeerable (COAST) mechanism to control the 2-DoF robotic neuroendoscope tool. While the COAST mechanism has been deployed previously for the single degree-of-freedom case of the guidewire, it can be extended to multiple degrees-of-freedom. To do so with multiple tendons within a larger inner cross-section of the neuroendoscope (in comparison to the guidewire) will likely produce promising challenges for modeling and control, and potential application of the endoscope tool.

3) Deployment of the FBG-based shape sensing modality within the neuroendoscope tool for closed-loop control is a significant future work that will allow the tool to move towards further autonomy. Combined with a COAST mechanism to control the degrees-of-freedom of the neuroendoscope tool, the clinician can simply highlight a target point at the floor of the ventricle for the tool to approach. Using intrinsic shape sensing and a compact actuation system similar to the one deployed in the COAST guidewire, the robot can use the commanded target point in the robot's task space and use shape feedback to reach the target successfully.

4) Incorporation of intrinsic tendon-force sensors within the tendon: Another future direction for the tendon-force sensor is the development of MEMS strain gauges to measure tendon-tension. As we develop more compact handheld controllers for our robots, the current miniature force sensors prove to be too large and bulky. Therefore, a significant research contribution is the further miniaturization of this sensor.

5) Finally, image-based navigation of the guidewire to a desired target site is current and

future work towards semi-autonomous navigation of the guidewire through vascular structures. For this purpose, pre-operative CT data is matched to real-time ultrasound and fluoro-images of the vasculature and guidewire to localize and update the map of the patient's vascular anatomy. Using this mapping and target sites indicated by a clinician, the COAST guidewire will be navigated to a target region using paths generated by a modified version of an A* algorithm.

Appendices

APPENDIX A

USE OF COPYRIGHTED MATERIALS AND PERMISSIONS

1. ©2020 IEEE. Reprinted, with permission, from **Yash Chitalia**, Seokhwan Jeong, Kent K. Yamamoto, Joshua J. Chern, Jaydev P. Desai, "Modeling and Control of a 2-DoF Meso-Scale Continuum Robotic Tool for Pediatric Neurosurgery", *IEEE Transactions on Robotics*, Nov. 2020.
2. ©2020 IEEE. Reprinted, with permission, from Seokhwan Jeong, **Yash Chitalia (co-first author)**, Jaydev P. Desai , "Design, Modeling, and Control of a Coaxially Aligned Steerable (COAST) Guidewire Robot", *IEEE Robotics and Automation Letters*, June 2020.
3. ©2020 IEEE. Reprinted, with permission, from Seokhwan Jeong, **Yash Chitalia**, Jaydev P. Desai, "Miniature force sensor based on dual-photointerrupter with high linearity and disturbance compensation", *IEEE Sensors Journal*, Feb. 2020.
4. ©2020 IEEE. Reprinted, with permission, from **Yash Chitalia**, Nancy Deaton, Seokhwan Jeong, Nahian Rahman, Jaydev P. Desai, "Towards fbg-based shape sensing for micro-scale and meso-scale continuum robots with large deflection", *IEEE Robotics and Automation Letters*, Jan. 2020.
5. ©2020 IEEE. Reprinted, with permission, from **Yash Chitalia**, Seokhwan Jeong, Nancy Deaton, Joshua J. Chern, Jaydev P. Desai, "Design and kinematics analysis of a robotic pediatric neuroendoscope tool body", *IEEE/ASME Transactions on Mechatronics*, Jan. 2020.
6. ©2019 IEEE. Reprinted, with permission, from **Yash Chitalia**, Seokhwan Jeong, Ji Bok, Vinh Nguyen, Shreyes Melkote, Joshua J. Chern, Jaydev P. Desai, "Towards the Design and Development of a Pediatric Neuroendoscope Tool", *2019 IEEE/RSJ International Conference on Intelligent Robots and Systems (IROS)*, Nov. 2019.
7. Reprinted by permission from Springer Nature: Springer Nature, In International Symposium on Experimental Robotics, pp. 24-33., Springer Cham., "Design and analysis of a bidirectional notch joint for a robotic pediatric neuroendoscope.", **Yash Chitalia**, Xuefeng Wang, Vinh Nguyen, Shreyes Melkote, Joshua Chern, Jaydev P. Desai ©(2018)
8. ©2018 IEEE. Reprinted, with permission, from **Yash Chitalia**, Xuefeng Wang, Jaydev P. Desai, "Design, modeling and control of a 2-dof robotic guidewire", *2018 IEEE International Conference on Robotics and Automation (ICRA)*, May 2018.

REFERENCES

[1] E. J. Benjamin, S. S. Virani, C. W. Callaway, A. M. Chamberlain, A. R. Chang, S. Cheng, S. E. Chiuve, M. Cushman, F. N. Delling, R. Deo, *et al.*, "Heart disease and stroke statistics-2018 update: A report from the american heart association.," *Circulation*, vol. 137, no. 12, e67, 2018.

[2] G. A. Roth, D. Abate, K. H. Abate, S. M. Abay, C. Abbafati, N. Abbasi, H. Abbastabar, F. Abd-Allah, J. Abdela, A. Abdelalim, *et al.*, "Global, regional, and national age-sex-specific mortality for 282 causes of death in 195 countries and territories, 1980–2017: A systematic analysis for the global burden of disease study 2017," *The Lancet*, vol. 392, no. 10159, pp. 1736–1788, 2018.

[3] T. Vos, C. Allen, M. Arora, R. M. Barber, Z. A. Bhutta, A. Brown, A. Carter, D. C. Casey, F. J. Charlson, A. Z. Chen, *et al.*, "Global, regional, and national incidence, prevalence, and years lived with disability for 310 diseases and injuries, 1990–2015: A systematic analysis for the global burden of disease study 2015," *The Lancet*, vol. 388, no. 10053, pp. 1545–1602, 2016.

[4] L. Richards, C. Hanson, M. Wellborn, and A. Sethi, "Driving motor recovery after stroke," *Topics in stroke rehabilitation*, vol. 15, no. 5, pp. 397–411, 2008.

[5] C. R. Narins, "Access strategies for peripheral arterial intervention," *Cardiology journal*, vol. 16, no. 1, pp. 88–97, 2009.

[6] G. Biondi-Zoccai, P. Agostoni, G. Sangiorgi, L. P. Dalla, F. Armano, S. Nicolini, J. Alek, and M. Fusaro, "Mastering the antegrade femoral artery access in patients with symptomatic lower limb ischemia: Learning curve, complications, and technical tips and tricks.," *Catheterization and cardiovascular interventions: official journal of the Society for Cardiac Angiography & Interventions*, vol. 68, no. 6, pp. 835–842, 2006.

[7] Merit Medical Systems, *Amplatz left*, https://meritoem.com/product-category/catheters-extrusions/diagnostic-cardiology/performa/amplatz-left/, [Online; accessed 11-February-2020].

[8] J.-F. Surmely and T. Suzuki, "Parallel-wire techniques," *Chronic Total Occlusions: A Guide to Recanalization*, pp. 83–86, 2009.

[9] N. Cox, F. S. Resnic, J. J. Popma, D. I. Simon, A. C. Eisenhauer, and C. Rogers, "Comparison of the risk of vascular complications associated with femoral and radial access coronary catheterization procedures in obese versus nonobese patients," *The American journal of cardiology*, vol. 94, no. 9, pp. 1174–1177, 2004.

[10] S. Yilmaz, T. Sindel, and E. Lüleci, "Ultrasound-guided retrograde popliteal artery catheterization: Experience in 174 consecutive patients," *Journal of Endovascular Therapy*, vol. 12, no. 6, pp. 714–722, 2005.

[11] M. Fusaro, A. Tashani, N. Mollichelli, M. Medda, L. Inglese, and G. G. Biondi-Zoccai, "Retrograde pedal artery access for below-the-knee percutaneous revascularisation," *Journal of Cardiovascular Medicine*, vol. 8, no. 3, pp. 216–218, 2007.

[12] S. G. Ellis, M. G. Vandormael, M. J. Cowley, G. DiSciascio, U. Deligonul, E. J. Topol, and T. M. Bulle, "Coronary morphologic and clinical determinants of procedural outcome with angioplasty for multivessel coronary disease. implications for patient selection. multivessel angioplasty prognosis study group.," *Circulation*, vol. 82, no. 4, pp. 1193–1202, 1990.

[13] J. J. Lee, J. S. Kim, W. S. Jeong, D. Y. Kim, S. M. Hwang, and S. Y. Lim, "A complication of subclavian venous catheterization: Extravascular kinking, knotting, and entrapment of the guidewire-a case report," *Korean journal of anesthesiology*, vol. 58, no. 3, p. 296, 2010.

[14] J.-b. Ge, "Current status of percutaneous coronary intervention of chronic total occlusion," *Journal of Zhejiang University SCIENCE B*, vol. 13, no. 8, pp. 589–602, 2012.

[15] N. Reifart, "Challenges in complicated coronary chronic total occlusion recanalisation," *Interventional Cardiology Review*, vol. 8, no. 2, p. 107, 2013.

[16] S. R. Atmakuri, E. I. Lev, C. Alviar, E. Ibarra, A. E. Raizner, S. L. Solomon, and N. S. Kleiman, "Initial experience with a magnetic navigation system for percutaneous coronary intervention in complex coronary artery lesions," *Journal of the American College of Cardiology*, vol. 47, no. 3, pp. 515–521, 2006.

[17] L. K. Wagner, M. D. McNeese, M. V. Marx, and E. L. Siegel, "Severe skin reactions from interventional fluoroscopy: Case report and review of the literature," *Radiology*, vol. 213, no. 3, pp. 773–776, 1999.

[18] L. W. Klein, Y. Tra, K. N. Garratt, W. Powell, G. Lopez-Cruz, C. Chambers, J. A. Goldstein, S. for Cardiovascular Angiography, and Interventions, "Occupational health hazards of interventional cardiologists in the current decade: Results of the 2014 scai membership survey," *Catheterization and Cardiovascular Interventions*, vol. 86, no. 5, pp. 913–924, 2015.

[19] J. F. Granada, J. A. Delgado, M. P. Uribe, A. Fernandez, G. Blanco, M. B. Leon, and G. Weisz, "First-in-human evaluation of a novel robotic-assisted coronary angioplasty system," *JACC: Cardiovascular Interventions*, vol. 4, no. 4, pp. 460–465, 2011.

[20] A. V. Kulkarni, J. M. Drake, C. L. Mallucci, S. Sgouros, J. Roth, S. Constantini, C. P. N. S. Group, *et al.*, "Endoscopic third ventriculostomy in the treatment of childhood hydrocephalus," *The Journal of pediatrics*, vol. 155, no. 2, pp. 254–259, 2009.

[21] M. Vinchon, H. Rekate, and A. V. Kulkarni, "Pediatric hydrocephalus outcomes: A review," *Fluids and Barriers of the CNS*, vol. 9, no. 1, p. 18, 2012.

[22] B. J. Iskandar, S. Tubbs, T. B. Mapstone, P. A. Grabb, A. A. Bartolucci, and W. J. Oakes, "Death in shunted hydrocephalic children in the 1990s," *Pediatric neurosurgery*, vol. 28, no. 4, pp. 173–176, 1998.

[23] L. Acakpo-Satchivi, C. N. Shannon, R. S. Tubbs, J. C. Wellons, J. P. Blount, B. J. Iskandar, and W. J. Oakes, "Death in shunted hydrocephalic children: A follow-up study," *Child's Nervous System*, vol. 24, no. 2, pp. 197–201, 2008.

[24] M. R. Gaab, "Instrumentation: Endoscopes and equipment," *World neurosurgery*, vol. 79, no. 2, S14–e11, 2013.

[25] B. J. Dlouhy, N. S. Dahdaleh, and J. D. Greenlee, "Emerging technology in intracranial neuroendoscopy: Application of the nico myriad," *Neurosurgical focus*, vol. 30, no. 4, E6, 2011.

[26] J. Mugamba and V. Stagno, "Indication for endoscopic third ventriculostomy," *World neurosurgery*, vol. 79, no. 2, S20–e19, 2013.

[27] S. Lam, D. Harris, B. G. Rocque, and S. A. Ham, "Pediatric endoscopic third ventriculostomy: A population-based study," *Journal of Neurosurgery: Pediatrics*, vol. 14, no. 5, pp. 455–464, 2014.

[28] H. W. Schroeder, W.-R. Niendorf, and M. R. Gaab, "Complications of endoscopic third ventriculostomy," *Journal of neurosurgery*, vol. 96, no. 6, pp. 1032–1040, 2002.

[29] B. C. Warf, "Comparison of endoscopic third ventriculostomy alone and combined with choroid plexus cauterization in infants younger than 1 year of age: A prospective study in 550 african children," *Journal of Neurosurgery: Pediatrics*, vol. 103, no. 6, pp. 475–481, 2005.

[30] I. C. Coulter, M. C. Dewan, J. Tailor, G. M. Ibrahim, and A. V. Kulkarni, "Endoscopic third ventriculostomy and choroid plexus cauterization (etv/cpc) for hydrocephalus of infancy: A technical review," *Child's Nervous System*, pp. 1–11, 2021.

[31] S. Wang, S. Stone, A. G. Weil, A. Fallah, B. C. Warf, J. Ragheb, S. Bhatia, and A. V. Kulkarni, "Comparative effectiveness of flexible versus rigid neuroendoscopy for

endoscopic third ventriculostomy and choroid plexus cauterization: A propensity score–matched cohort and survival analysis," *Journal of Neurosurgery: Pediatrics*, vol. 19, no. 5, pp. 585–591, 2017.

[32] J. G. Torres-Corzo, L. Rangel-Castilla, M. A. Islas-Aguilar, and R. R.-D. Vecchia, "A novel approach of navigation-assisted flexible neuroendoscopy," *Operative Neurosurgery*, vol. 14, no. 3, E33–E37, 2018.

[33] K. W. Eastwood, V. P. Bodani, and J. M. Drake, "Three-dimensional simulation of collision-free paths for combined endoscopic third ventriculostomy and pineal region tumor biopsy: Implications for the design specifications of future flexible endoscopic instruments," *Operative Neurosurgery*, vol. 12, no. 3, pp. 231–238, 2015.

[34] A. Carpentier, D. Loulmet, B. Aupecle, J. Kieffer, D. Tournay, P. Guibourt, A. Fiemeyer, D. Meleard, P. Richomme, and C. Cardon, "Computer assisted open heart surgery. first case operated on with success," *Comptes rendus de l'Academie des sciences. Serie III, Sciences de la vie*, vol. 321, no. 5, pp. 437–442, 1998.

[35] F. W. Mohr, V. Falk, A. Diegeler, and R. Autschback, "Computer-enhanced coronary artery bypass surgery," *The Journal of thoracic and cardiovascular surgery*, vol. 117, no. 6, pp. 1212–1214, 1999.

[36] D. H. Boehm, H. Reichenspurner, H. Gulbins, C. Detter, B. Meiser, P. Brenner, H. Habazettl, and B. Reichart, "Early experience with robotic technology for coronary artery surgery," *The Annals of thoracic surgery*, vol. 68, no. 4, pp. 1542–1546, 1999.

[37] M. D. Diodato and R. J. Damiano, "Robotic cardiac surgery: Overview," *Surgical Clinics*, vol. 83, no. 6, pp. 1351–1367, 2003.

[38] A. Pourdjabbar, L. Ang, R. R. Reeves, M. P. Patel, and E. Mahmud, "The development of robotic technology in cardiac and vascular interventions," *Rambam Maimonides medical journal*, vol. 8, no. 3, 2017.

[39] A. Ali, D. H. Plettenburg, and P. Breedveld, "Steerable catheters in cardiology: Classifying steerability and assessing future challenges," *IEEE Transactions on Biomedical Engineering*, vol. 63, no. 4, pp. 679–693, 2016.

[40] W. Ram and H. Meyer, "Heart catheterization in a neonate by interacting magnetic fields: A new and simple method of catheter guidance," *Catheterization and cardiovascular diagnosis*, vol. 22, no. 4, pp. 317–319, 1991.

[41] M. N. Faddis, W. Blume, J. Finney, A. Hall, J. Rauch, J. Sell, K. T. Bae, M. Talcott, and B. Lindsay, "Novel, magnetically guided catheter for endocardial mapping and

radiofrequency catheter ablation," *Circulation*, vol. 106, no. 23, pp. 2980–2985, 2002.

[42] S. Ernst, F. Ouyang, C. Linder, K. Hertting, F. Stahl, J. Chun, H. Hachiya, D. Bänsch, M. Antz, and K.-H. Kuck, "Initial experience with remote catheter ablation using a novel magnetic navigation system: Magnetic remote catheter ablation," *Circulation*, vol. 109, no. 12, pp. 1472–1475, 2004.

[43] S. Ernst, F. Ouyang, C. Linder, K. Hertting, F. Stahl, J. Chun, H. Hachiya, U. Krumsdorf, M. Antz, and K.-H. Kuck, "Modulation of the slow pathway in the presence of a persistent left superior caval vein using the novel magnetic navigation system niobe," *EP Europace*, vol. 6, no. 1, pp. 10–14, 2004.

[44] C. Pappone, G. Vicedomini, F. Manguso, F. Gugliotta, P. Mazzone, S. Gulletta, N. Sora, S. Sala, A. Marzi, G. Augello, *et al.*, "Robotic magnetic navigation for atrial fibrillation ablation," *Journal of the American College of Cardiology*, vol. 47, no. 7, pp. 1390–1400, 2006.

[45] J. K.-R. Chun, S. Ernst, S. Matthews, B. Schmidt, D. Bansch, S. Boczor, A. Ujeyl, M. Antz, F. Ouyang, and K.-H. Kuck, "Remote-controlled catheter ablation of accessory pathways: Results from the magnetic laboratory," *European heart journal*, vol. 28, no. 2, pp. 190–195, 2007.

[46] F. Kiemeneij, M. S. Patterson, G. Amoroso, G. Laarman, and T. Slagboom, "Use of the stereotaxis niobe® magnetic navigation system for percutaneous coronary intervention: Results from 350 consecutive patients," *Catheterization and Cardiovascular Interventions*, vol. 71, no. 4, pp. 510–516, 2008.

[47] F. Carpi and C. Pappone, "Stereotaxis niobe® magnetic navigation system for endocardial catheter ablation and gastrointestinal capsule endoscopy," *Expert review of medical devices*, vol. 6, no. 5, pp. 487–498, 2009.

[48] J. Hwang, J.-y. Kim, and H. Choi, "A review of magnetic actuation systems and magnetically actuated guidewire-and catheter-based microrobots for vascular interventions," *Intelligent Service Robotics*, vol. 13, no. 1, pp. 1–14, 2020.

[49] G. Bassil, S. M. Markowitz, C. F. Liu, G. Thomas, J. E. Ip, B. B. Lerman, and J. W. Cheung, "Robotics for catheter ablation of cardiac arrhythmias: Current technologies and practical approaches," *Journal of cardiovascular electrophysiology*, vol. 31, no. 3, pp. 739–752, 2020.

[50] Jodie Elrod, *Anew option for catheter guidance control and imaging: Interview with jose l. merino, md, phd, fesc*, https://www.eplabdigest.com/articles/New-Option-Catheter-Guidance-Control-and-Imaging-Interview-Jose-L-Merino-MD-PhD-FESC, [Online].

[51] E. S. Gang, B. L. Nguyen, Y. Shachar, L. Farkas, L. Farkas, B. Marx, D. Johnson, M. C. Fishbein, C. Gaudio, and S. J. Kim, "Dynamically shaped magnetic fields: Initial animal validation of a new remote electrophysiology catheter guidance and control system," *Circulation: Arrhythmia and Electrophysiology*, vol. 4, no. 5, pp. 770–777, 2011.

[52] B. L. Nguyen, J. L. Merino, Y. Shachar, A. Estrada, D. Doiny, S. Castrejon, B. Marx, D. Johnson, W. Marfori, and E. S. Gang, "Non-fluoroscopic transseptal catheterization during electrophysiology procedures using a remote magnetic navigation system," *Journal of atrial fibrillation*, vol. 6, no. 4, 2013.

[53] D. Filgueiras-Rama, A. Estrada, J. Shachar, S. Castrejón, D. Doiny, M. Ortega, E. Gang, and J. L. Merino, "Remote magnetic navigation for accurate, real-time catheter positioning and ablation in cardiac electrophysiology procedures," *Journal of visualized experiments: JoVE*, no. 74, 2013.

[54] M. P. Kummer, J. J. Abbott, B. E. Kratochvil, R. Borer, A. Sengul, and B. J. Nelson, "Octomag: An electromagnetic system for 5-dof wireless micromanipulation," *IEEE Transactions on Robotics*, vol. 26, no. 6, pp. 1006–1017, 2010.

[55] B. E. Kratochvil, M. P. Kummer, S. Erni, R. Borer, D. R. Frutiger, S. Schürle, and B. J. Nelson, "Minimag: A hemispherical electromagnetic system for 5-dof wireless micromanipulation," in *Experimental Robotics*, Springer, 2014, pp. 317–329.

[56] S. Jeon, A. K. Hoshiar, S. Kim, S. Lee, E. Kim, S. Lee, K. Kim, J. Lee, J.-y. Kim, and H. Choi, "Improving guidewire-mediated steerability of a magnetically actuated flexible microrobot," *Micro and Nano Systems Letters*, vol. 6, no. 1, pp. 1–10, 2018.

[57] S. Jeon, A. K. Hoshiar, K. Kim, S. Lee, E. Kim, S. Lee, J.-y. Kim, B. J. Nelson, H.-J. Cha, B.-J. Yi, *et al.*, "A magnetically controlled soft microrobot steering a guidewire in a three-dimensional phantom vascular network," *Soft robotics*, vol. 6, no. 1, pp. 54–68, 2019.

[58] C. Chautems and B. J. Nelson, "The tethered magnet: Force and 5-dof pose control for cardiac ablation," in *2017 IEEE international conference on robotics and automation (ICRA)*, IEEE, 2017, pp. 4837–4842.

[59] J. Sikorski, I. Dawson, A. Denasi, E. E. Hekman, and S. Misra, "Introducing bigmag—a novel system for 3d magnetic actuation of flexible surgical manipulators," in *2017 IEEE International Conference on Robotics and Automation (ICRA)*, IEEE, 2017, pp. 3594–3599.

[60] V. Lalande, F. P. Gosselin, M. Vonthron, B. Conan, C. Tremblay, G. Beaudoin, G. Soulez, and S. Martel, "In vivo demonstration of magnetic guidewire steerability in a mri system with additional gradient coils," *Medical physics*, vol. 42, no. 2, pp. 969–976, 2015.

[61] J. Sikorski, A. Denasi, G. Bucchi, S. Scheggi, and S. Misra, "Vision-based 3-d control of magnetically actuated catheter using bigmag—an array of mobile electromagnetic coils," *IEEE/ASME transactions on mechatronics*, vol. 24, no. 2, pp. 505–516, 2019.

[62] M. Richter, V. K. Venkiteswaran, and S. Misra, "Multi-point orientation control of discretely-magnetized continuum manipulators," *IEEE Robotics and Automation Letters*, vol. 6, no. 2, pp. 3607–3614, 2021.

[63] Y. Kim, G. A. Parada, S. Liu, and X. Zhao, "Ferromagnetic soft continuum robots," *Science Robotics*, vol. 4, no. 33, eaax7329, 2019.

[64] B. L. Nguyen, J. L. Merino, and E. S. Gang, "Remote navigation for ablation procedures–a new step forward in the treatment of cardiac arrhythmias," *European Cardiology*, vol. 6, no. 3, pp. 50–56, 2010.

[65] R. Beyar, L. Gruberg, D. Deleanu, A. Roguin, Y. Almagor, S. Cohen, G. Kumar, and T. Wenderow, "Remote-control percutaneous coronary interventions: Concept, validation, and first-in-humans pilot clinical trial," *Journal of the American College of Cardiology*, vol. 47, no. 2, pp. 296–300, 2006.

[66] Y. Haga, T. Mineta, and M. Esashi, "Active catheter, active guide wire and related sensor systems," in *Automation Congress, 2002 Proceedings of the 5th Biannual World*, IEEE, vol. 14, 2002, pp. 291–296.

[67] E. Ayvali and J. P. Desai, "Towards a discretely actuated steerable cannula," in *2012 IEEE international conference on robotics and automation*, IEEE, 2012, pp. 1614–1619.

[68] T. Mineta, T. Mitsui, Y. Watanabe, S. Kobayashi, Y. Haga, and M. Esashi, "An active guide wire with shape memory alloy bending actuator fabricated by room temperature process," *Sensors and Actuators A: Physical*, vol. 97, pp. 632–637, 2002.

[69] J. Abadie, N. Chaillet, and C. Lexcellent, "Modeling of a new sma micro-actuator for active endoscopy applications," *Mechatronics*, vol. 19, no. 4, pp. 437–442, 2009.

[70] A. T. Tung, B.-H. Park, A. Koolwal, B. Nelson, G. Niemeyer, and D. Liang, "Design and fabrication of tubular shape memory alloy actuators for active catheters,"

in *The First IEEE/RAS-EMBS International Conference on Biomedical Robotics and Biomechatronics, 2006. BioRob 2006.*, IEEE, 2006, pp. 775–780.

[71] E. Ayvali, C.-P. Liang, M. Ho, Y. Chen, and J. P. Desai, "Towards a discretely actuated steerable cannula for diagnostic and therapeutic procedures," *The International journal of robotics research*, vol. 31, no. 5, pp. 588–603, 2012.

[72] J.-E. Shim, Y.-J. Quan, W. Wang, H. Rodrigue, S.-H. Song, and S.-H. Ahn, "A smart soft actuator using a single shape memory alloy for twisting actuation," *Smart Materials and Structures*, vol. 24, no. 12, p. 125 033, 2015.

[73] J. Sheng, X. Wang, T.-M. L. Dickfeld, and J. P. Desai, "Towards the development of a steerable and MRI-compatible cardiac catheter for atrial fibrillation treatment," *IEEE robotics and automation letters*, vol. 3, no. 4, pp. 4038–4045, 2018.

[74] K. Ikuta, H. Ichikawa, and K. Suzuki, "Safety-active catheter with multiple-segments driven by micro-hydraulic actuators," in *International Conference on Medical Image Computing and Computer-Assisted Intervention*, Springer, 2002, pp. 182–191.

[75] K. Ikuta, Y. Matsuda, D. Yajima, and Y. Ota, "Pressure pulse drive: A control method for the precise bending of hydraulic active catheters," *IEEE/ASME Transactions on Mechatronics*, vol. 17, no. 5, pp. 876–883, 2011.

[76] M. Ikeuchi and K. Ikuta, "Membrane micro emboss following excimer laser ablation (meme-x) process for pressure-driven micro active catheter," in *Micro Electro Mechanical Systems, 2008. MEMS 2008. IEEE 21st International Conference on*, IEEE, 2008, pp. 62–65.

[77] Y. Haga, Y. Muyari, T. Mineta, T. Matsunaga, H. Akahori, and M. Esashi, "Small diameter hydraulic active bending catheter using laser processed super elastic alloy and silicone rubber tube," in *Microtechnology in Medicine and Biology, 2005. 3rd IEEE/EMBS Special Topic Conference on*, IEEE, 2005, pp. 245–248.

[78] H. Clogenson, J. Dankelman, and J. van den Dobbelsteen, "Steerable guidewire for magnetic resonance guided endovascular interventions," *Journal of Medical Devices*, vol. 8, no. 2, p. 021 002, 2014.

[79] H. Clogenson, A. Simonetto, and J. van den Dobbelsteen, "Design optimization of a deflectable guidewire," *Medical engineering & physics*, vol. 37, no. 1, pp. 138–144, 2015.

[80] A. Al-Ahmad, J. D. Grossman, and P. J. Wang, "Early experience with a computerized robotically controlled catheter system," *Journal of Interventional Cardiac Electrophysiology*, vol. 12, no. 3, pp. 199–202, 2005.

[81] W. Saliba, J. E. Cummings, S. Oh, Y. Zhang, T. N. Mazgalev, R. A. Schweikert, J. D. Burkhardt, and A. Natale, "Novel robotic catheter remote control system: Feasibility and safety of transseptal puncture and endocardial catheter navigation," *Journal of cardiovascular electrophysiology*, vol. 17, no. 10, pp. 1102–1105, 2006.

[82] W. Saliba, V. Y. Reddy, O. Wazni, J. E. Cummings, J. D. Burkhardt, M. Haissaguerre, J. Kautzner, P. Peichl, P. Neuzil, V. Schibgilla, *et al.*, "Atrial fibrillation ablation using a robotic catheter remote control system: Initial human experience and long-term follow-up results," *Journal of the American College of Cardiology*, vol. 51, no. 25, pp. 2407–2411, 2008.

[83] P. Kanagaratnam, M. Koa-Wing, D. T. Wallace, A. S. Goldenberg, N. S. Peters, and D. W. Davies, "Experience of robotic catheter ablation in humans using a novel remotely steerable catheter sheath," *Journal of Interventional Cardiac Electrophysiology*, vol. 21, no. 1, pp. 19–26, 2008.

[84] C. V. Riga, N. J. Cheshire, M. S. Hamady, and C. D. Bicknell, "The role of robotic endovascular catheters in fenestrated stent grafting," *Journal of vascular surgery*, vol. 51, no. 4, pp. 810–820, 2010.

[85] C. Duran, A. B. Lumsden, and J. Bismuth, "A randomized, controlled animal trial demonstrating the feasibility and safety of the magellan™ endovascular robotic system," *Annals of vascular surgery*, vol. 28, no. 2, pp. 470–478, 2014.

[86] C. V. Riga, C. D. Bicknell, A. Rolls, N. J. Cheshire, and M. S. Hamady, "Robot-assisted fenestrated endovascular aneurysm repair (fevar) using the magellan system," *Journal of Vascular and Interventional Radiology*, vol. 24, no. 2, pp. 191–196, 2013.

[87] W. Clements, M. Scicchitano, J. Koukounaras, T. Joseph, and G. S. Goh, "Use of the magellan robotic system for conventional transarterial chemoembolization (ctace): A 6-patient case series showing safety and technical success," *J. Clin. Intervent. Radiol. ISVIR*, vol. 3, no. 02, pp. 142–146, 2019.

[88] A. E. Rolls, C. V. Riga, C. D. Bicknell, L. Regan, N. J. Cheshire, and M. S. Hamady, "Robot-assisted uterine artery embolization: A first-in-woman safety evaluation of the magellan system," *Journal of Vascular and Interventional Radiology*, vol. 25, no. 12, pp. 1841–1848, 2014.

[89] Y. Kim, S. S. Cheng, M. Diakite, R. P. Gullapalli, J. M. Simard, and J. P. Desai, "Toward the development of a flexible mesoscale mri-compatible neurosurgical continuum robot," *IEEE Transactions on Robotics*, vol. 33, no. 6, pp. 1386–1397, 2017.

[90] D. B. Camarillo, C. R. Carlson, and J. K. Salisbury, "Configuration tracking for continuum manipulators with coupled tendon drive," *IEEE Transactions on Robotics*, vol. 25, no. 4, pp. 798–808, 2009.

[91] Y. Kim, S. S. Cheng, and J. P. Desai, "Towards the development of a spring-based continuum robot for neurosurgery," in *Medical Imaging 2015: Image-Guided Procedures, Robotic Interventions, and Modeling*, International Society for Optics and Photonics, vol. 9415, 2015, 94151Q.

[92] B. L. Conrad and M. R. Zinn, "Interleaved continuum-rigid manipulation: An approach to increase the capability of minimally invasive surgical systems," *IEEE/ASME Transactions on Mechatronics*, vol. 22, no. 1, pp. 29–40, 2016.

[93] R. Roy, L. Wang, and N. Simaan, "Modeling and estimation of friction, extension, and coupling effects in multisegment continuum robots," *IEEE/ASME Transactions on Mechatronics*, vol. 22, no. 2, pp. 909–920, 2017.

[94] Y. S. Kwoh, J. Hou, E. A. Jonckheere, and S. Hayati, "A robot with improved absolute positioning accuracy for ct guided stereotactic brain surgery," *IEEE Transactions on Biomedical Engineering*, vol. 35, no. 2, pp. 153–160, 1988.

[95] J. M. Drake, M. Joy, A. Goldenberg, and D. Kreindler, "Computer-and robot-assisted resection of thalamic astrocytomas in children," *Neurosurgery*, vol. 29, no. 1, pp. 27–33, 1991.

[96] H. Fankhauser, D. Glauser, P. Flury, Y. Piguet, M. Epitaux, J. Favre, and R. Meuli, "Robot for ct-guided stereotactic neurosurgery," *Stereotactic and functional neurosurgery*, vol. 63, no. 1-4, pp. 93–98, 1994.

[97] D. Glauser, P. Flury, and C. Burckhardt, "Mechanical concept of the neurosurgical robot 'minerva'," *Robotica*, vol. 11, no. 6, pp. 567–575, 1993.

[98] D. Glauser, H. Fankhauser, M. Epitaux, J.-L. Hefti, and A. Jaccottet, "Neurosurgical robot minerva: First results and current developments," *Journal of image guided surgery*, vol. 1, no. 5, pp. 266–272, 1995.

[99] K. Cleary and C. Nguyen, "State of the art in surgical robotics: Clinical applications and technology challenges," *Computer Aided Surgery*, vol. 6, no. 6, pp. 312–328, 2001.

[100] Q. H. Li, L. Zamorano, A. Pandya, R. Perez, J. Gong, and F. Diaz, "The application accuracy of the neuromate robot—a quantitative comparison with frameless and frame-based surgical localization systems," *Computer Aided Surgery*, vol. 7, no. 2, pp. 90–98, 2002.

[101] D. von Langsdorff, P. Paquis, and D. Fontaine, "In vivo measurement of the frame-based application accuracy of the neuromate neurosurgical robot," *Journal of neurosurgery*, vol. 122, no. 1, pp. 191–194, 2015.

[102] T. Varma and P. Eldridge, "Use of the neuromate stereotactic robot in a frameless mode for functional neurosurgery," *The International Journal of Medical Robotics and Computer Assisted Surgery*, vol. 2, no. 2, pp. 107–113, 2006.

[103] B. Jerbić, G. Nikolić, D. Chudy, M. Švaco, and B. Šekoranja, "Robotic application in neurosurgery using intelligent visual and haptic interaction," *International journal of simulation modelling*, vol. 14, no. 1, pp. 71–84, 2015.

[104] M. Švaco, B. Šekoranja, F. Šuligoj, J. Vidaković, B. Jerbić, and D. Chudy, "A novel robotic neuronavigation system: Ronna g3," *Strojniški Vestnik/Journal of Mechanical Engineering*, vol. 63, no. 12, pp. 725–735, 2017.

[105] D. Dlaka, M. Švaco, D. Chudy, B. Jerbić, B. Šekoranja, F. Šuligoj, J. Vidaković, F. Almahariq, and D. Romić, "Brain biopsy performed with the ronna g3 system: A case study on using a novel robotic navigation device for stereotactic neurosurgery," *The International Journal of Medical Robotics and Computer Assisted Surgery*, vol. 14, no. 1, e1884, 2018.

[106] B. Jerbić, M. Švaco, D. Chudy, B. Šekoranja, F. Šuligoj, J. Vidaković, D. Dlaka, N. Vitez, I. Župančić, L. Drobilo, *et al.*, "Ronna g4—robotic neuronavigation: A novel robotic navigation device for stereotactic neurosurgery," in *Handbook of Robotic and Image-Guided Surgery*, Elsevier, 2020, pp. 599–625.

[107] M. Lefranc, C. Capel, A.-S. Pruvot-Occean, A. Fichten, C. Desenclos, P. Toussaint, D. Le Gars, and J. Peltier, "Frameless robotic stereotactic biopsies: A consecutive series of 100 cases," *Journal of neurosurgery*, vol. 122, no. 2, pp. 342–352, 2015.

[108] S. Vadera, A. Chan, T. Lo, A. Gill, A. Morenkova, N. M. Phielipp, N. Hermanowicz, and F. P. Hsu, "Frameless stereotactic robot-assisted subthalamic nucleus deep brain stimulation: Case report," *World neurosurgery*, vol. 97, 762–e11, 2017.

[109] C. Neudorfer, S. Hunsche, M. Hellmich, F. El Majdoub, and M. Maarouf, "Comparative study of robot-assisted versus conventional frame-based deep brain stimulation stereotactic neurosurgery," *Stereotactic and functional neurosurgery*, vol. 96, no. 5, pp. 327–334, 2018.

[110] A. De Benedictis, A. Trezza, A. Carai, E. Genovese, E. Procaccini, R. Messina, F. Randi, S. Cossu, G. Esposito, P. Palma, *et al.*, "Robot-assisted procedures in pediatric neurosurgery," *Neurosurgical focus*, vol. 42, no. 5, E7, 2017.

[111] D. Y. Dadey, A. A. Kamath, E. C. Leuthardt, and M. D. Smyth, "Laser interstitial thermal therapy for subependymal giant cell astrocytoma: Technical case report," *Neurosurgical focus*, vol. 41, no. 4, E9, 2016.

[112] M. Zimmermann, R. Krishnan, A. Raabe, and V. Seifert, "Robot-assisted navigated endoscopic ventriculostomy: Implementation of a new technology and first clinical results," *Acta neurochirurgica*, vol. 146, no. 7, pp. 697–704, 2004.

[113] E. J. Butler, R. Hammond-Oakley, S. Chawarski, A. H. Gosline, P. Codd, T. Anor, J. R. Madsen, P. E. Dupont, and J. Lock, "Robotic neuro-emdoscope with concentric tube augmentation," in *2012 IEEE/RSJ International Conference on Intelligent Robots and Systems*, IEEE, 2012, pp. 2941–2946.

[114] K. W. Eastwood, T. Looi, H. E. Naguib, and J. M. Drake, "Design optimization of neuroendoscopic continuum instruments for third ventriculostomy and tumor biopsy," in *Engineering in Medicine and Biology Society (EMBC), 2015 37th Annual International Conference of the IEEE*, IEEE, 2015, pp. 4853–4856.

[115] P. E. Dupont, S. Chawarski, E. J. Butler, R. Hammond-Oakley, A. H. Gosline, P. Codd, T. Anor, J. R. Madsen, and J. Lock, "Extending the reach and stability of manually steerable neuroendoscopes through robotics," in *Proceedings of Hamlyn Symposium, London*, 2012.

[116] J. Wang, J. Ha, and P. E. Dupont, "Steering a multi-armed robotic sheath using eccentric precurved tubes," in *2019 International Conference on Robotics and Automation (ICRA)*, IEEE, 2019, pp. 9834–9840.

[117] K. W. Eastwood, H. Azimian, B. Carrillo, T. Looi, H. E. Naguib, and J. M. Drake, "Kinetostatic design of asymmetric notch joints for surgical robots," in *2016 IEEE/RSJ International Conference on Intelligent Robots and Systems (IROS)*, IEEE, 2016, pp. 2381–2387.

[118] T. Kato, I. Okumura, S.-E. Song, A. J. Golby, and N. Hata, "Tendon-driven continuum robot for endoscopic surgery: Preclinical development and validation of a tension propagation model," *IEEE/ASME Transactions on Mechatronics*, vol. 20, no. 5, pp. 2252–2263, 2015.

[119] F. Jelınek, E. A. Arkenbout, P. W. Henselmans, R. Pessers, and P. Breedveld, "Classification of joints used in steerable instruments for minimally invasive surgery," *Journal of Medical Devices*, vol. 8, no. 3, p. 030 914, 2014.

[120] F. Jelinek, E. A. Arkenbout, P. W. Henselmans, R. Pessers, and P. Breedveld, "Classification of joints used in steerable instruments for minimally invasive surgery—a review of the state of the art," *Journal of Medical Devices*, vol. 9, no. 1, p. 010 801, 2015.

[121] K. W. Eastwood, P. Francis, H. Azimian, A. Swarup, T. Looi, J. M. Drake, and H. E. Naguib, "Design of a contact-aided compliant notched-tube joint for surgical manipulation in confined workspaces," *Journal of Mechanisms and Robotics*, vol. 10, no. 1, p. 015 001, 2018.

[122] P. A. York, P. J. Swaney, H. B. Gilbert, and R. J. Webster, "A wrist for needle-sized surgical robots," in *Robotics and Automation (ICRA), 2015 IEEE International Conference on*, IEEE, 2015, pp. 1776–1781.

[123] T. Kato, I. Okumura, H. Kose, K. Takagi, and N. Hata, "Extended kinematic mapping of tendon-driven continuum robot for neuroendoscopy," in *Intelligent Robots and Systems (IROS 2014), 2014 IEEE/RSJ International Conference on*, IEEE, 2014, pp. 1997–2002.

[124] S. Coemert, A. Gao, J. P. Carey, M. F. Traeger, R. H. Taylor, T. C. Lueth, and M. Armand, "Development of a snake-like dexterous manipulator for skull base surgery," in *2016 38th Annual International Conference of the IEEE Engineering in Medicine and Biology Society (EMBC)*, IEEE, 2016, pp. 5087–5090.

[125] A. Gao, J. P. Carey, R. J. Murphy, I. Iordachita, R. H. Taylor, and M. Armand, "Progress toward robotic surgery of the lateral skull base: Integration of a dexterous continuum manipulator and flexible ring curette," in *2016 IEEE International Conference on Robotics and Automation (ICRA)*, IEEE, 2016, pp. 4429–4435.

[126] Y. Gao, K. Takagi, T. Kato, N. Shono, and N. Hata, "Continuum robot with follow the leader motion for endoscopic third ventriculostomy and tumor biopsy," *IEEE Transactions on Biomedical Engineering*, 2019.

[127] K. Xu and N. Simaan, "An investigation of the intrinsic force sensing capabilities of continuum robots," *IEEE Transactions on Robotics*, vol. 24, no. 3, pp. 576–587, 2008.

[128] A. Bajo and N. Simaan, "Kinematics-based detection and localization of contacts along multisegment continuum robots," *IEEE Transactions on Robotics*, vol. 28, no. 2, pp. 291–302, 2011.

[129] R. Leach, *Fundamental principles of engineering nanometrology*. Elsevier, 2014.

[130] P. J. Kyberd and P. H. Chappell, "A force sensor for automatic manipulation based on the hall effect," *Measurement Science and Technology*, vol. 4, no. 3, p. 281, 1993.

[131] Y. Amarasinghe, A. Kulasekera, and T. Priyadarshana, "Quantum tunneling composite (qtc) based tactile sensor array for dynamic pressure distribution measure-

ment," in *2013 Seventh International Conference on Sensing Technology (ICST)*, IEEE, 2013, pp. 1–4.

[132] D. Tsetserukou, R. Tadakuma, H. Kajimoto, and S. Tachi, "Optical torque sensors for implementation of local impedance control of the arm of humanoid robot," in *Proceedings 2006 IEEE International Conference on Robotics and Automation, 2006. ICRA 2006.*, IEEE, 2006, pp. 1674–1679.

[133] S. Shams, J. Y. Lee, and C. Han, "Compact and lightweight optical torque sensor for robots with increased range," *Sensors and Actuators A: Physical*, vol. 173, no. 1, pp. 81–89, 2012.

[134] G. M. Gu, Y. K. Shin, J. Son, and J. Kim, "Design and characterization of a photosensor based force measurement unit (fmu)," *Sensors and Actuators A: Physical*, vol. 182, pp. 49–56, 2012.

[135] J.-C. Kim, K.-S. Kim, and S. Kim, "Note: A compact three-axis optical force/torque sensor using photo-interrupters," *Review of Scientific Instruments*, vol. 84, no. 12, p. 126 109, 2013.

[136] A. A. Potdar, S. Fletcher, and A. P. Longstaff, "Performance characterisation of a new photo-microsensor based sensing head for displacement measurement," *Sensors and Actuators A: Physical*, vol. 238, pp. 60–70, 2016.

[137] S. H. Jeong, H. J. Lee, K.-R. Kim, and K.-S. Kim, "Design of a miniature force sensor based on photointerrupter for robotic hand," *Sensors and Actuators A: Physical*, vol. 269, pp. 444–453, 2018.

[138] Y. Liu, T. Tian, J. Chen, F. Wang, and D. Zhang, "A highly reliable embedded optical torque sensor based on flexure spring," *Applied bionics and biomechanics*, vol. 2018, 2018.

[139] Y. Shan, J. E. Speich, and K. K. Leang, "Low-cost ir reflective sensors for submicrolevel position measurement and control," *IEEE/ASME transactions on mechatronics*, vol. 13, no. 6, pp. 700–709, 2008.

[140] Y. Noh, J. Bimbo, S. Sareh, H. Wurdemann, J. Fraś, D. Chathuranga, H. Liu, J. Housden, K. Althoefer, and K. Rhode, "Multi-axis force/torque sensor based on simply-supported beam and optoelectronics," *Sensors*, vol. 16, no. 11, p. 1936, 2016.

[141] S. Hirose and K. Yoneda, "Development of optical six-axial force sensor and its signal calibration considering nonlinear interference," in *Proceedings., IEEE International Conference on Robotics and Automation*, IEEE, 1990, pp. 46–53.

[142] G. Palli and S. Pirozzi, "A miniaturized optical force sensor for tendon-driven mechatronic systems: Design and experimental evaluation," *Mechatronics*, vol. 22, no. 8, pp. 1097–1111, 2012.

[143] P. J. Berkelman, L. L. Whitcomb, R. H. Taylor, and P. Jensen, "A miniature microsurgical instrument tip force sensor for enhanced force feedback during robot-assisted manipulation," *IEEE Transactions on Robotics and Automation*, vol. 19, no. 5, pp. 917–921, 2003.

[144] J. Peirs, J. Clijnen, D. Reynaerts, H. Van Brussel, P. Herijgers, B. Corteville, and S. Boone, "A micro optical force sensor for force feedback during minimally invasive robotic surgery," *Sensors and Actuators A: Physical*, vol. 115, no. 2-3, pp. 447–455, 2004.

[145] L. Jiang, K. Low, J. Costa, R. J. Black, and Y.-L. Park, "Fiber optically sensorized multi-fingered robotic hand," in *2015 IEEE/RSJ International Conference on Intelligent Robots and Systems (IROS)*, IEEE, 2015, pp. 1763–1768.

[146] H. Xie, A. Jiang, H. A. Wurdemann, H. Liu, L. D. Seneviratne, and K. Althoefer, "Magnetic resonance-compatible tactile force sensor using fiber optics and vision sensor," *IEEE Sensors Journal*, vol. 14, no. 3, pp. 829–838, 2013.

[147] W. Yuan, S. Dong, and E. Adelson, "Gelsight: High-resolution robot tactile sensors for estimating geometry and force," *Sensors*, vol. 17, no. 12, p. 2762, 2017.

[148] S. H. Jeong, K.-S. Kim, and S. Kim, "Designing anthropomorphic robot hand with active dual-mode twisted string actuation mechanism and tiny tension sensors," *IEEE Robotics and Automation Letters*, vol. 2, no. 3, pp. 1571–1578, 2017.

[149] G. Palli and S. Pirozzi, "Force sensor based on discrete optoelectronic components and compliant frames," *Sensors and Actuators A: Physical*, vol. 165, no. 2, pp. 239–249, 2011.

[150] C. Shi, X. Luo, P. Qi, T. Li, S. Song, Z. Najdovski, H. Ren, and T. Fukuda, "Shape sensing techniques for continuum robots in minimally invasive surgery: A survey," *IEEE Transactions on Biomedical Engineering*, 2016.

[151] A. M. Franz, T. Haidegger, W. Birkfellner, K. Cleary, T. M. Peters, and L. Maier-Hein, "Electromagnetic tracking in medicine—a review of technology, validation, and applications," *IEEE transactions on medical imaging*, vol. 33, no. 8, pp. 1702–1725, 2014.

[152] E. J. Lobaton, J. Fu, L. G. Torres, and R. Alterovitz, "Continuous shape estimation of continuum robots using x-ray images," in *Proceedings 2013 IEEE International Conference on Robotics and Automation (ICRA)*, IEEE, 2013, pp. 725–732.

[153] J. Burgner, S. D. Herrell, and R. J. Webster, "Toward fluoroscopic shape reconstruction for control of steerable medical devices," in *ASME 2011 Dynamic Systems and Control Conference and Bath/ASME Symposium on Fluid Power and Motion Control*, American Society of Mechanical Engineers Digital Collection, 2012, pp. 791–794.

[154] K. O. Hill and G. Meltz, "Fiber bragg grating technology fundamentals and overview," *Journal of lightwave technology*, vol. 15, no. 8, pp. 1263–1276, 1997.

[155] R. J. Roesthuis, M. Kemp, J. J. van den Dobbelsteen, and S. Misra, "Three-dimensional needle shape reconstruction using an array of fiber bragg grating sensors," *IEEE/ASME transactions on mechatronics*, vol. 19, no. 4, pp. 1115–1126, 2013.

[156] F. Araújo, L. Ferreira, J. Santos, and F. Farahi, "Temperature and strain insensitive bending measurements with d-type fibre bragg gratings," *Measurement Science and Technology*, vol. 12, no. 7, p. 829, 2001.

[157] O. Okhotnikov, F. Araújo, and J. Salcedo, "Wavelength switching in pump-diode-modulated mode-locked and q-switched er-fiber laser," *Applied physics letters*, vol. 65, no. 23, pp. 2910–2912, 1994.

[158] R. Reilink, S. Stramigioli, and S. Misra, "3d position estimation of flexible instruments: Marker-less and marker-based methods," *International journal of computer assisted radiology and surgery*, vol. 8, no. 3, pp. 407–417, 2013.

[159] R. Xu, A. Yurkewich, and R. V. Patel, "Curvature, torsion, and force sensing in continuum robots using helically wrapped fbg sensors," *IEEE Robotics and Automation Letters*, vol. 1, no. 2, pp. 1052–1059, 2016.

[160] H. Liu, A. Farvardin, S. A. Pedram, I. Iordachita, R. H. Taylor, and M. Armand, "Large deflection shape sensing of a continuum manipulator for minimally-invasive surgery," in *2015 IEEE International Conference on Robotics and Automation (ICRA)*, IEEE, 2015, pp. 201–206.

[161] H. Liu, A. Farvardin, R. Grupp, R. J. Murphy, R. H. Taylor, I. Iordachita, and M. Armand, "Shape tracking of a dexterous continuum manipulator utilizing two large deflection shape sensors," *IEEE sensors journal*, vol. 15, no. 10, pp. 5494–5503, 2015.

[162] S. Sefati, F. Alambeigi, I. Iordachita, M. Armand, and R. J. Murphy, "Fbg-based large deflection shape sensing of a continuum manipulator: Manufacturing optimization," in *2016 IEEE SENSORS*, IEEE, 2016, pp. 1–3.

[163] J. Sheng, N. J. Deaton, and J. P. Desai, "A large-deflection fbg bending sensor for sma bending modules for steerable surgical robots," in *2019 International Conference on Robotics and Automation (ICRA)*, IEEE, 2019, pp. 900–906.

[164] S. Sefati, R. Hegeman, F. Alambeigi, I. Iordachita, and M. Armand, "Fbg-based position estimation of highly deformable continuum manipulators: Model-dependent vs. data-driven approaches," in *2019 International Symposium on Medical Robotics (ISMR)*, IEEE, 2019, pp. 1–6.

[165] F. Cepolina and R. Michelini, "Review of robotic fixtures for minimally invasive surgery," *The international Journal of Medical Robotics and Computer Assisted Surgery*, vol. 1, no. 1, pp. 43–63, 2004.

[166] J. Catherine, C. Rotinat-Libersa, and A. Micaelli, "Comparative review of endoscopic devices articulations technologies developed for minimally invasive medical procedures," *Applied Bionics and Biomechanics*, vol. 8, no. 2, pp. 151–171, 2011.

[167] Y. Haga, Y. Muyari, S. Goto, T. Matsunaga, and M. Esashi, "Development of minimally invasive medical tools using laser processing on cylindrical substrates," *Electrical Engineering in Japan*, vol. 176, no. 1, pp. 65–74, 2011.

[168] F. Dewaele, A. F. Kalmar, F. De Ryck, N. Lumen, L. Williams, E. Baert, H. Vereecke, J. P. Kalala Okito, C. Mabilde, B. Blanckaert, *et al.*, "A novel design for steerable instruments based on laser-cut nitinol," *Surgical innovation*, vol. 21, no. 3, pp. 303–311, 2014.

[169] S. C. Ryu, P. Renaud, R. J. Black, B. L. Daniel, and M. R. Cutkosky, "Feasibility study of an optically actuated mr-compatible active needle," in *Intelligent Robots and Systems (IROS), 2011 IEEE/RSJ International Conference on*, Ieee, 2011, pp. 2564–2569.

[170] J. Peirs, H. Van Brussel, D. Reynaerts, and G. De Gersem, "A flexible distal tip with two degrees of freedom for enhanced dexterity in endoscopic robot surgery," in *Proceedings of the 13th micromechanics europe workshop*, 2002, pp. 271–274.

[171] J. Peirs, D. Reynaerts, H. Van Brussel, G. De Gersem, and H.-W. Tang, "Design of an advanced tool guiding system for robotic surgery," in *Robotics and Automation, 2003. Proceedings. ICRA'03. IEEE International Conference on*, IEEE, vol. 2, 2003, pp. 2651–2656.

[172] T. Yoneyama, T. Watanabe, H. Kagawa, J.-i. Hamada, Y. Hayashi, and M. Nakada, "Force detecting gripper and flexible micro manipulator for neurosurgery," in *Engineering in Medicine and Biology Society, EMBC, 2011 Annual International Conference of the IEEE*, IEEE, 2011, pp. 6695–6699.

[173] J. Liu, B. Hall, M. Frecker, and E. W. Reutzel, "Compliant articulation structure using superelastic nitinol," *Smart materials and structures*, vol. 22, no. 9, p. 094 018, 2013.

[174] T. Kato, I. Okumura, H. Kose, K. Takagi, and N. Hata, "Tendon-driven continuum robot for neuroendoscopy: Validation of extended kinematic mapping for hysteresis operation," *International journal of computer assisted radiology and surgery*, vol. 11, no. 4, pp. 589–602, 2016.

[175] Y. Chitalia, X. Wang, and J. P. Desai, "Design, modeling and control of a 2-dof robotic guidewire," in *2018 IEEE International Conference on Robotics and Automation (ICRA)*, IEEE, 2018, pp. 32–37.

[176] A. C. Barnett, J. A. Jones, Y.-S. Lee, and J. Z. Moore, "Compliant needle vibration cutting of soft tissue," *Journal of Manufacturing Science and Engineering*, vol. 138, no. 11, p. 111 011, 2016.

[177] A. Gao, R. J. Murphy, H. Liu, I. I. Iordachita, and M. Armand, "Mechanical model of dexterous continuum manipulators with compliant joints and tendon/external force interactions," *IEEE/ASME Transactions on Mechatronics*, vol. 22, no. 1, pp. 465–475, 2017.

[178] J. A. Jones, Y.-S. Lee, and J. Z. Moore, "Parametric study for asymmetric flexure hinge design for tissue cutting," *Proceedings of the Institution of Mechanical Engineers, Part B: Journal of Engineering Manufacture*, p. 0 954 405 418 774 587, 2018.

[179] D. B. Camarillo, C. F. Milne, C. R. Carlson, M. R. Zinn, and J. K. Salisbury, "Mechanics modeling of tendon-driven continuum manipulators," *IEEE Transactions on Robotics*, vol. 24, no. 6, pp. 1262–1273, 2008.

[180] P. Breedveld, "Steerable laparoscopic cable-ring forceps," *Journal of Medical Devices*, vol. 4, no. 2, p. 027 518, 2010.

[181] R. J. Webster III and B. A. Jones, "Design and kinematic modeling of constant curvature continuum robots: A review," *The International Journal of Robotics Research*, vol. 29, no. 13, pp. 1661–1683, 2010.

[182] G. J. Vrooijink, A. Denasi, J. G. Grandjean, and S. Misra, "Model predictive control of a robotically actuated delivery sheath for beating heart compensation," *The International Journal of Robotics Research*, vol. 36, no. 2, pp. 193–209, 2017.

[183] G. J. Vrooijink, T. T. Ellenbroek, P. Breedveld, J. G. Grandjean, and S. Misra, "A preliminary study on using a robotically-actuated delivery sheath (rads) for

transapical aortic valve implantation," in *Robotics and Automation (ICRA), 2014 IEEE International Conference on*, IEEE, 2014, pp. 4380–4386.

[184] B. Siciliano, L. Sciavicco, L. Villani, and G. Oriolo, "Robotics: Modelling, planning and control, ser. advanced textbooks in control and signal processing," *Springer*, vol. 26, p. 29, 2009.

[185] T. Soyama, D. Yoshida, Y. Sakuhara, R. Morita, D. Abo, and K. Kudo, "The steerable microcatheter: A new device for selective catheterisation," *Cardiovascular and interventional radiology*, vol. 40, no. 6, pp. 947–952, 2017.

[186] K. Ikuta, M. Tsukamoto, and S. Hirose, "Shape memory alloy servo actuator system with electric resistance feedback and application for active endoscope," in *Proceedings. 1988 IEEE International Conference on Robotics and Automation*, Ieee, 1988, pp. 427–430.

[187] A. Degani, H. Choset, A. Wolf, and M. A. Zenati, "Highly articulated robotic probe for minimally invasive surgery," in *Proceedings 2006 IEEE International Conference on Robotics and Automation, 2006. ICRA 2006.*, IEEE, 2006, pp. 4167–4172.

[188] A. Degani, H. Choset, A. Wolf, T. Ota, and M. A. Zenati, "Percutaneous intrapericardial interventions using a highly articulated robotic probe," in *The First IEEE/RAS-EMBS International Conference on Biomedical Robotics and Biomechatronics, 2006. BioRob 2006.*, IEEE, 2006, pp. 7–12.

[189] T. Ota, A. Degani, D. Schwartzman, B. Zubiate, J. McGarvey, H. Choset, and M. A. Zenati, "A novel highly articulated robotic surgical system for epicardial ablation," in *2008 30th Annual International Conference of the IEEE Engineering in Medicine and Biology Society*, IEEE, 2008, pp. 250–253.

[190] P. Sears and P. Dupont, "A steerable needle technology using curved concentric tubes," in *2006 IEEE/RSJ international conference on intelligent robots and systems*, IEEE, 2006, pp. 2850–2856.

[191] R. J. Webster, A. M. Okamura, and N. J. Cowan, "Toward active cannulas: Miniature snake-like surgical robots," in *2006 IEEE/RSJ international conference on intelligent robots and systems*, IEEE, 2006, pp. 2857–2863.

[192] H. B. Gilbert and R. J. Webster, "Can concentric tube robots follow the leader?" In *2013 IEEE international conference on robotics and automation*, IEEE, 2013, pp. 4881–4887.

[193] H. B. Gilbert, J. Neimat, and R. J. Webster, "Concentric tube robots as steerable needles: Achieving follow-the-leader deployment," *IEEE Transactions on Robotics*, vol. 31, no. 2, pp. 246–258, 2015.

[194] A. Garriga-Casanovas and F. Rodriguez y Baena, "Complete follow-the-leader kinematics using concentric tube robots," *The International Journal of Robotics Research*, vol. 37, no. 1, pp. 197–222, 2018.

[195] R. J. Webster III, J. M. Romano, and N. J. Cowan, "Mechanics of precurved-tube continuum robots," *IEEE Transactions on Robotics*, vol. 25, no. 1, pp. 67–78, 2008.

[196] J.-S. Kim, D.-Y. Lee, K. Kim, S. Kang, and K.-J. Cho, "Toward a solution to the snapping problem in a concentric-tube continuum robot: Grooved tubes with anisotropy," in *2014 IEEE International Conference on Robotics and Automation (ICRA)*, IEEE, 2014, pp. 5871–5876.

[197] Y. Chitalia, X. Wang, V. Nguyen, S. Melkote, J. Chern, and J. P. Desai, "Design and analysis of a bidirectional notch joint for a robotic pediatric neuroendoscope," in *International Symposium on Experimental Robotics*, 2018 (in press).

[198] S. Jeong, Y. Chitalia, and J. P. Desai, "Miniature force sensor based on dual-photointerrupter with high linearity and disturbance compensation," *IEEE Sensors Journal*, vol. 20, no. 11, pp. 5855–5864, 2020.

[199] C. B. Bargeron, G. M. Hutchins, G. W. Moore, O. J. Deters, F. F. Mark, and M. H. Friedman, "Distribution of the geometric parameters of human aortic bifurcations.," *Arteriosclerosis: An Official Journal of the American Heart Association, Inc.*, vol. 6, no. 1, pp. 109–113, 1986.

[200] L. Chen, "An integral approach for large deflection cantilever beams," *International Journal of Non-Linear Mechanics*, vol. 45, no. 3, pp. 301–305, 2010.

[201] S. Ghuku and K. N. Saha, "A theoretical and experimental study on geometric nonlinearity of initially curved cantilever beams," *Engineering Science and Technology, an International Journal*, vol. 19, no. 1, pp. 135–146, 2016.

[202] P. E. Dupont, J. Lock, B. Itkowitz, and E. Butler, "Design and control of concentric-tube robots," *IEEE Transactions on Robotics*, vol. 26, no. 2, pp. 209–225, 2009.

[203] S. S. Cheng, X. Wang, and J. P. Desai, "Design and analysis of a remotely-actuated cable-driven neurosurgical robot," in *2017 IEEE/RSJ International Conference on Intelligent Robots and Systems (IROS)*, IEEE, 2017, pp. 1685–1690.

[204] S. Jeong, Y. Chitalia, and J. P. Desai, "Design, modeling, and control of a coaxially aligned steerable (coast) guidewire robot," *IEEE Robotics and Automation Letters*, vol. 5, no. 3, pp. 4947–4954, 2020.

[205] R. M. Murray, Z. Li, S. S. Sastry, and S. S. Sastry, *A Mathematical Introduction to Robotic Manipulation*. CRC press, 1994.

[206] J. J. Craig, *Introduction to Robotics: Mechanics and Control, 3/E*. Pearson Education India, 2009.

[207] Y. Chitalia, N. J. Deaton, S. Jeong, N. Rahman, and J. P. Desai, "Towards fbg-based shape sensing for micro-scale and meso-scale continuum robots with large deflection," *IEEE Robotics and Automation Letters*, 2020.

[208] L. Antiga, B. Ene-Iordache, and A. Remuzzi, "Centerline computation and geometric analysis of branching tubular surfaces with application to blood vessel modeling," 2003.

[209] J. Tervonen, V. Leinonen, J. E. Jääskeläinen, S. Koponen, and T. J. Huttunen, "Rate and risk factors for shunt revision in pediatric patients with hydrocephalus—a population-based study," *World neurosurgery*, vol. 101, pp. 615–622, 2017.

[210] H. W. Schroeder, "General principles and intraventricular neuroendoscopy: Endoscopic techniques," *World neurosurgery*, vol. 79, no. 2, S14–e23, 2013.

[211] P. E. Dupont, J. Lock, B. Itkowitz, and E. Butler, "Design and control of concentric-tube robots," *IEEE transactions on robotics: a publication of the IEEE Robotics and Automation Society*, vol. 26, no. 2, p. 209, 2010.

[212] Y. Chitalia, S. Jeong, J. Bok, V. Nguyen, S. Melkote, J. Chern, and J. P. Desai, "Towards the design and development of a pediatric neuroendoscope tool," in *Intelligent Robots and Systems (IROS), 2019 IEEE/RSJ International Conference on*, IEEE, 2019 (accepted).

[213] Y. Chitalia, X. Wang, and J. P. Desai, "Design, modeling and control of a 2-dof robotic guidewire," in *2018 IEEE International Conference on Robotics and Automation (ICRA)*, IEEE, 2018, pp. 32–37.

[214] E. Sariyildiz and K. Ohnishi, "A guide to design disturbance observer," *Journal of Dynamic Systems, Measurement, and Control*, vol. 136, no. 2, p. 021 011, 2014.

[215] Y. C. Chitalia, S. Jeong, N. Deaton, J. J. Chern, and J. P. Desai, "Design and kinematics analysis of a robotic pediatric neuroendoscope tool body," *IEEE/ASME Transactions on Mechatronics*, 2020.

[216] S. Jeong, Y. Chitalia, and J. P. Desai, "Miniature force sensor based on dual-photointerrupter with high linearity and disturbance compensation," *IEEE Sensors Journal*, pp. 1–1, 2020.

[217] R. Kusy and A. Stush, "Geometric and material parameters of a nickel-titanium and a beta titanium orthodontic arch wire alloy," *Dental Materials*, vol. 3, no. 4, pp. 207–217, 1987.

[218] J. M. McNaney, V. Imbeni, Y. Jung, P. Papadopoulos, and R. Ritchie, "An experimental study of the superelastic effect in a shape-memory nitinol alloy under biaxial loading," *Mechanics of materials*, vol. 35, no. 10, pp. 969–986, 2003.

[219] A. Saigal and M. Fonte, "Solid, shape recovered "bulk" nitinol: Part i—tension–compression asymmetry," *Materials Science and Engineering: A*, vol. 528, no. 16-17, pp. 5536–5550, 2011.

[220] S. Gao and S. Yi, "Experimental study on the anisotropic behavior of textured niti pseudoelastic shape memory alloys," *Materials Science and Engineering: A*, vol. 362, no. 1-2, pp. 107–111, 2003.

[221] S. Katsura, Y. Matsumoto, and K. Ohnishi, "Modeling of force sensing and validation of disturbance observer for force control," *IEEE Transactions on industrial electronics*, vol. 54, no. 1, pp. 530–538, 2007.

[222] M. Controzzi, C. Cipriani, and M. C. Carrozza, "Design of artificial hands: A review," in *The Human Hand as an Inspiration for Robot Hand Development*, Springer, 2014, pp. 219–246.

[223] H. Yousef, M. Boukallel, and K. Althoefer, "Tactile sensing for dexterous in-hand manipulation in robotics—a review," *Sensors and Actuators A: physical*, vol. 167, no. 2, pp. 171–187, 2011.

[224] Z. Kappassov, J.-A. Corrales, and V. Perdereau, "Tactile sensing in dexterous robot hands," *Robotics and Autonomous Systems*, vol. 74, pp. 195–220, 2015.

[225] H. Kawasaki, T. Komatsu, and K. Uchiyama, "Dexterous anthropomorphic robot hand with distributed tactile sensor: Gifu hand ii," *IEEE/ASME transactions on mechatronics*, vol. 7, no. 3, pp. 296–303, 2002.

[226] D. P. Cotton, P. H. Chappell, A. Cranny, N. M. White, and S. P. Beeby, "A novel thick-film piezoelectric slip sensor for a prosthetic hand," *IEEE sensors journal*, vol. 7, no. 5, pp. 752–761, 2007.

[227] K. Sato, K. Kamiyama, N. Kawakami, and S. Tachi, "Finger-shaped gelforce: Sensor for measuring surface traction fields for robotic hand," *IEEE Transactions on Haptics*, vol. 3, no. 1, pp. 37–47, 2009.

[228] Y.-L. Park, K. Chau, R. J. Black, and M. R. Cutkosky, "Force sensing robot fingers using embedded fiber bragg grating sensors and shape deposition manufacturing," in *Proceedings 2007 IEEE International Conference on Robotics and Automation*, IEEE, 2007, pp. 1510–1516.

[229] H. Muhammad, C. Oddo, L. Beccai, C. Recchiuto, C. Anthony, M. Adams, M. Carrozza, D. Hukins, and M. Ward, "Development of a bioinspired mems based capacitive tactile sensor for a robotic finger," *Sensors and Actuators A: Physical*, vol. 165, no. 2, pp. 221–229, 2011.

[230] F. Beyeler, A. Neild, S. Oberti, D. J. Bell, Y. Sun, J. Dual, and B. J. Nelson, "Monolithically fabricated microgripper with integrated force sensor for manipulating microobjects and biological cells aligned in an ultrasonic field," *Journal of microelectromechanical systems*, vol. 16, no. 1, pp. 7–15, 2007.

[231] M. B. Hong and Y.-H. Jo, "Design and evaluation of 2-dof compliant forceps with force-sensing capability for minimally invasive robot surgery," *IEEE Transactions on Robotics*, vol. 28, no. 4, pp. 932–941, 2012.

[232] Y. Chitalia, S. Jeong, N. Deaton, J. J. Chern, and J. P. Desai, "Design and kinematics analysis of a robotic pediatric neuroendoscope tool body," *IEEE/ASME Transactions on Mechatronics*, vol. 25, no. 2, pp. 985–995, 2020.

[233] W. Smith, *Modern Optical Engineering, 4th Ed.* Mcgraw-hill, 2007, ISBN: 9780071476874.

[234] S. T. Smith, *Flexures: elements of elastic mechanisms*. Crc Press, 2014.

[235] S. Sefati, R. J. Murphy, F. Alambeigi, M. Pozin, I. Iordachita, R. H. Taylor, and M. Armand, "Fbg-based control of a continuum manipulator interacting with obstacles," in *2018 IEEE/RSJ International Conference on Intelligent Robots and Systems (IROS)*, IEEE, 2018, pp. 6477–6483.

[236] N. Rahman, N. J. Deaton, J. Sheng, S. S. Cheng, and J. P. Desai, "Modular fbg bending sensor for continuum neurosurgical robot," *IEEE Robotics and Automation Letters*, vol. 4, no. 2, pp. 1424–1430, 2019.

[237] S. C. Ryu and P. E. Dupont, "Fbg-based shape sensing tubes for continuum robots," in *2014 IEEE International Conference on Robotics and Automation (ICRA)*, IEEE, 2014, pp. 3531–3537.

[238] I. D. Mayergoyz, *Mathematical models of hysteresis*. Springer Science & Business Media, 2012.

[239] M. E. Shirley and R. Venkataraman, "On the identification of preisach measures," in *Smart Structures and Materials 2003: Modeling, Signal Processing, and Control*, International Society for Optics and Photonics, vol. 5049, 2003, pp. 326–336.

[240] J. P. Desai and Y. C. Chitalia, *Systems and methods for steering guidewires*, US Patent App. 16/491,680, May 2021.

VITA

Yash Chitalia received a B.E. degree in electronics engineering from the Mumbai University, Mumbai, India, in 2011 and an M.S. degree in electrical engineering from the University of Michigan, Ann Arbor, MI, USA in 2013. In August 2014, he began his doctoral program in Robotics in the George W. Woodruff School of Mechanical Engineering at the Georgia Institute of Technology, Atlanta, GA, USA. His research interests include mechanical design, mechatronics, medical robot modeling and control of surgical robots and medical devices.